Provenance, structural geology, and sedimentation of the Miocene and Pliocene Californias

Thesis by

Leah Sabbeth

In Partial Fulfillment of the Requirements for
the degree of
Doctor of Philosophy in Geology

CALIFORNIA INSTITUTE OF TECHNOLOGY
Pasadena, California

2020
(Defended July 30, 2020)

To my family and Jonathan, whose endless love and support made this possible.

Leah Sabbeth
ORCID: 0000-0001-6615-7949

ACKNOWLEDGMENTS

I cannot express enough how grateful I am to have had Joann Stock and Brian Wernicke as advisors throughout my time at Caltech. You each contributed to vastly different facets of my graduate school experience. Joann, you took me on as a summer research student from Cynthia Ebinger in 2011, and have continued to advise me up until today. Your remarkable attention for scientific details makes for rich scientific stories. From your excitement about field work along the Gulf of California, to supporting women in geology, you've contributed to my desire to continue in the field. I so appreciate your warmth and understanding during my most challenging experiences of graduate school, both research and otherwise.

Brian, thank you for sharing your passion for southwestern geology with me. From your skill in recalling geological history, I have a better understanding of geology living around us. Your animation about Grand Canyon geology got me hooked onto the Sespe project, which defined a substantial part of my graduate school experience, and set me on the rafting trip of a lifetime. TAing your 101 class left me a better teacher and geologist.

In addition to my research advisors my thesis advisory committee has been remarkably helpful. Jean-Philippe Avouac, thank you for being my academic advisor, and for your good advice. The freedom I had in TAing structural geology allowed me to discover my interest in teaching, and I quite enjoyed the short time I spent working on the Ventura Avenue anticline.

George Rossman, your curious and thoughtful nature has made it such a joy to seek advice from you. I've been delighted to come to you with questions since my first stint in 2012, and I always look forward to leaving your office with different questions than when I entered. Thank you for being so kind, inquisitive, and caring.

Claire Bucholz, thank you for teaching me to use equipment in your lab, for being so patient with my missing geochemistry background, and remaining interested in my research. I am grateful that you and your lab appeared at Caltech just as I wanted to delve into XRF geochemistry and needed some guidance.

Joe Kirschvink, thank you for adding to the rich aura of the department. Your new ideas keep everyone on their toes, and your care for the student body is immense. Thank you for advising me as I worked in your lab, for being excited about my research, and for your kind nature.

Dr. Jennifer Weaver at the CTLO encouraged and deepened my interest in learning about pedagogy. Students in classes I've TAed have helped me gain practice in teaching, and have made the experiences rewarding for me.

It may sound hyperbolic, but this thesis would be unrecognizable without expert geology advice and good humor from Scott Bennett. Thank you for accompanying me twice to IAG, battling cows, rattlesnakes, and cars, and then hiking strong through 110° weather, and keeping me reassured that the funky-sounding panga motor would make it across the Ballenas Channel. Your patience with me and your passion for Gulf of California geology and natural history have been instrumental in my scientific growth. Thank you also for connecting me to Mark Stelten, whose help with argon dating and patience in explaining the argon system has been integral to this research. Arturo Martin-Barajas, thank you for guiding my field excursions, and for being so kind and helpful both with science and logistics. I've enjoyed working alongside your students.

Ricardo Arce and his boat crew, Mario and Isaiah, transported me and field workers to and from IAG four times. I am so appreciative for such safe, careful panga driving. Winds were reliably strong, and I was relieved to have such experienced boatmen. You all were meticulous with safety, both in the water and out. You picked campspots for us, sheltered from wind and fishermen, and slept in the pangas to make sure the boats would still be there for us in the morning. Mario and Ricardo drove an hour outside of BLA to rescue us after the cow incident. Ricardo and Isaiah made some delicious ceviche!

Adriana Piña-Paez, you let me supervise your SURF project in 2018. An expert in petrology, you contributed to my XRF and petrographic data, and you helped me better understand geochemistry. I am grateful for the opportunity to be your advisor for a summer, and am so proud of you for winning a student oral presentation competition at INAGEQ. Congratulations on your successful thesis defense!

Friends and colleagues here have undoubtedly made graduate school more special and enjoyable. Certainly I will unintentionally omit some individuals, but I'd be remiss to not call out a few. Amber W, you were delightful as a field TA, friend, and colleague, and you made me feel like part of a lab group in GPS. Daven Q, you always have cool geology apps to share and are a joy to catch up with. Jason P, you enthusiastically showed me some very tedious mineral separation processes, and it has since been a delightful surprise whenever you pop up. Sarah S, thank you for imparting upon me an interest in paleomag early on, and for being such an excellent TA. Steve S, thank you for any and all IAG-related wisdom you've left me with. Ted P, thank you for being a jovial voice down the hall, and especially for going into lab to find my photomicrographs. Lee S, thank you for being a less jovial voice down the hall, but still a pleasure to chat with, and an excellent resource for good recipes (how are our names so similar!). Usha L and Hao X, you've been such lovely officemates. Alistair, thank you for the rare and insightful moments. Peter M, thank you for telling it like it is - if I recall correctly, you predicted the 2016 election. Dan J, thank you for being so kind and open. Celeste L, thank you for your good company and your dedication to WinG. Preston K, thank you for lending me your remote-controlled car. Clare S, thank you for bonding with me about sibling age differences, and for the early morning hikes. Voon L, I miss you so much in Australia – you are always such a joy, and always find a silver lining. Elizabeth B, thank you for introducing me to quality cooking knives, early morning hikes, and Venus (!). Juliet RD, thank you for all the sporadic moments of wisdom and humor you bring me. Sarah Z, thank you for being the friend who always understands. Joe B, thank you for addressing so many of my paleomag related questions, and for the expertly planned Enrichment Trip to the Arctic. Madison D, I am so glad to have found you as both a flute duet partner, and as a fellow Grand Canyon enthusiast - flute duets have been such a special part of the last few years.

Maddie L, you've been on so many adventures with me, and have consistently kept me safe. I cannot thank you enough for coming to IAG with me and Scott and the UCLA folks. Your expert field assistance and humor made for a great trip, you helped me with igneous rocks, and I know you will always look at cows differently. I loved driving through Alaska with you, and was so glad that found me after I fell down a whole flight of icy metal stairs. Your hard work on the art committee reached so many students, and we should all be grateful for your artistic creativity in addition to your skill in geology.

Mali Z, thank you for being such a sincere friend, and for taking me on a trip of a lifetime. Matt O, thanks for always being there – I'll try and remember your birthday. Hye Sung, thank you for keeping me playing flute. Thank you to Claudia at the pool for all the swimming tips.

Jay, thank you for your GIS and Agisoft help, and for understanding when the drone came back less than perfect. Mark G, thank you for making every field excursion of mine possible – particularly for the tow rope and new radios. Lisa Christiansen, you've been patiently helping me with ArcGIS struggles since 2011, I so appreciate your kindness. Donna Mireles, you've watched after every field trip of mine, and made sure each one went smoothly and that I was reimbursed. Liz Boyd, thank you for organizing my visiting weekend and making my first year go smoothly. Julie Lee, you've kept me out of academic "trouble" and have been so kind every time I've come to your office. Julia Z and Aleen, thank you for looking out for our safety and well-being. Thank you to janitorial staff - you have been so friendly in early mornings, have kept spaces I work in safe and clean, and I so appreciate your extra hard work during the pandemic.

Kathy, you first welcomed me to LA; Jim, you taught me how to drive on LA highways; Myron and Anita, you've been so curious about my research; Eve, I know you would be proud. Chandler, thank you for being such a loving friend. Katie, Nico, and Rosie, thank you for your love and support from afar.

My parents, Danny and Barbara, you have been so loving and so supportive from so far. I miss you so much, and can't wait to see you in person. Somehow upon choosing Caltech, I didn't realize that I would be so far for so long, and the distance has not been easy. Thank you for caring so much about me and my well-being, for imparting upon me a curiosity in what goes on around me, and for ultimately for being so loving and thoughtful.

Jonathan, I am so grateful for your culinary skill, for your joyful nature, particularly each time I returned from the island, and, more than anything, for making most of this PhD so doable. You've been so patient, kind, loving, and supportive, and I can't thank you enough for always being this way. Your heart is so big, and I love you so much.

ABSTRACT

The first chapter of this thesis documents a provenance study, in which orthoquartzite clasts deposited in the Miocene Sespe Formation are linked to the Mesoproterozoic Shinumo Quartzite. The Sespe Formation outcrops in the Santa Monica Mountains and the Santa Ana Mountains, both in California. The Shinumo Quartzite outcrops only in Grand Canyon. We determine that the Shinumo Quartzite can be distinguished from other sources that may feed the Sespe Formation through its unique combination of a moderate paleomagnetic inclination and 1.2, 1.4, and 1.7 Ga detrital zircon spectrum peaks. This provenance link places an important constraint on the drainage of a paleo-Colorado River from Grand Canyon during Miocene time.

The second and third chapters of this thesis are hinged upon a geologic mapping project on Isla Ángel de la Guarda, a microcontinental block, in Baja California, Mexico. A plate reorganization at the end of the late Miocene andesitic arc marks the transfer of Baja California and the not-yet-rifted Isla Ángel de la Guarda to the Pacific plate from the North American plate. Between 3 and 2 Ma, the plate boundary jumped again, northward along the Ballenas Transform fault. In this Pliocene time, units mapped in this study were deposited.

The oldest units mapped are Miocene-Pliocene volcanic flows, for which we have no lower age constraint. The oldest volcanic flow dated is a Pliocene andesite lava (3.916 ± 0.088 Ma from $^{40}Ar/^{39}Ar$). We map Miocene to Pliocene volcanic flows and Pliocene to Quaternary sedimentary units in two field areas. The sedimentary units are probably results of Pliocene rifting-related basin subsidence. Geochemical data from X-ray fluorescence indicate that lavas are compositionally similar to ~12 Ma arc-related rocks mapped in the Puertecitos Volcanic Province. In the southern field area, the sedimentary units are overlain by a Pliocene basaltic andesite with an $^{40}Ar/^{39}Ar$ age of 2.754 ± 0.021 Ma. We map several NNE-striking faults throughout both field areas, which cut NNW-striking bedding in Pliocene units. The Pliocene volcanic flows and sedimentary units were probably tilted

before faulting, and the faults are likely linked to the Northern Salsipuedes Basin, offshore of the island in the Ballenas Channel. Both of these events may be results of 3-2 Ma rifting.

PUBLISHED CONTENT AND CONTRIBUTIONS

Leah Sabbeth, Brian P. Wernicke, Timothy D. Raub, Jeffrey A. Grover, E. Bruce Lander, Joseph L. Kirschvink; Grand Canyon provenance for orthoquartzite clasts in the lower Miocene of coastal southern California. Geosphere ; 15 (6): 1973–1998. doi: https://doi.org/10.1130/GES02111.1

Sabbeth collected and prepared samples, ran paleomagnetic experiments and analysis, analyzed detrital zircon data, organized and analyzed pre-existing data, conceived the paleomagnetic inclination spectra, and co-wrote the publication with Wernicke.

Supplemental Tables (not included in this thesis)

Table S1: Columns show sample number, measurement type (alternating field—AF; thermal—TT), field strength (mT) or temperature (T), declination and inclination, publicly available in full form at the MagIC Data Repository (https://earthref.org/MagIC/16684).

Table S2: Sheets in Excel file include detrital zircon ages from LaserChron and Apatite to Zircon of Sespe orthoquartzite clasts and Shinumo Formation, publicly available in California Institute of Technology Research Data Repository (https://data.caltech.edu/records/1245).

Table of Contents

List of Figures

Figure Number Page

Chapter 1

Chapter 2

Chapter 3

List of Tables

Introduction

This thesis is motivated by the rich geological history of the Californias, spanning from well before 20 Ma to ~2.5 Ma. Before substantial right-lateral shear along the San Andreas system, the Sespe Formation was deposited at the mouth of a paleo-Colorado River, with clasts derived from the continental interior. Later, at the end of the Miocene volcanic arc, plate reorganization separated Pacific Plate, including Baja California, from the North American Plate. Between 3 and 2 Ma, extension moved northward along the Ballenas Channel, from the Northern Salsipuedes to the Lower Delfin Basin, and units mapped in this study were deposited. Isla Ángel de la Guarda became its own block, separated from Baja California. Isla Ángel de la Guarda is most similar to geologically, and part of geopolitically, the state of Baja California in Mexico.

Chapter one adds an important timing constraint to the carving of Grand Canyon. Models of erosion in the region existing before this study rely mainly on thermochronologic data. Models of thermochronological data place a kilometer-scale unroofing event c. 28-18 Ma. Although this is a point of agreement amongst researchers, the data has not led to consensus regarding the role of the c. 6 Ma Colorado River versus the drainage systems from as long ago as the Laramide in carving Grand Canyon. This study, independent of thermochronological data, places a minimum age constraint on the time at which the canyon was carved.

We examine a depocenter along the margins of the Cordillera and take advantage of the arrival of unique clast types in the c. 27-20 Ma Sespe Formation, which were observed by previous researchers. If the Shinumo Formation, a Mesoproterozoic orthoquartzite, were a correlation to clasts in the Sespe Formation, this match would indicate that a paleo-Colorado River carved to the depth of the Shinumo Formation by the time the Sespe Formation was deposited. After examination of possible sources for the clasts, which include Grand Canyon (Shinumo Formation), the Death Valley-Mojave region, the central Arizona highlands, and the Caborca area of NW Sonora, Mexico, we determined that the Shinumo Formation is unique from the other sources with its combination of a moderate paleomagnetic inclination and detrital zircon age spectra with peaks of 1.2, 1.4, and 1.7 Ga. Eight orthoquartzite clasts from the Sespe Formation displayed the combined moderate paleomagnetic inclination and 1.2, 1.4, and 1.7 Ga detrital zircon age spectra peaks, indicating that the clasts are derived from the Shinumo Formation. This demonstrated inclusion of Shinumo clasts in the Sespe drainage system confirms that the Upper Granite Gorge of eastern Grand Canyon had been eroded to within a few hundred meters of its current depth (to the depth of Shinumo) by c. 20 Ma (deposition of the Sespe Formation). Of course, the Sespe Formation has since been translated ~200 km by right-lateral shear of the San Andreas system. The Colorado River currently drains to the Colorado River Delta at the northern tip of the Gulf of California.

Chapters two and three focus on Miocene to Pliocene volcanic flows and Pliocene to Quaternary sedimentary units in two field areas on southeastern Isla Ángel de la Guarda. These units were deposited just before and during the plate boundary shift along the Ballenas Channel between 3 and 2 Ma. We discuss geological mapping, X-ray fluorescence geochemical data, $^{40}Ar/^{39}Ar$ geochronology, and a Pliocene sedimentary sequence indicative of a marine incursion.

Based on X-ray fluorescence geochemical data, the lavas are compositionally intermediate, and similar to ~12 Ma arc-related rocks mapped in the Puertecitos Volcanic Province. However, the oldest sample for which we have an $^{40}Ar/^{39}Ar$ age is 3.916 ± 0.088 Ma, well after the andesitic arc was active. Possibly the lavas are derived from deep-seated mafic rocks, or melts of pre-existing continental crust.

Contact relationships between lavas are most clear in the northern field area, which has lava compositions ranging from dacite to andesite. Most units throughout both field areas dip gently and become younger to the East. In the southeastern-most area of our mapping, compositions determined by XRF range from rhyolite to basalic andesite and Pliocene sediments are exposed. These sediments are both underlain and overlain by lavas. The older lava, a dacite, has an $^{40}Ar/^{39}Ar$ age of 2.925 ± 0.012 Ma; the younger basaltic andesitic lava has three $^{40}Ar/^{39}Ar$ ages of 2.754 ± 0.021 Ma, 2.756 ± 0.079 Ma, and 3.16 ± 0.42 Ma (a maximum age). These ages constrain the sedimentary unit to a time period of ~170 ka.

The base of the Pliocene sedimentary unit contains inversely graded pumice and lithic fragments, indicating that the fragments were sorted by water that they fell into. The unit locally contains fossils, including pectens and oysters, which are indicative of a marine depositional environment. The top of the marine unit is well defined by both a baked contact from the overlying basaltic andesite, and by a lava bomb within the top of the unit exhibiting a paleoliquifaction structure as the matrix around it. The Pliocene sediments mapped in this study are remarkably similar in composition and in age to those mapped in Bahia de Guadalupe. Although Bahia de Guadalupe and southeastern Isla Ángel de la Guarda would have been ~50 km apart during the time of deposition, it is apparent that similar depocenters frequented the western shores of the Gulf of California during late Pliocene time.

Faults are pervasive throughout both field areas, and generally are subparallel, striking NNE. These faults cut both mapped lavas and Quaternary terraces. The faults are recent, evident from sag ponds and rearranged sediments in arroyos. The faults are mostly east-dipping, with vertical separation down-to-the-east, and subequal amounts of separation are found on faults throughout the study area. Many faults continue for kilometers, and some extend through the island towards and possibly into the Northern Salsipuedes Basin. These east-dipping faults and east-dipping stratigraphy are indicative of a particular geometry that embodies a major west-dipping normal fault, at depth, which would crop out east of Isla Ángel de la Guarda, under water in the Gulf of California.

C h a p t e r 1

Chapter 1: Grand Canyon provenance for orthoquartzite clasts in the lower Miocene of coastal southern California

Leah Sabbeth, Brian P. Wernicke, Timothy D. Raub, Jeffrey A. Grover, E. Bruce Lander, Joseph L. Kirschvink; Grand Canyon provenance for orthoquartzite clasts in the lower Miocene of coastal southern California. Geosphere: 15 (6): 1973–1998. doi: https://doi.org/10.1130/GES02111.1

ABSTRACT

Orthoquartzite detrital source regions in the Cordilleran interior yield clast populations with distinct spectra of paleomagnetic inclinations and detrital zircon ages that can be used to trace the provenance of gravels deposited along the western margin of the Cordilleran orogen. An inventory of characteristic remnant magnetizations (CRMs) from >700 sample cores from orthoquartzite source regions defines a low-inclination population of Neoproterozoic-Paleozoic age in the Mojave Desert-Death Valley region (and in correlative strata in Sonora, Mexico), and a moderate- to high-inclination population in the 1.1 Ga Shinumo Formation in eastern Grand Canyon. Detrital zircon ages can be used to distinguish Paleoproterozoic to mid-Mesoproterozoic (1.84 to 1.20 Ga) clasts derived from the central Arizona highlands region from clasts derived from younger sources that contain late Mesoproterozoic zircons (1.20 to 1.00 Ga). Characteristic paleomagnetic magnetizations were measured in 44 densely cemented orthoquartzite clasts, sampled from lower Miocene portions of the Sespe Formation in the Santa Monica and Santa Ana mountains, and from a middle Eocene section in Simi Valley. Miocene Sespe clast inclinations define a bimodal

population with modes near 15° and 45°. Eight samples from the steeper Miocene mode for which detrital zircon spectra were obtained all have spectra with peaks at 1.2, 1.4, and 1.7 Ga. One contains Paleozoic and Mesozoic peaks and is probably Jurassic. The remaining seven define a population of clasts with the distinctive combination of moderate to high inclination and a cosmopolitan age spectrum with abundant grains younger than 1.2 Ga. The moderate to high inclinations rule out a Mojave Desert-Death Valley or Sonoran region source population, and the cosmopolitan detrital zircon spectra rule out a central Arizona highlands source population. The Shinumo Formation, presently exposed only within a few hundred meters elevation of the bottom of eastern Grand Canyon, thus remains the only plausible, known source for the moderate- to high-inclination clast population. If so, then the Upper Granite Gorge of the eastern Grand Canyon had been eroded to within a few hundred meters of its current depth by early Miocene time (c. 20 Ma). Suh an unroofing event in the eastern Grand Canyon region is independently confirmed by (U-Th)/He thermochronology. Inclusion of the eastern Grand Canyon region in the Sespe drainage system is also independently supported by detrital zircon age spectra of Sespe sandstones. Collectively, these data define a mid-Tertiary, SW-flowing "Arizona River" drainage system between the rapidly eroding eastern Grand Canyon region and coastal California.

INTRODUCTION

Among the most difficult problems in geology is constraining the kilometer-scale erosion kinematics of mountain belts (e.g. Stüwe et al., 1994, House et al., 1998). A celebrated example of the problem, and the subject of vigorous contemporary debate, is the post-100 Ma erosion kinematics of the Colorado Plateau of western North America (e.g. Pederson et al., 2002), and especially of the Grand Canyon region (e.g. Polyak et al., 2008; Karlstrom et al., 2008, 2014, Flowers et al., 2008, Wernicke, 2011, Beard et al., 2011; Flowers and Farley, 2012, 2015; Lucchitta, 2013; Hill and Polyak, 2014; Darling and Whipple, 2015; Fox et al., 2017; Winn et al., 2017). The erosion problem of the plateaus is particularly well-posed. It was a broad cratonic region that lay near sea level for most of Paleozoic and Mesozoic time (e.g. Burchfiel et al., 1992). During the Late Cretaceous-Paleogene Laramide orogeny, the Cordilleran orogen roughly doubled in width. The Colorado Plateau and southern Rocky Mountains thus underwent a transition from residing near sea level, as a retroarc Cordilleran foreland basin during the Late Cretaceous, to a mountain belt residing at elevations of 1 to 2 km during Paleogene and younger time (e.g., Elston and Young, 1991, Flowers et al., 2008, Hill et al., 2016, Huntington et al., 2010, Karlstrom et al., 2014, Winn et al., 2017). The key challenge posed by this framework lies in using thermochronological information on the unroofing history, and the distribution of sedimentary source regions and corresponding depocenters, to constrain erosion kinematics.

Existing models of erosion kinematics of the region differ mainly in the role they assign to the modern Colorado River (c. 6 Ma and younger), versus more ancient drainage systems dating back to Laramide time. Despite the lack of consensus, a significant and recent point of agreement, based primarily on thermochronological data, is that a kilometer-scale erosional unroofing event occurred in mid-Tertiary time (c. 28-18 Ma) in the eastern Grand Canyon region (Figure 1; Flowers et al., 2008; Lee et al., 2013; Karlstrom et al. 2014; Winn et al., 2017). This unroofing event (described in more detail in the next section) is relatively localized compared with erosion histories of adjacent regions across orogenic strike to the SW and NE, also defined by thermochronological data. To the SE in the Arizona Transition Zone and Mojave-Sonora Desert region, unroofing to near-present levels occurred in Laramide time (c. 80-40 Ma), with the exception of rocks tectonically exhumed by Tertiary extension (Bryant et al., 1991; Foster et al., 1992; Spotila et al., 1998; Blythe et al., 2000; Mahan et al., 2009; Fitzgerald et al., 1991, 2009). To the NE, in the Colorado Plateau interior, erosional unroofing occurred mainly after 10 Ma, presumably as a result of integration of the Colorado River drainage system at 6 Ma (e.g., Pederson et al., 2002; Flowers et al., 2008; Wernicke, 2011; Hoffman et al., 2011; Winn et al., 2017; Karlstrom et al., 2017).

Independent of thermochronological data, constraints on erosion kinematics are imposed by the arrival of specific clast types within basins along the flanks, placing a minimum age on the time at which any particular clast type was exposed to erosion. The overall pattern of unroofing thus motivates examination of depocenters along the margins of the Cordillera for evidence of unroofing in the Cordilleran interior, such as migration of drainage divides toward the interior (e.g. Ingersoll et al., 2018). In particular, the mid-Tertiary unroofing event predicts the appearance of eroded detritus from the eastern Grand Canyon region in mid-Oligocene to early Miocene depocenters.

We investigate this hypothesis by applying a new technique that combines paleomagnetic inclination spectra and detrital zircon age spectra of conglomerate clast populations to the gravel fraction of the Sespe Formation, a mid-Tertiary conglomeratic sandstone interval that is broadly distributed throughout coastal southern California (Figure 2) (Howard, 2000, 2006; Ingersoll et al., 2013, 2018). We focus on the orthoquartzite clast population (as opposed to volcanic, metavolcanic, and metaquartzite clasts also abundant in the Sespe Formation), because it is both ultradurable and its potential sources are widely exposed in the headwater regions of all proposed major paleodrainages tributary to the Sespe basin (Figure 1). The scope of our study includes characteristic remnant magnetizations (CRMs) from 44 samples from the Sespe orthoquartzite clast population, collected from three well-dated Sespe exposure areas. We compare these data with CRMs of some 700 samples from potential source regions in the Death Valley-Mojave region, the central Arizona highlands, Grand Canyon, and Sonora, Mexico. Our study also includes 936 detrital zircon ages from 12 Sespe orthoquartzite clasts, which we compare to 1,870 detrital zircon ages from 23 samples of potential sources.

GEOLOGIC BACKGROUND

Sespe Formation

The modern outcrop distribution of the Sespe Formation (Figure 2) has been substantially modified by right-lateral shear on the San Andreas fault system and transrotation of the Western Transverse Ranges (e.g. Howard, 1996; Atwater and Stock, 1998). The mid-Tertiary configuration of the Sespe basin can be determined with a high degree of confidence on the basis of palinspastic reconstructions (e.g. Atwater and Stock, 1998; McQuarrie and Wernicke, 2005; Jacobson et al., 2011; Ingersoll et al., 2018), all of which restore the most proximal Sespe depocenters (Santa Monica and Santa Ana mountains) to a position near the modern Colorado River delta (Figure 1).

The middle Eocene to lower Miocene Sespe Formation consists predominantly of fluvial to deltaic sandstone and conglomerate, ranging from a few hundred up to 1,000 meters thick (e.g. Howard, 1989, 2000; Schoellhamer et al., 1981). Although much of the Sespe Formation appears to be Eocene, it also contains an Oligocene to early Miocene component that includes tongues of marine strata. The younger strata have locally been defined as the ca. 27-20 Ma Piuma Member, the upper part of which is paleontologically dated as Hemingfordian in the Santa Monica and Santa Ana mountains (e.g. Lander, 2011, 2013). Compositionally, Sespe sandstones are lithic-poor arkoses derived predominantly from granitic source rocks, with 50% to 95% of detrital zircon ages indicating provenance within the Mesozoic Cordilleran arc, and the remainder derived from various primary and recycled sources of pre-300 Ma grains (Ingersoll et al., 2013, 2018).

Sespe Formation conglomerates are dominated by populations of highly survivable volcanic, metavolcanic, and quartzitic clasts, with smaller populations of less durable rock types (Woodford et al., 1968; Abbott and Peterson, 1978; Howard, 1989; Belyea and Minch, 1989; Minch et al., 1989). The quartzite clast population can be subdivided into orthoquartzites and metaquartzites. Orthoquartzite is defined as an unmetamorphosed quartz arenite with a densely cemented silica matrix (Howard, 2005) and is distinguished from metaquartzite petrographically, due to the destruction of detrital grain boundaries beginning under sub-greenschist to lower greenschist facies conditions (Wilson, 1973; Howard, 2005). Our focus on orthoquartzite is motivated by two key considerations.

First, crystalline sources tend to be proximal to the coast, and consist mainly of feldspathic rock types that are only moderately durable, with the exception of ultradurable metarhyolite, chert, and metaquartzite clasts (e.g., Abbott and Peterson, 1978). It has long been established that orthoquartzite clasts in the Sespe Formation are derived from relatively distant sources within the Cordilleran interior (Howard, 1996, 2000), generally well NE of source regions for clasts of metaquartzites and most crystalline rocks (Figure 1). Crystalline source regions also occur in the Cordilleran interior, but, given the moderate durability of crystalline clasts (owing to both the mechanical weakness of cleavage and solubility of feldspar), they tend to be eliminated from the gravel fraction during long transport, especially in the presence of ultradurable quartzitic clasts (e.g., Abbott and Peterson, 1978). Fingerprinting of orthoquartzite clasts in the basins thus affords a broad aperture for the observation of erosion kinematics using this approach (Howard, 1989, 2000). Second, one potential Sespe orthoquartzite source, the 1.1 Ga Shinumo Formation, is at present only exposed within a few hundred meters elevation of the bottom of eastern Grand Canyon, in the Upper Granite Gorge area (Figure 3). Its appearance in the Sespe Formation would therefore constrain the time by which eastern Grand Canyon was in existence, more-or-less as it is today, greatly limiting the extant range of erosion models.

Orthoquartzite Source Regions

Eastern Grand Canyon is, however, only one of four potential source regions in the Cordilleran interior for orthoquartzite clasts (Figure 1). The other three include (1) the Death Valley-Mojave region, which contains Neoproterozoic-Cambrian orthoquartzites (e.g. Stewart et al, 2001; Shoenborn et al., 2012), (2) the central Arizona highlands, which contain late Paleoproterozoic to mid-Mesoproterozoic orthoquartzites (e.g. Mulder et al., 2017; Doe et al, 2012), and (3) the Caborca area of NW Sonora, Mexico, which contains Neoproterozic-Cambrian orthoquartzites in strata correlative with the Death Valley-Mojave strata (Gehrels and Stewart, 1998; Stewart et al., 2001). In the broader Sonoran region (mainly south of the area shown in Figure 1), widespread exposures of Jurassic conglomerates (Coyotes Formation and equivalents) contain orthoquartzite clasts of presumed Proterozoic-early Paleozoic age (Stewart and Roldán-Quintana, 1991). In NW Sonora, the only known Mesoproterozoic quartzites, which may or may not be orthoquartzite, occur in a small exposure (6.5 km^2) at Sierra Prieta (Figure 1), where they are intruded by ca. 1.08 Ga anorthosite sills (Izaguirre and Iriondo, 2007; Molina-Garza and Izaguirre, 2008).

Various Tertiary paleodrainages have been proposed to connect these potential source regions with mid-Tertiary coastal basins in southern California (Howard, 2000, 2006; Ingersoll et al., 2018). These include the Poway (Abbot and Smith, 1989), Amargosa (Howard, 2000), Gila (Howard, 2000), Arizona (Wernicke, 2011), and Tejon (Lechler and Niemi, 2011) paleodrainage systems (Figure 1).

To distinguish among these source regions, we augment previous studies of orthoquartzite clasts and sources (Howard, 1989, 1996, 2000, 2006) with a novel method, using the combination of paleomagnetic inclination and detrital zircon spectra of orthoquartzite clast populations, to trace provenance (Wernicke et al., 2010, 2012; Wernicke, 2011; Raub et al., 2013). A key finding from the earlier conglomerate studies was that lowest Sespe sources appear to be dominated by a Gila paleodrainage system, which included (1) Paleoproterozoic orthoquartzites from the central Arizona highlands, and (2) metarhyolite clasts derived from southeastern Arizona. The system appears to have evolved by Oligocene time into a more latitudinally extensive system to include a component of metavolcanic and orthoquartzite clasts from the Death Valley-Mojave region (Howard, 2000, 2006).

An important distinction between the Sespe Formation and its Eocene equivalent in the San Diego area, the Poway Group, is the percentage and petrology of quartz porphyry metarhyolite clasts (Belyea and Minch, 1989; Woodford et al., 1968, 1972). In the Poway Group, quartzites constitute up to 24% of the clast population, which averages 73% quartz porphyry metarhyolite clasts (Bellemin and Merriam, 1958). These "Poway-type" metarhyolite clasts have been texturally and geochemically traced to bedrock sources in the Caborca region of Sonora, Mexico (Figure 1)

(Abbott and Smith, 1989). The Sespe Formation, in contrast, contains a much smaller percentage (<10%) of metarhyolite clasts, which are petrographically and geochemically dissimilar to Poway-type clasts and Sonora metarhyolites, but are similar to Jurassic metarhyolites from the Mt. Wrightson Formation of southeastern Arizona (Abbott et al., 1991). These relations are generally interpreted to indicate that the Poway Group and Sespe Formation represent distinct drainage basins in Eocene time (Woodford et al., 1968, 1972; Kies and Abbott, 1983; Belyea and Minch, 1989; Abbott et al., 1991; Howard, 2000, 2006). Although there may be some overlap of the two source areas (e.g., Ingersoll et al., 2018), transport of significant quantities of Caborca-area orthoquartzites (either Mesoproterozoic Sierra Prieta or Neoproterozoic-Cambrian strata, Figure 1) in a regional drainage system of any age would also result in a preponderance (≥3:1) of Poway-type clasts relative to the orthoquartzite component, as suggested by the clast composition of the Poway group. The lack of Sonora-derived metarhyolite clasts in the Sespe drainage basin thus strongly suggests the absence of any significant drainage connection between NW Sonora and the Sespe basin.

Two key attributes have the potential to distinguish between a population of clasts with Shinumo provenance from populations derived from Death Valley-Mojave or central Arizona highlands sources: (1) moderate to high paleomagnetic inclination, and (2) the presence of late Mesoproterozoic (1.3-1.0 Ga) or "Grenville-age" detrital zircon. Whereas orthoquartzite populations from the Death Valley-Mojave region generally contain abundant 1.3-1.0 Ga detrital zircons, their CRMs are of low inclination (0-30°), contrasting them with the Shinumo population. Whereas orthoquartzite populations from the central Arizona highlands may have moderate to high inclinations, they are mostly too old to contain 1.3-1.0 Ga detrital zircons, distinguishing them from the Shinumo population. Therefore, identification of these attributes within a population of Sespe orthoquartzite clasts has the potential to distinguish a Shinumo source from the other sources. If the Shinumo Formation is a Sespe gravel source, it would strengthen the “Arizona River” hypothesis (Wernicke, 2011), independent of low-temperature thermochronometry studies on which it is based (e.g. Flowers et al., 2008, 2015; Wernicke, 2011 Flowers and Farley, 2012; 2013). According to this hypothesis, the mid-Tertiary drainage configuration of the Cordillera included a paleoriver system with headwaters cut near the modern level of erosion of the Upper Granite Gorge area in the eastern Grand Canyon region.

Below, we present paleomagnetic and detrital zircon data from three Sespe clast populations and one potential source rock from the Shinumo Formation, as well as a compilation of existing paleomagnetic and detrital zircon data from the literature. We then compare data from the various source populations with data from Sespe clast populations, focused on the issue of which, if any, of the Sespe clast populations indicate a Shinumo provenance.

Mid-Tertiary (28 to 18 Ma) Unroofing of the Southwestern Colorado Plateau

As noted above, the primary erosional event in the Cordilleran interior during upper Sespe (Piuma) time occurred within a NW-trending zone, running from the eastern Grand Canyon region through east-central Arizona (Figure 1), contrasting it with predominantly Laramide unroofing to the SW in the Mojave-Sonoran region and post-10 Ma unroofing to the NE on the Colorado Plateau. In addition to thermochronological data, this event is recorded by kilometer-scale erosion between aggradation of the Eocene to lower Oligocene Chuska Formation and aggradation of the Miocene Bidahochi Formation, whose ages bracket the unroofing event between 26 and 16 Ma

(Cather et al., 2008). Numerous thermochronological cooling models indicate approximately 30 °C of cooling at that time, from about 60 °C prior to 28 Ma (with some interpretations of the data suggesting temperatures as high as 80-90 °C in the Upper Granite Gorge prior to 28 Ma) to <30 °C after 18 Ma (Flowers et al., 2008; Flowers and Farley, 2012; Lee et al., 2013; Karlstrom et al., 2014; Winn et al., 2017).

In the Upper Granite Gorge of eastern Grand Canyon, where the Shinumo Formation is exposed (Figure 3), the 30 °C (or less) temperatures at the end of the 28-18 Ma erosion event were probably very close to surface temperatures in the SW US, indicating very little post-18 Ma erosion (Flowers et al., 2008; Flowers and Farley, 2012, 2014; Wernicke, 2011; Karlstrom et al., 2014; Winn et al., 2017). Modern surface temperatures measured throughout the interior of the SW US (Sass et al., 1994) vary according to

$$T_s(h) = (29 \pm 2)°C + (-8 \pm 1°C/km)h,$$

where T_s is surface temperature, and h is elevation above sea level (Equation 7 in Wernicke, 2011). Early Miocene surface temperatures were at least 3°C, and perhaps as much as 8°C, warmer than today (e.g. Huntington et al., 2010). Hence, assuming no erosion, rocks now exposed at a modern elevation of 600 m at the bottom of eastern Grand Canyon, would have T_s in the range of 27°C to 32°C, depending on the degree of atmospheric cooling since 20 Ma. However, some additional erosion must have occurred after the 28-18 Ma unroofing event. Given a very conservative upper temperature limit for river-level samples of 40°C after mid-Tertiary erosion ended (see discussion of error sources for these estimates in Wernicke, 2011, p. 1303-1305) and an early Miocene upper crustal geothermal gradient of 25°C/km (based on thermochronometric profiles through tilted fault blocks in the eastern Lake Mead region; e.g. Quigley et al., 2010, and discussion on p. 1295 in Wernicke, 2011), net erosion since 18 Ma would lie in the range

$$(8 \text{ to } 13°C)/(25\ °C/km)/(1000\ m/km) = 320 \text{ to } 520\ m,$$

which corresponds to a maximum average regional erosion rate of 18 to 29 m/Myr.

This erosion rate for the bottom of eastern Grand Canyon is in good agreement with the late Tertiary erosional history of the surrounding plateau region based on stratigraphic constraints. Just south of eastern Grand Canyon, the basalt at Red Butte, which lies on an erosion surface 220 m above the surrounding Coconino Plateau, is 9 Ma (Reynolds et al., 1986), indicating an average erosion rate of 24 m/Myr since then (Figure 3). East of Grand Canyon, average regional erosion since 16 Ma (i.e., regional unroofing below the basal Bidahochi unconformity) is at most 300 to 400 m (e.g. Fig. 15 in Cather et al., 2008), suggesting rates of 19-25 m/Myr, albeit much of the erosion may have been concentrated in the last 6 Myr at higher rates (Karlstrom et al., 2017).

In the Upper Granite Gorge area, the Shinumo Formation is the most erosionally resistant unit within the gently north-tilted Grand Canyon Supergroup. It is the only stratified unit in eastern Grand Canyon that contains abundant ultradurable orthoquartzite. It eroded into steep, south-facing cuestiform ridges, during both Cenozoic erosion and erosion prior to the Cambrian Sauk transgression, when it formed a series of paleoislands (Figure 3). The Cambrian paleoislands rose 100 to 200 m above the coastal plain, around which Tonto Group strata, including sandstones of the Tapeats Formation, were deposited in buttress unconformity (Figure 3; Noble, 1910, 1914; Sharp, 1940; McKee and Resser, 1945; Billingsley et al., 1996; Karlstrom and Timmons, 2012). At present, the Shinumo Formation crops out in a 70 km-long, quasi-linear array of seven exposure areas, with each area 2 to 5 km long, as measured parallel to the array, mostly on the north side of the modern Colorado River (e.g. Figure 3.1 in Hendricks and Stevenson, 2003). The Shinumo Formation is now preserved at elevations as much as 600 m above the modern river level (Billingsley et al., 1996). If our estimate of 300-500 m of post-18 Ma erosion is correct, the Shinumo Formation would have been a highly proximal source of ultradurable, gravel-sized clasts in the high-relief headwaters of a mid-Tertiary Arizona River (Figure 3).

A second significant source of orthoquartzite in the Grand Canyon region is the Tapeats Formation, but only in the Lower Granite Gorge area of western Grand Canyon (Figure 1) where it is the oldest exposed stratified unit. In eastern Grand Canyon, exposures of the Tapeats Formation, in contrast to much of the Shinumo Formation, are not densely cemented orthoquartzites (Billingsley et al., 1996). In the Lower Granite Gorge area, however, a large fraction of the Tapeats Formation is "quartzitic and very hard," in contrast to relatively weak sandstones in the remainder (p. 16 in McKee and Resser, 1945).

SAMPLING AND METHODS

We sampled Sespe gravel clasts from the Santa Ana and Santa Monica mountains and from Simi Valley (Figure 2). We also collected several samples of potential source rocks, in order to reproduce results from extensive existing paleomagnetic and detrital zircon data (Elston and Grommé, written commun., 1994; Bloch et al., 2006; Mulder et al., 2017), including one sample of the Shinumo Formation, and one sample each of the Shinumo and Tapeats formations from the Caltech sample archive (Table 1).

Because dated Sespe sections range broadly in age, from middle Eocene to early Miocene (c. 48 to 20 Ma), sample locations (Figure 2) were restricted to three sections with local paleontological, radiometric, and magnetostratigraphic control of depositional age. They included (1) a middle Eocene section in Simi Valley (exposed along View Lane Drive at the terminus of exit 22A of California Highway 118; Kelly and Whistler, 1994; Kelly et al., 1991; Lander, 2013), (2) the lower Miocene Piuma Member in the Saddle Peak area of the western Santa Monica Mountains (exposed along upper Piuma Road and upper Schueren Road, along and near the range crest) (Lander, 2011, 2013), and (3) correlative lower Miocene strata in the Limestone Canyon Park area of the Santa Ana Mountains (Red Rock Canyon Trail and a nearby roadcut through the "marker conglomerate" horizon (Belyea and Minch, 1989) on Santiago Canyon Road (Figure 2).

In these areas of exposure, in situ paleomagnetic sampling of orthoquartzite clasts in quantity proved to be unfeasible, precluding a conglomerate test. Steep badlands topography along ridgecrest exposures of the Sespe Formation results in a scarcity of exposed orthoquartzite clasts in outcrops that are both sufficiently indurated and accessible for in-situ drilling. Orthoquartzite clasts were mainly sampled from thin, proximal colluvial deposits within a few meters of their Sespe bedrock sources. As discussed further below, the results of Hillhouse (2010) and this study indicate that the CRMs of Sespe orthoquartzite clasts predate weathering, transport, and deposition of the clasts, and diagenesis of their sandstone matrix.

A total of 92 Sespe clasts were collected, including 71 from the Miocene sections (30 from Piuma Road, 19 from Schueren Road, and 22 from the Santa Ana Mountains), and 21 from the Eocene section (Table 2). Following petrographic screening (mainly to distinguish orthoquartzites from metaquartzites and other rock types), and assessment of the quality of preserved stratification (often best observed on cut or drilled surfaces; Figure S1 shows representative examples), 49 samples were selected for paleomagnetic analysis. These included 34 samples from Miocene Sespe sections (17 from Piuma Road, 13 from Schueren Road, 4 from the Santa Ana Mountains), and 15 samples from the Eocene Sespe section. All 34 samples from the Miocene Sespe Formation yielded interpretable paleomagnetic data, but only 10 of the 15 samples from the Eocene section yielded interpretable data. We therefore report paleomagnetic data for a total of 44 Sespe orthoquartzite clasts (Tables 3 and 4; Table S1).

Our general approach is to compare the distribution of inclinations within clast populations with those of potential source regions, which requires comparison of inclination-only data from the clast populations with three-dimensional paleomagnetic vectors of the source populations. Whereas the latter can be expressed using Fisher statistics, the former cannot, and at present there is no parametric test of statistical distributions applicable to such comparisons (p. 135 in Fisher et al., 1987; McFadden and Reid, 1982). Further, we cannot rigorously define any sort of mean for our clast populations, because as shown below, the clast populations are not normally distributed.

Following paleomagnetic analysis, detrital zircon spectra were determined for a subset of 12 of the 44 Sespe clast samples. This subset was selected based on quality of paleomagnetic data (good orientation statistics and demagnetization temperatures suggestive, in most cases, of hematite as the carrier phase), and included 2 samples with low inclination, and 10 samples with moderate to high inclination. Of the 10 with moderate to high inclination, 8 were from the Miocene

Sespe, and 2 were from the Eocene. The two samples with low inclination were both from the Miocene Sespe, from the roadcut on Santiago Canyon Road (Table 4).

Paleomagnetic Analysis

All selected Sespe orthoquartzite clasts and the Shinumo sample were cut along their bedding planes with a non-magnetic brass blade, and then cored in-lab using an electric drill with a nonmagnetic bit. Sample cores were soaked in dilute HCl for up to 36 hours to remove any possible fluid-related magnetic signatures, and then stored in a magnetically-shielded room.

Demagnetization and paleomagnetic measurements were carried out at the California Institute of Technology Paleomagnetics Laboratory using 2G™ Enterprises rock magnetometers with three-axis DC SQuID sensors with sensitivities of 2 x 10^{-13} Am^2 per axis, using a RAPID automatic sample changer. Details of the equipment and demagnetization procedures are described in Kirschvink et al. (2008). After measuring the natural remnant magnetization (NRM), we used five alternating field (AF) steps of 2 to 10 mT to remove viscous components of multi-domain magnetite and other soft magnetic components. To thermally demagnetize our samples, we heated them in a magnetically-shielded ASC furnace in steps of 5 – 50 °C, from 0 °C up to a maximum of 710 °C to constrain the CRM. Magnetization components were defined by least squares using the principal component analysis technique of Kirschvink (1980) and software of Jones (2002).

Detrital Zircon Analysis

Mineral separations and U-Pb isotopic analyses were performed for a total of 13 samples, 12 from Sespe clasts and one from the Shinumo Formation. Six of these samples, including 4 samples from the Santa Ana Mountains, 1 sample from the Santa Monica Mountains, and 1 sample of Shinumo Formation (Tables 1 and 2) were separated and analyzed by Apatite to Zircon, Inc., using standard separation techniques and Laser Ablation-Inductively Coupled Plasma-Mass Spectrometry. Analysis and preparation of zircon age data followed procedures described in Moore et al. (2015). For the 7 additional samples, including 5 from the Santa Monica Mountains and 2 from the Simi Valley area, zircon extractions, using standard techniques, were performed at the California Institute of Technology and the University of Arizona. U-Pb analyses were performed at the University of Arizona Laserchron Center. Zircon grains were mounted in epoxy with Sri Lanka, FC-1, and R33 primary standards. The epoxy mount was sanded down to 20 μm, polished, and imaged with a Hitachi 3400N scanning electron microscope (SEM). Laboratory procedures for U-Pb isotopic analyses and screening for discordant grains follow methods described in Gehrels et al. (2006, 2008) and Gehrels and Pecha (2014).

RESULTS

Paleomagnetic Data

Demagnetization data for all samples are summarized in Table 4 and presented in complete form in Table S1. Demagnetization plots for all samples are shown in Figure S2. Representative demagnetizations of Sespe cobbles, including two from Miocene (Figure 5a, b) and two from Eocene (Figure 5c, d) sections, show well-preserved, high-temperature CRMs of moderate to high inclination. Measured remnant magnetizations of the sample suite have intensities ranging from 10^{-9} – 10^{-6} Am^2, well above instrument sensitivity of 10^{-13} Am^2. Up to five steps of alternating field (AF) demagnetization in 20 mT increments up to 100 mT generally had little effect on remanence, indicating magnetite is not a significant carrier. Characteristic directions in most samples are defined by multiple demagnetization steps ranging from 590 to 670° C, suggesting that hematite is the main carrier of magnetization in these samples. This observation is consistent with petrographic evidence that samples typically contain pigmentary hematite, which imparts their characteristic red and red-purple hues (Figure S1). However, in 15 of the 44 samples with interpretable data, the carrier phases were magnetite or other lower temperature phases. Maximum angular deviations (MAD) calculated from principal component analysis average about 5° in our sample set (Table 4).

Distributions of paleomagnetic inclination from the Sespe clast populations, plotted in Figure 6 in 4° bins, show that both Miocene and Eocene populations exhibit bimodal distributions with maxima near 15° and 45°, and minima near 30° (Figure 6). The Miocene population, however, has a stronger peak near 45° and the Eocene population has a stronger peak near 15°, although the latter population includes only 10 samples. For the dataset as a whole, only 3 of 44 samples lie in the three bins between 24° and 36°. By comparison, the three bins between 12° and 24° contain 13 samples, and the three bins between 36° and 48° contain 11 samples.

In addition to the new data, we compiled existing paleomagnetic data from possible source regions (references provided in Table 5), which we present as (1) directions from individual, demagnetized sample cores, corrected for bedding tilt (Figure 7), and (2) histograms showing spectra of inclinations (Figures 7 and 9). The compilation is limited to Neoproterozoic-Cambrian strata from the Death Valley-Mojave region, the Caborca region, the Shinumo and Tapeats formations in Grand Canyon, and the Tapeats Formation and equivalents in the central Arizona highlands. The only published paleomagnetic study on Proterozoic strata in the central Arizona highlands were measurements of the NRM of Mesoproterozoic strata of the Apache Group

(Pioneer Shale), which did not differ significantly from the modern field (Runcorn, 1964). Diabase sills that intruded the Apache Group at 1.1 Ga yield moderate inclinations (Harlan, 1993), as expected for late Mesoproterozoic time (e.g., Evans et al, 2016; Meert and Stuckey, 2002). Although we might expect moderate inclinations for central Arizona orthoquartzites, at present there is no basis to assume any particular distribution of inclinations from a population of Proterozoic clasts derived from the central Arizona highlands.

Because any given clast population represents a regional mixture of individual pebbles and cobbles from disparate sources, clast magnetizations are best compared with regional populations of magnetizations from individual paleomagnetic cores, as opposed to, for example, any particular site mean. In this form, a ready comparison can be made between a clast population and source populations according to some defined area. The Shinumo data (Figure 7a and 7b) show well-grouped, moderate to high inclination, with only a few measurements (3 of 95) below 30°. The Tapeats Formation cores in Grand Canyon (Figure 7c and 7d) are shallowly inclined and well-grouped into an east-west orientation. The Tapeats and related strata in the central Arizona highlands (Figure 7e and 7f) are also mostly of low inclination, but are far more scattered in declination, likely due in part to their more complex thermal and tectonic history. The Death Valley-Mojave region data (Figure 7g and 7h) are also generally of low inclination, and fairly diverse in declination. These data generally reflect a period of long residence of SW Laurentia at low paleolatitude in Neoproterozoic-Paleozoic time, not returning to higher paleolatitudes until the Jurassic. In sum, the extant data from potential source populations show broadly unimodal, shallow inclination spectra, except for the Shinumo Formation, which shows a moderate- to high-inclination spectrum.

Detrital Zircon Data

Detrital zircon age spectra of orthoquartzites from both potential sources and the Sespe Formation, including new data presented here and a compilation of published data (Table 5), are presented in Figure 8. Representative spectra from sources in Grand Canyon, including the Shinumo Formation and Tapeats Formation, are shown in the left-hand column (Figure 8a-8h), which includes sample IC-1-35 obtained for this study (Figure 8e). Representative spectra from potential sources in the Death Valley-Mojave region (Figure 8u and 8v) and central Arizona highlands (Figure 8w-8aa) are shown in the right-hand column. Also shown in the right-hand column, for reasons discussed in detail below, are representative spectra from the Westwater Canyon Member of the Upper Jurassic Morrison Formation, which appears to be a source for one of the Sespe clasts. Representative spectra from the Death Valley region include the Zabriskie and upper Stirling Formations, and from the Arizona region include the Troy, Dripping Springs, Del Rio, Blackjack, Yankee Joe and White Ledges Formations. Samples in the center column include 10 clasts from the Miocene Sespe Formation and 2 clasts from the Eocene Sespe. As noted above, of the 10 Miocene Sespe samples, 8 have moderate to high paleomagnetic inclinations, and 2 have low paleomagnetic inclinations. As noted above, the low inclination samples (Figure 8q and 8r) were both collected from the same outcrop of "marker conglomerate" at the base of the Sespe along Santiago Canyon Road in the Santa Ana Mountains. The two clasts from Eocene Sespe both have moderate inclination. Analytical data for the 13 samples analyzed for this study are presented in Table S2.

The most prominent observation regarding the source spectra is that Grand Canyon and Death Valley sources both have multimodal ("cosmopolitan") spectra, with discernable peaks near

1.2, 1.4, and 1.7 Ga. In contrast, the central Arizona highlands sources tend to have unimodal or bimodal spectra, and include small numbers of pre-2.0 Ga grains. The only central Arizona highlands source with a Grenville-age peak is the Troy Quartzite, which features a strong peak at 1.26 Ga and a broad distribution of older ages, with a much weaker peak at 1.48 Ga (Figure 8w). The only other source with any Grenville component is the Dripping Springs Formation, which contains a few ages (<5%) younger than 1.3 Ga, associated with a broad peak at 1.4 Ga. The youngest zircons in the Dripping Springs and Troy formations are 1.23 and 1.20 Ga, respectively. Depositional ages of the other central Arizona orthoquartzite bodies are too old to contain Grenville-aged zircons, and tend to be strongly unimodal at 1.7 Ga. Therefore, either (1) strong unimodality or (2) absence of pre-1.20 Ga Grenville-aged zircons, discriminate central Arizona sources from both Death Valley-Mojave region sources and Grand Canyon sources.

The data from the 12 Sespe clasts fall into two basic groups, which include 9 samples with cosmopolitan spectra (Figure 8i-q), and 3 with strongly unimodal spectra (Figure 8r-t). The cosmopolitan spectra tend to have 3 modes near 1.2 Ga, 1.4 Ga, and 1.7 Ga, and minor amounts of pre-2.0 Ga grains. Although the modes are variable in detail, they are mostly subequal, with the exception of sample BW4809, in which Grenville-age grains are much less abundant than in other cosmopolitan samples. The three samples with unimodal spectra all have peaks near 1.7 Ga, and each have a few pre-2.0 Ga grains.

Three of the nine cosmopolitan spectra also contain a small but significant fraction (ca. 5%) of Paleozoic and Mesozoic grains. The Paleozoic grains in sample LS1114 average 331 Ma, and a single Mesozoic age is 153.0 +/- 2.8 (1 sigma) Ma (Figure 8l). There are six Paleozoic grains in sample BW4809 that define a tightly clustered unimodal peak at 485 Ma, and no Mesozoic grains (Figure 8p). In sample BW1609, five Mesozoic grains cluster tightly near 168 Ma and a single Paleozoic grain is 510 +/- 10 Ma (Figure 8q).

We observe a general distinction in detrital zircon spectra between the Miocene and Eocene Sespe clast populations. In the Miocene population, 9 of 10 spectra contain abundant Grenville-aged zircons, with 8 of these 9 having a well-defined peak. All 9 samples contain grains younger than 1.20 Ga in their populations. The one remaining sample is unimodal with a 1.7 Ga peak. In contrast to the cosmopolitan spectra, the Eocene Sespe clasts are both unimodal with 1.7 Ga peaks.

DISCUSSION

Paleomagnetic inclination analysis

Comparison of Sespe Formation clasts and sandstone matrix

Paleomagnetic data from Piuma Member sandstones, collected in the same area that we collected orthoquartzite clasts along Piuma Road, have a tilt-corrected mean inclination of 39°+/- 6° (α_{95}) (Hillhouse, 2010). The CRM is carried by elongate, authigenic hematite that grew along cleavage planes within detrital biotite (Hillhouse, 2010). Because orthoquartzite clasts are generally devoid of detrital micas (Figure 4c, d) and other soluble phases, it is highly unlikely that the clasts carry this magnetization.

Further, in unmetamorphosed redbeds in general, the permeabilities of ultradurable clasts, such as orthoquartzite and metarhyolite ($<10^{-4}$ darcy), are at least 3 orders of magnitude lower than those of their porous sandstone matrix (0.1-1 darcy: e.g., Table 2.2 in Freeze and Cherry, 1979). This, in turn, suggests a strong contrast between clasts and matrix in exposure to diagenetic pore fluids. Thus, the elimination and replacement of the pre-depositional, CRM in orthoquartzite clasts with an early Miocene magnetization, similar to that of the Sespe sandstone matrix, is unlikely. We also note that, whereas the clast CRMs are of high coercivity and unblocking temperature, peak temperatures of the Sespe Formation are generally well below 150 °C, based on maximum burial depths of 5,000 m in the Saddle Peak area (e.g. Section D-D' of Dibblee, 1993) and 3,000 m in the northern Santa Ana Mountains (e.g. Section F-F' of Schoellhamer et al., 1981). These clasts, therefore, tend to retain their original CRMs during transport, deposition, and diagenesis in the shallow crust, especially if those magnetizations are of high coercivity and unblocking temperature (e.g., Hodych and Buchan, 1994; Pan and Symons, 1993).

Comparison of Sespe clasts to possible sources

Histograms of inclination data from each potential source formation are plotted at a uniform scale for comparison with histograms from clasts in the Sespe Formation at a suitably expanded vertical scale (Figure 9). An important assumption in any comparison of Sespe clasts to source data is that the latter are representative of the source region as a whole. In other words, we assume it is unlikely that the inclination distribution of 188 randomly sampled orthoquartzites in the Death Valley-Mojave region would differ significantly from the 188 samples shown in the left-hand column of Figure 9. The fact that distributions from individual samples and formations are, without exception, similar to the overall distribution, suggests that the extant dataset is representative of the region. There are probably sources where moderate to high inclinations are recorded by Death Valley-Mojave orthoquartzites, for example, by remagnetization in the contact aureoles of Mesozoic or Tertiary intrusions. But, such sources, if present, would occupy only a small fraction of the very extensive drainage area of Sespe gravels, and so they would be unlikely to influence the inclination distribution of the clast population as a whole.

With respect to sources in Figure 9, the low-inclination population of clasts from the Miocene and Eocene Sespe Formation could only have been derived from sources in the left-hand column, which includes Neoproterozoic/Cambrian formations in the Death Valley-Mojave region, the Tapeats Formation (both in the central Arizona highlands and in Grand Canyon), and Neoproterozoic-Cambrian strata of the Caborca region. The moderate- to high-inclination population of clasts, however, could not have been derived from the Neoproterozoic-Cambrian source populations, and require either a Shinumo Formation source, shown in the upper right-hand portion of Figure 9, or some other unidentified source with similar paleomagnetic characteristics. Such a source could plausibly be Mesoproterozoic or Paleoproterozoic orthoquartzites in the central Arizona highlands, where as noted above, paleomagnetic data are lacking, or less plausibly from NW Sonora. Summations of the low-inclination distributions (from the Tapeats Formation and the Death Valley-Mojave region) and the moderate- to high-inclination distributions (Shinumo Formation) each define two unimodal distributions (Figure 10). A comparison of these distributions with the distribution of the Miocene Sespe clast population suggests that neither source alone could produce the bimodal clast distribution, but a combination of the two sources could.

Cumulative distribution functions (CDFs) from the Miocene and Eocene Sespe clast populations are compared to those from each of the three source regions in Figure 11. Distributions from the Death Valley-Mojave region, both as individual formations (including the Rainstorm

Member of the Johnnie Formation, the Wood Canyon Formation, and the Zabriskie Formation), and as a whole, lie well to the left (low-inclination side) of the Miocene Sespe distribution, and somewhat to the left of the Eocene Sespe distribution (Figure 11a). Distributions from the Grand Canyon region lie either well to the left (Tapeats Formation) or well to the right (Shinumo Formation) of both Miocene and Eocene Sespe distributions (Figure 11b). A distribution from the central Arizona highlands region (Tapeats Formation) lies to the left of the Sespe distributions (Figure 11c).

The comparisons in Figure 11a-c appear to exclude the Death Valley-Mojave region as a sole source for the Miocene and Eocene Sespe distributions. However, because the central Arizona highlands region may contain sources with moderate to high inclinations, it cannot be ruled out as a source for either the Miocene or Eocene Sespe clast distributions. Linear combinations of the two Grand Canyon sources (Tapeats and Shinumo Formations as endmembers) compare well with the Miocene Sespe clast distribution for a broad range of mixtures (Figure 11d). For Shinumo fractions ranging from about 30 to 60%, Kolmogorov-Smirnov tests yield p-values of 0.05 or greater (Figure 12), indicating that the derivation of Sespe clasts from this range of mixtures cannot be ruled out at 95% confidence. There is a strong maximum value of p for these mixtures of $p = 0.34$ for a Shinumo fraction of 35 to 40%. The same comparison of Grand Canyon sources and Eocene Sespe clasts is not as strong. For these mixtures, p-values of 0.05 or greater are restricted to Shinumo fractions of about 10 to 15%, with a maximum of only $p = 0.07$. These comparisons suggest that a sole Grand Canyon source comprising a mixture of Tapeats and Shinumo Formation clasts is a viable explanation of the inclination distributions the Sespe clast populations, and is particularly strong for the Miocene population. As noted earlier, ultradurable orthoquartzites in the Tapeats

Formation are not exposed in eastern Grand Canyon, but are characteristic of western Grand Canyon exposures. Therefore, a roughly equal mixture of Tapeats and Shinumo clasts implies that the source areas included both the Upper Granite Gorge of eastern Grand Canyon and the Lower Granite Gorge of western Grand Canyon.

These comparisons, of course, may be equally well explained with mixtures that include components from both Death Valley-Mojave and central Arizona highlands sources, either with or without a very small contribution from Sonoran sources. Death Valley-Mojave sources cannot be distinguished from the Tapeats Formation in Grand Canyon, and Proterozoic sources from the central Arizona highlands may have moderate to high inclinations, and thus be indistinguishable from the Shinumo Formation. The key to distinguishing a Shinumo contribution to the Sespe clast population thus lies in a simple test that distinguishes the Shinumo Formation from orthoquartzites in the central Arizona highlands, using detrital zircon age spectra.

Detrital zircon analysis

Here, we apply the detrital zircon test to our analysis of populations of paleomagnetic inclinations, in order to discriminate source regions, both for individual clasts, and for the population of clasts as a whole in the Piuma Member and Eocene Sespe populations (Table 6).

In this analysis, it is important to first consider the three orthoquartzite clast samples containing small but significant populations of Paleozoic and Mesozoic grains (LS1114, BW4809, and BW1609; Figures 8l, 8p and 8q). These data raise the question of whether those grains are detrital components of the orthoquartzite, or whether they are “allochthonous” and incorporated upon or into the clast during weathering and transport.

Sample LS1114 (Figure 8l), from the Piuma Member, has a unique detrital zircon spectrum relative to all other samples, and its source is therefore quite uncertain. Based on comparison with the extensive detrital zircon dataset from Mesozoic sandstones on the Colorado Plateau (Dickinson and Gehrels, 2008), its most likely source is the Upper Jurassic Morrison Formation (Table 6). Similar to the Morrison, LS1114 has a moderate paleomagnetic inclination, scarcity of grains between 0.5 and 1 Ga in its detrital zircon spectrum, and is a well-indurated, light pinkish-gray, medium to coarse-grained orthoquartzite. Although the Mesozoic peak in the Sespe spectrum is not as prominent as in the two Morrison spectra, the ratio of Mesozoic to Proterozoic grains is more similar between LS1114 and CP21, from the Morrison, than it is between the two Morrison samples.

In contrast to LS1114, we interpret the Paleozoic grains in samples BW4809 and BW1609 (Figure 8p and q) to be allochthonous. Both samples were collected from the Miocene Sespe in the Santiago Canyon roadcut. Their detrital zircon spectra are a poor match for any known Paleozoic or Mesozoic sandstone in having a small, single Paleozoic mode. Further, clasts from this outcrop exhibit petrographic evidence for the extensive development of silica glaze on the clast surface, beneath which thin films of allochthonous grains are adhered to the clast exterior, and narrow fractures in the clast interior that also locally contain allochthonous grains (Figure 13). Both of these clasts are densely-cemented, purple-hued orthoquartzites that are a poor lithologic match for even the most densely-cemented late Paleozoic or Mesozoic sandstones in the potential source regions. These samples both have low inclination but contrasting detrital zircon spectra (Figure 8q and 8r). The unimodal spectrum of BW1809 (Figure 8r) indicates that it was derived from the central Arizona highlands, suggesting that the inclination distribution of central Arizona orthoquartzites may include shallowly inclined samples. Sample BW1609 (Figure 8q), which has a strong Grenville-age peak, is probably derived from the Death Valley-Mojave region, based on its inclination, densely cemented grains, and purple hue (Table 6). This, of course, assumes that its small population of Mesozoic grains is allochthonous.

The two Eocene Sespe clasts with moderate inclinations both have unimodal peaks at 1.7 Ga and a smattering of Archaean grains, indicating derivation from the central Arizona highlands (Figure 8s, t, Table 6).

The remaining 7 samples were all collected from the Piuma Member (5 from the Piuma Road section, and 2 from the Red Rock Trail section), and have both moderate to high inclination and relatively broad Grenville-age zircon peaks. Among known potential sources, these characteristics restrict this population to a Shinumo Formation source, among known sources. As noted above, the Troy Quartzite at the top of the Apache Group is the only Proterozoic orthoquartzite in the central Arizona highlands to contain appreciable Grenville-age zircons (Figure 8w, versus Figures 8x-8ad), and therefore could be a potential source. However, the Troy data are dominated by an early Grenville peak near 1.26 Ga, with no grains younger than 1.20 Ga, and very weak peaks near 1.4 and 1.7 Ga. In contrast, Miocene Sespe clasts and the Shinumo Formation are both characterized by broader Grenville peaks (including many grains between 1.0 and 1.20 Ga), and much stronger peaks at 1.4 and 1.7 Ga. A K-S test comparing the Troy data (Figure 8w) with Miocene Sespe clasts LS0814 and LS1214 (Figures 8j and 8m) yields p-values of 2.1×10^{-5} and 3.5×10^{-4}, respectively, ruling out derivation of sands in the Troy Formation and sands in the Miocene Sespe clasts from the same source. Therefore, extant data from the Apache

Group do not provide a compelling match for orthoquartzite clasts in the Miocene Sespe Formation.

Interpretive complications

We consider here three important issues in interpreting the Shinumo Formation as the bedrock source for the moderately inclined mode of orthoquartzite clasts in the Miocene Sespe Formation. These include (1) primary structures within source formations, such as cross-stratification, and their influence on the inclination spectra of clast populations, (2) recycling of clasts from gravel sources that are intermediate in age between the Shinumo and Sespe Formations, which may compromise the interpretation of a Shinumo source for Miocene Sespe clasts, and (3) buried or now-eroded sources for the clasts outside of the eastern Grand Canyon region.

Primary structure

Orthoquartzites in the southwestern United States are substantially compacted after deposition, commonly cross-stratified, and locally contain paleoliquefaction structures. An analysis of the potential effects of primary structures on paleomagnetic inclination spectra is provided in Supplemental Text S1 and Figure S4. Our analysis suggests that primary structures, especially cross-stratification, may have a measurable effect on the distribution of paleomagnetic inclinations in any given sample population. Relationships between the measured orientations of foresets and of paleomagnetic inclinations in potential source regions indicate that the difference between low inclination and moderate- to high-inclination populations would be augmented to some degree by this effect. Depending on the volume fraction of foreset laminations sampled by the clast population, such augmentation would be in the range of 0° to 15°, which serves to slightly enhance the distinction between the two populations, rather than obscure it.

Recycling of clasts

An additional complication in any provenance study is the possibility of recycling of clasts from secondary sources. It is possible that a significant fraction of Sespe gravel clasts are derived from conglomeratic strata that are intermediate in age between the time of exposure of their bedrock source and the time of Sespe deposition (e.g. Dickinson, 2008). As noted above, in the case of the Shinumo bedrock source region, extensive thermochronometric data demonstrate that unroofing of the Upper Granite Gorge in the eastern Grand Canyon region, which includes all known exposures of the Shinumo Formation, did not occur before c. 28-18 Ma (Flowers et al., 2008; Flowers and Farley, 2012; Lee et al., 2013; Karlstrom et al, 2014; Winn et al., 2017). Therefore, assuming lower Miocene Sespe orthoquartzites are indeed derived, in part, from the Shinumo Formation, the possibility of clast recycling does not alter the conclusion that sedimentary transport from Upper Granite Gorge bedrock sources to coastal California occurred between c. 28 and 20 Ma.

There is also the possibility that the clasts are recycled from conglomeratic strata that contain orthoquartzite detritus, either derived from the Shinumo Formation, or from an unknown source with similar paleomagnetic and detrital zircon characteristics. Because the Shinumo Formation was buried in Cambrian time, and remained so until the Oligocene, any pre-Oligocene recycling path must have begun prior to Cambrian burial. For example, Shinumo clasts could have been eroded into Neoproterozoic rift basins in the Death Valley region, and then supplied to the Sespe Formation via an Amargosa paleoriver. Other potential recycled sources include the Jurassic cobble and boulder conglomerates of the Coyote Formation near Hermosillo, Mexico, and possible equivalents exposed as far north as the Caborca area, but these are unlikely as Sespe sources, as noted above. These and other recycling histories, although possible, thus require postulation of either distant or unknown reservoirs of orthoquartzite clasts that would somehow overwhelm extant, broadly exposed reservoirs in their contributions to the Miocene Sespe basin.

Buried or now-eroded sources

As in any provenance study, it is possible that an unknown source, either eroded away since 20 Ma or buried beneath the extensive alluvial deposits in the Basin and Range region, could have provided a clast population with any combination of the paleomagnetic and detrital zircon characteristics needed to explain the Sespe (clast) data. Nearly all of the moderate- to high-inclination clast population in the Piuma Road section has Shinumo characteristics (7 out of the 8 measured clasts, or 88%). Our results agree well with the observation (described above in Introduction and Geologic Setting) that the Shinumo Formation lies within the only known region in the Cordilleran interior that underwent kilometer-scale erosional denudation during Piuma time (c. 28-18 Ma). In other words, the Shinumo Formation is apparently the dominant source for the moderate- to high-inclination clast population. In contrast, the hypothesis that Piuma orthoquartzite clasts are substantially derived from the central Arizona highlands can be rejected at a high level of confidence, because eight out of eight clasts (Figure 14) failed the detrital zircon test. Deriving the Piuma orthoquartzite clast population from now-eroded or -buried sources in the Mojave region is clearly possible. However, it is inconsistent with the Laramide unroofing history of the region (80-40 Ma, versus the c. 20 Ma depositional age), which suggests a fairly stable landscape from 40 to c. 20 Ma (e.g. Spotila et al., 1998). In sum, we interpret our results to support the hypothesis stated in the Introduction, that the mid-Tertiary, rapid unroofing event in the eastern Grand Canyon source region is reflected in an abundance of eastern Grand Canyon orthoquartzite clasts in coeval basins of coastal southern California.

Detrital zircon spectra in Sespe sandstone

In modern Colorado River sands, 20% of the detrital zircon population ranges in age from 300 to 900 Ma, reflecting the dominant contribution of Permian through Jurassic aeolianites widely exposed throughout the Colorado River drainage basin (Kimbrough et al., 2015). The Arizona River drainage proposed here (Figure 1) and in Wernicke (2011) includes part of the southwestern margin of the Colorado Plateau that, in turn, contains part of the region of 28-18 Ma erosion (stippled region in Figure 1). The area of the plateau included within the Arizona River drainage is nominally 30,000 km^2 (Figure 1), which is about 6% of the area of the modern Colorado River drainage basin that includes the Colorado Plateau and environs (about 500,000 km^2, Table 1 in Kimbrough et al., 2015). Thus, if the modern Colorado River drainage were limited to a Gila, Amargosa, and Colorado River with headwaters restricted to the eastern Grand Canyon region, the expected contribution of 300 to 900 Ma zircon grains would be (0.06) (0.20) = 0.012, or about 1% of the population. Detrital zircon age determinations from 22 samples of the Sespe Formation (including 1,378 total grains) yielded a contribution of 0.7% of 300 to 900 Ma detrital zircons (Table 1 in Ingersoll et al., 2013; Spafford, 2010), in reasonable agreement with the expected ratio. This 300 to 900 Ma population could be derived entirely from Mojave-Sonora region, entirely from the Grand Canyon region, or most likely from some combination of the two. In other words, the sandstone detrital zircon data are insufficient to discriminate between Mojave-Sonora and Grand Canyon sources for the 300 to 900 Ma detrital zircon component, contrary to the conclusion of Ingersoll et al. (2013) that the data indicate no drainage link between southern California river deltas and the Grand Canyon region during Sespe time.

CONCLUSION

As summarized in Table 6 and Figure 14, our results show that combined intraclast paleomagnetic inclination and detrital zircon data provide significant new insights into the provenance of Sespe clast populations that cannot be derived from either dataset alone. The eight moderate- to high-inclination clasts from the Miocene Sespe for which we obtained detrital zircon spectra uniformly contain Grenville-age detrital zircon peaks (Figure 14), ruling out both the Death Valley-Mojave and central Arizona highlands regions as source populations. With the exception of LS1114, which appears to be Jurassic, we interpret them all as being derived from the Shinumo Formation (Figure 3, Figure 14). The two Miocene Sespe clasts that have low inclination were both collected from the Santiago Canyon Road locality, from the basal conglomerate of the lower Miocene Sespe Formation. Given that one yielded a unimodal detrital zircon peak at 1.7 Ga and the other a cosmopolitan spectrum, the central Arizona highlands and Death Valley-Mojave region both appear to be possible sources for the broader Miocene orthoquartzite population (Howard, 1996). The two Eocene Sespe clasts with moderate paleomagnetic inclinations yielded unimodal zircon age spectra with peaks at 1.7 Ga, indicating derivation from the central Arizona highlands. Clearly, more data will be required to further test the hypothesis that the Eocene Sespe is predominantly sourced from the central Arizona highlands (e.g. Howard, 2000, 2006). It is noteworthy, however, that the outcome of moderate inclination plus a unimodal 1.7 Ga peak observed in the Eocene Sespe was not observed in any of the ten Miocene Sespe samples. Therefore, regardless of how one interprets these data in terms of provenance, they have clear potential to identify and characterize contrasting clast populations (Figure 14).

Because all seven of the moderate- to high-inclination Miocene Sespe clasts of pre-Mesozoic age contain post-1.2 Ga zircons, it is likely that most or all of the total population of moderate- to high-inclination clasts (19 of 34 samples, or 56%) have similar characteristics. Therefore, if our interpretation is correct that these characteristics indicate a Shinumo source, it places an important constraint on the erosion kinematics of the Cordillera post-Laramide. Because the only known exposures of the Shinumo Formation lie within a few hundred meters elevation of the bottom of eastern Grand Canyon, our interpretation supports the existence of a mid-Tertiary drainage connection, or Arizona River, between high-relief, eroding uplands in the eastern Grand Canyon region and the coast. Further, it is highly unlikely that a SW-flowing Arizona River running near the bottom of eastern Grand Canyon would have "jumped" out of Grand Canyon before reaching the coast. Assuming it did not, the only plausible course would have run through an existing western Grand Canyon, as also implied by a roughly equal mixture of ultradurable Tapeats (exposed only in western Grand Canyon) and Shinumo clasts suggested by the simple linear mixing models of the Piuma inclination spectra. Our results thus provide independent support for models that suggest western Grand Canyon was carved to within a few hundred meters of its current depth no later than 20 Ma, and perhaps as early as Late Cretaceous/Paleocene time, based on thermochronological evidence (e.g., Flowers et al., 2008; Wernicke, 2011; Flowers and Farley, 2012).

ACKNOWLEDGMENTS

This research was supported by NSF grants EAR 10-19896 and EAR 14-51055 awarded to B. Wernicke, EAR 17-28690 awarded to J. Stock, and OPP 13-41729 awarded to J. Kirschvink. We also acknowledge NSF grant EAR 16-49254 awarded to G. Gehrels at the University of Arizona for support of the Arizona LaserChron Center. We thank Jonathan Hagstrum of the U.S. Geological Survey for providing the unpublished paleomagnetic data of D. Elston and S. Grommé from the Shinumo Formation. Guidance from the Associate Editor and reviewers R. Molina-Garza and R. V. Ingersoll substantially improved the manuscript.

SUPPLEMENTAL MATERIAL

Table S1. Columns show sample number, measurement type (alternating field, AF, thermal, TT), field strength (mT) or temperature (T), declination and inclination, publicly available in MagIC Data Repository upon publication (https://earthref.org/MagIC/16652/0fc080bf-3661-45e4-bd5f-487142ef2f91).

Table S2. Sheets in Excel file include detrital zircon ages from LaserChron and Apatite to Zircon of Sespe orthoquartzite clasts and Shinumo Formation, publicly available in California Institute of Technology Research Data Repository (https://data.caltech.edu/records/1245).

Figure S1. Photos of 7 representative clasts showing stratification.

Figure S2. Zijderveld demagnetization plots for all paleomagnetic data.

Figure S3. Photomicrographs of selected samples.

Figure S4. Relationship between cross-stratification and paleomagnetic inclination in Neoproterozoic-Cambrian and Shinumo strata.

Text S1. Discussion of effect of primary structures on paleomagnetic inclination spectra.

REFERENCES CITED

Abbott, P. L., and Peterson, G.L., 1978, Effects of abrasion durability on conglomerate clast populations: examples from Cretaceous and Eocene conglomerates of the San Diego area, California: Journal of Sedimentary Research, v. 48, p. 31-42.

Abbott, P. L., Smith, T.E., 1989, Sonora, Mexico, source for the Eocene Poway conglomerate of southern-California: Geology, v. 17, p. 329-332.

Abbott, P. L., Smith, T. E., and Huang, C. H., 1991, On the origin of some rhyolitic clasts in the basal Sespe Formation, Los Angeles area, California: Society for Economic Paleontologists and Mineralogists, Pacific Section, Book 68, p. 93-98.

Atwater, T., and Stock, J., 1998, Pacific-North America plate tectonics of the Neogene southwestern United States: an update: International Geology Review, v. 40, p. 375-402.

Beard, L. S., Karlstrom, K. E., Young, R. A., and Billingsley, G.H., 2011, CRevolution 2 - Origin and Evolution of the Colorado River System, Workshop Abstracts: U.S. Geological Survey Open-File Report 2011–1210, 300 p.

Bellemin, G. J., and Merriam, R., 1958, Petrology and origin of the Poway Conglomerate, San Diego County, California: Geological Society of America Bulletin, v. 69, p. 199-220.

Belyea, R. R., and Minch, J. A., 1989, Stratigraphy and depositional environments of the Sespe Formation, northern Santa Ana Mountains, California, in Colburn, I. P. et al., eds., Conglomerates in Basin Analysis: a Symposium Dedicated to A. O. Woodford: Pacific Section, Society of Economic Paleontologists and Mineralogists, Bakersfield, p. 281-300.

Billingsley, G. H., and 12 others, 1996, Geologic map of the eastern part of the Grand Canyon National Park: Grand Canyon, Arizona, Grand Canyon Association, scale 1:65,500, 1 sheet.

Bloch, J. D., Timmons, J. M., Crossey, L. J., Gehrels, G. E. and Karlstrom, K. E., 2006, Mudstone petrology of the Mesoproterozoic Unkar Group, Grand Canyon, USA: Provenance, weathering, and sediment transport on intracratonic Rodinia: Journal of Sedimentary Research, v. 76, p. 1106-1119.

Blythe, A. E., Burbank, D. W., Farley, K. A., and Fielding, E. J., 2000, Structural and topographic evolution of the central Transverse Ranges, California, from apatite fission-track, (U-Th)/He and digital elevation model analyses: Basin Research, v. 12, p. 97–114.

Bryant, B., Naeser, C.W., and Fryxell, J.E., 1991, Implications of low-temperature cooling on a transect across the Colorado Plateau–Basin and Range boundary: Journal of Geophysical Research, v. 96, p. 12,375– 12,388, doi:10.1029/90JB02027.

Burchfiel, B. C., Davis, G. A., and Cowan, D. S., 1992, Tectonic overview of the Cordilleran orogen in the western United States, in Burchfiel, B. C., Lipman, P. W., and Zoback, M. L., eds. The Cordilleran Orogen: Conterminous U. S.: Boulder, Colorado, Geological Society of America, The Geology of North America, v. G3, p. 407-479.

Cather, S. M., Connell, S. D., Chamberlin, R. M., McIntosh, W. C., Jones, G. E., Potochnik, A. R., Lucas, S. G., and Johnson, P. S., 2008, The Chuska erg: Paleogeomorphic and paleoclimatic implications of an Oligocene sand sea on the Colorado Plateau: Geological Society of America Bulletin, v. 120, no. 1-2, p. 13-33.

Daneker, T. M., 1975, Sedimentology of the Precambrian Shinumo Sandstone, Grand Canyon, Arizona: M.S. thesis, Northern Arizona University, 195 p.

Darling, A., and Whipple, K., 2015, Geomorphic constraints on the age of the western Grand Canyon: Geosphere, v. 11, no. 4, doi:10.1130/GES01131.1.

Dibblee, T. W., Jr., 1993, Geologic map of the Malibu Beach quadrangle, Los Angeles County, California: Santa Barbara, California, Dibblee Geological Foundation, Map DF-47, scale 1:24,000.

Dickinson, W. R., 2008, Impact of differential zircon fertility of granitoid basement rocks in North America on age populations of detrital zircons and implications for granite petrogenesis: Earth and Planetary Science Letters, v. 275, p. 80–92.

Dickinson, W. R., and Gehrels, G. E., 2008, Sediment delivery to the Cordilleran foreland basin: Insights from U-Pb ages of detrital zircons in Upper Jurassic and Cretaceous strata of the Colorado Plateau: American Journal of Science, v. 308, p. 1041-1082.

Doe, M. F., Jones III, J. V., Karlstrom, K. E., Thrane, K., Frei, D., Gehrels, G., and Pecha, M., 2012, Basin formation near the end of the 1.60–1.45 Ga tectonic gap in southern Laurentia:

Mesoproterozoic Hess Canyon Group of Arizona and implications for ca. 1.5 Ga supercontinent configurations: Lithosphere, v. 4, p. 77-88.

Elston, D. P., and Bressler, S. L., 1977, Paleomagnetic poles and polarity zonation from Cambrian and Devonian strata of Arizona: Earth and Planetary Science Letters, v. 36, p. 423-433.

Elston, D. P., and Grommé, C. S., 1994, Middle Proterozoic magnetostratigraphic polar path and polarity zonation from Grand Canyon, Northern Arizona, US Geological Survey, Menlo Park (ms.).

Elston, D. P., and Young, R. A., 1991, Cretaceous-Eocene (Laramide) landscape development and Oligocene-Pliocene drainage reorganization of transition zone and Colorado Plateau, Arizona: Journal of Geophysical Research: Solid Earth, v. 96, p. 12389-12406.

Evans, D. A., Veselovsky, R. V., Petrov, P. Y., Shatsillo, A. V., and Pavlov, V. E., 2016, Paleomagnetism of Mesoproterozoic margins of the Anabar Shield: A hypothesized billion-year partnership of Siberia and northern Laurentia: Precambrian Research, v. 281, p. 639-655.

Fisher, N. I., Lewis, T., Embleton, B. J. J., 1987, Statistical analysis of spherical data: Cambridge University Press, 329 p.

Fitzgerald, P. G., Fryxell, J. E., and Wernicke, B. P., 1991, Miocene crustal extension and uplift in southeastern Nevada: Constraints from fission track analysis: Geology, v. 19, p. 1013-1016.

Fitzgerald, P. G. Duebendorfer, E. M., Faulds, J. E. and O'Sullivan, P., (2009), South Virgin–White Hills detachment fault system of SE Nevada and NWArizona: Applying apatite fission track thermochronology to constrain the tectonic evolution of a major continental detachment fault: Tectonics, v. 28, doi:10.1029/2007TC002194.

Flowers, R. M., and Farley, K. A., 2012, Apatite $^4He/^3He$ and (U-Th)/He evidence for an ancient Grand Canyon: Science, v. 338, p. 1616-1619.

Flowers, R. M., and Farley, K. A., 2013, Response to comments on "Apatite $^4He/^3He$ and (U-Th)/He evidence for an ancient Grand Canyon": Science, v. 340, p. 143-143.

Flowers, R. M., Wernicke, B. P., and Farley, K. A., 2008, Unroofing, incision, and uplift history of the southwestern Colorado Plateau from apatite (U-Th)/He thermochronometry: Geological Society of America Bulletin, v. 120, p. 571-587.

Flowers, R. M., Farley, K. A., and Ketcham, R. A., 2015, A reporting protocol for thermochronologic modeling illustrated with data from the Grand Canyon: Earth and Planetary Science Letters, v. 432, p. 425-435.

Foster, D. A., Gleadow, A. J. W., Reynolds, S. J., and Fitzgerald, P. G., 1993, Denudation of metamorphic core complexes and the reconstruction of the Transition Zone, west-central Arizona - Constraints from apatite fission-track thermochronology: Journal of Geophysical Research-Solid Earth, v. 98, no. B2, p. 2167-2185.

Fox, M., Tripathy-Lang, A., Shuster, D. L., Winn, C., Karlstrom, K., and Kelley, S., 2017, Westernmost Grand Canyon incision: testing thermochronometric resolution: Earth and Planetary Science Letters, v. 474, p. 248-256.

Freeze, R. A., and Cherry, J. A., 1979, Groundwater: Prentice-Hall, Englewood Cliffs, N. J., 604 p.

Gehrels, G. E., and Stewart, J. H., 1998, Derital zircon U-Pb geochronology of Cambrian to Triassic miogeoclinal and eugeoclinal strata of Sonora, Mexico: Journal of Geophysical Research, v. 103, p. 2471-2487.

Gehrels, G., Valencia, V., and Pullen, A., 2006, Detrital zircon geochronology by laser-ablation multicollector ICPMS at the Arizona LaserChron Center: The Paleontological Society Papers, v. 12, p. 67-76.

Gehrels, G. E., Valencia, V. A., and Ruiz, J., 2008, Enhanced precision, accuracy, efficiency, and spatial resolution of U-Pb ages by laser ablation–multicollector–inductively-coupled plasma–mass spectrometry: Geochemistry, Geophysics, Geosystems, v. 9, no. 3.

Gehrels, G. E., Blakey, R., Karlstrom, K. E., Timmons, J. M., Dickinson, B., and Pecha, M., 2011, Detrital zircon U-Pb geochronology of Paleozoic strata in the Grand Canyon, Arizona: Lithosphere, v. 3, p. 183-200.

Gehrels, G., and Pecha, M., 2014, Detrital zircon U-Pb geochronology and Hf isotope geochemistry of Paleozoic and Triassic passive margin strata of western North America: Geosphere, v. 10, p. 49-65.

Gillett, S. L., and Van Alstine, D. R., 1979, Paleomagnetism of Lower and Middle Cambrian sedimentary rocks from the Desert Range, Nevada: Journal of Geophysical Research: Solid Earth, v. 84, p. 4475-4489.

Harlan, S. S., 1993, Paleomagnetism of Middle Proterozoic diabase sheets from central Arizona: Canadian Journal of Earth Sciences, v. 30, p. 1415-1426.

Hereford, R., 1977, Deposition of the Tapeats Sandstone (Cambrian) in central Arizona: Geological Society of America Bulletin, v. 88, p. 199-211.

Hill, C. A., and Polyak, V. J., 2014, Karst piracy: A mechanism for integrating the Colorado River across the Kaibab uplift, Grand Canyon, Arizona, USA: Geosphere, v. 10, p. 627–640, doi:10.1130/GES00940.1.

Hill, C. A., Polyak, V. J., and Asmerom, Y., 2016, Constraints on a Late Cretaceous uplift, denudation, and incision of the Grand Canyon region, southwestern Colorado Plateau, USA, from U-Pb dating of lacustrine limestone: Tectonics, v. 35, p. 896-906.

Hillhouse, J. W., 2010, Clockwise rotation and implications for northward drift of the western Transverse Ranges from paleomagnetism of the Piuma Member, Sespe Formation, near Malibu, California: Geochemistry, Geophysics, Geosystems, v. 11, no. 7.

Hodych, J. P., and Buchan, K. L., 1994, Early Silurian palaeolatitude of the Springdale Group redbeds of central Newfoundland: a palaeomagnetic determination with a remanence anisotropy test for inclination error: Geophysical Journal International, v. 117, p. 640-652.

Hoffman, M., Stockli, D. F., Kelley, S. A., Pederson, J., and Lee, J., 2011, Mio-Pliocene erosional exhumation of the central Colorado Plateau, eastern Utah—New insights from apatite (U-Th)/He thermochronometry, in Beard, L.S., et al., eds., CRevolution 2 - Origin and Evolution of the Colorado River System, workshop abstracts: U.S. Geological Survey Open-File Report 2011–1210, p. 132-136.

House, M. A., Wernicke, B. P., and Farley, K. A., 1998, Dating topography of the Sierra Nevada, California, using apatite (U–Th)/He ages: Nature, v. 396, p. 66.

Howard, J. L., 1989, Conglomerate clast populations of the upper Paleogene Sespe Formation, southern California, in Colburn, I. P. et al., eds., Conglomerates in Basin Analysis: a Symposium Dedicated to A. O. Woodford: Pacific Section, Society of Economic Paleontologists and Mineralogists, Bakersfield, p. 269-280.

Howard, J. L., 1996, Paleocene to Holocene paleodeltas of ancestral Colorado River offset by the San Andreas fault system, southern California: Geology, v. 24, p. 783-786.

Howard, J. L., 2000, Provenance of quartzite clasts in the Eocene–Oligocene Sespe Formation: Paleogeographic implications for southern California and the ancestral Colorado River: Geological Society of America Bulletin, v. 112, p. 1635-1649.

Howard, J. L., 2005, The quartzite problem revisited: Journal of Geology, v. 113, no. 6, p. 707-713.

Howard, J. L., 2006, Provenance of metavolcanic clasts in the upper Paleogene Sespe Formation near Los Angeles, and its bearing on the origin of the Colorado River in Southern California, in Girty, G. H. and Cooper, J. D. eds. Stratigraphy, sedimentology, and geochemistry to unravel the geologic history of the southwestern Cordillera, Society of Economic Paleontologists and Mineralogists, Pacific Section, Book 101, p. 179-192.

Huntington, K. W., Wernicke, B. P., and Eiler, J., 2010, Influence of climate change and uplift on Colorado Plateau paleotemperatures from carbonate clumped isotope thermometry, Tectonics, v. 29, TC3005, doi:10.1029/2009TC002449.

Ingersoll, R. V., Grove, M., Jacobson, C. E., Kimbrough, D. L., and Hoyt, J. F., 2013, Detrital zircons indicate no drainage link between southern California rivers and the Colorado Plateau from mid-Cretaceous through Pliocene: Geology, v. 41, p. 311–314.

Ingersoll, R. V., Spafford, C. D., Jacobson, C. E., Grove, M., Howard, J. L., Hourigan, J., and Pedrick, J., 2018, Provenance, paleogeography and paleotectonic implications of the mid-Cenozoic Sespe Formation, coastal southern California, USA, in Ingersoll, R.V., Lawton, T. F., and Graham, S. A., eds., Tectonics, sedimentary basins, and provenance: A celebration of the career of William R. Dickinson: Geological Society of America Special Paper 540, p. 441-462.

Izaguirre-Pompa, A. and Iriondo, A., 2007, Mesoproterozoic (~1.2 Ga) quartzite and intruding anorthosite (~1.08 Ga) from Sierra Prieta, NW Sonora: Mexican additions to the Precambrian history of SW Laurentia, in Ores and Orogenesis, Program with Abstracts, Arizona Geological Society, Tucson, Arizona, p. 147-148.

Jacobson, C. E., Grove, M., Pedrick, J. N., Barth, A. P., Marsaglia, K. M., Gehrels, G. E., and Nourse, J. A., 2011, Late Cretaceous–early Cenozoic tectonic evolution of the southern

California margin inferred from provenance of trench and forearc sediments: Geological Society of America Bulletin, v. 123, p. 485-506.

Jones, C. H., 2002, User-driven integrated software lives: "PaleoMag" Paleomagnetics analysis on the Macintosh: Computers and Geosciences, v. 28, p. 1145-1151.

Karlstrom, K. E., and Timmons J. M., 2012, Many unconformities make one 'Great Unconformity': Geological Society of America, *Special Paper* 489, p73-79. DOI: 10.1130/2012.2489(04).

Karlstrom, K. E., Crow, R., Crossey, L. J., Coblentz, D., and Van Wijk, J. W., 2008, Model for tectonically driven incision of the younger than 6 Ma Grand Canyon: Geology, v. 36, p. 835-838.

Karlstrom, K. E., Lee, J., Kelley, S., Crow, R., Crossey, L., Young, D., Beard, L. S., Ricketts, J., Fox, M., and Shuster, D., 2014, Formation of the Grand Canyon 5 to 6 million years ago through integration of older palaeocanyons: Nature Geoscience , v. 7, p. 239–244, doi:10.1038/ngeo2065.

Karlstrom, K. E., Crossey, L. J., Embid, E., Crow, R., Heizler, M., Hereford, R., Beard, L. S., Ricketts, J.W., Cather, S., and Kelley, S., 2017, Cenozoic incision history of the Little Colorado River: Its role in carving Grand Canyon and onset of rapid incision in the past ca. 2 Ma in the Colorado River System: Geosphere, v. 13, no. 1, p. 49–81, doi:10.1130 /GES01304.1.

Kelly, T. S., Lander, E. B., Whistler, D. P., Roeder, M. A., and Reynolds, R. E., 1991, Preliminary report on a paleontologic investigation of the lower and middle members, Sespe Formation, Simi Valley Landfill, Ventura County, California: PaleoBios , v. 13, p. 1-13.

Kelly, T. S., and Whistler, D. P., 1994, Additional Uintan and Duchesnean (middle and late Eocene) mammals from the Sespe Formation, Simi Valley, California: Natural History Museum of Los Angeles County, Contributions to Science, v. 439, p. 1-29.

Kies, R. P., and Abbott, P. L., 1983, Rhyolite clast populations and tectonics in the California continental borderland: Journal of Sedimentary Research, v. 53, p. 461-475.

Kimbrough, D. L., Grove, M., Gehrels, G. E., Dorsey, R. J., Howard, K. A., Lovera, O., Aslan, A., House, P. K., and Pearthree, P. A., 2015, Detrital zircon U-Pb provenance of the Colorado River: A 5 m.y. record of incision into cover strata overlying the Colorado Plateau and adjacent regions: Geosphere, v. 11, p. 1719-1748.

Kirschvink, J. L., 1980, The least-squares line and plane and the analysis of paleomagnetic data: Royal Astronomical Society Geophysical Journal, v. 62, p. 699-718.

Kirschvink, J. L., Kopp, R. E., Raub, T. D., Baumgartner, C. T., and Holt, J. W., 2008. Rapid, precise, and high-sensitivity acquisition of paleomagnetic and rock-magnetic data: Development of a low-noise automatic sample changing system for superconducting rock magnetometers: Geochemistry, Geophysics, Geosystems, v. 9, no. 5, doi:10.1029/2007GC001856.

Lander, E. B., 2011, Stratigraphy, biostratigraphy, biochronology, geochronology, magnetostratigraphy, and plate tectonic history of the early middle Eocene to late early Miocene Sespe, Vaqueros, and lower Topanga Formations, east-central Santa Monica Mountains, Los Angeles County, southern California: Western Association of Vertebrate Paleontologists 2011 Annual Meeting Field Trip Volume and Guidebook, Altadena, CA, 65 p.

Lander, E. B., 2013, Stratigraphy, biostratigraphy, biochronology, geochronology, magnetostratigraphy, and plate tectonic history of the early middle Eocene to late early Miocene Sespe, Vaqueros, and lower Topanga Formations, east-central Santa Monica Mountains, Los Angeles County, southern California: Society of Vertebrate Paleontology 73rd Annual Meeting Field Trip Volume and Guidebook on Arikareean and Hemingfordian Mammalian Vertebrate Paleontology of the Santa Monica Mountains National Recreation Area, Los Angeles County, Southern California, Altadena, CA.

Lechler, A. R., and Niemi, N. A., 2011, Sedimentologic and isotopic constraints on the Paleogene paleogeography and paleotopography of the southern Sierra Nevada, California: Geology, v. 39, n. 4, p. 379-382.

Lee, J. P., Stockli, D. F., Kelley, S. A., Pederson, J. L., Karlstrom, K. E., and Ehlers, T. A., 2013, New thermochronometric constraints on the Tertiary landscape evolution of the central and eastern Grand Canyon, Arizona: Geosphere, v. 9, p. 216-228.

Lucchitta, I., 2013, Comment on “Apatite $^{4}He/^{3}He$ and (U-Th)/He evidence for an ancient Grand Canyon:" Science, v. 340, no. 6129, p. 143-143.

Mahan, K. H., Guest, B., Wernicke, B. P. and Niemi, N. A., 2009, Low-temperature thermochronologic constraints on the kinematic history and spatial extent of the eastern California shear zone, Geosphere, v. 5 (6), p. 1–13; doi: 10.1130/GES00226.1.

McFadden, P. L., and Reid, A. B., 1982, Analysis of palaeomagnetic inclination data: Royal Astronomical Society Geophysical Journal, v. 69, p. 307–319.

McQuarrie, N. and Wernicke, B. P., 2005, An animated tectonic reconstruction of southwestern North America since 36 Ma: Geosphere, v. 1, no. 3, p. 1-20. doi: 10.1130/GES00016.1.

McKee, E. D., and Resser, C. E., 1945, Cambrian History of the Grand Canyon Region: Carnegie Institute Publications, v. 563, 232 p.

Meert, J. G., and Stuckey, W., 2002, Revisiting the paleomagnetism of the 1.476 Ga St. Francois Mountains igneous province, Missouri: Tectonics, v. 21, no. 2.

Minch, J. A., Howard, J. L., and Belyea, R. R., 1989, Sespe Formation conglomerates in the northern Santa Ana and Santa Monica Mountains: a field trip guide, in Colburn, I. P. et al., eds., Conglomerates in Basin Analysis: a Symposium Dedicated to A. O. Woodford: Pacific Section, Society of Economic Paleontologists and Mineralogists, Bakersfield, p. 301-312.

Minguez, D., Kodama, K. P., and Hillhouse, J. W., 2015, Paleomagnetic and cyclostratigraphic constraints on the synchroneity and duration of the Shuram carbon isotope excursion, Johnnie Formation, Death Valley Region, CA: Precambrian Research, v. 266, p. 395-408.

Molina-Garza, R. S., Acton, G. D, and Geissman, J. W., 1998, Carboniferous through Jurassic paleomagnetic data and their bearing on rotation of the Colorado Plateau: J. Geophys. Res., v. 103, p. 24,179–24,188.

Molina-Garza, R. S., and Geissman, J. W., 1999, Paleomagnetic data from the Caborca terrane, Mexico: implications for Cordilleran tectonics and the Mojave Sonora megashear hypothesis: Tectonics, v. 18, p. 293-325.

Moore, T. E., O'Sullivan, P. B., Potter, C. J., and Donelick, R. A., 2015, Provenance and detrital zircon evolution of early Brookian foreland basin deposits of the western Brooks Range, Alaska, and implications for early Brookian tectonism: Geosphere, v. 11, p. 93–122, doi:10.1130/GES01043.1.

Mulder, J. A., Karlstrom, K.E., Fletcher, K., Heizler, M.T., Timmons, J.M., Crossey, L.J., Gehrels, G.E., and Pecha, M., 2017, The syn-orogenic sedimentary record of the Grenville Orogeny in southwest Laurentia: Precambrian Research, 294, p. 33-52.

Noble, L. F., 1910, Contributions to the geology of the Grand Canyon Arizona: The geology of the Shinumo area: American Journal of Science, v. 29, no. 173, p. 369-386.

Noble, L. F., 1914, The Shinumo quadrangle, Grand Canyon district, Arizona: U.S. Geological Survey Bulletin 549, 100 p.

Pan, H., and Symons, D. T. A., 1993, The Pictou red beds' Pennsylvanian pole: Could Phanerozoic rocks in the interior United States be remagnetized?: Journal of Geophysical Research: Solid Earth, v. 98, p. 6227-6235.

Pederson, J., Mackley, R. D. and Eddleman, J. L., 2002, Colorado Plateau uplift and erosion evaluated using GIS: GSA Today, p. 4-10.

Polyak, V. J., Hill, C. A., and Asmerom, Y., 2008, Age and evolution of the Grand Canyon revealed by U-Pb dating of water table-type speleothems: Science, v. 319, p. 1377–1380, doi:10.1126/science.1151248.

Quigley, M., Karlstrom, K., Kelley, S. and Heizler, M., 2010, Timing and mechanisms of basement uplift and exhunation in the Colorado Plateau-Basin and Range Transition Zone, Virgin Mountain Anticline, Nevada-Arizona, in Umhoefer, P., Lamb, M. and Beard, L. S., eds., Miocene tectonics of the Lake Mead region, central Basin and Range:, Geological Society of America Special Paper 463, p. 311-329.

Raub, T. D., 2013, Miocene Grand Canyon with base level in Precambrian strata? Testing a Shinumo source scenario for seemingly special Sespe clasts using paleomagnetism: Geological Society of America Abstracts with Programs, 45, n. 7, 400.

Reynolds S. J., Florence, E. P. Welty, J.W., Roddy, M. S., Currier, D. A., Anderson, A. V. and Keith, S. B., 1986, Compilation of radiometric age determinations in Arizona: Arizona Bureau of Geology and Mineral Technology, Geological Survey Branch, Bulletin 197, 252 p.

Runcorn, S. K., 1964, Paleomagnetic results from Precambrian sedimentary rocks in the western United States: Geological Society of America Bulletin, v. 75, p. 687-704.

Sass, J. H., Lachenbruch, A. H., Galanis, S. P., Morgan, P., Priest, S. S., Moses, T. H. and Munroe, R. J., 1994, Thermal regime of the southern Basin and Range province 1.

Heat-flow data from Arizona and the Mojave Desert of California and Nevada: Journal of Geophysical Research-Solid Earth, v. 99, p. 22093-22119.

Schoenborn, W. A., Fedo, C. M., and Farmer, G. L., 2012, Provenance of the Neoproterozoic Johnnie Formation and Stirling Quartzite, southeastern California, determined by detrital zircon geochronology and Nd isotope geochemistry: Precambrian Research, v. 206, p. 182-199.

Schoellhamer, J. E., Vedder, J. G., Yerkes, R. F., and Kinney, D. M., 1981, Geology of the Northern Santa Ana Mountains, California: U. S. Geological Survey Professional Paper 420-D, 107 p.

Sharp, R. P., 1940, Ep-Archean and Ep-Algonkian erosion surfaces, Grand Canyon, Arizona: Bulletin of the Geological Society of America, v. 51, no. 5/8, p. 1235-1269.

Spafford, C. D., 2010, Provenance implications of sandstone petrology and detrital-zircon analysis of the mid-Cenozoic Sespe Formation, coastal southern California [M.S. thesis]: Los Angeles, University of California, 117 p.

Spencer, J. E., Pecha, M. E., Gehrels, G. E., Dickinson, W. R., Domanik, K. J., and Quade, J., 2016, Paleoproterozoic orogenesis and quartz-arenite deposition in the Little Chino Valley area, Yavapai tectonic province, central Arizona, USA: Geosphere, v. 12, p. 1774-1794.

Spotila, J. A., Farley, K. A., and Sieh, K., 1998, Uplift and erosion of the San Bernardino Mountains associated with transpression along the San Andreas fault, California, as constrained by radiogenic helium thermochronometry: Tectonics, v. 17, p. 360-378.

Stewart, J. H., Gehrels, G. E., Barth, A. P., Link, P. K., Christie-Blick, N., and Wrucke, C. T., 2001, Detrital zircon provenance of Mesoproterozoic to Cambrian arenites in the western United States and northwestern Mexico: Geological Society of America Bulletin, v. 113, p. 1343-1356.

Stewart. J. H., and Roldán-Quintana, J., 1991, Upper Triassic Barranca Group; Nonmarine and shallow-marine rift-basin deposits of northwestern Mexico: Geological Society of America Special Paper 254, p. 19-36.

Stewart, J. H., 1970, Upper Precambrian and Lower Cambrian strata in the southern Great Basin, California and Nevada: U.S. Geological Survey Professional Paper 620, 206 p.

Stüwe, K., White, L., and Brown, R., 1994, The influence of eroding topography on steady-state isotherms. Application to fission track analysis: Earth and Planetary Science Letters, v. 124, p. 63-74.

Tauxe, L., Kent, D. V., 2004, A simplified statistical model for the geomagnetic field and the detection of shallow bias in paleomagnetic inclinations: Was the ancient magnetic field dipolar?, in Timescales of the Paleomagnetic Field, American Geophysical Union, Washington, D. C., Geophysical Monograph Series, v. 145, p. 101-115.

Van Alstine, D. R., and Gillett, S. L., 1979, Paleomagnetism of Upper Precambrian sedimentary rocks from the Desert Range, Nevada: Journal of Geophysical Research, v. 84, p. 4490-4500.

Wernicke, B., 2011, The California River and its role in carving Grand Canyon: Geological Society of America Bulletin, v. 123, no. 7-8, p. 1288-1316.

Wernicke, B., Raub, T. D., Grover, J. A., and Lander, B. E., 2010, Possible clasts of Shinumo Quartzite (eastern Grand Canyon) in lower Miocene conglomerates of the Sespe Formation (coastal southern California), and implications for the uplift and erosion history of the southwestern US: Geological Society of America Abstracts with Programs, 42, n. 5, p. 185.

Wernicke, B., Raub, T. D., Lander, B. E., and Grover, J. A., 2012, Testing the Arizona River hypothesis: Detrital zircon spectra from orthoquartzite clasts in the mid-Tertiary Sespe Formation of coastal southern California: Geological Society of America Abstracts with Programs, 44, n. 6, p. 80.

Wilson, C. J. L., 1973, The prograde microfabric in a deformed quartzite sequence, Mount Isa, Australia: Tectonophysics, v. 19, p. 39–81.

Winn, C., Karlstrom, K. E., Shuster, D. L., Kelley, S., and Fox, M., 2017, 6 Ma age of carving westernmost Grand Canyon: Reconciling geologic data with combined AFT, (U–Th)/He, and $^{4}He/^{3}He$ thermochronologic data: Earth and Planetary Science Letters, v. 474, p. 257-271.

Woodford, A. O., Welday, E. E., and Merriam, R., 1968, Siliceous tuff clasts in the upper Paleogene of southern California: Geological Society of America Bulletin, v. 79, p. 1461-1486.

Woodford, A. O., McCulloh, T. J., and Schoellhamer, J. E., 1972, Paleogeographic significance of metatuff boulders in middle Tertiary strata, Santa Ana Mountains, California: Geological Society of America Bulletin, v. 83, p. 3433-3436.

FIGURES

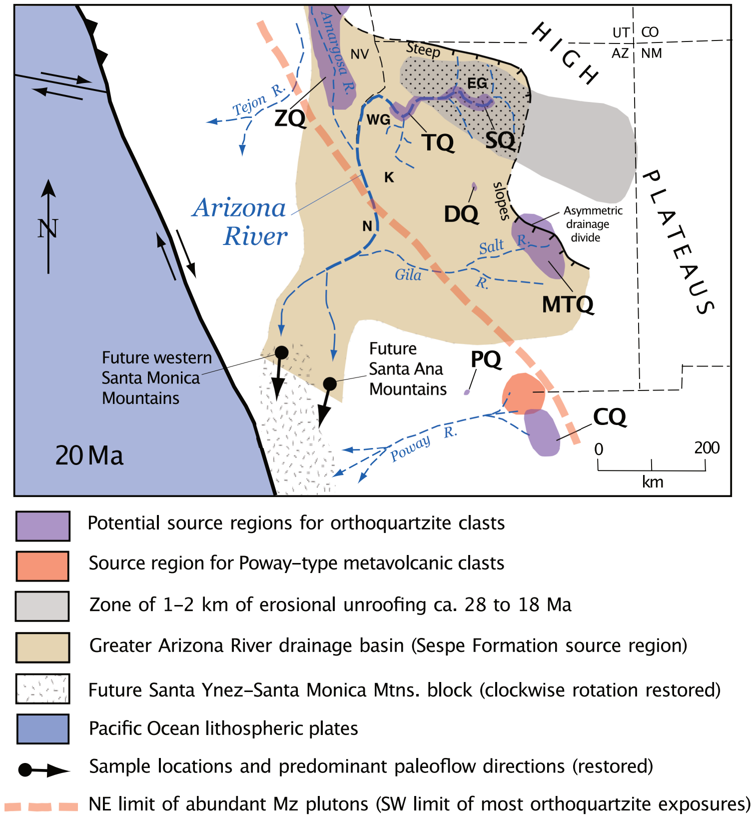

Figure 1: Geologic reconstruction of early Miocene positions of the Sespe Fm.

Geologic reconstruction, based on McQuarrie and Wernicke (2005), showing the early Miocene positions of Sespe Formation depocenters in the Santa Monica and Santa Ana Mountains with dominant paleoflow directions, and the extent of the Sespe Formation source regions, as inferred by Howard (2000, 2006) and Ingersoll et al. (2018), but including a portion of the southwestern Colorado Plateau, after Wernicke (2011). Stippled area inside zone of 28 to 18 Ma erosional unroofing delimits 30,000 km^2 area potentially contributing detritus to the Piuma Member of the Sespe Formation. The four main regions of exposed orthoquartzite (purple) include: (1) Death Valley-Mojave region, with Lower Cambrian Zabriskie Formation (ZQ) and associated Neoproterozoic orthoquartzites; (2) Grand Canyon region, with Shinumo Formation (SQ) of

Mesoproterozoic age in eastern Grand Canyon (EG), and quartzitic portions of the Tapeats Formation (TQ) of Cambrian age in western Grand Canyon (WG); (3) central Arizona highlands Paleo- to Mesoproterozoic rocks including Mazatzal, Tonto, and Hess Canyon groups (MTQ) and Del Rio Formation (DQ); (4) Neoproterozoic-Cambrian orthoquartzites (including clasts recycled in Jurassic conglomerates) in the Caborca area of Sonora, Mexico (CQ) and Mesoproterozoic quartzites at Sierra Prieta (PQ) in NW Sonora. Proposed paleorivers discussed in text shown in blue dashed lines. K, Kingman, Arizona, N, Needles, California.

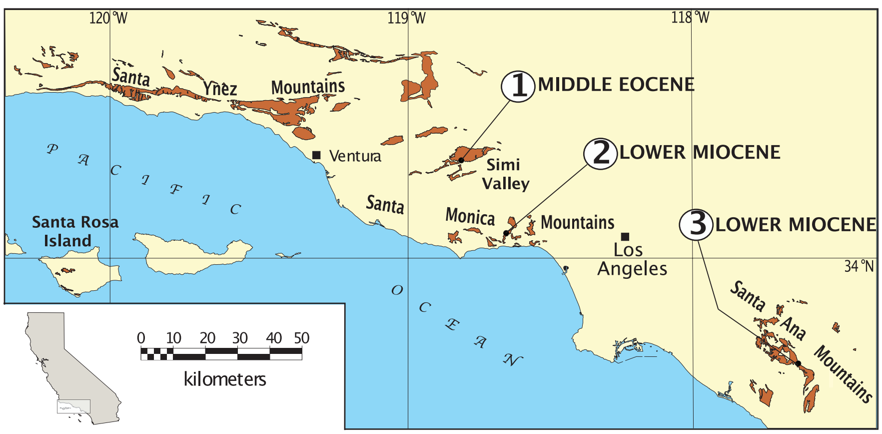

Figure 2: Map exposed early to mid-Tertiary Sespe Formation

Map showing distribution of surface exposures of early to mid-Tertiary Sespe Formation (reddish-brown shading) in the Los Angeles region (after Lander et al., 2011), and sample localities (black dots) with Sespe depositional ages, including: 1, View Lane Drive locality in Simi Valley, 2, Piuma Road and Scheuren Road localities in the Santa Monica Mountains, and 3, Red Rock Trail in Limestone Canyon Park, and Santiago Canyon Road localities in the Santa Ana Mountains (Tables 2 and 3).

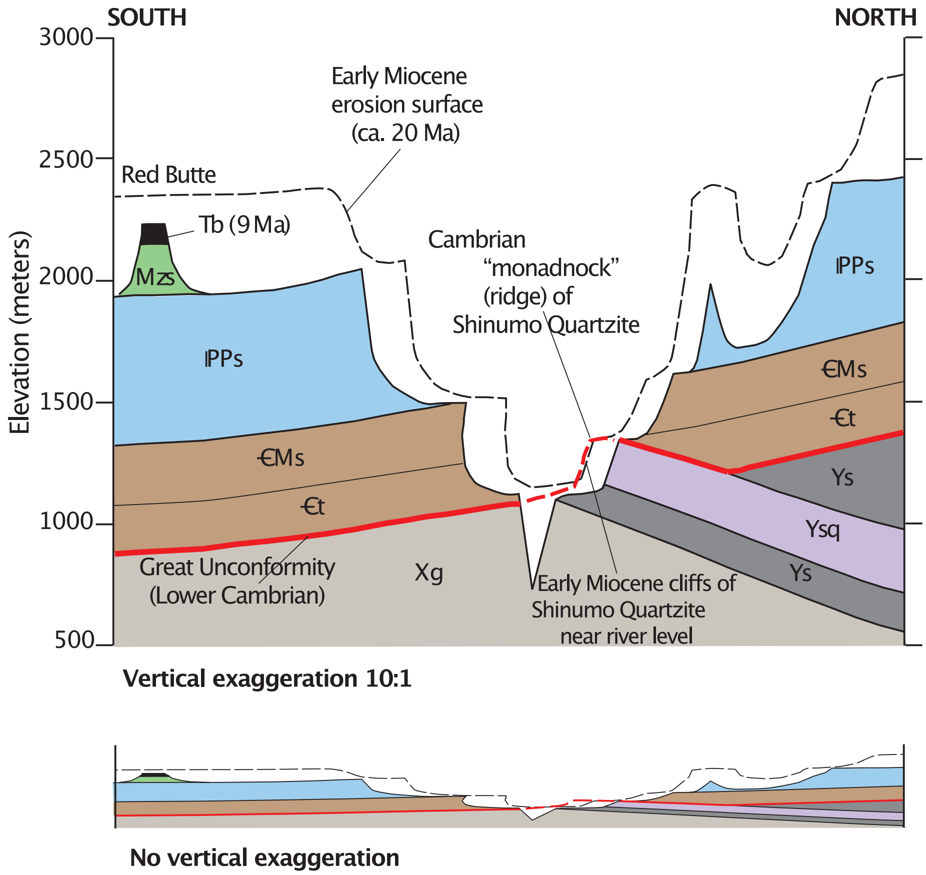

Figure 3: N-S Cross-section through Upper Granite Gorge area of eastern Grand Canyon

Generalized north-south cross-section through the Upper Granite Gorge area of eastern Grand Canyon region showing the disposition of the Shinumo Formation (Ysq) relative to a nominal early Miocene erosion surface. Xg, Paleoproterozoic gneiss, Ys, Mesoproterozoic strata, **€**t, Cambrian Tonto Group, **€**Ms, Cambrian through Mississippian strata, PPs, Pennsylvanian through Permian strata, Mzs, Mesozoic strata, and Tb, Tertiary basalt.

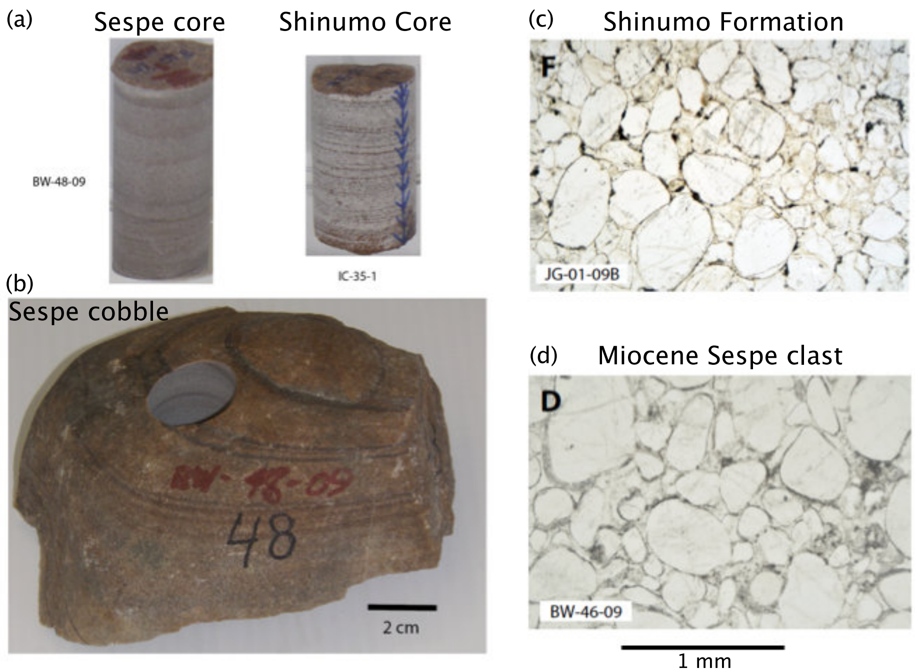

Figure 4: Photographs and photomicrographs of paleomagnetic cores of clasts

(a) Photograph of paleomagnetic cores of orthoquartzites, drilled perpendicular to bedding, from a Miocene Sespe Formation clast (left) and a bedrock sample of the Shinumo Formation (right). (b) Photograph of a Sespe Formation orthoquartzite cobble showing sedimentary lamination and drill-hole for left-hand paleomagnetic core shown in (a). (c, d) Photomicrographs of orthoquartzites from the Shinumo Formation and a clast from the Miocene Sespe Formation, respectively.

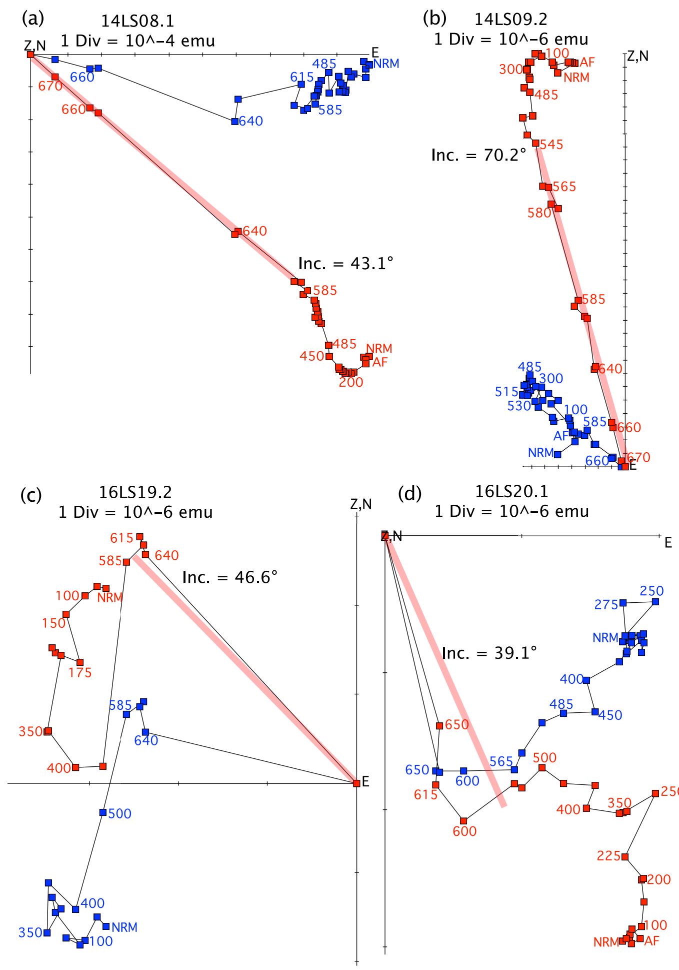

Figure 5: Zijderfeld plots of thermal demagnetizations for clasts

Zijderfeld plots showing thermal demagnetization histories of samples of orthoquartzite clasts from Miocene (a, b) and Eocene (c, d) Sespe Formation conglomerates. Detrital zircon spectra were determined for all four samples, as annotated on Figure 8.

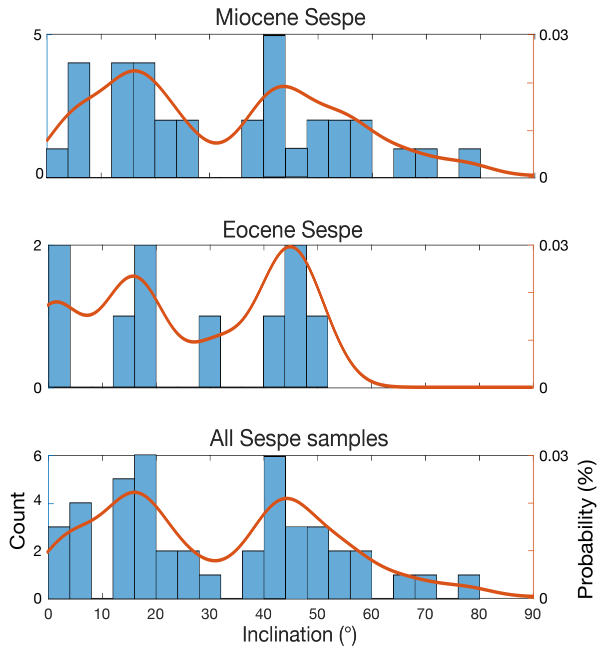

Figure 6: Histograms of paleomagnetic inclinations

Histograms and population density functions (PDFs) of paleomagnetic inclinations measured in clasts of the Miocene (a) and Eocene (b) Sespe Formation, shown as a sum in (c).

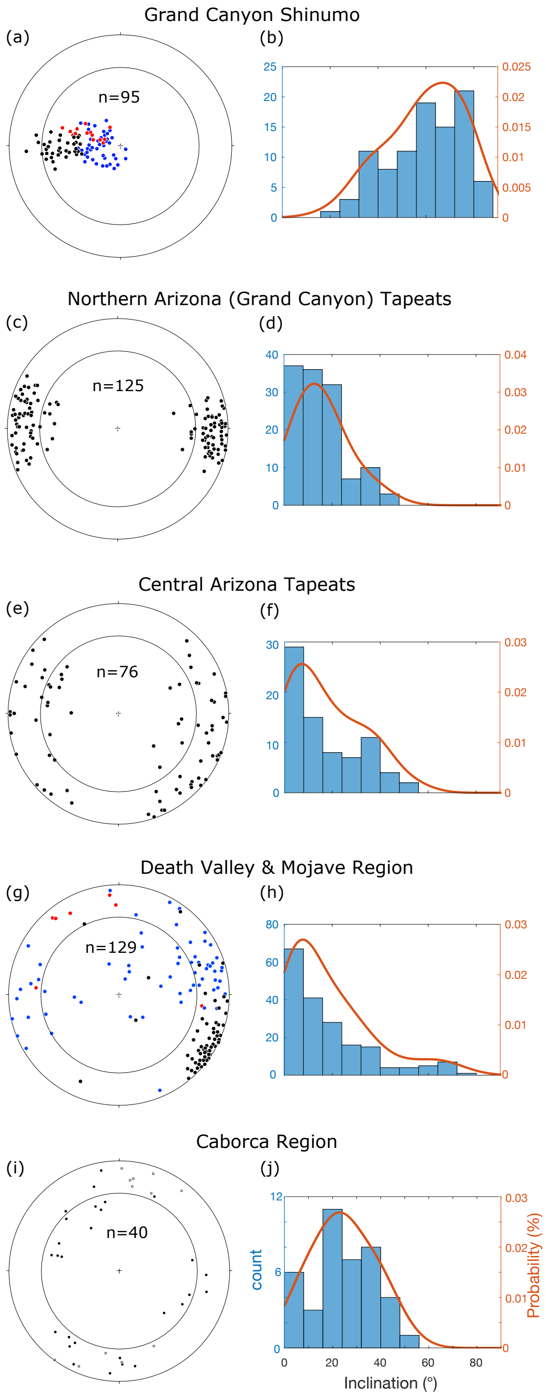

Figure 7: Inventory of published paleomagnetic data for source regions

Inventory of published orientations of CRMs for >700 individual paleomagnetic cores from known sources of orthoquartzite in southwestern North America. Stereograms of orientations of individual core samples are shown in (a), (c), (e), and (g) and respective histograms and PDFs of paleomagnetic inclinations are shown in (b), (d), (f), and (h). (a, b) Shinumo Formation, including lower (red dots), middle (black dots), and upper (blue dots) stratigraphic levels (D. Elston and S. Gromme, written commun., 1994), eastern Grand Canyon; (c, d) Tapeats Formation, Grand Canyon (Elston and Bressler, 1977); (e, f) central Arizona highlands, including Tapeats sandstone and equivalent strata, (Elston and Bressler, 1977); (g, h) Neoproterozoic-Cambrian strata of the Death Valley-Mojave region, including the Zabriskie Formation (red, Gillett and Van Alstine, 1979), the Wood Canyon Formation (black, Gillett and Van Alstine, 1979), and the Rainstorm Member of the Johnnie Formation (blue, Van Alstine and Gillett, 1979). A 30° inclination contour is shown as a small circle on each stereogram.

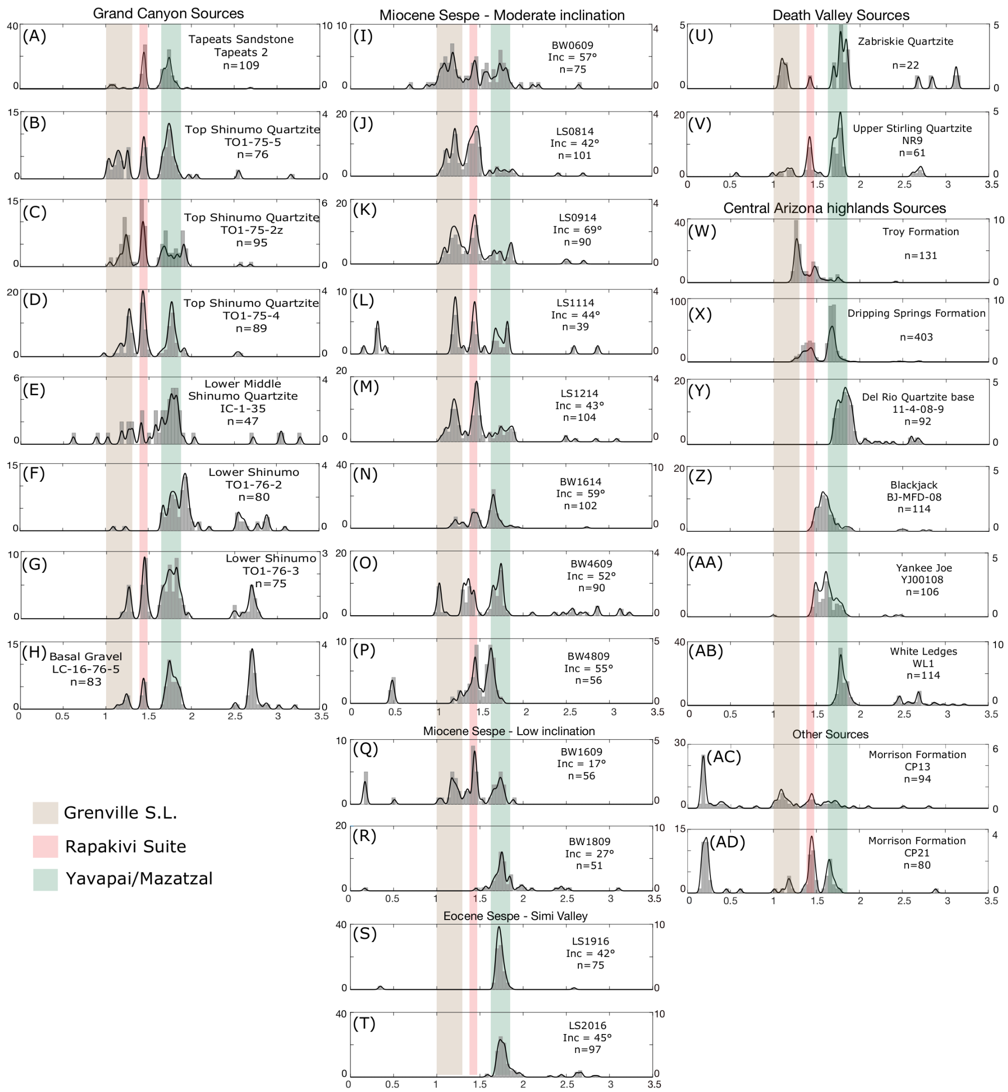

Figure 8: Detrital zircon spectra of potential sources and Sespe clasts

Detrital zircon spectra of potential sources and Sespe clasts. Potential Grand Canyon sources in the left column include the Tapeats Formation (a) and the Shinumo Formation (b-h). The center column includes Miocene Sespe clasts with moderate inclinations (i-p), Miocene Sespe clasts with low inclination (q, r), and Eocene Sespe clasts with moderate inclination (s, t). The right column shows Death Valley sources including the Zabriskie Quartzite (u) and Upper Stirling Quartzite (v), and central Arizona highland sources including the Troy Quartzite (3 samples) (w), the Dripping

Springs Formation (3 samples) (x), the Del Rio Quartzite base (y), the Blackjack (z), Yankee Joe (aa), and White Ledges (ab). We also include two samples of the Morrison Formation (ac) and (ad). Data sources are listed in Table 4.

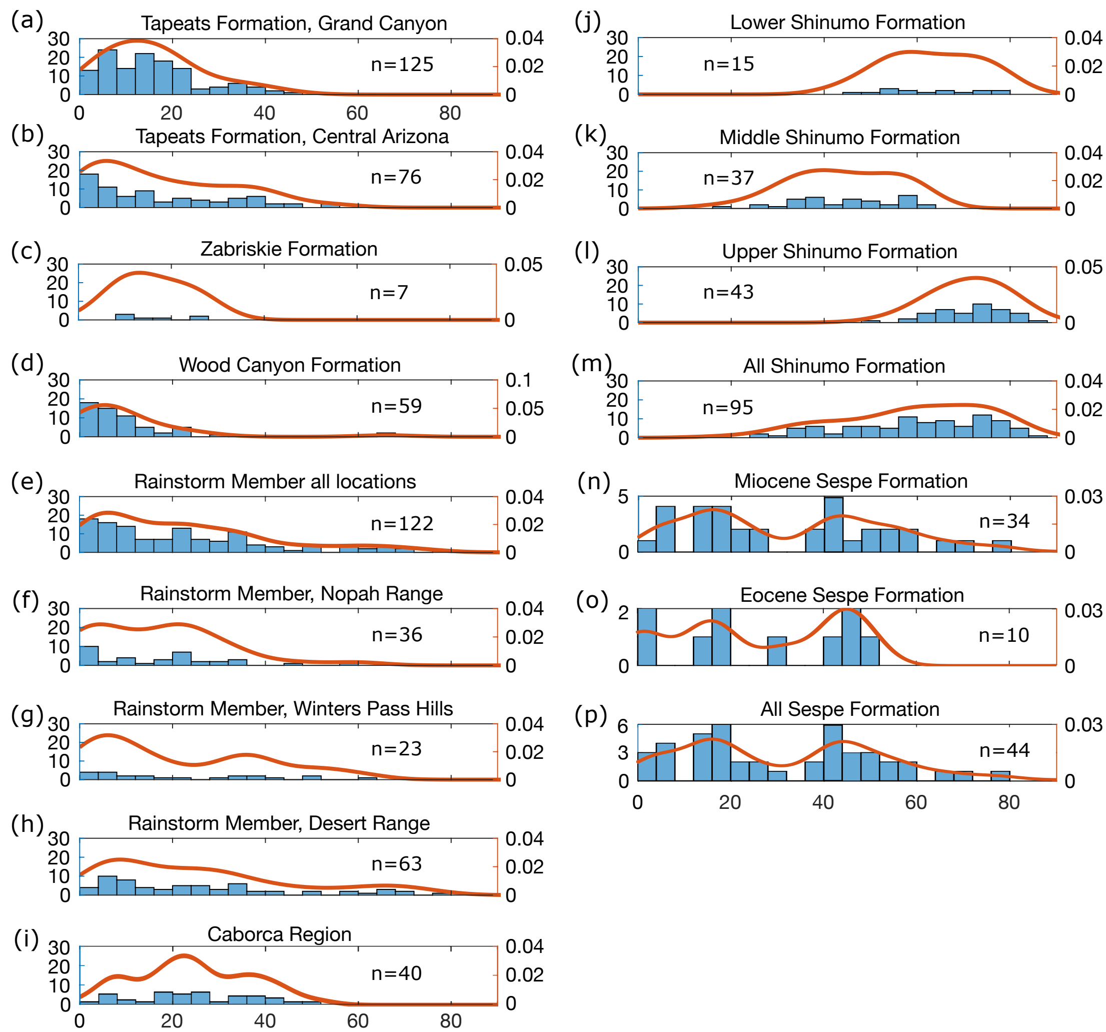

Figure 9: Histograms of paleomagnetic inclinations from potential sources and Sespe Formation

Histograms of paleomagnetic inclinations from potential sources, plotted at a uniform scale, and from clasts in the Sespe Formation, plotted at a suitably expanded scale. Potential sources from Grand Canyon include the Tapeats Formation (a) and the Shinumo Formation (j, k, l, and m). Potential sources from the central Arizona highlands include the Tapeats Formation (b). Potential

Death Valley sources include the the Zabriskie Formation (c), Wood Canyon Formation (d), Rainstorm Member of the Johnnie Formation (e, f, g, and h). Potential sources from Caborca include Ediacaran-Cambrian strata, mainly the El Arpa, Caborca, Clemente, Papalote, and Cerro Prieto formations (i). Paleomagnetic inclinations were measured in this study from the Miocene Sespe Formation (n) and the Eocene Sespe Formation (o), shown also as a sum (p). Paleomagnetic inclinations of the Rainstorm Member from the Nopah Range and Winters Pass Hills were measured after thermal demagnetization of 500-610 °C (Minguez et al., 2015), and inclinations of the Rainstorm Member from the Desert Range were demagnetized to 650 °C (Van Alstine and Gillett, 1979). Directions from the Wood Canyon (red-purple mudstones only) and Zabriskie Formations, both in the Desert Range, measured after thermal demagnetization to 640 °C (Gillett and Van Alstine, 1979 Figs 3f and 4). Paleomagnetic inclinations from the Tapeats Formation in the central Arizona highlands and in Grand Canyon were measured after thermal demagnetization at temperatures of 500-590 °C (Elston and Bressler, 1977). Inclinations from the lower Shinumo Formation were measured after demagnetization at 550 °C, from the middle Shinumo at 500-620 °C (data referred to as “Pole 4”), and from the upper Shinumo at 500-620 °C (Elston and Grommé, unpub.). Inclinations from clasts in the Miocene Sespe Formation (m) and clasts in the Eocene (n) are from this study, plotted also as a sum (o). Data sources are listed in Table 4.

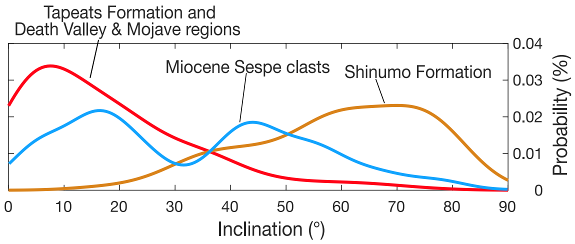

Figure 10: PDFs of inclination data from Sespe Formation and possible sources

Comparisons of probability density functions (PDFs) of paleomagnetic inclination data from Miocene Sespe orthoquartzite clasts (yellow curve), a summed population of Tapeats Formation, from both Grand Canyon and central Arizona highlands, and formations from the Death Valley-Mojave regions (blue curve), and the Shinumo Formation (red curve).

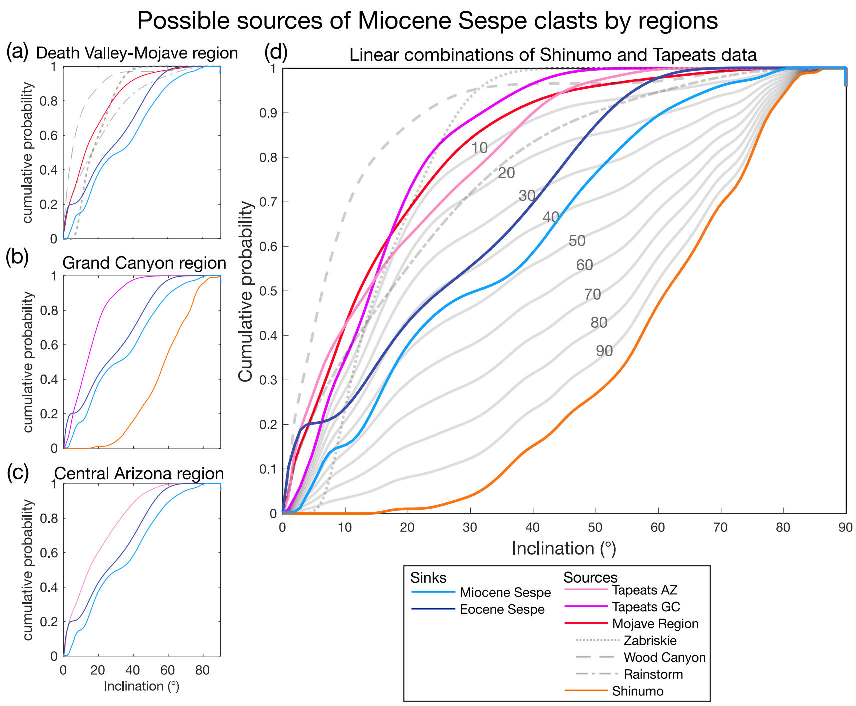

Figure 11: CDFs of inclination data from Sespe clasts and possible sources.

Comparisons of cumulative distribution functions (CDFs) of inclination data from Sespe orthoquartzite clasts (blue-hued curves) and possible sources (red-hued curves), including (a) Death Valley-Mojave region sources, (b) Grand Canyon region sources, and (c) central Arizona highlands sources. The three gray curves in (a) are summed to yield an average for the Death Valley-Mojave region (red). (d) Summary plot showing linear mixtures of Tapeats Formation from Grand Canyon and Shinumo Formations as endmembers, contoured in 10% increments (solid gray curves).

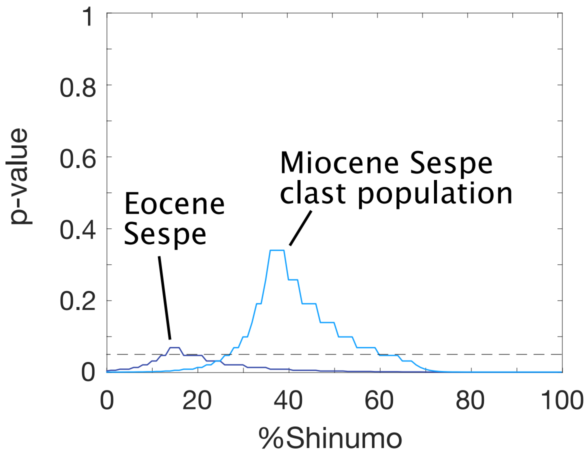

Figure 12: P-values for comparing Miocene and Eocene Sespe Fm to Grand Canyon sources

P-values for comparisons of CDFs from Figure 10, including (a) Eocene Sespe and (b) Miocene Sespe inclination populations, and mixtures of Tapeats Formation from eastern Grand Canyon (right endmembers) and Shinumo Formation (left endmembers) inclination populations.

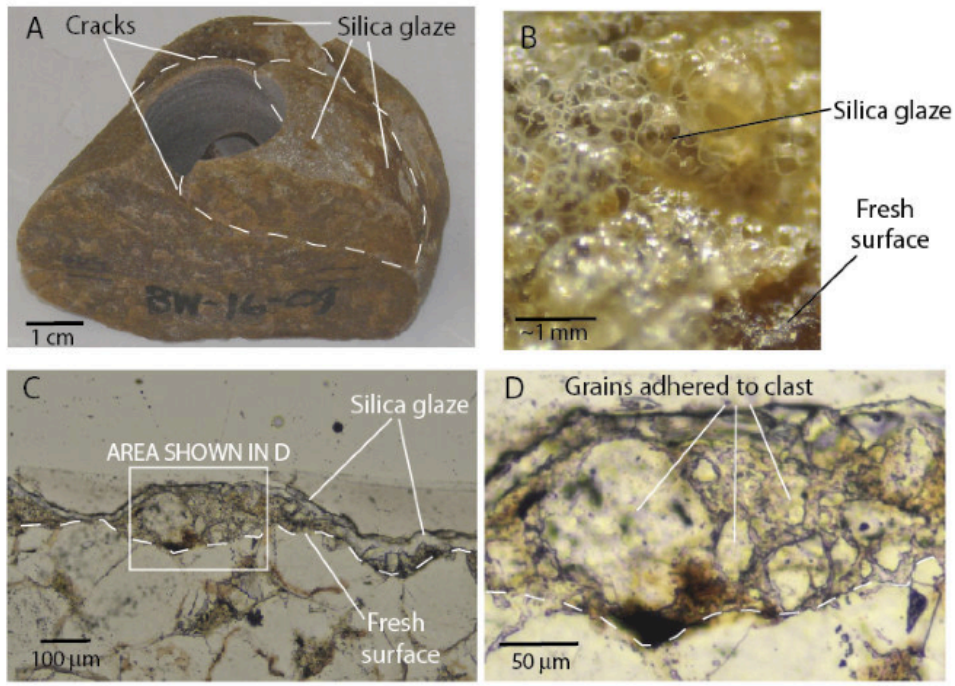

Figure 13: Silica glaze on Sespe orthoquartzite clast

Images of silica glaze on a Sespe orthoquartzite clast from roadcut on Santiago Canyon Road. (a) Photo showing light brown weathering patches of silica glaze on clast exterior, and the location of cracks within the sample that locally contain detrital material external to the clast, (b) photo showing small-scale mammillary texture of silica glaze in reflected light, (c, d) photomicrographs of thin sections cut normal to clast exterior showing silica glaze in cross-section, which includes external grains adhered to the clast, in transmitted light.

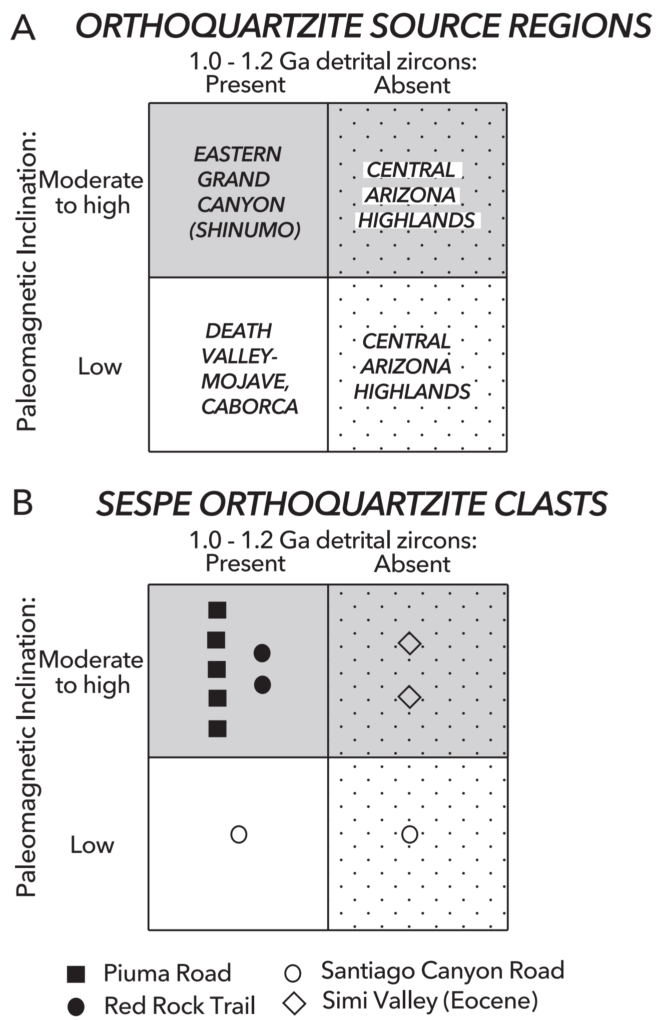

Figure 14: Summary matrix

Matrices summarizing research outcomes of paleomagnetic and detrital zircon data for (A) orthoquartzite detrital source regions and (B) pre-Mesozoic orthoquartzite clasts in which both paleomagentic inclination and detrital zircon data were obtained (n=11), keyed to sample collection locality.

TABLE 1. COLLECTED SAMPLES FROM GRAND CANYON SOURCES

Sample number	Location Lat (°N)	Long (°W)	Formation
Grand Canyon, South Kaibab Trail			
IC-1-35[*†§]	36°05'30"N (approx)	112°05'20" W (approx)	Shinumo
Grand Canyon, Clear Creek Trail			
IC-503-35[*]	36°06'20"N (approx)	112°04'50" W (approx)	Tapeats
Grand Canyon, River Mile 75			
JG -01-09[*]	36° 03' 15.6"N	111 54' 03.37"W	Shinumo

[*]Petrography

[†]Paleomagnetic analysis

[§]Detrital zircon analysis

Table 1: Collected samples from Grand Canyon sources

TABLE 2. COLLECTED SAMPLES OF SESPE CLASTS FROM SOUTHERN CALIFORNI

Sample number	Location Lat (°N)	Location Long (°W)	Age
Piuma Road, Malibu			
BW-01-09	34° 04' 13.0"N	118 39' 59.86"W	Miocene
BW-02-09	34° 04' 13.0"N	118 39' 59.86"W	Miocene
BW-03-09	34° 04' 13.0"N	118 39' 59.86"W	Miocene
BW-04-09	34° 04' 13.0"N	118 39' 59.86"W	Miocene
BW-05-09	34° 04' 13.0"N	118 39' 59.86"W	Miocene
BW-06-09[*†§]	34° 04' 13.0"N	118 39' 59.86"W	Miocene
BW-07-09	34° 04' 13.0"N	118 39' 59.86"W	Miocene
BW-08-09	34° 04' 13.0"N	118 39' 59.86"W	Miocene
BW-16-14[*†§]	34° 4'20.25"N	118°39'29.08"W	Miocene
BW-17-14[*†]	34° 4'20.25"N	118°39'29.08"W	Miocene
14LS01[*†]	34° 4'20.25"N	118°39'29.08"W	Miocene
14LS02[*†]	34° 4'20.25"N	118°39'29.08"W	Miocene
14LS03[*]	34° 4'20.25"N	118°39'29.08"W	Miocene
14LS04[*†]	34° 4'20.25"N	118°39'29.08"W	Miocene
14LS05[*]	34° 4'20.25"N	118°39'29.08"W	Miocene
14LS06[*†]	34° 4'20.25"N	118°39'29.08"W	Miocene
14LS07[*†]	34° 4'20.25"N	118°39'29.08"W	Miocene
14LS08[*†§]	34° 4'20.25"N	118°39'29.08"W	Miocene
14LS09[*†§]	34° 4'20.25"N	118°39'29.08"W	Miocene
14LS10[*]	34° 4'20.25"N	118°39'29.08"W	Miocene
14LS11[*†§]	34° 4'20.25"N	118°39'29.08"W	Miocene
14LS12[*†§]	34° 4'20.25"N	118°39'29.08"W	Miocene
14LS13[*]	34° 4'20.25"N	118°39'29.08"W	Miocene
14LS14[*†]	34° 4'20.25"N	118°39'29.08"W	Miocene
14LS15[*†]	34° 4'12.22"N	118°40'5.59"W	Miocene
14LS16[*]	34° 4'12.22"N	118°40'5.59"W	Miocene
14LS17[*]	34° 4'12.22"N	118°40'5.59"W	Miocene
14LS18[*]	34° 4'12.22"N	118°40'5.59"W	Miocene
14LS19[*†]	34° 4'12.22"N	118°40'5.59"W	Miocene
14LS20[*†]	34° 4'12.22"N	118°40'5.59"W	Miocene
Santiago Canyon Road			
BW-11-09	33° 42' 9.0"N	117 38' 31.4"W	Miocene
BW-12-09	33° 42' 9.0"N	117 38' 31.4"W	Miocene
BW-13-09	33° 42' 9.0"N	117 38' 31.4"W	Miocene
BW-14-09	33° 42' 9.0"N	117 38' 31.4"W	Miocene
BW-15-09	33° 42' 9.0"N	117 38' 31.4"W	Miocene
BW-16-09[*†§]	33° 42' 9.0"N	117 38' 31.4"W	Miocene
BW-17-09	33° 42' 9.0"N	117 38' 31.4"W	Miocene
BW-18-09[*†§]	33° 42' 9.0"N	117 38' 31.4"W	Miocene
BW-19-09	33° 42' 9.0"N	117 38' 31.4"W	Miocene
BW-20-09	33° 42' 9.0"N	117 38' 31.4"W	Miocene
BW-21-09	33° 42' 9.0"N	117 38' 31.4"W	Miocene
BW-22-09	33° 42' 9.0"N	117 38' 31.4"W	Miocene
BW-23-09	33° 42' 9.0"N	117 38' 31.4"W	Miocene
BW-24-09	33° 42' 9.0"N	117 38' 31.4"W	Miocene
Red Rock Trail, Limestone Canyon Park			
BW-46-09[*†§]	33° 42' 10.3"N	117 38' 56.65"W	Miocene
BW-47-09	33° 42' 10.3"N	117 38' 56.65''W	Miocene
BW-48-09[*†§]	33° 42' 10.3"N	117 38' 56.65"W	Miocene
BW-49-09	33° 42' 10.3"N	117 38' 56.65''W	Miocene
BW-50-09	33° 42' 10.3"N	117 38' 56.65''W	Miocene
BW-51-09	33° 42' 10.3"N	117 38' 56.65''W	Miocene
BW-52-09	33° 42' 10.3"N	117 38' 56.65''W	Miocene

BW-53-09	33° 42' 10.3"N	117 38' 56.65''W	Miocene
Schueren Road, Malibu			
15LS01†	34° 4'42.78"N	118°38'57.60"W	Miocene
15LS02†	34° 4'42.78"N	118°38'57.60"W	Miocene
15LS03†	34° 4'42.78"N	118°38'57.60"W	Miocene
15LS04	34° 4'42.78"N	118°38'57.60"W	Miocene
15LS05	34° 4'42.78"N	118°38'57.60"W	Miocene
15LS06†	34° 4'42.78"N	118°38'57.60"W	Miocene
15LS07†	34° 4'42.78"N	118°38'57.60"W	Miocene
15LS08†	34° 4'42.78"N	118°38'57.60"W	Miocene
15LS09	34° 4'42.78"N	118°38'57.60"W	Miocene
15LS10†	34° 4'42.78"N	118°38'57.60"W	Miocene
15LS11	34° 4'42.78"N	118°38'57.60"W	Miocene
15LS12†	34° 4'42.78"N	118°38'57.60"W	Miocene
15LS13†	34° 4'42.78"N	118°38'57.60"W	Miocene
15LS14†	34° 4'42.78"N	118°38'57.60"W	Miocene
15LS15†	34° 4'42.78"N	118°38'57.60"W	Miocene
15LS16†	34° 4'42.78"N	118°38'57.60"W	Miocene
15LS17	34° 4'49.18"N	118°38'49.61"W	Miocene
15LS18	34° 4'49.18"N	118°38'49.61"W	Miocene
15LS19†	34° 4'49.18"N	118°38'49.61"W	Miocene
Simi Valley, Ventura County			
16LS01†	34°17'9.97"N	118°47'35.11"W	Eocene
16LS02†	34°17'9.97"N	118°47'35.11"W	Eocene
16LS03†	34°17'9.97"N	118°47'35.11"W	Eocene
16LS04	34°17'9.97"N	118°47'35.11"W	Eocene
16LS05†	34°17'9.97"N	118°47'35.11"W	Eocene
16LS06†	34°17'9.97"N	118°47'35.11"W	Eocene
16LS07†	34°17'9.97"N	118°47'35.11"W	Eocene
16LS08†	34°17'9.97"N	118°47'35.11"W	Eocene
16LS09	34°17'9.97"N	118°47'35.11"W	Eocene
16LS10†	34°17'9.97"N	118°47'35.11"W	Eocene
16LS11	34°17'9.97"N	118°47'35.11"W	Eocene
16LS12†	34°17'9.97"N	118°47'35.11"W	Eocene
16LS13†	34°17'9.97"N	118°47'35.11"W	Eocene
16LS14†	34°17'9.97"N	118°47'35.11"W	Eocene
16LS15	34°17'9.97"N	118°47'35.11"W	Eocene
16LS16†	34°17'9.97"N	118°47'35.11"W	Eocene
16LS17	34°17'9.97"N	118°47'35.11"W	Eocene
16LS18	34°17'9.97"N	118°47'35.11"W	Eocene
16LS19†§	34°17'9.97"N	118°47'35.11"W	Eocene
16LS20†§	34°17'9.97"N	118°47'35.11"W	Eocene
16LS21†	34°17'9.97"N	118°47'35.11"W	Eocene

*Petrography

†Paleomagnetic analysis

§Detrital zircon analysis

Table 2: Collected samples from Southern California

TABLE 3. SUMMARY OF ANALYSES PERFORMED ON SESPE CLAST SAMPLES

Location	Number collected	Stratified orthoquartzites	Interpretable paleomagnetic vector	Zircon analyses
Miocene Sespe				
Santa Monica Mountains				
Piuma Road	30	17	17	6
Schueren Road	19	13	13	0
Santa Ana Mountains				
Limestone Canyon Park	8	2	2	2
Santiago Canyon Road	14	2	2	2
Eocene Sespe				
Simi Valley Landfill	21	15	10	2
Total	92	49	44	12

Table 3: Summary of analyses performed on Sespe clasts

TABLE 4. SUMMARY OF PALEOMAGNETIC RESULTS

				Location	
Clast	Inclination (°)	MAD	Peak Temp. (°C)	Lat (°N)	Long (°W)
South Kaibab Trail, Grand Canyon					
IC-1-35†	54.9	7.7	672	36.0917	112.0889
Bolero Lookout - Santiago Cyn Rd					
BW16-09†	17.1	4.2	660	33.702500	117.642056
BW18-09†	27	6.4	672	33.702500	117.642056
Red Rock Trail, Limestone Canyon Park					
BW46-09†	51.6	4.9	500	33.702861	117.649069
BW48-09†	55	9.8	672	33.702861	117.649069
Saddle Peak - Piuma Rd					
BW0609†	56.6	3.8	672	34.070278	118.666628
14LS01*	53.1	2.2	640-680	34.072292	118.658078
14LS02	17.6	12.7	650	34.072292	118.658078
14LS04*	21.2	7.6	650-660	34.072292	118.658078
14LS06	5.5	8.9	650	34.072292	118.658078
14LS07	7.0	2.2	670	34.072292	118.658078
14LS08*†	42.3	1.3	670-680	34.072292	118.658078
14LS09*†	68.7	1.7	670	34.072292	118.658078
14LS11†	43.6	5.3	660	34.072292	118.658078
14LS12†	43.4	1.7	660	34.072292	118.658078
14LS14	48.2	13.0	650	34.072292	118.658078
14LS15*	38.8	12.1	615-630	34.070061	118.668219
14LS17*	23.5	2.5	575-585	34.070061	118.668219
14LS19	13.6	9.0	555	34.070061	118.668219
14LS20	13.2	6.4	650	34.070061	118.668219
14BW16*†	58.5	2.2	680	34.072292	118.658078
14BW17	43.8	11.9	565	34.072292	118.658078
Saddle Peak - Schueren Rd					
15LS01*	17.9	7.0	650	34.078550	118.649333
15LS02*	4.3	2.8	615-650	34.078550	118.649333
15LS03	24.9	4.9	670	34.078550	118.649333
15LS06	77.2	7.5	600	34.078550	118.649333
15LS07	6.2	7.2	500	34.078550	118.649333
15LS08	36.6	1.6	660	34.078550	118.649333
15LS10	64.6	4.2	575	34.078550	118.649333
15LS12*	45.8	3.3	400-450	34.078550	118.649333
15LS13	14.4	1.3	580	34.078550	118.649333
15LS14	17.5	5.9	500	34.078550	118.649333
15LS15	40.1	7.0	515	34.078550	118.649333
15LS16	15.0	5.3	350	34.078550	118.649333
15LS19	3.2	1.8	585	34.080328	118.647114

Simi Valley					
16LS01*	12.8	1.2	670	34.286103	118.793086
16LS02	45.6	3.0	515	34.286103	118.793086
16LS06	18.7	8.0	660	34.286103	118.793086
16LS08*	50.0	0.7	640	34.286103	118.793086
16LS09	1.9	0.9	670	34.286103	118.793086
16LS12	0.4	7.1	545	34.286103	118.793086
16LS13	16.4	5.6	575	34.286103	118.793086
16LS16	31.2	4.2	650	34.286103	118.793086
16LS19*†	41.5	2.2	640	34.286103	118.793086
16LS20†	44.8	4.8	650	34.286103	118.793086

*Multiple cores

†Zircon analysis

Table 4: Summary of paleomagnetic results

TABLE 5: REFERENCES FOR PREVIOUS DETRITAL ZIRCON AND PALEOMAGNETIC DATA

Figure	Sample or Formation	Reference	
Detrital Zircon Data			
8a	Tapeats 2	Gehrels et al., 2011	
8b	Shinumo TO1-75-5	Bloch et al., 2006	
8c	Shinumo TO1-75-2z	Bloch et al., 2006	
8b	Shinumo TO1-75-4	Bloch et al., 2006	
8f	Shinumo TO1-76-2	Bloch et al., 2006	
8g	Shinumo TO1-76-3	Bloch et al., 2006	
8h	Shinumo Basal Gravel LC-16-76-5	Mulder et al., 2017	
8u	Zabriskie Quartzite	Stewart et al., 2001	
8v	Upper Stirling NR9S	Shoenborn et al., 2012	
8w	Troy Formation	Stewart et al., 2001; Mulder et al., 2017	
8x	Dripping Springs Formation	Stewart et al., 2001; Mulder et al., 2017	
8y	Del Rio Quartzite	Spencer et al., 2016	
8z	Blackjack	Doe et al., 2012	
8aa	Yankee Joe	Doe et al., 2012	
8ab	White Ledges	Doe et al., 2012	
8ac	Morrison Formation	Dickinson and Gehrels, 2008	
8ad	Morrison Formation	Dickinson and Gehrels, 2008	
Paleomagnetic data			Maximum Demagnetization Temperature (°C)
9a	Tapeats, Grand Canyon	Elston and Bressler, 1977	500-590
9b	Tapeats, central Arizona	Elston and Bressler, 1977	undetermined
9c	Zabriskie Formation	Gillett and Van Alstine, 1979	640
9d	Wood Canyon Fm (red-purple mudstones only)	Gillett and Van Alstine, 1979 (Fig 3f and 4)	640
9e	Rainstorm, all locations	Minguez et al., 2015 and Van Alstine and Gillett, 1979	500-610
9f	Rainstorm, Nopah Range	Minguez et al., 2015	500-610
9g	Rainstorm, Winters Pass Hills	Minguez et al., 2015	500-610
9h	Rainstorm, Desert Range	Van Alstine and Gillett, 1979	650
9i	Neoproterozoic - Cambrian, Caborca Region	Molina-Garza and Geissman, 1999	355-660 (avg. 530)
9j	Lower Shinumo	Elston and Grommé, 1994	550
9k	Middle Shinumo (Pole 4)	Elston and Grommé, 1994	500-620
9l	Upper Shinumo	Elston and Grommé, 1994	650
9m	All above Shinumo	Elston and Grommé, 1994	see above

Table 5: References for previous paleomagnetic and detrital zircon data

TABLE 6: SUMMARY OF RESULTS FOR SAMPLES WITH PALEOMAGNETIC AND DETRITAL ZIRCON DATA

Sample and location	Paleomagnetic Inclination (°)	Grenville DZ Peak?	Interpreted source region
Miocene Sespe – moderate & high inclination			
Piuma Road			
LS1114	44	Yes	Morrison Formation
BW0609	57	Yes	Grand Canyon (Shinumo)
LS0814	42	Yes	Grand Canyon (Shinumo)
LS0914	69	Yes	Grand Canyon (Shinumo)
LS1214	43	Yes	Grand Canyon (Shinumo)
BW1614	59	Yes	Grand Canyon (Shinumo)
Red Rock Trail, Limestone Canyon Park			
BW4609*	52	Yes	Grand Canyon (Shinumo)
BW4809	55	Yes	Grand Canyon (Shinumo)
Miocene Sespe – low inclination			
Santiago Canyon Road			
BW1609	17	Yes	Death Valley
BW1809	27	No	Central Arizona highlands
Eocene Sespe – moderate inclination			
Simi Valley			
LS1916	42	No	Central Arizona highlands
LS2016	45	No	Central Arizona highlands

* Characteristic magnetization is carried by magnetite, which has not been observed in the extant database for Shinumo

Table 6: Summary of results for samples with paleomagnetic and detrital zircon data

SUPPLEMENTAL FIGURES


14LS08


15LS16


16LS09

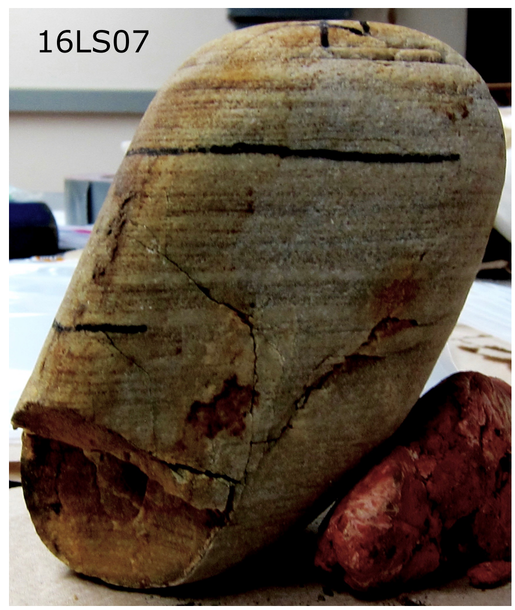
16LS07

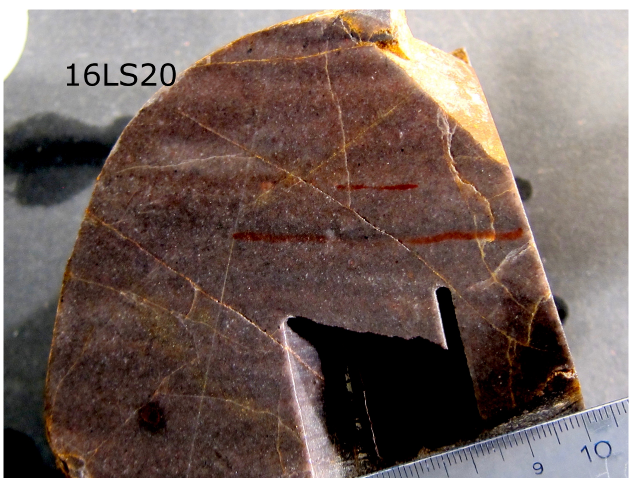
16LS20

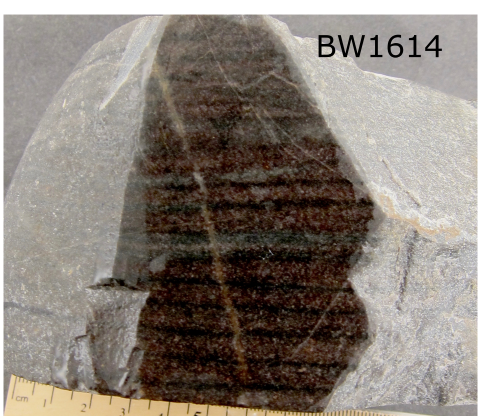
BW1614


14LS09

Figure S1: Photographs of seven representative clasts showing stratification.

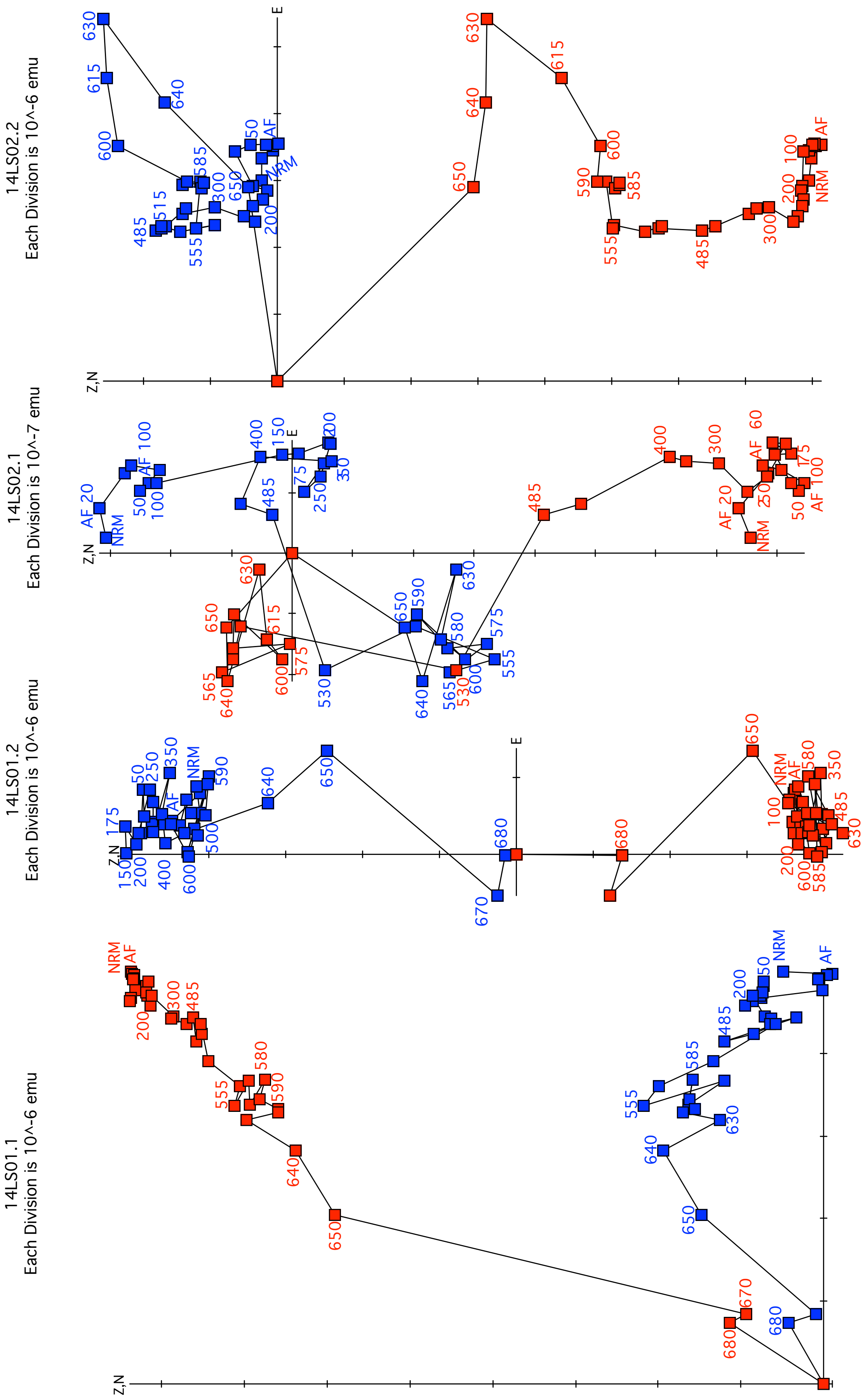
14LS01.1
Each Division is 10^-6 emu
14LS01.2
Each Division is 10^-6 emu
14LS02.1
Each Division is 10^-7 emu
14LS02.2
Each Division is 10^-6 emu

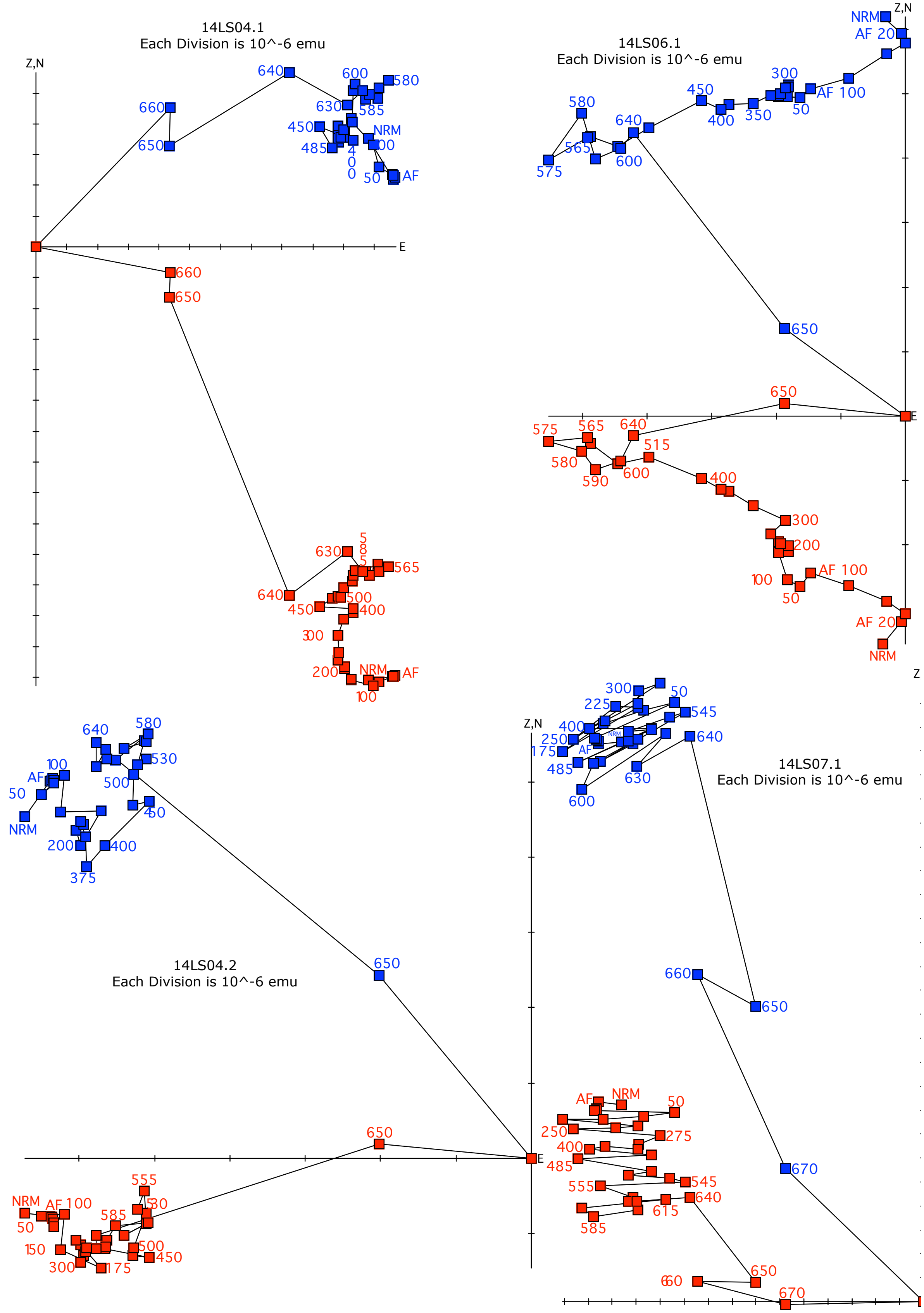
14LS04.1
Each Division is 10^-6 emu
14LS06.1
Each Division is 10^-6 emu
14LS04.2
Each Division is 10^-6 emu
14LS07.1
Each Division is 10^-6 emu
Z,N
E

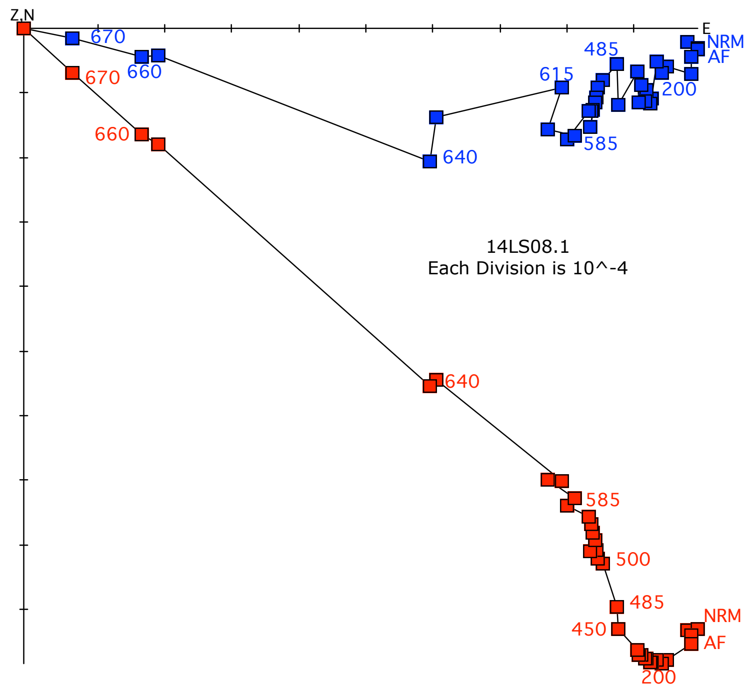
Z,N
E
14LS08.1
Each Division is 10^-4
NRM
AF
200
485
615
585
640
660
670
450
500

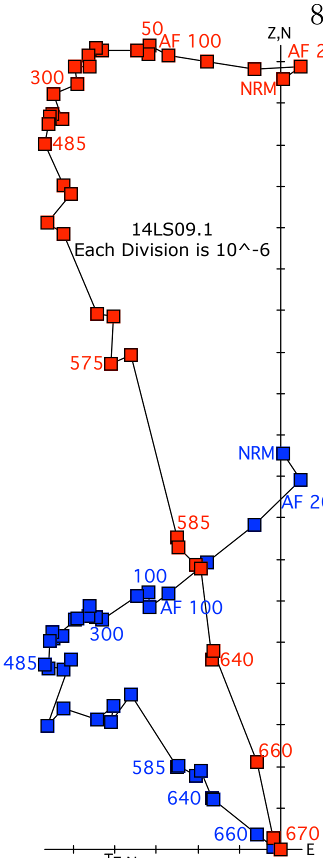
Z,N
E
14LS09.1
Each Division is 10^-6
NRM
50
AF 100
300
485
575
585
640
660
670
100
300
585

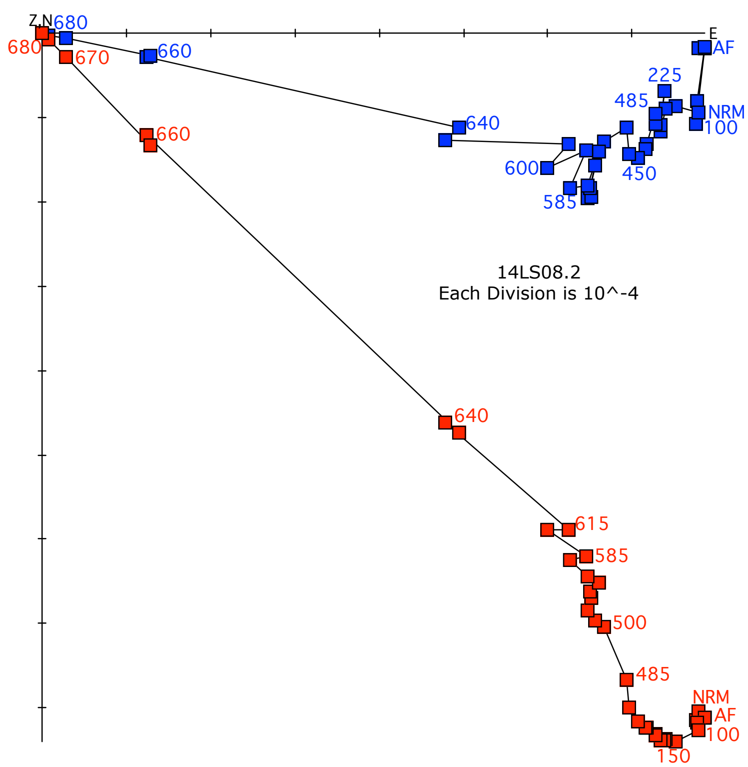
Z,N
E
680
670
660
640
14LS08.2
Each Division is 10^-4
AF
NRM
100
225
485
450
600
585
615
500
150

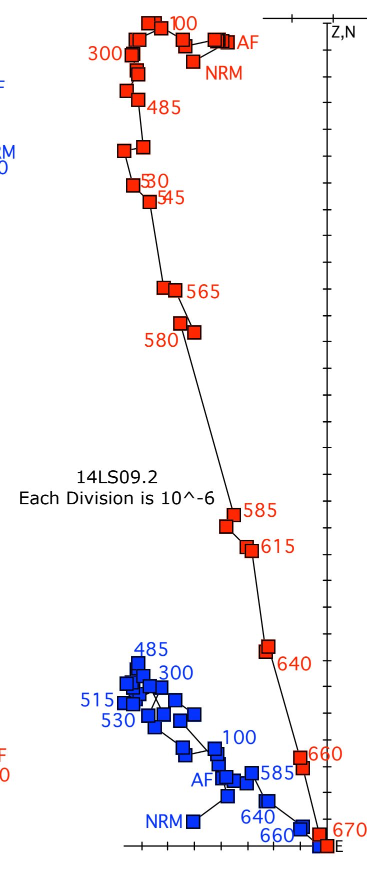
Z,N
E
14LS09.2
Each Division is 10^-6
100
AF
NRM
300
485
565
580
585
615
640
660
670
515
530
100

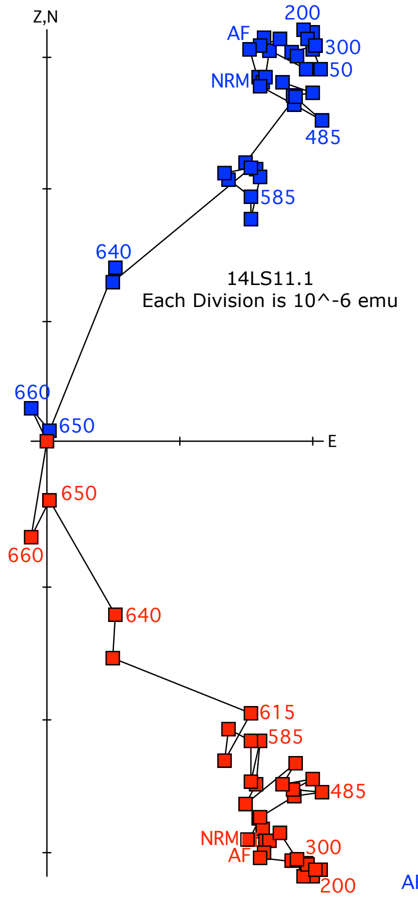
Z,N
E
14LS11.1
Each Division is 10^-6 emu

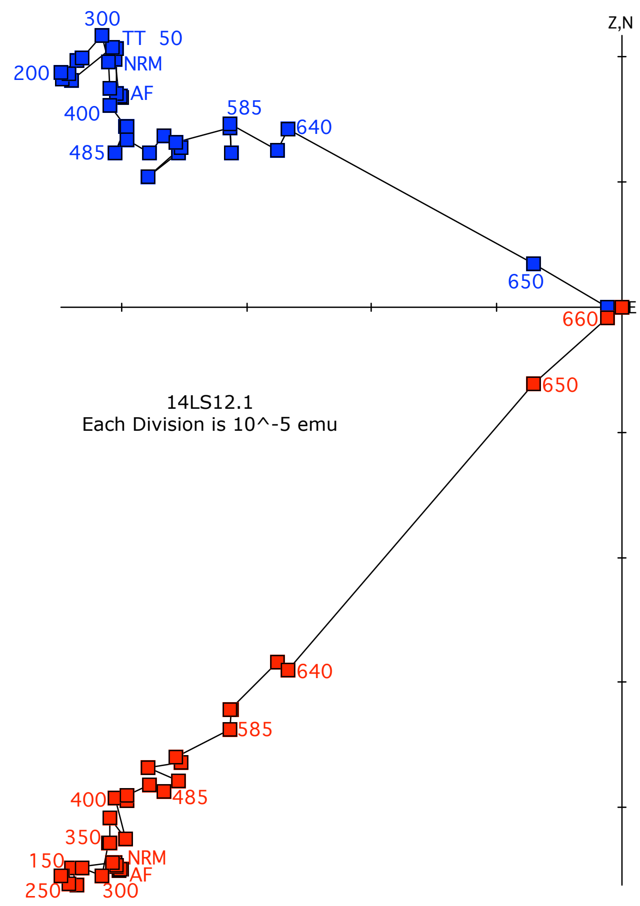
Z,N
E
14LS12.1
Each Division is 10^-5 emu

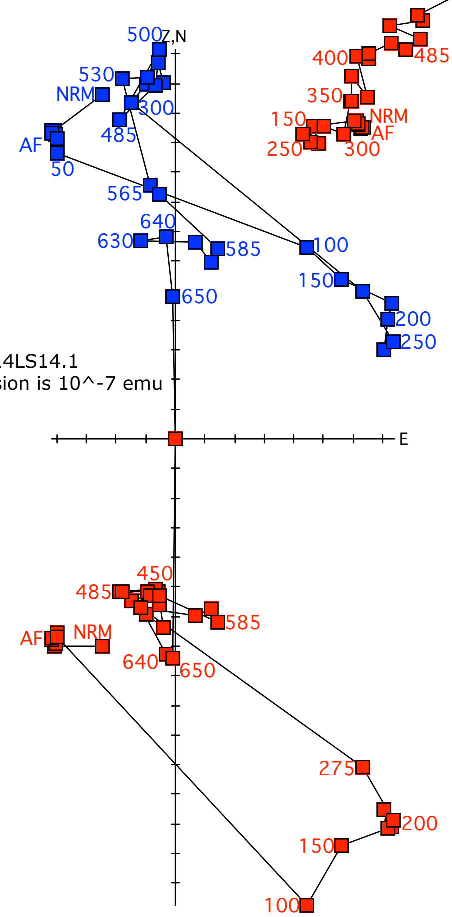
Z,N
E
14LS14.1
Each Division is 10^-7 emu

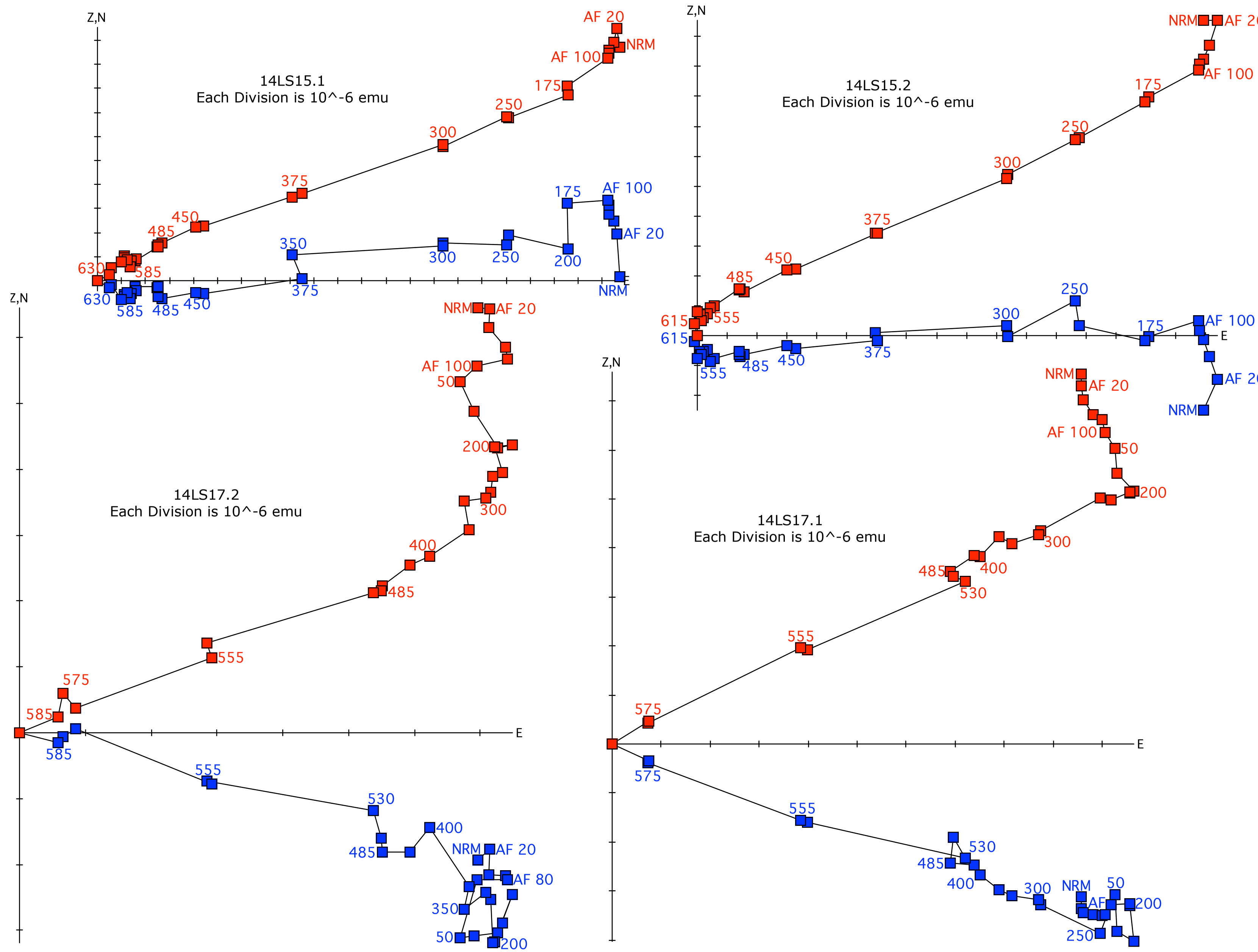
14LS15.1
Each Division is 10^-6 emu
14LS15.2
Each Division is 10^-6 emu
14LS17.2
Each Division is 10^-6 emu
14LS17.1
Each Division is 10^-6 emu
Z,N
E

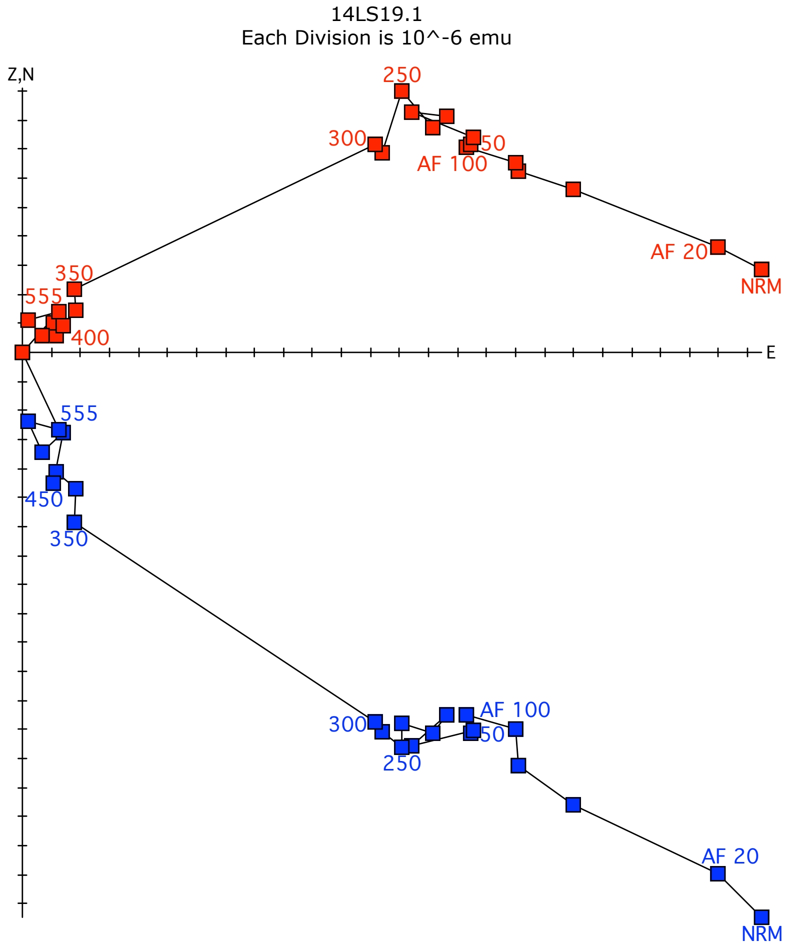
14LS19.1
Each Division is 10^-6 emu
Z,N
E
250
300
AF 100
350
555
400
AF 20
NRM
450
AF 100
250
AF 20
NRM

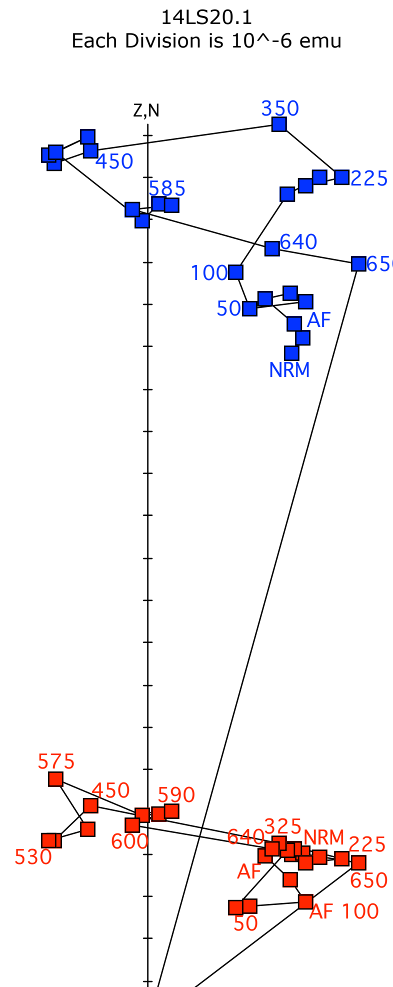
14LS20.1
Each Division is 10^-6 emu
Z,N
E
350
450
225
585
640
100
50
AF
NRM
575
450
590
530
600
640
325
NRM
225
AF
650
AF 100
50

15LS01.1
Each Division is 10^-6

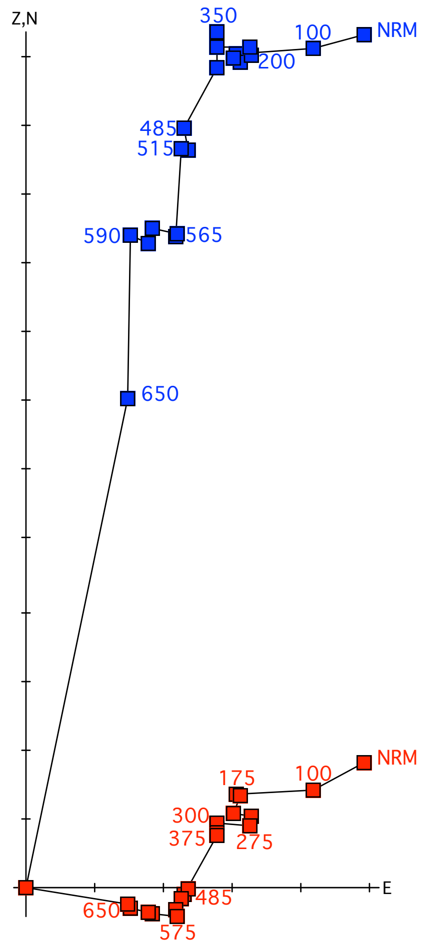

15LS01.2
Each Division is 10^-6

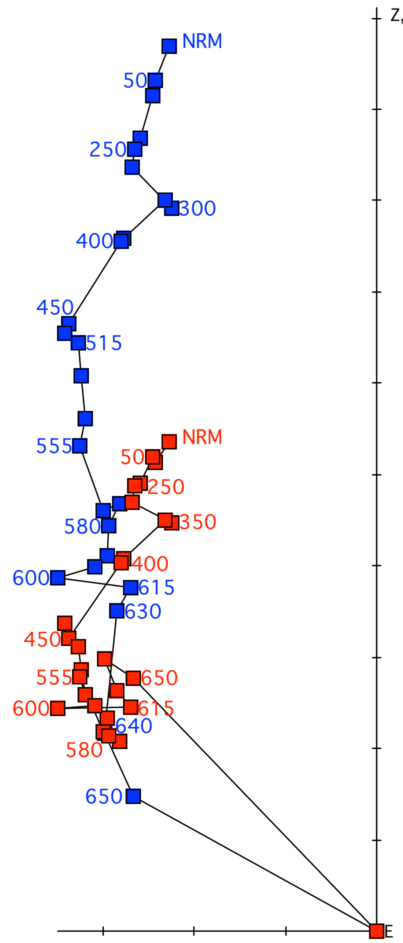

15LS02.1
Each Division is 10^-6

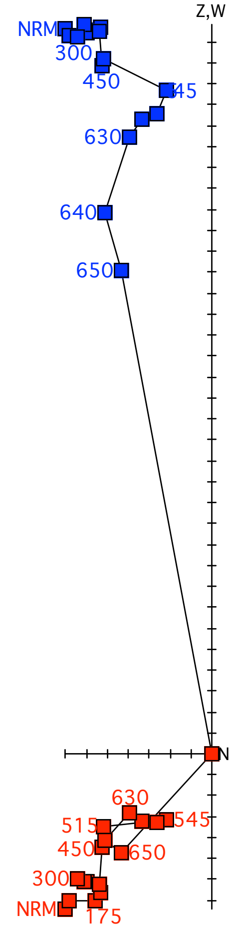

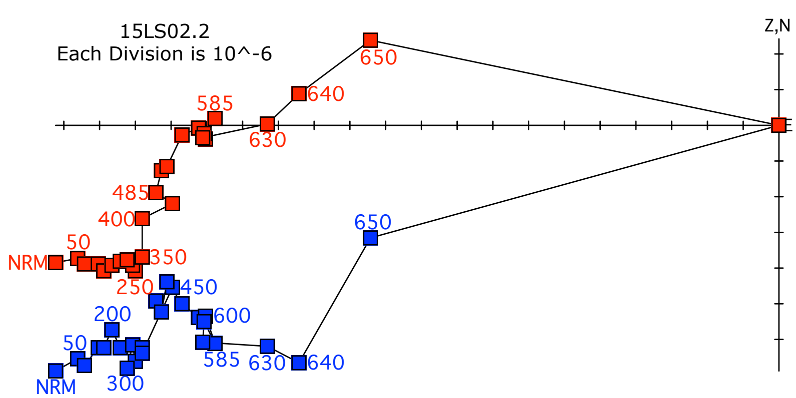

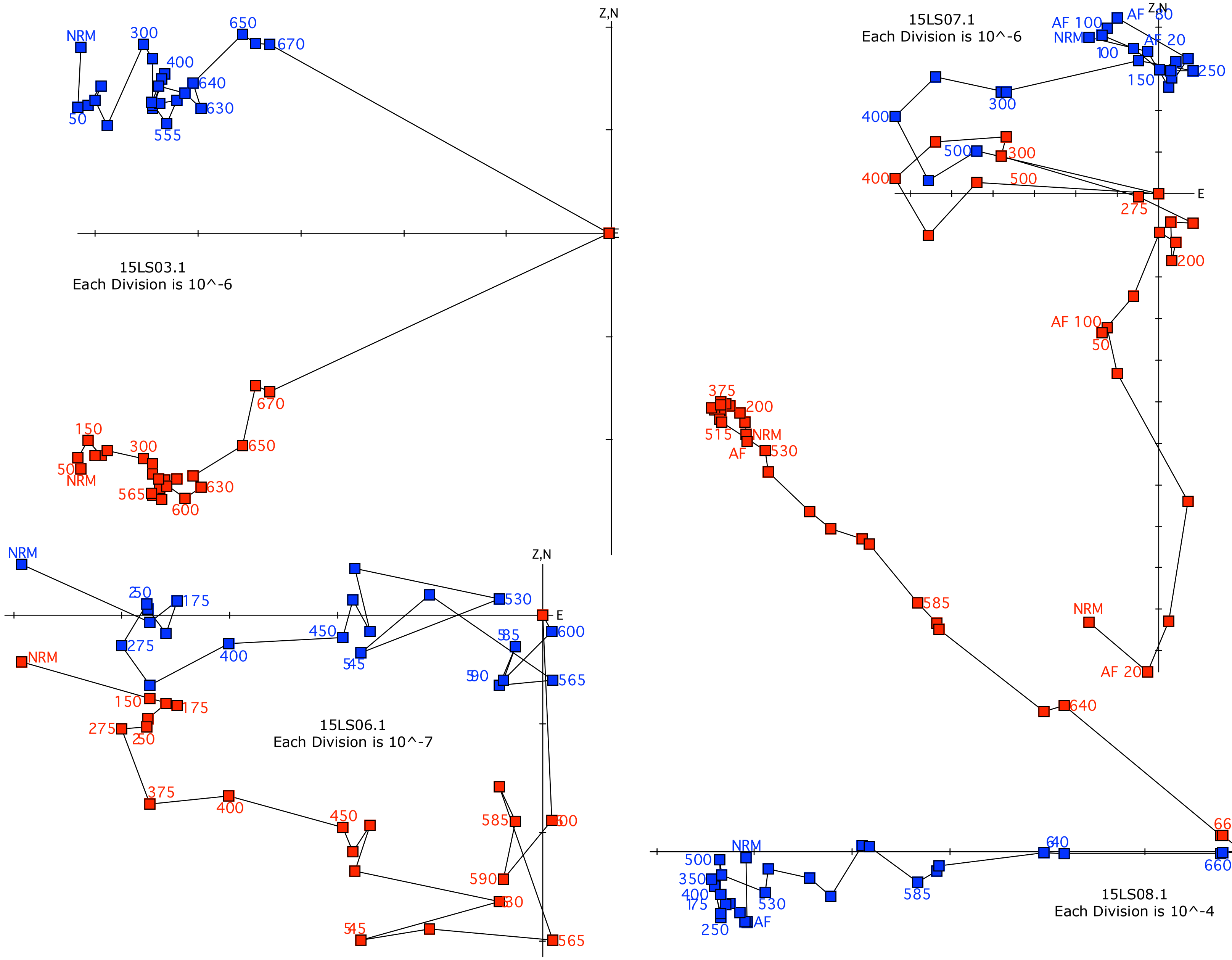
15LS03.1
Each Division is 10^-6
15LS07.1
Each Division is 10^-6
15LS06.1
Each Division is 10^-7
15LS08.1
Each Division is 10^-4
Z,N
E
NRM

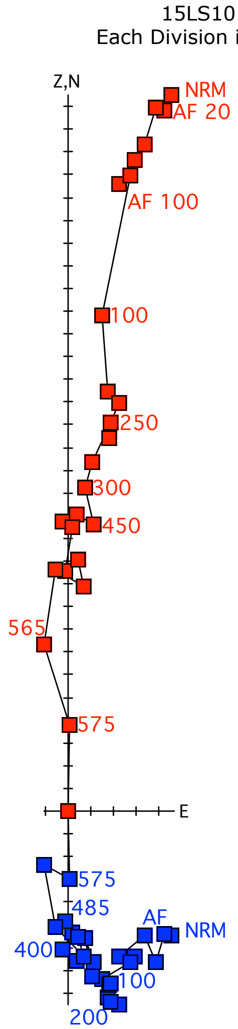
15LS10.1
Each Division is 10^-7
Z,N
E
NRM
AF 20
AF 100
100
250
300
450
565
575
485
AF
NRM
400
100
200

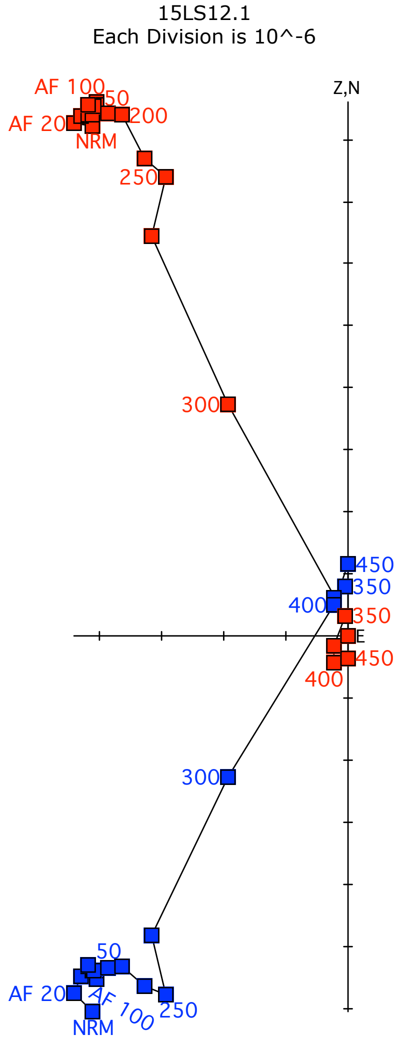
15LS12.1
Each Division is 10^-6
Z,N
E
AF 100
50
AF 20
200
NRM
250
300
450
350
400
350
450
400
300
50
AF 20
AF 100
NRM
250

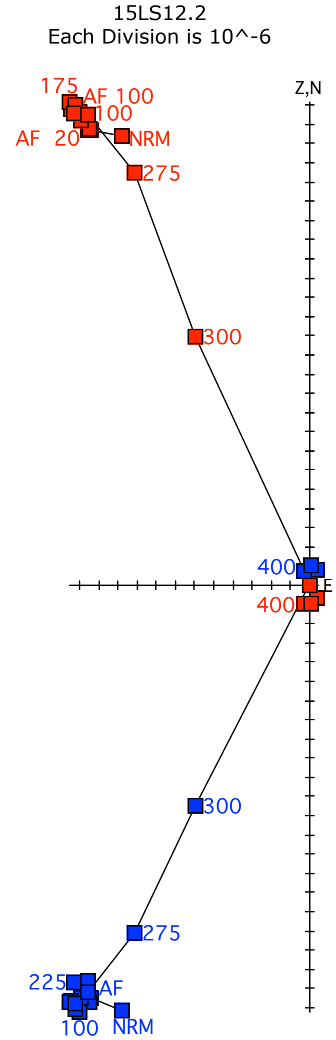
15LS12.2
Each Division is 10^-6
Z,N
E
175
AF 100
100
AF 20
NRM
275
300
400
400
300
275
225
AF
100
NRM

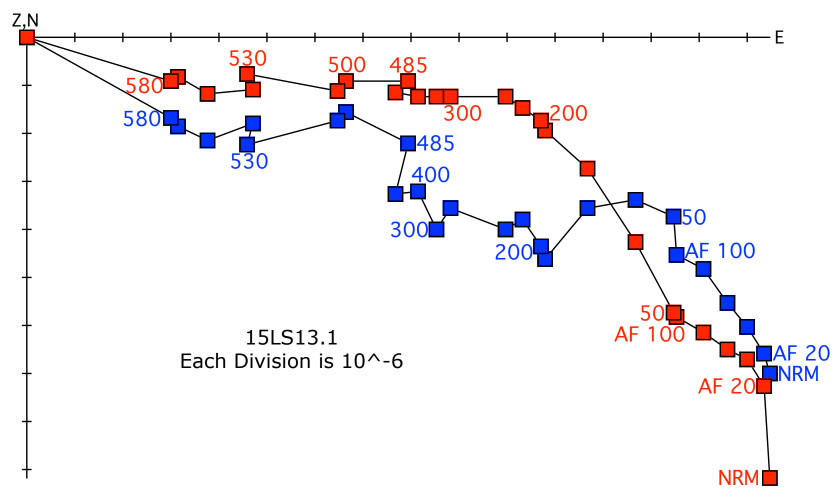
Z,N
E
530
500
485
580
300
200
580
485
530
400
300
200
50
AF 100
50
AF 100
AF 20
NRM
AF 20
NRM
15LS13.1
Each Division is 10^-6

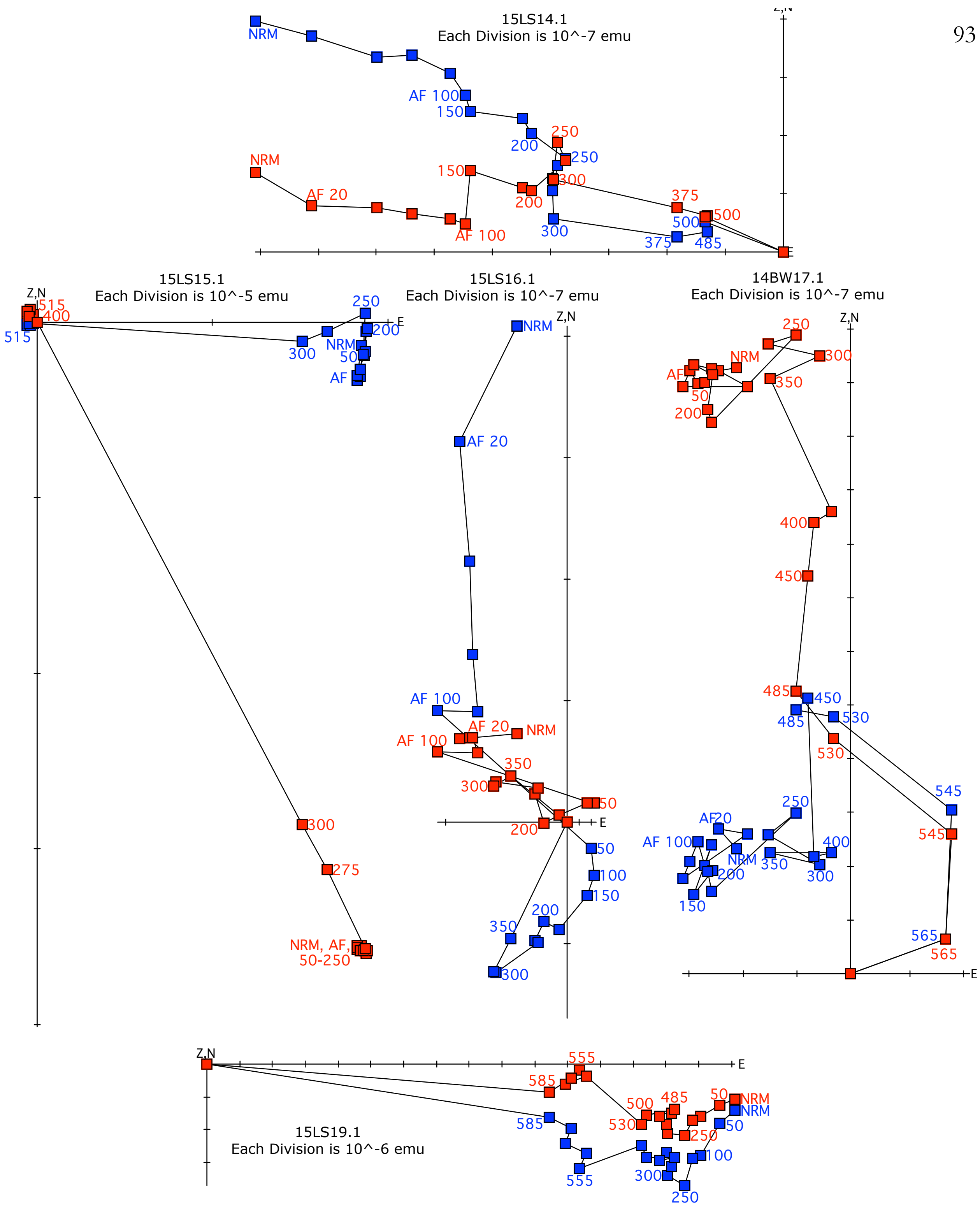
15LS14.1
Each Division is 10^-7 emu
NRM
AF 100
150
200
250
300
375
500
485
AF 20
AF 100
15LS15.1
Each Division is 10^-5 emu
515
400
250
200
300
NRM
50
AF
275
NRM, AF,
50-250
15LS16.1
Each Division is 10^-7 emu
NRM
AF 20
AF 100
350
300
200
50
100
150
14BW17.1
Each Division is 10^-7 emu
250
NRM
300
350
AF
50
200
400
450
485
530
545
565
AF20
AF 100
15LS19.1
Each Division is 10^-6 emu
555
585
500
485
530
250
NRM
50
100
300
Z,N
E

14BW16.1
Each Division is 10^-4 emu

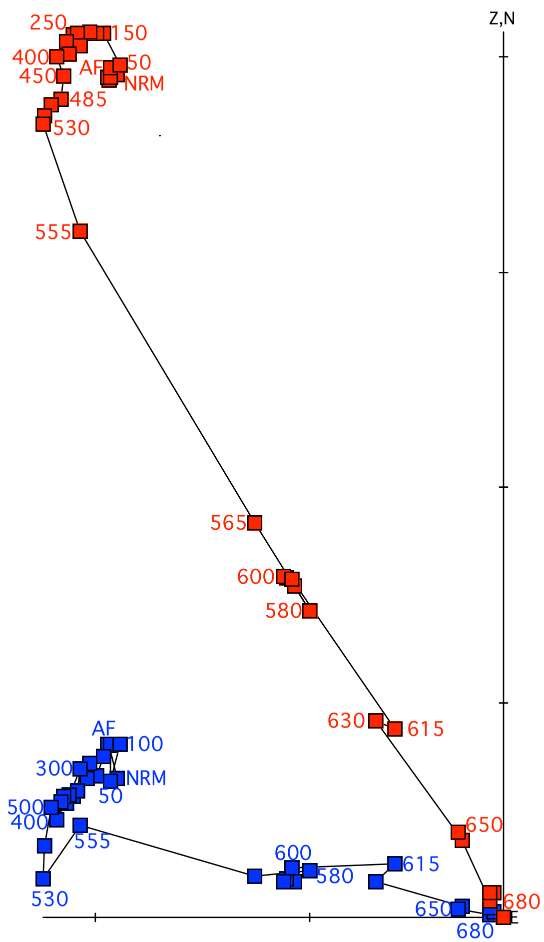

14BW16.2
Each Division is 10^-4 emu

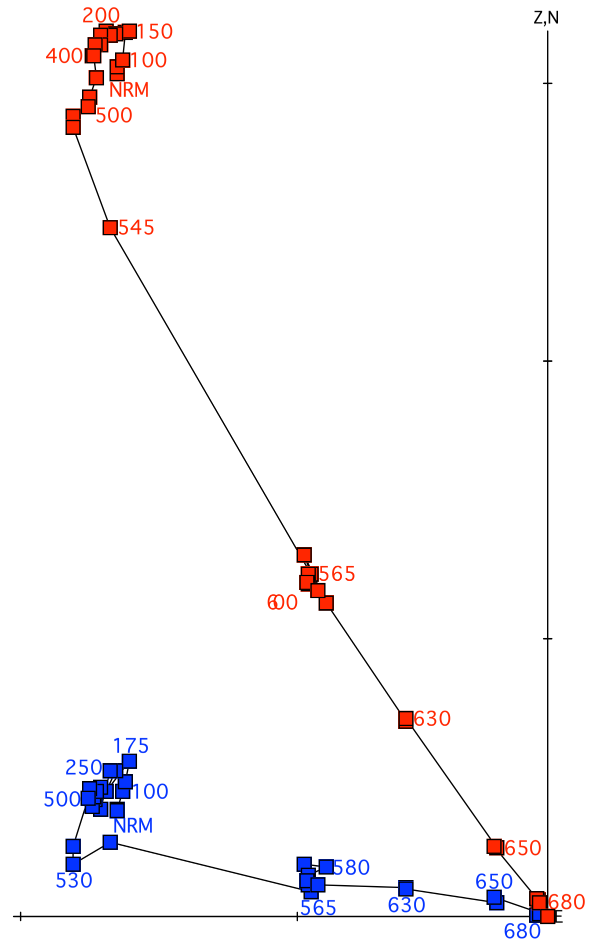

14BW16.3
Each Division is 10^-4 emu

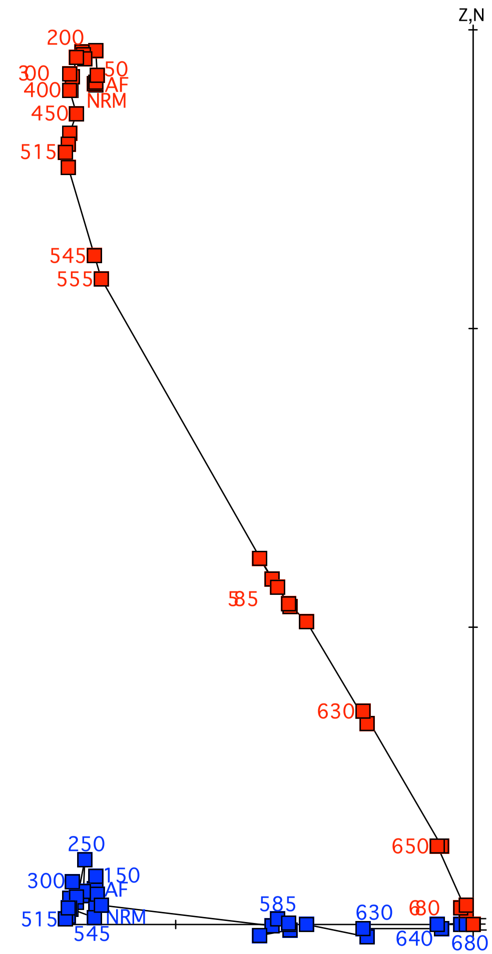

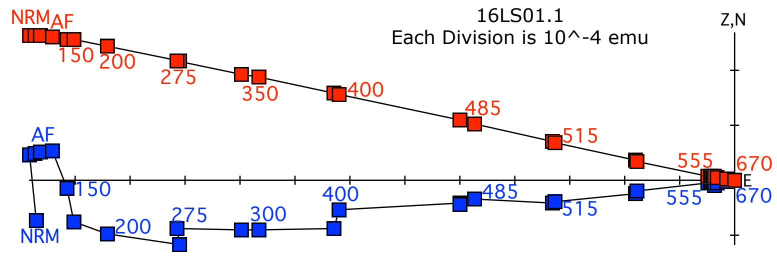
16LS01.1
Each Division is 10^-4 emu
Z,N
E
NRM
AF
150
200
275
300
350
400
485
515
555
670

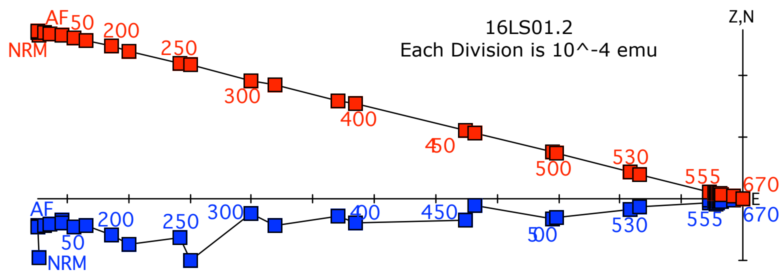
16LS01.2
Each Division is 10^-4 emu
Z,N
E
NRM
AF
50
200
250
300
400
450
500
530
555
670

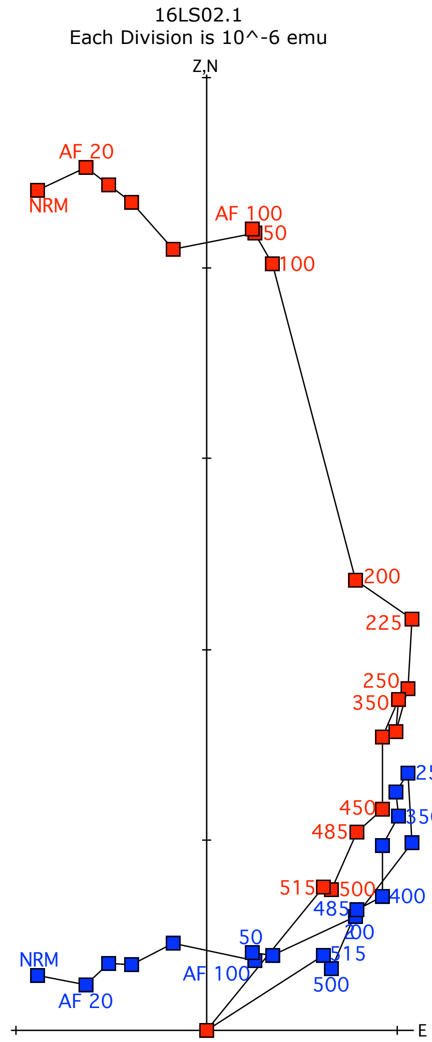
16LS02.1
Each Division is 10^-6 emu
Z,N
E
NRM
AF 20
AF 100
50
100
200
225
250
350
400
450
485
500
515

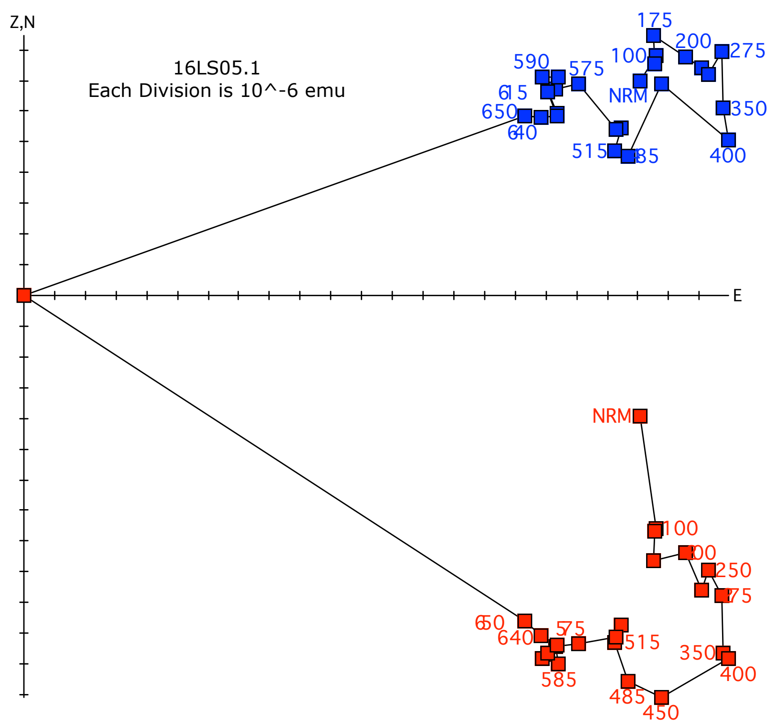
16LS05.1
Each Division is 10^-6 emu
Z,N
E
NRM
100
175
200
250
275
350
400
450
485
515
575
585
590
615
640
650

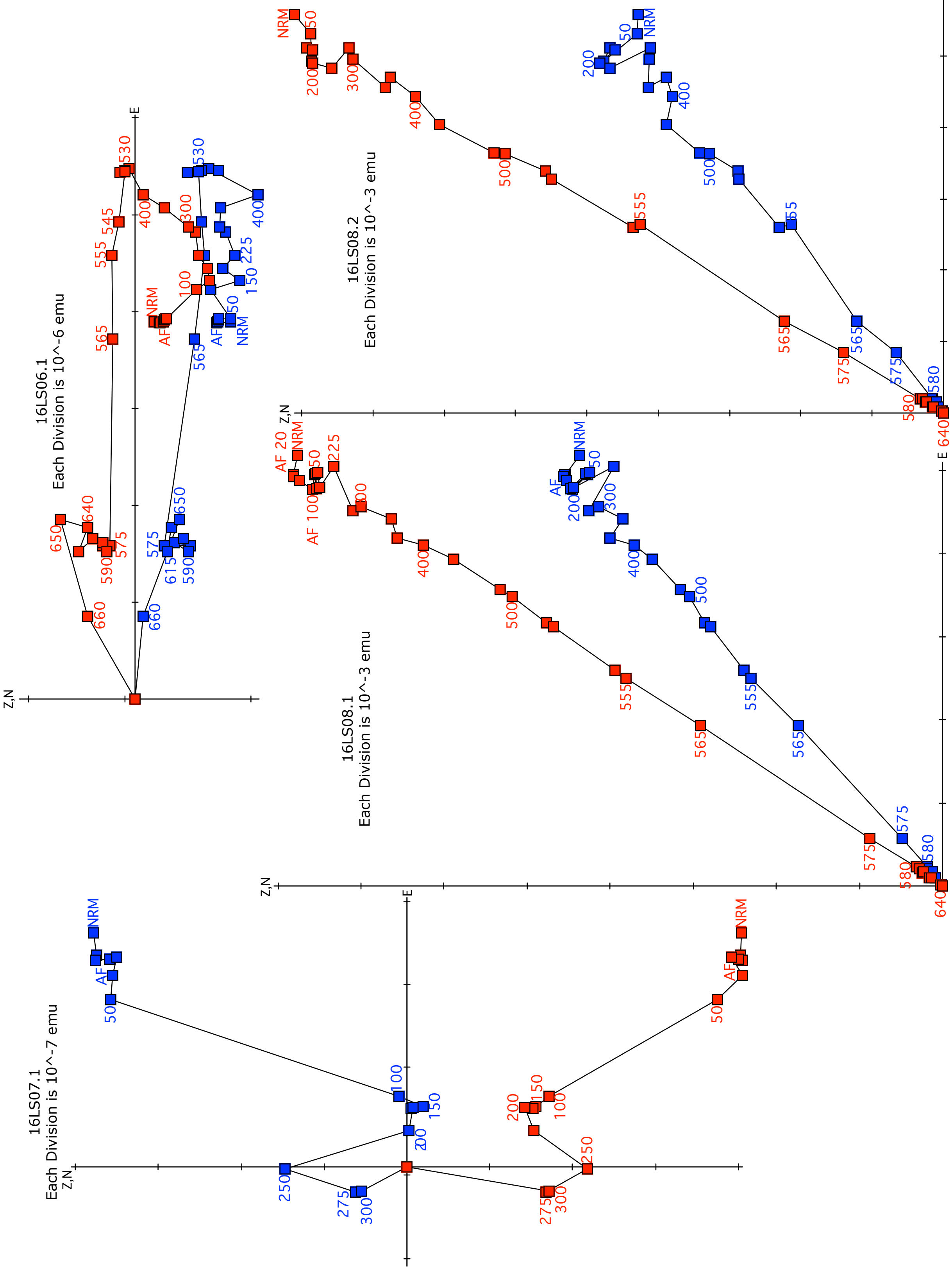
16LS07.1
Each Division is 10^-7 emu
16LS06.1
Each Division is 10^-6 emu
16LS08.1
Each Division is 10^-3 emu
16LS08.2
Each Division is 10^-3 emu

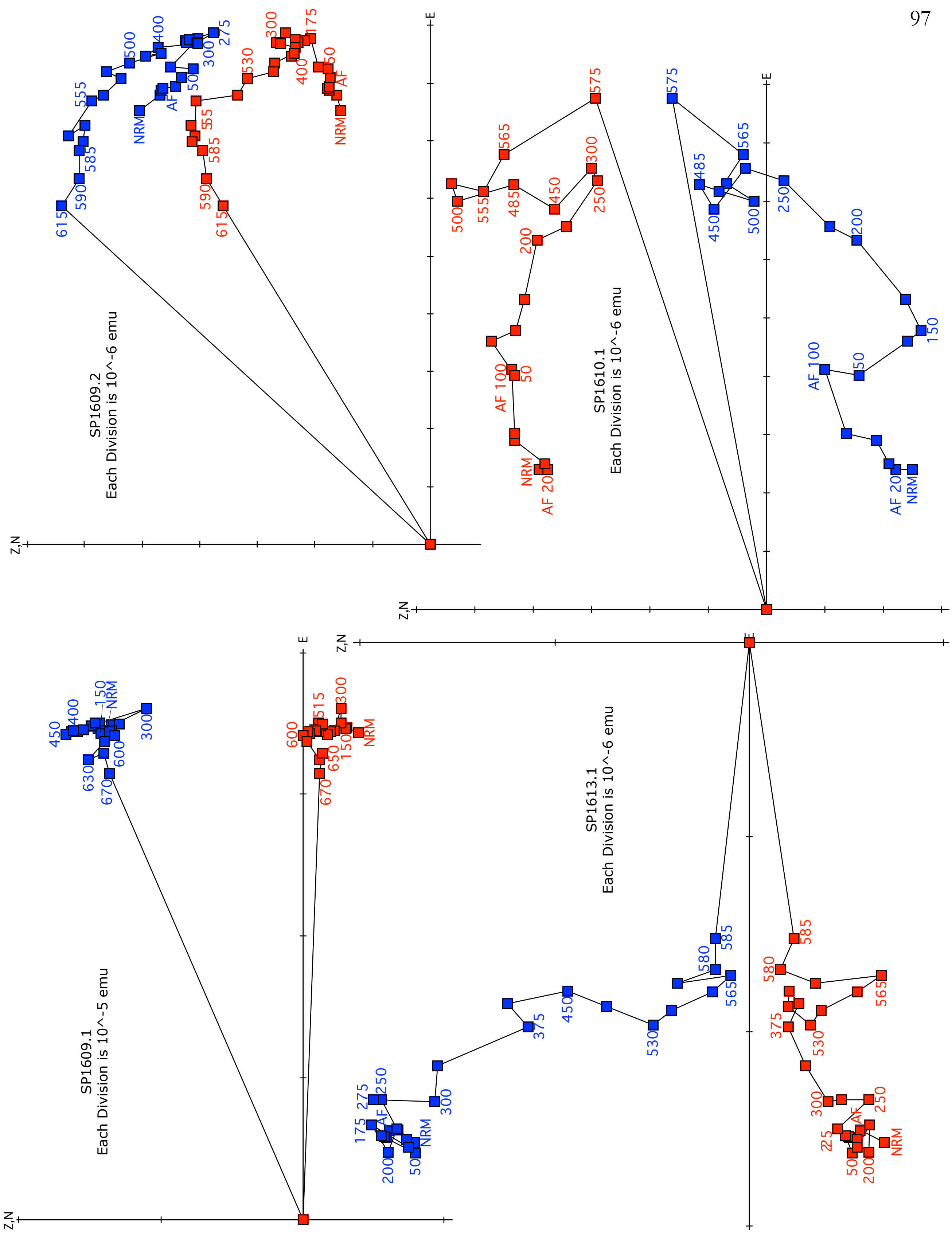
SP1609.2
Each Division is 10^-6 emu
SP1610.1
Each Division is 10^-6 emu
SP1609.1
Each Division is 10^-5 emu
SP1613.1
Each Division is 10^-6 emu
Z,N
E

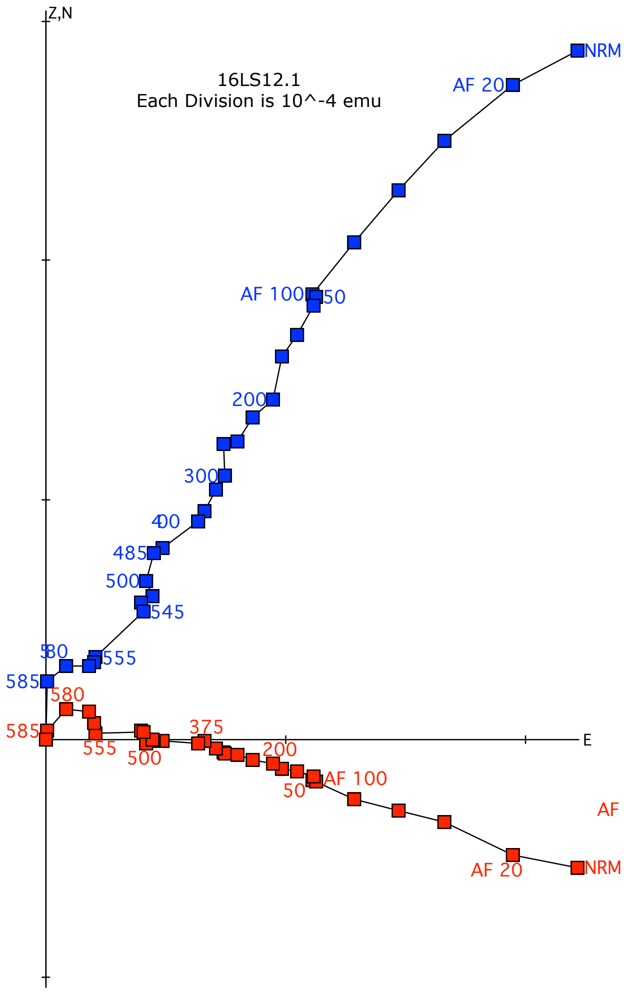
Z,N
E
16LS12.1
Each Division is 10^-4 emu
NRM
AF 20
AF 100
585

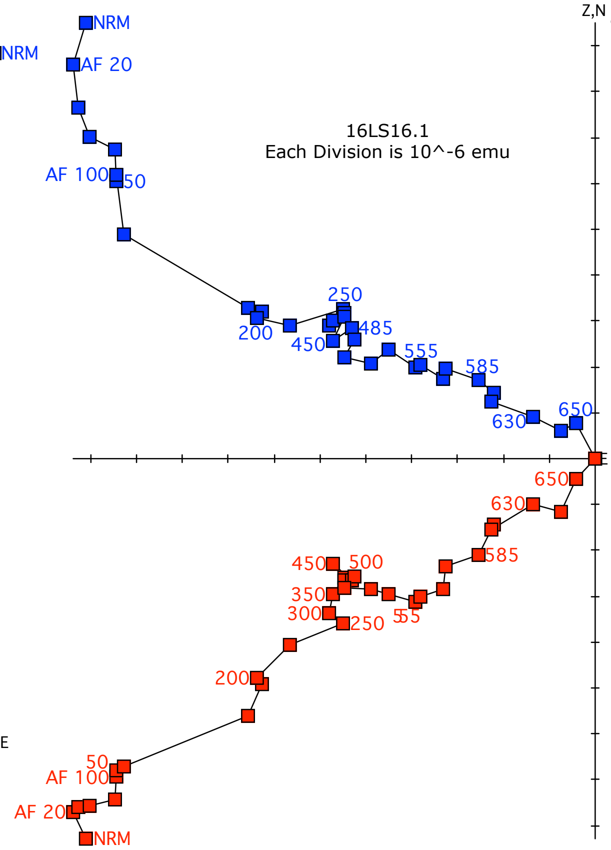
Z,N
16LS16.1
Each Division is 10^-6 emu
NRM
AF 20
AF 100
650

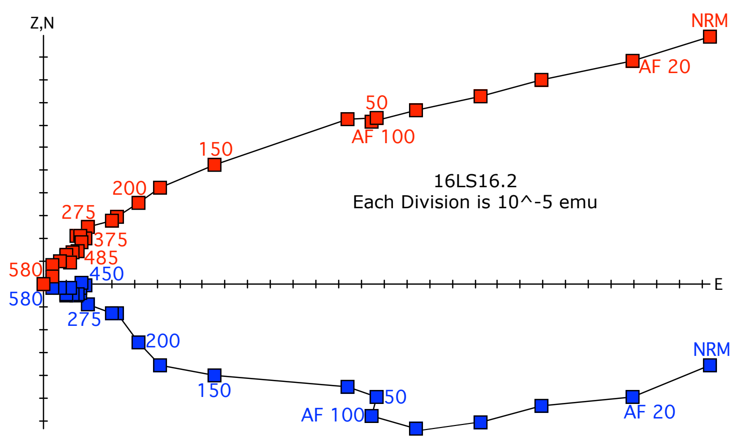
Z,N
E
16LS16.2
Each Division is 10^-5 emu
NRM
AF 20
AF 100
580

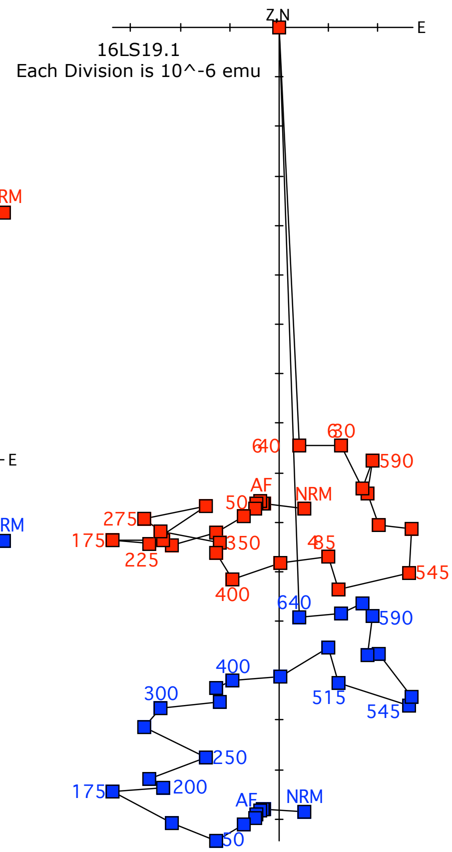
Z,N
E
16LS19.1
Each Division is 10^-6 emu
NRM
640

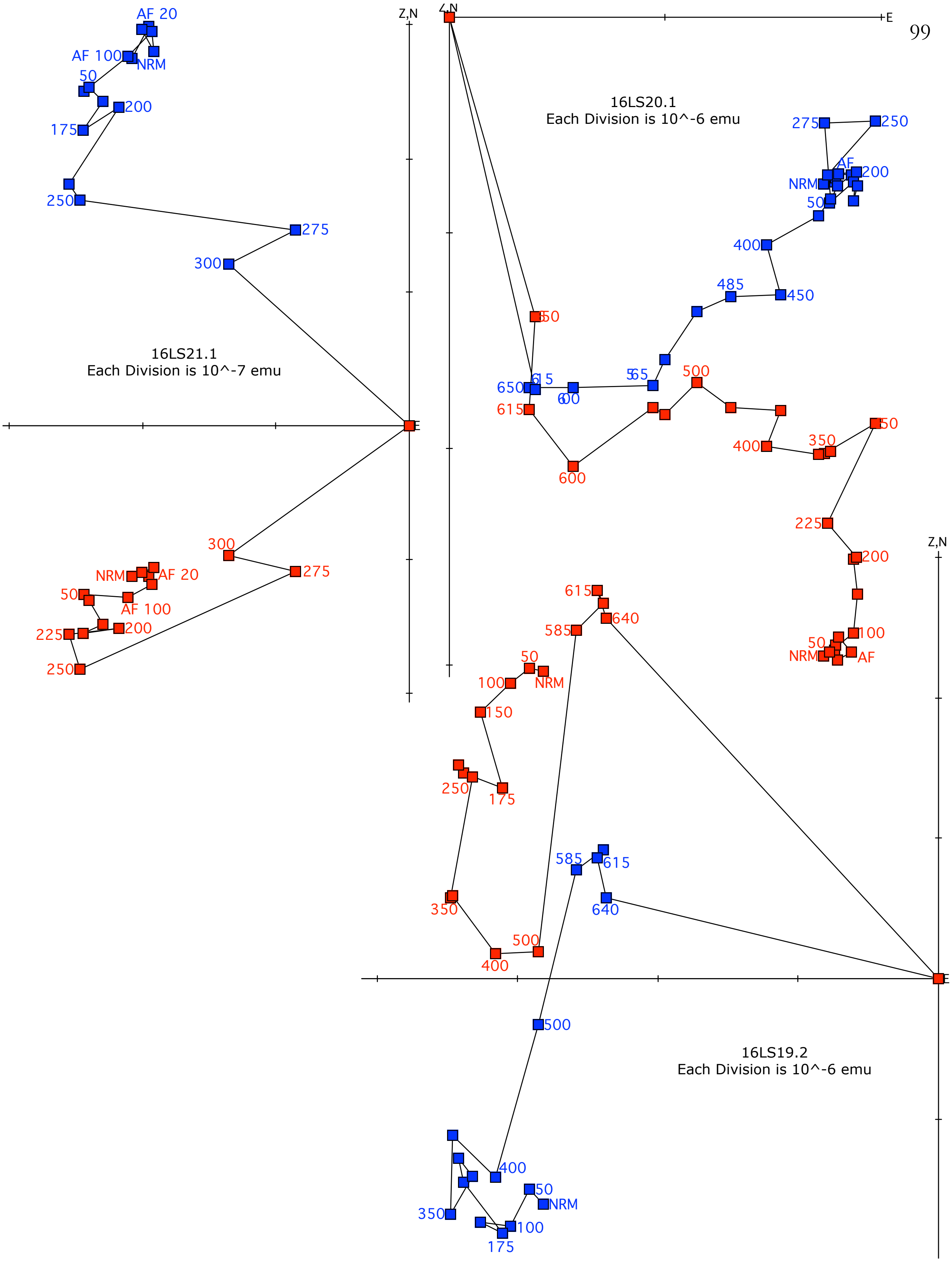
16LS21.1
Each Division is 10^-7 emu
16LS20.1
Each Division is 10^-6 emu
16LS19.2
Each Division is 10^-6 emu
Z,N
E
NRM
AF 20
AF 100

Figure S2: Zijderveld demagnetization plots for all paleomagnetic data

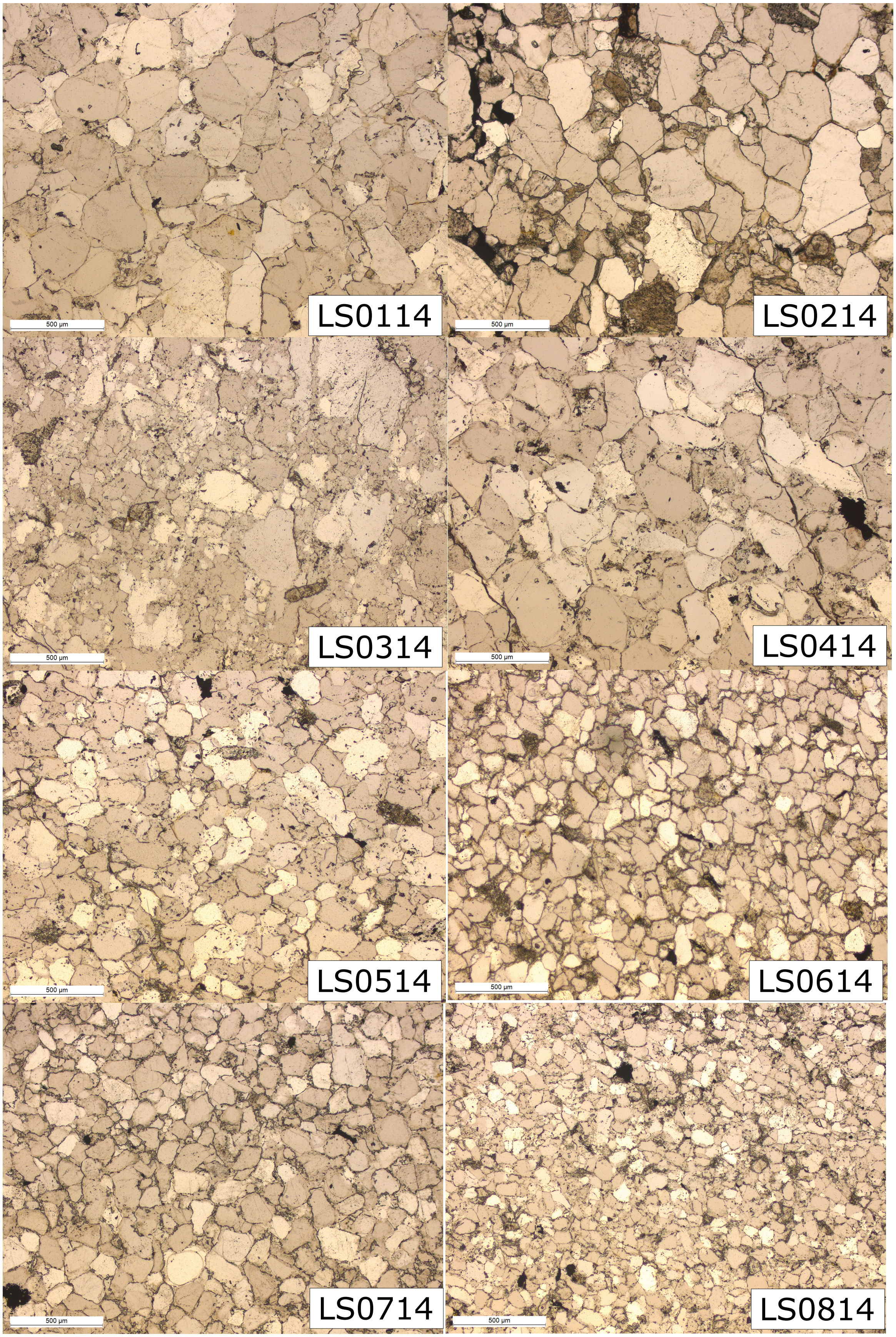
LS0114
500 µm
LS0214
500 µm
LS0314
500 µm
LS0414
500 µm
LS0514
500 µm
LS0614
500 µm
LS0714
500 µm
LS0814
500 µm

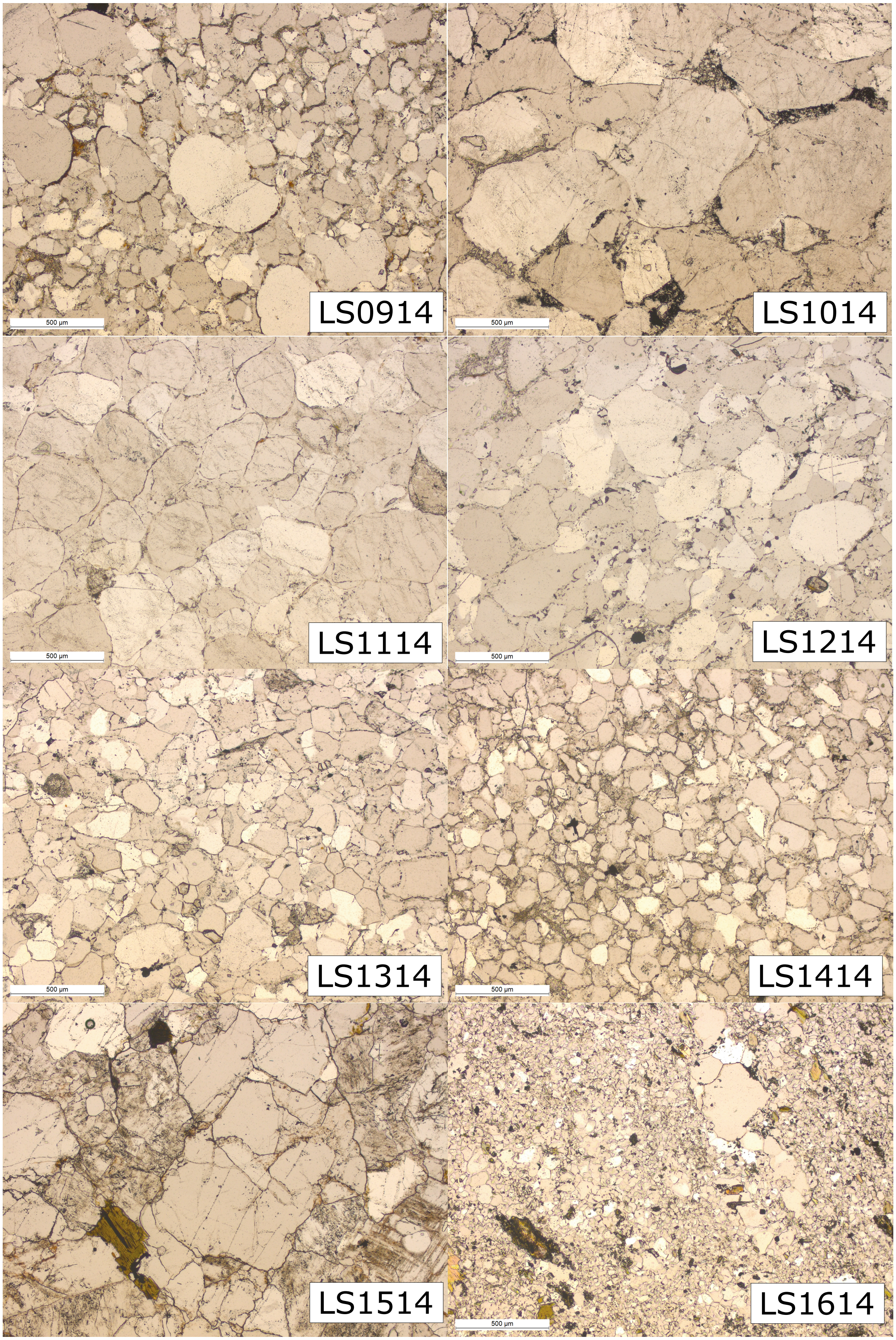
LS0914
LS1014
LS1114
LS1214
LS1314
LS1414
LS1514
LS1614

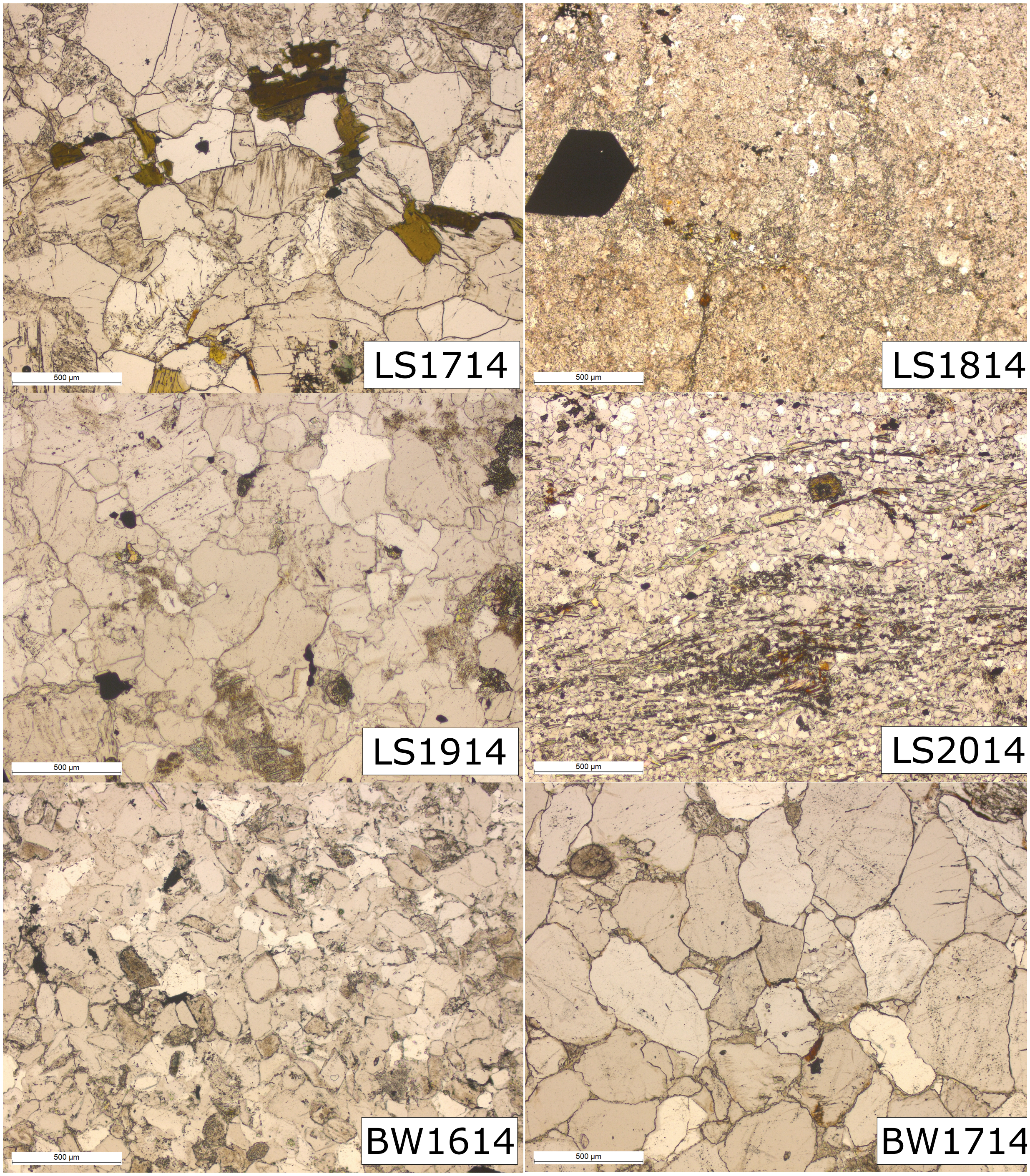

Figure S3. Photomicrographs of selected samples

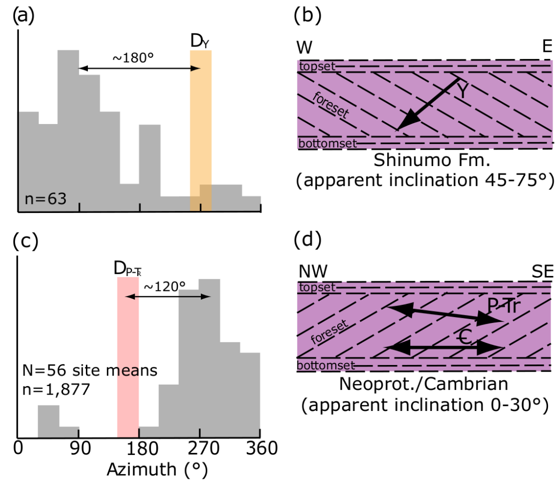

Figure S4: Relationship between paleomagnetic vectors and foreset dip directions

Orientation histograms (grey shading) and schematic cross-sections showing relationship between paleomagnetic vectors and foreset dip directions in Shinumo Formation (a) and (b), and Neoproterozoic-Cambrian formations (c) and (d). DY, mean declination of Mesoproterozoic Shinumo Formation; DP-Tr, mean declination of Permian/Triassic strata. Foreset orientation data in (a) from Appendix I in Daneker (1975) and in (c) from Table 2 in Stewart (1970).

SUPPLEMENTAL TEXT

Primary Structure

Orthoquartzites in the southwestern United States are substantially compacted after deposition, commonly cross-stratified, and locally contain paleoliquefaction structures. These features, to the extent that they are sampled by our clast populations, could potentially affect the distinction between clasts derived from low-inclination Neoproterozoic-Cambrian strata and moderate- to high-inclination Shinumo clasts. In the case of compaction (Tauxe and Kent, 2004), we note that the degree of this effect is probably fairly uniform over the sample population, and therefore would not be expected to blur the distinction between low and high-inclination populations. In the case of cross-stratification, if foreset bedding systematically dips in the opposite direction of the paleomagnetic plunge, it would produce a population of clasts with “apparent inclination” that is skewed to steeper angles, because the magnetic plunge and foreset dip would be roughly additive (Figure S4).

Alternatively, if foreset bedding tended to dip in the same direction as paleomagnetic plunge, then the clast population would be skewed to shallower inclinations.

We can evaluate this issue because there are abundant data available on dip directions of foreset laminations for nearly every major orthoquartzite body in the southwestern US. Data from both the Shinumo Formation and Neoproterozoic-Cambrian strata from the Death Valley-Mojave region show preferred orientations in dip of foreset stratification relative to topset and bottomset bedding. Based on 63 measurements in the upper, non-feldspathic part of the Shinumo Formation (Figure S4a), there is a strong tendency for foreset laminations to dip eastward (Figure S4a). There is approximately a 180° difference between the mode in foreset dip directions at 90° azimuth and the mean direction of paleomagnetic plunge at 270° (Figure 7a). These observations suggest that the component of Sespe clasts derived from foresets will skew the population from moderate to steeper apparent inclination, in direct proportion to the amount of foreset dip (Figure S4b). Assuming a mean foreset dip of 15° and paleomagnetic inclination of 45°, this population would yield an apparent mean inclination of 60°.

Neoproterozoic-Cambrian strata distributed throughout the Death Valley-Mojave region (Table 2 in Stewart, 1970), and Cambrian strata in the Grand Canyon and central Arizona regions (Figure 9 in McKee and Resser, 1945; Table 1 in Hereford, 1977) show a strong tendency for foreset laminations to dip westward. Based on 1,877 measurements from the Johnnie, Stirling, Wood Canyon, and Zabriskie formations, the dip directions of foresets show a well-defined peak at an azimuth of 270°, with orientations scattering broadly between 180° and 360° (Figure S4c). As noted earlier, the expected magnetization directions in these strata are either Ediacaran-Cambrian or Permian-Triassic in age, with inclinations of 0° to 30° (Figure 7g). Ediacaran-Cambrian magnetizations generally plunge shallowly to the east or west, and Permian-Triassic magnetizations are expected to plunge gently SE (e.g., Molina-Garza et al., 1998; Figure S4c). Given these observations, the population of clasts derived from foresets with Neoproterozoic-Cambrian magnetization would be expected to record inclinations either steeper or shallower than true inclination by the amount of foreset dip, dispersing the population to somewhat higher and lower values. In the population of clasts derived from foresets with Permian-Triassic magnetizations, the situation is somewhat more complex because of the SE magnetic declination. For the case of foresets dipping due west 30° recording a Permian magnetization oriented with D=150°, I=15° (near the upper end of Permian inclinations for southwestern North America), the apparent inclination would be 28°, only 13° steeper than the true inclination.

Thus, to the extent that the Sespe orthoquartzite clast population samples foreset laminations in these formations, the overall effect of the foreset population would be to steepen the inclination distributions by adding a component of clasts with inclinations that range from 10° to 30° steeper than the remainder of the population, with the exception of Neoproterozoic-Cambrian magnetizations, which would be either shallower or steeper by a similar amount. Even if every clast in the Sespe population were derived from steeply dipping foresets optimally oriented to maximize the apparent inclination, the steepening would be expected to affect both the Neoproterozoic-Cambrian and Shinumo populations by a similar, relatively modest amount, thus preserving the difference in inclination. In general, however, the volume fraction of orthoquartzite sources that are moderately to steeply cross-stratified is low in most formations, and is therefore not likely to have a major effect on the distributions of inclinations. Nonetheless, the tendency for rather shallow eastward inclination in data from the Death Valley-Mojave region may be a reflection of this effect (compare Figure 7g and Figure S4d).

Convoluted bedding associated with paleoliquefaction represents at most 10% of the volume of the upper part of the Shinumo Formation in sections where it is most commonly exposed (Daneker, 1975). These convoluted strata are generally not developed in densely cemented orthoquartzite. Thus, although some of these samples may affect the clast population in the Sespe, there is little chance that they would form a statistically significant fraction of the clast population.

References Cited

Daneker, T. M., 1975, Sedimentology of the Precambrian Shinumo Sandstone, Grand Canyon, Arizona: M.S. thesis, Northern Arizona University, 195 p.

Hereford, R., 1977, Deposition of the Tapeats Sandstone (Cambrian) in central Arizona: Geological Society of America Bulletin, v. 88, p. 199-211.

McKee, E. D., and Resser, C. E., 1945, Cambrian History of the Grand Canyon Region: Washington, D. C., Carnegie Institute Publications, v. 563, 232 p.

Molina-Garza, R. S., Acton, G. D, and Geissman, J. W., 1998, Carboniferous through Jurassic paleomagnetic data and their bearing on rotation of the Colorado Plateau: J. Geophys. Res., v. 103, p. 24,179–24,188.

Stewart, J. H., 1970, Upper Precambrian and Lower Cambrian strata in the southern Great Basin, California and Nevada: U.S. Geological Survey Professional Paper 620, 206 p.

Tauxe, L., Kent, D. V., 2004, A simplified statistical model for the geomagnetic field and the detection of shallow bias in paleomagnetic inclinations: Was the ancient magnetic field dipolar?, in Timescales of the Paleomagnetic Field, American Geophysical Union, Washington, D. C., Geophysical Monograph Series, v. 145, p. 101-115.

C h a p t e r 2

Chapter 2: Geologic map, geochemistry, age and interpreted structure of volcanic and sedimentary strata, Isla Ángel de la Guarda, Mexico: study of a microcontinental fragmentation in the actively rifting Gulf of California.

ABSTRACT

Geological mapping of two field areas in the southeastern part of Isla Angel de la Guarda, provides a basis for characterization of two distinct sets of volcanic flows and sedimentary units. Most units dip moderately to gently to the east. Geochemical data from X-ray fluorescence suggests that the units are largely intermediate toward the northwest, and become less silicic towards the southeast. Correlation on the basis of major element composition show that units sampled in this study area are broadly similar to Early Miocene arc-related rocks mapped in the Puertecitos Volcanic Province. *Trace element data confirm that lava flows are of affinity.* $^{40}Ar/^{39}Ar$ geochronology shows that the volcanic flows sampled are generally younger than the Puertecitos volcanics, ranging in age from 3.916 ± 0.088 Ma to 2.754 ± 0.021 Ma.

We mapped at least three generations of extensive, non-marine terraces, distinguished by differences in elevation and surface roughness. With satellite imagery, drone-based DEMs, and field geology, we mapped several sub-parallel, NNE-striking normal faults that cut the terraces and volcanic flows. Fault motion is dominantly down-to-the-east with <100 m of total offset per fault. A few faults show

evidence for dextral motion. Our results indicate that IAG is actively accommodating extensional strain adjacent to the Ballenas transform fault zone to the west.

INTRODUCTION

Isla Ángel de la Guarda is a microcontinental block fragment immediately east of Baja California in the Gulf of California that records transtensional rifting on the Pacific-North America plate boundary (REF). Rifting first began in a middle to late Miocene andesitic arc (Stock, 2000). Final subduction of the Farallon plate and development of a transform margin led to the eventual cessation of arc-related volcanism in Miocene time. The end of arc-related volcanism coincides with a plate reorganization (Gastil et al., 1979), transferring Baja California from the North American to Pacific plate during southward migration of a ridge-transform-trench triple junction (e.g., Seiler et al., 2009). Reconstructions show at least two southward relocations of extensional basins during oblique rifting of Baja California from the mainland: from the Upper Tiburón to the Upper Delfin basin between 3 and 2 Ma, and from the Lower Tiburón to Lower Delfin basin by 2 Ma (Nagy and Stock, 2000; Stock, 2000). These relocations define Pliocene northward and westward migration of the plate boundary, wherein the Tiburon transform connected the upper and lower Tiburon basins prior to c. 2-3 Ma, and the transform separated the upper and lower Delfin basins after 2 Ma. This process incorporated Isla Angel de la Guarda into the North American plate at 3 to 2 Ma.

The objective of this and the following chapters is to study volcanic, sedimentary, and structural features coeval with the transfer of the Isla Angel de la Guarda block in Pliocene time. Extensional tectonic features surround the island on all sides. The Ballenas Transform Fault, which separates the North American Plate from Baja California, runs through the Ballenas channel and separates the island from Baja California on its western side (Figure 1). The plate boundary is evident in large numbers of earthquake epicenters mapped along the Ballenas Channel, but not to the east of Isla Ángel de la Guarda (Castro et al., 2017). Active extension associated with the Ballenas Transform occurs NNW of the island in the Lower Delfin Basin, and on the southwest side of the island in the Northern Salsipuedes Basin, which defines a right-stepping rift basin on the east and west sides of the Ballenas transform, respectively. The fossil Tiburón Transform lies on the eastern side of the island, and allowed for strike-slip separation of Isla Tiburón and Isla Ángel de la Guarda between 6 and 3 Ma (Stock, 2000).

During early oblique rifting (late Miocene), IAG and Baja California were transferred as a block from the North America plate to the Pacific plate. IAG and Baja CA were translated northwest >100 km along the Tiburón fracture zone (east of IAG, Figure 1b). The plate boundary jumped west into the Baja CA peninsula ca. 3–2 Ma, which transferred IAG back to the North America plate and isolated it as a large island of continental crust.

GEOLOGIC SETTING

The eastern side of IAG is dominated by Pliocene basaltic andesite flows, mapped in areas with dark-colored rocks, which is surrounded by units of Pliocene fluvial material, Pliocene sedimentary rocks, and Quaternary alluvium (Figure 2a; Gastil et al., 1975). The western mountains of Miocene to Pliocene volcanic units on IAG are distinct from darker volcanic units on the eastern side (Gastil et al., 1975), both in their mountainous nature and lighter yellow or orange color in imagery (Figure 2b).

We expect units in our field area (Figure 2b) to be similar to Pliocene units mapped in the Puertecitos area based on reconstructions placing northern IAG adjacent to Puertecitos (Nagy and Stock, 2000; Stock, 2000; Seiler et al., 2010; Bennett et al., 2016).

Puertecitos Volcanic Province

Three distinct volcanic sequences have been mapped in the eastern Puertecitos Volcanic Province using petrology and Ar^{40}/Ar^{39} geochronology: (1) a lower unit of middle Miocene (20-16 Ma) arc-related andesitic lava flows and minor basaltic lava flows, (2) a middle unit consisting of two packages of late Miocene (6.4-5.8 Ma) synrift rhyolites, and (3) an upper Pliocene (3.2-2.7 Ma) unit consisting of ash-flow tuffs, pumice-lapilli pyroclastic density current deposits, and minor andesitic lavas (Martín-Barajas et al., 1995). Synrift rhyolite domes are aligned with predominantly NNE- and NNW-striking faults (Martín-Barajas et al., 1995).

Units in the Puertecitos Volcanic Province (Figure 1a, 3a) have been dated and grouped into three volcanic events: a ~16 Ma arc-related event producing andesite lavas, a late Miocene synrift event erupting mainly rhyolites and tuffs, and Pliocene synrift event erupting more ignimbrites (Martín-Barajas et al., 1995) (Figure 3a). Similar to the ~16 Ma ages of arc-related andesites in Puertecitos, units identified in Valle Chico, southwest of San Felipe, have ages of 20-14.5 Ma, and include pyroclastic flows, andesitic breccias, basaltic lavas, reworked tuffs, and epiclastic deposits (Stock, 1989; Martín-Barajas et al., 1995). In the Puertecitos area and including Sierra San Fermin, these andesitic rocks overlie Mesozoic granitic and metamorphic basement (Lewis, 1994). Arc-related andesites ~10 km southwest of Puertecitos have porphyritic to microporphyritic texture with glassy to microcrystalline matrix. These andesites have phenocrysts of zoned plagioclase, with hornblende as the most common mafic mineral (Martín-Barajas et al., 1995).

The late Miocene synrift rhyolite flows and tuffs described near Puertecitos thicken westward and northwestward of Puertecitos, and are covered by younger rocks south of Puertecitos (Martín-Barajas et al., 1995). The rhyolites began erupting by 6.4 Ma as far north as Sierra San Fermin, and ceased eruption ~5 km south of Puertecitos by 5.5 Ma (Lewis, 1994; Martín-Barajas et al., 1995). Lower rhyolite lavas in Arroyo La Cantera are massive and devitrified with pervasive hydrothermal alteration, and contain 5-10% phenocrysts, including oligoclase, augite, and ferrohypersthene. The Tuff of El Canelo has a basal unit with ≤ 30% phenocrysts (plagioclase and quartz, and lesser opaque minerals and alkali feldspar), middle units with ≤ 10 % phenocrysts (plagioclase, orthopyroxene, clinopyroxene, opaques, and hornblende), and an upper rheomorphic facies, which is glassy and largely aphanitic with ≤ 5 % phenocrysts (Na-plagioclase, clinopyroxene, opaques) (Martín-Barajas et al., 1995).

A final Pliocene period of synrift explosive volcanism includes rhyolites, dacites, and some younger andesitic lava flows (Martín-Barajas et al., 1995). These ignimbrites were erupted from a source east of the late Miocene rhyolites and the present coastline, and some were deposited in a shallow marine environment. The stratigraphic top and youngest dated andesite flow of this period is 2.6 ± 0.1 Ma. Basal tuffs are composed of phenocrysts of pyroxene, biotite, clinopyroxene, with rare hornblende and rarer quartz. The tuffs have lithic fragments of rhyolite, and minor andesite porphyry, basaltic andesite, and granite. Upsection are thin, welded pyroclastic density current deposits with phenocrysts of orthopyroxene and clinopyroxene, and some olivine. Andesitic lavas at the top of the section vary texturally from aphanitic to porphyritic, with up to 20% phenocrysts of orthopyroxene, clinopyroxene, and olivine in a microcrystalline groundmass of plagioclase, pyroxene, and opaques (Martín-Barajas et al., 1995).

Isla Tiburòn

Isla Tiburòn is composed of Cretaceous plutons in the southwest and northeast, with Cenozoic strata, including bedded cherts associated with carbonates and clastic rocks, mapped in the central and northeast parts of the island (Gastil and Krummenacher, 1977).

Isla Ángel de la Guarda

Isla Ángel de la Guarda was first described in Reconnaissance Geology of the State of Baja California by Gastil et al. (1975). The study examined the coastline of the island, but the majority of the island "has not been checked on the ground or [and] air photo coverage" (Gastil et al., 1975, fig. 3). Older, possibly Miocene volcanic units on the western side of the island (Tmv) were correctly distinguished from Pliocene volcanic flows on the eastern side (Tpb) (Figure 2a). A ~25 km long NNE-striking fault is mapped extending from the southwestern shore to the northeastern shore of the area. Presumably this fault was inferred from a change from the mountainous, volcanic western side to the alluvium-covered eastern side of the island. Alluvium in the southeasternmost part of the island was all mapped as Pliocene marine rocks (Tpm), with small, scattered areas of Quaternary alluvium (Gastil et al., 1975).

Although few geologic studies on Isla Ángel de la Guarda are published, some mapping has been included as parts of masters or doctoral dissertations. In the central part of the island, ~25 km northwest of our northern study area, several arrays of extensional north-trending faults are mapped (Cavazos Álvarez, 2015). Mapped units include Miocene to Pliocene basaltic andesite lavas, rhyolites, andesitic lavas dacite lavas, and sediments (Cavazos Álvarez, 2015). Another study mapped lithologies on Isla Ángel de la Guarda from air photos, collected samples along the shore of the island, and field-checked their map on foot in a ~6 km^2 area on the west-central part of the island (Delgado Argote, 2000, fig. 8). Interestingly, air photos from this study did not cover any meaningful part of our study area.

Several volcanic flows have been dated on Isla Ángel de la Guarda (Figure 3). On the northern end of the island, dacite lava flows are reported to have early Miocene $^{40}Ar/^{39}Ar$ and K/Ar ages in hornblende: 17.7 ± 0.5 and 18.1 ± 0.8 Ma, respectively (Delgado Argote, 2000). In the central part of the island, the Tuff of San Felipe is mapped and yields an $^{40}Ar/^{39}Ar$ age of 12.1 ± 0.1 Ma (Cavazos Álvarez, 2015). Another a late Miocene tuff is reported with an $^{40}Ar/^{39}Ar$ age of 6.35 ± 0.1 Ma, and a Quaternary dacite is reported with an $^{40}Ar/^{39}Ar$ age of 0.598 ± 0.119 Ma (Cavazos Álvarez, 2015). On southern Isla Ángel de la Guarda, two dacitic lava samples yield biotite $^{40}Ar/^{39}Ar$ and K/Ar ages of 3 ± 0.1 Ma and 3.4 ± 0.2, respectively (Delgado Argote, 2000).

FIELD ACCESS AND LOGISTICS

Legal access to our field areas (Figure 2b) on Isla Ángel de la Guarda, which is within the Islas del Golfo reserve, was acquired by permit. The island has no inhabitants, potable water, or electricity. IAG has historically been visited by indigenous peoples (Bowen, 2004), and more recently by local fishermen and diving groups. The latter brought cats to the island to help control pests in a diving operation, but the small group of cats became a large population of feral cats, which sustain themselves by consuming iguanas unique to the island's ecosystem. Most current visitors to the island come from Bahia de los Angeles, in Baja California, as fishermen and tourists. Bahia de los Angeles is accessed by MX Federal Highway 1, which turns East at 29.044859, -114.151843, towards the Gulf of California.

The field area is only accessible by boat. The west side of the island is almost entirely inaccessible, due to its rocky coastline. The east side of the island has several rocky beaches, some of which can be approached by a panga (~20 foot fishing boat). Our pangas were captained by Ricardo and Mario Arce of Ricardo's Diving Tours from Bahia de los Angeles, and a typical boat travel time to our campsite was 1.5 hours in good weather. Field crew size was limited by the size of the panga, and 4-5 scientists came on each expedition, along with 1-2 boat drivers. Hiking groups were never smaller than two people, and communication was only possible via satellite phone (Garmin InReach). Rattlesnake encounters and heat exhaustion were not uncommon.

Visits to the island are limited to time between the very hot summer, from May to October, and the very windy winter, from November to April. Because the island has no resources making it hospitable to humans, all drinking water, food, and electricity sources must be carried by panga. These finite resources, which were required to fit into the panga, dictated the maximum length of our field trips. Drone flying time was also limited by the battery power we could bring, or any solar power we could generate. Solar power was a semi-reliable but slow way of generating electricity. Two to three days were needed to get sufficient power to fly a drone. Our weeklong expeditions were carefully planned to lie on the borders of summer/winter, or winter/fall, making for the lowest likelihood of dangerously windy seas or dangerously hot weather. Typical daytime weather was 95° F, with temperatures often reaching 100° F, and occasionally ≥110° F. Hurricanes and windy conditions shortened two of our trips. Often, mornings were the only wind-free time, greatly limiting the amount of time drones could fly. Days of field work which required a panga commute were limited by wind and tide conditions. Several days we had to wait for a tide to come in and un-beach a panga so we could commute to another part of the island.

The boat drivers chose campsites such that the beach would not be too rocky or windy for the boat, and so that fishermen would not see the campsite from the water, since our campsite was often unguarded during the day. We stayed at two campsites over the four expeditions located at WGS 84 coordinates: 29.066463° N, -113.149740° E for the first two trips, and 29.056233° N, -113.123485° E for the second two trips.

METHODS

Mapping from satellite imagery identified a ~5 km-wide zone of generally north-striking faults, with local domains striking variably NNE or NNW, across the southernmost part of IAG between the active Ballenas transform fault zone and the inactive Tiburón fracture zone. The NNE-trending zone aligns with the offshore North Salsipuedes Basin. This fault zone guided our bedrock and tectonic geomorphic mapping to characterize the timing, geometry, and kinematics of deformation. The four week-long field expeditions enabled us to map faults and lithologic units, collect bedrock samples for geochemical analysis and geochronology, and fly drone surveys to create high-resolution digital elevation models.

Satellite Imagery

Reconnaissance work to identify areas of interest made use of satellite imagery and altimetry in GoogleEarth and in Planet Explorer (Planet Team, 2017) within a box bound by the following latitude and longitude coordinates: (1) 29.127344°, -113.219187°; (2) 29.020336°, -113.130273°; (3) 29.054993°, -113.099504°; (4) 29.124811°, -113.172879°. Google Earth was initially the only available topographic data to us for the island. A group from UCLA working with us purchased a 2.5 m DEM for our study area within the above coordinates, but since topography was not usually high-relief, these maps were not particularly helpful. Geologic maps are presented as they were mapped in the field: overlain on GeoEye imagery accessed through ArcGIS.

Satellite imagery is particularly useful for distinguishing mountainous terrain from gently sloping fans, dark volcanic units from lighter-colored sedimentary units and terraces, and occasionally for highlighting compositional variations within volcanic units of varying color. Topographic profiles made in GoogleEarth allowed us to plan feasible hiking transects for field work on the island. Fault zones have discontinuous, locally complex faults strands which appear “cut-up” in texture. Surface traces visible on the image from individual faults throughout the area. More continuous, longer faults are observed throughout the field area, and are distinguishable by their more continuous lineations.

Geologic Mapping, Stratigraphy, and Sampling

Between November, 2017, and April 2019, the four week-long field expeditions to Isla Ángel de la Guarda enabled us to make detailed geologic maps of key areas, including maps of marine shorelines, terraces, lithologies, and faults. We mapped at 1:15,000 scale onto a transparent overlay on Google Earth imagery, using a Garmin inReach Explorer+ for UTM coordinates in Zone 12 of WGS 84. All UTM coordinates and latitude and longitude reported in this study use WGS 84.

Field lithology was determined in volcanic units by phenocrysts, and in sedimentary units by grain size or presence of fossils. Faults were identified by clear offsets within volcanic units, often best seen from an arroyo, or pronounced, linear steps on the tops of terraces or volcanic units. On one occasion, we could calculate fault slip using a terrace riser as a piercing point. Young faults also were clearly visible in hilly or mountainous terrain by offset drainages (Leeder and Jackson, 1993).

Terraces are often distinguishable by their surface features and relative elevations. Some terraces are notable for their smooth surfaces, and the ease with which one can traverse them; others are rocky and challenging to hike over. Older terraces are easier to distinguish due to their higher elevation and continuity. Lower terrace numbers are assigned to older terraces (i.e., Terrace 0 is oldest).

Stratigraphy is defined from mapped relationships between geologic units. Structural measurements of contacts, foliation, and bedding consistently show that Pliocene volcanic flows and sedimentary units dip toward the northeast. Generally, units in the northwest part of our study area are oldest, and units in the southeast are youngest. Exceptions exist for the terrace deposits, the conglomerate overlying MPv in the southern field area (MPcg), and the rhyolite dome in the southern field area (MPr).

Sampling was restricted to good outcrops so that volcanic material would be fresh and identifiable. These outcrops often are deep within arroyos, since volcanic flows and other units are often covered by meter scale thicknesses of terrace material or altered volcanic flow rocks. Samples are listed in Table 1.

Samples of volcanic rocks were collected for petrography, geochemistry, and geochronology. When sampling, care was taken to avoid weathered surfaces trimming much larger pieces that were first removed from outcrops. To maximize sample usability and minimize carrying weight, outer portions of samples and any seemingly weathered surfaces were removed on-site as much as possible when time permitted. Sedimentary rock samples were taken when we suspected that units would contain reworked ash or other datable material, or when units contained pectens, oysters, or possible microfossils, in case of fossil identification or age determinations. Any pliable or fragile samples, including shells, sandy units, and gypsum beds, were wrapped with care to avoid damage during transport.

Petrography

Billets for thin sections were prepared with a rock saw and sent to Spectrum Petrographic and Wagner Petrographic LLC. Thin sections were imaged with an Olympus BH-2 petrographic microscope, and photomicrographs were taken with the Infinity Analyze program. Several thin sections were analyzed by A. Piña-Paez as noted in Table 1.

Geochemistry

A subset of samples were prepared for X-ray fluorescence analysis at the California Institute of Technology in the Bucholz geochemistry laboratory. Care was taken to select only the freshest samples, and to remove any surface that had been weathered or at all exposed prior to sampling. Samples of 200-800 g representative of the bulk unit were cut into ~5 cm cubes with a saw, and all saw marks were sanded off to remove any contaminants. Samples were then sonicated in DI water to further reduce the possibility of contamination and to remove vug-filling materials. Samples were further wrapped in paper and broken down with a hammer to ~2 cm fragments, and finally crushed with a chipmunk crusher to <3 mm. Crushate was divided into fair splits on printer paper in order to obtain ~15 mL of homogenous crushate. Each ~15 mL sample was pulverized in a Retsch PM100 Planetary Ball Mill using agate grinding vessels and agate beads at 600 rpm to a powder of ≤30 μm.

Following ball mill preparation, samples were prepared for determination of loss on ignition (LOI). Powders were dried overnight in a low temperature 110 °C oven to remove moisture. Ceramic crucibles containing ~1.1 g of sample powder were placed into a 1050 °C furnace for an hour to burn off volatiles. Samples were reweighed 10 minutes after being removed from the high-temperature oven, such that the sample was not too hot (heated air is no longer expanded) and not too cold (recarbonization has not begun) to calculate LOI. Burned off (post-LOI) sample was rehomogenized with an agate mortar and pestle before preparing beads for XRF analysis.

Fused glass beads were prepared with a Claisse Eagon 2 machine. Each 0.9000 g of sample was mixed with 9.0000 g of flux material, a LiT/LiM/LiI (in 66.67/32.83/0.50 ratio) (LiT = $Li_2B_4O_7$, di-lithium tetraborate; LiM = $LiBO_2$, lithium metaborate; LiI = Lithium iodide) in a platinum crucible. Platinum crucibles of this sample/flux mixture and platinum casting dishes were placed into the Eagon 2 machine, which produced one bead per sample. This bead was placed directly on the 4 kW Zetium Panalytical X-ray fluorescence analyzer for whole-rock analyses for concentrations of major oxides (SiO_2, TiO_2, Al_2O_3 Fe_2O_3, MgO, CaO, Na_2O, K_2O, P_2O_5, and MnO) and trace elements (Sc, V, Ni, Cr, Ba, Rb, Sr, Zr, Y, Nb, Cu, Zn, Ga, Pb, La, Ce, Th, Nd, U. Concentrations were renormalized to account for LOI. Standards from the United States Geologic Survey were run along with samples from this study for calibration.

Total alkali versus silica diagrams, AlO_2 – FeO – MgO ternary diagrams, and trace element spider plots were produced with the Geochemical Data Toolkit (Janoušek et al., 2006, 2011). Geochemical data is included in Table 2.

Geochronology

A subset of samples was chosen for $^{40}Ar/^{39}Ar$ geochronology based on their importance in our stratigraphic and structural interpretations, volume, and weathering characteristics. Crushed samples were separated for groundmass (typically <500 μm), and plagioclase crystals (typically 0.5-1 mm). Feldspar crystals were screened using a Frantz Isodynamic Magnetic Separator at 1.6 amps with a tilt of 20° to retain only the least magnetic grains. Separates were sent to the United States Geological Survey at Menlo Park for further preparation and analysis, as outlined in Chapter 3. A summary of geochronologic results is provided in Table 3, with compositional data listed in Table S1.

Drone Survey DEMs

Drone surveys were flown in several areas of interest to create sub-meter digital elevation models. Among other geologic features, areas of interest included (1) sag ponds, identified both in a reconnaissance mapping expedition in 2009, and in Google Earth air photos, (2) areas with a high density of faults in alluvial terraces and volcanic rock, (3) fleets of terraces cut by faults. Several ground control points were used in drone surveys when possible. Because we aimed to fly drones before wind picked up in the afternoons, we were often time-limited in placing ground control points, which ultimately greatly reduced (or eliminated altogether) the number of possible ground control points in a drone survey.

Structure-from-motion was used to create DEMs with drone photographs. In the southern part of our study area, a total of four sub-meter DEMs were created, each ~2 km^2, all of which overlapped with our geologic mapping. In the northern part of our study area, another four DEMs were created, and about half of their total area overlapped with our geologic mapping. DEMs from structure-from-motion can be very useful for identifying faults and fault traces (Johnson et al., 2014). Topographic profiles orthogonal to fault strikes were used to highlight steps in terraces and volcanic units, illuminating exact locations of faults. DEMs were also used to create aspect maps, which assign colors to downslope flow directions. These colorized aspect maps illuminate further lineations from tilted terraces and offset streams.

RESULTS

Satellite Imagery

The northern section of our study area lies within the latitude and longitude boundary coordinates, (1) 29.127344°, -113.219187°; (2) 29.094516°, -113.198519°; (3) 29.105695°, -113.163366°; (4) 29.124811°, -113.172879°, (Figures 2 and 3). In this section, towards the center of the island at latitude 29.1° N, topography changes from a mountainous western side of the island, with slopes of ~15° to the W, to a much more gradual slope of ~1.5° to the E, more-or-less constant from the center of the island to the beach on the eastern shore. Imagery from Google Earth shows dark, resistant units that appear banded in the center of the island, which we observed in the field to be a sequence of volcanic units of variable compositions. Towards the eastern shore, satellite imagery shows a pronounced dark unit surrounded by lighter material – representing a basalt or andesite lava surrounded by alluvial or marine terraces (Gastil, 1975). South of this basaltic unit is a ~5 km^2 fault zone, distinguished by its cut-up appearance. Longer and more isolated faults strike NNE, are usually traceable throughout the extent of the field area, separated by 200 to 500 m.

The southern section of our study area is bound by the latitude and longitude coordinates, (1) 29.045545°, -113.169561°; (2) 29.020336°, -113.130273°; (3) 29.054993°, -113.099504°; (4) 29.069029°, -113.149875°. Similar to the northern area, the same shift from the mountainous western half of the island to gently sloping terraces on the eastern half of the island is apparent in the southern area. Again, there is a ~2 km^2 dark volcanic unit towards the shore, surrounded by lighter marine and/or alluvial material. In the western part of this region, older volcanic units, longer faults tend to extend through the field area, and are spaced ~150 m apart. Likely, faults of the same age are buried under alluvial terraces between UTM Eastings 290000 and 294000.

Geologic Mapping and Sampling

In the northern field area we define 10 volcanic units and 8 sedimentary units (including alluvial, beach, and terrace material), detailed in the next section. Also detailed partially in the next section are units from the southern field area: 3 volcanic units and 10 sedimentary units (again, including alluvial, colluvial, beach, and terrace material). More detailed descriptions of sedimentary units from the southern field area are documented in Chapter 3.

Although some volcanic flow units are massive and have no reliable indicators of paleohorizontal, other units strike to the NNW and dip ~20° to the east. Units to the west are older volcanic units, some with xenoliths of tonalite. Tonalite xenoliths are likely from Cretaceous batholithic rocks underlying the vent region, similar to the batholithic rocks seen in the Baja California peninsula. We have one sample of batholithic basement outside of our field area.

Units are separated from one another by contacts. In our study area, we see only depositional and fault contacts, and no intrusive contacts. Depositional contacts are categorized as certain, inferred, and uncertain. Certain contacts have been field-checked, or continue undoubtedly in imagery. Inferred contacts are less distinguishable in the field and in satellite imagery, usually due to a gradational nature. Uncertain contacts are continuations of certain or inferred contacts, which are not clear in the field or in imagery.

Faults in this area record small amounts of slip. Sometimes enough slip has been generated to place different units in contact with one another along, particularly in the northern area. Fault contacts are categorized in mapping as certain, covered, inferred, and uncertain. Certain faults display visible offset or steps in drainages, and often trace for several hundreds of meters. Covered faults are covered by alluvium younger than the most recent rupture – typically Qal. Inferred faults are often visible in imagery, creating offset or displacing units. Uncertain faults are generally continuations of other more certain faults, which do not otherwise have an obvious path of continuation.

We collected a total of 77 samples in our study area and the surrounding region, including 1 basement sample, 2 clasts of welded tuff in alluvium, 2 felsic dike samples, 1 sample of fault material, 2 granitic inclusions samples, 1 mafic inclusion, 2 autolithic inclusions in a volcanic breccia, 1 tuff sample, 1 pyroclastic breccia, 41 lava flow samples (andesites, basalts, rhyolites), and 24 samples of sedimentary units, 5 of which are pumiceous or ashy, and 12 of which contain macrofossils or likely microfossils. Sample details and analyses are documented in Table 1.

Stratigraphic Units

Stratigraphic units are divided into the northern and southern mapping areas (Figures 6 and 7, respectively). Terraces are degradational, and we suspect that terrace designations T1 through T3 are consistent through both areas. Lithologies and units are considered entirely separately in the two map areas (Figures 6 and 7). According to a scheme of units gently dipping, and therefore younging, to the E, units in the southern area are younger than those in the north. Units in the northwest dip somewhat more moderately, and those to the northwest outside our study area dip steeply. In naming of units, we describe relative ages. Absolute ages from $^{40}Ar/^{39}Ar$ geochronology are only known for the following units in the northern area: Pliocene andesite lava 2 (Pa2) and Pliocene andesite lava 1 (Pa1). In the southern area, $^{40}Ar/^{39}Ar$ ages for the following units are reported in Chapter 3: Miocene-Pliocene volcanic flows (MPv) and Pliocene basaltic andesite (Pba). These ages, all between 2 and 4 Ma, indicate broadly coeval deposition of the younger and gently dipping Pliocene units in the northern and southern areas.

During this time period, geologic structures in the Gulf of California were actively rifting. Although the volcanic units may appear close in time and space, small differences in their ages may represent separate volcanic centers active during different events as the island was separated from Baja California. We continue to question the relationships between different volcanic flows.

Northern Area

The Northern area consists of Miocene (?) to Pliocene volcanic units, with a thin sedimentary sequence including a conglomerate and sandstone, capped by an andesite (Figure 4). Terraces T0 through T3 are Quaternary in age, determined by the UCLA group. Field photographs (Figure 8) show several representative units in the area.

Miocene-Pliocene Rhyolite (MPr1)

The stratigraphically lowest unit mapped in the northern area is a greyish red, flow-banded rhyolite with 2-5 mm phenocrysts of plagioclase and amphibole. Near the top and sometimes interstratified within the unit is MPpy (Figure 8b).

Miocene-Pliocene Yellow Pyroclastic flow (MPpy)

Overlying MPr1 or within its top ~100 m is a ~20 m thick yellow pyroclastic surge deposit (Figure 8b). The pyroclastic unit is composed of poorly to moderately stratified ash rhyolite tuff with <5 cm lithics. MPpy is overlain by MPr1 or MPd.

Pliocene Dacite (Pd)

Above the rhyolite or pyroclastic flow is a ~160 m thick (measured from cross-section) blue-grey dacite with 2-4 mm phenocrysts of plagioclase, quartz, biotite, and minor hornblende. Above the dacite is a basaltic andesite.

Pliocene Basaltic Andesite (Pab)

The ~60 m thick basaltic andesite lies directly on top of the dacite, and has phenocrysts of plagioclase and olivine. The basaltic andesite becomes more silicic stratigraphically upward, ~60 m from the base of the unit, and is referred to as an andesitic flow (Pa).

Pliocene Andesite (Pa1)

Pliocene andesite is ~40 m thick. Plagioclase from the andesite (LS19IAG31) has an $^{40}Ar/^{39}Ar$ age of 3.916 ± 0.088 Ma. Pa is overlain by a second rhyolite unit, Pr2.

Pliocene Rhyolite (Pr2)

This rhyolite unit overlies the Pliocene basaltic andesite (Pba), and is ~150 m thick, measured from cross-section. The unit has a brecciated base, and weathered surfaces are a conspicuous pink color. Pr2 is overlain by Prr, Pliocene red rhyolite.

Pliocene red rhyolite (Prr)

The red rhyolite has a thickness of ~25m, measured from outcrop patterns projected onto cross-section.

Pliocene conglomerate (Pcg)

A conglomerate overlies Prr, and is ~5-10 m thick, based off cross-sectional thickness. The conglomerate has ~5 cm thick beds. Clasts are typically 2 cm in diameter, ranging up to 5 cm, with some boulders ~1 m in diameter. Clast compositions are mostly andesite and basalt, but also include metamorphosed quartzite, phyllite, possible tonalite, and other undifferentiated volcanic rocks. Clasts are imbricated in some areas, indicating flow to the E (Figure 8b). The conglomerate is likely overlain by Pliocene sandstone (Ps), although the presumed contact is concealed beneath outcrops of a younger andesitic flow and terrace material.

Pliocene sandstone (Ps)

Pliocene sandstone (Figure 8c, d) has a bedding attitude of 311°, 24°E, consistent with underlying Pliocene bedding rather than similarly appearing Quaternary deposits.

The sandstone, mapped in only one outcrop area (Figure 6), is 4-5 m thick, with internally thin,very finely to finely laminated beds ~10 cm thick (Figure 8d). The sandstone is well sorted and immature with abundant silty matrix. About 1 m below the top of the outcrop is a ~10 cm thick white ash bed.

Although the absolute contact is not exposed, Pliocene andesite 2 (Pa2) presumably overlies Pliocene sandstone (Ps).

Pliocene andesite 2 (Pa2)

Pliocene andesite 2 presumably conformably overlies Pliocene sandstone (Ps), and has a consistent bedding attitude of 314°, 26°E. Groundmass in this andesite has an $^{40}Ar/^{39}Ar$ age of 2.986 ± 0.009 Ma.

Terraces 0-3 (T0, T1, T2, T3)

Quaternary terraces are most easily distinguished from one another by morphology and elevation. The oldest terrace, T0, is at the highest elevation, and is scarcely observed since it has been largely carved away by more recent terraces. Often, T0 remnants are found high up in erosional notches into the underlying Pa2. T1 is commonly observed to be cut into Pa2, also at higher elevation. T1 is subdivided into T1ss in a small area, known as "the bathtub," which denotes a fine white-hued sandstone at elevations consistent with T1. T1a is similar in morphology to T1, but lies at a slightly lower elevation and is therefore somewhat younger than T1. T2 is the best defined, most continuous set of terraces. It is morphologically smooth (easy to walk on), such that faults that cut it are well defined (Figure 8e). T3 is the youngest observed terrace, and is at the lowest elevation. In contrast to T2, T3 is morphologically rough (unpleasant to walk over), and sometimes nearly indistinguishable from surfaces developed on Quaternary alluvium in modern washes (Qal).

Quaternary Alluvium (Qal)

Quaternary alluvium encompasses all recently aggraded sediment, usually in arroyos. Along with Qb, Qal is the youngest mapped unit and is generally < 5 m thick.

Quaternary beach (Qb)

These deposits are recent and beach deposits along the modern coast.

Southern Area

The Southern area has Miocene (?) to Pliocene volcanic flows, a ~100 m thick sedimentary sequence, and a capping basaltic andesite flow (Figures 5 and 7). A Miocene or Pliocene conglomerate overlies older, possibly Miocene volcanic rocks, in a buttress unconformity, in the southwestern part of the Southern study area. A rhyolite dome is observed in the southeast part of the study area.

Quaternary terraces T1 through T3 are mapped, and T2 has a marine terrace, T2m, probably temporally equivalent to T2 terraces in the northern area. Quaternary alluvium (Qal) and colluvium (Qc, from landslides) are among the youngest deposits. Field photographs are included in Chapter 3.

Miocene-Pliocene Volcanic rocks (MPv)

Miocene-Pliocene volcanic flows observed within the study area are largely composed of andesite flows, which have phenocrysts of plagioclase and lesser hornblende. Possible dacitic composition (with possible quartz phenocrysts) is observed at 29.040921° N, -113.158986° E. In the arroyo to the north, near 29.050358° N, -113.161834° E, the unit is a field-designated flow-banded rhyolite. Further wet into the arroyo, composition is basalt with weathered out olivine crystals. This particular arroyo opens up, and toward the back end of it (29.056095° N, -113.176806° E), a tuff makes up a ~10 m^2 outcrop with xenoliths of at least four lithic types: granodiorite, grey lithics, red lithics, and yellow-weathering pumice. The granodiorite contains quartz, plagioclase, biotite, and hornblende, and is presumably from Cretaceous basement. Additional granitic xenoliths are reported within an autobrecciated andesitic flow (29.059759° N, -113.156382° E). An andesite flow from the southernmost part of this study area

(29.031695° N, -113.126953° E) has an $^{40}Ar/^{39}Ar$ age of 2.925 ± 0.012 Ma.

Miocene-Pliocene conglomerate (MPcg)

A Neogene conglomerate is observed at elevations of 160 to 190 m above sea level, buttressed against older Miocene-Pliocene volcanic rocks. Clast compositions include quartzite and several different volcanic rocks. Implications are discussed in Chapter 3 discussion.

Miocene-Pliocene rhyolite dome (MPr)

A dome of highly foliated purple and white banded rhyolite is found in the eastern-most corner of our study area. Folds are isoclinal, and the rhyolite has phenocrysts of plagioclase, amphibole, alkali feldspar, and hornblende.

Pliocene sedimentary rocks (Ps)

Discussed in further detail in Chapter 3, ~100 m of Pliocene sandstone are mapped in the study area. Pliocene sedimentary rocks are overlain by Pba, Pliocene basaltic andesite.

Pliocene sedimentary marine rocks (Psm)

Detailed further in Chapter 3 is a marine section of the Pliocene sedimentary rocks which are fossiliferous, denoted Pliocene sedimentary-marine: Psm.

Pliocene Basaltic Andesite (Pba)

Pliocene basaltic andesite lava overlies the Pliocene sedimentary rocks and marine sediments, and occupies the ~6km^2 recognizable dark area in the southeastern part of the island near the ocean closest to Isla Vibora. The stratigraphic relationship between the Pliocene sedimentary rocks and the Pliocene basaltic andesite is well-documented by the following: (1) a baked contact with the basalt baking underlying sedimentary rocks, (2) a ballistic volcanic bomb of the basaltic andesite fell into soft sedimentary rock. These contacts are discussed in further detail in Chapter 3. Two well-constrained $^{40}Ar/^{39}Ar$ ages and one maximum $^{40}Ar/^{39}Ar$ age from plagioclase separates are reported for this basaltic andesite flow: 2.754 ± 0.021 Ma, 2.756 ± 0.079 Ma, and 3.16 ± 0.042 Ma, respectively, with the latter representing a maximum consistent with the eruptive age of the two younger samples. Data and analysis for these ages are presented in Chapter 3.

Samples of the basaltic andesite flow have phenocrysts of plagioclase, and some have minor amphibole.

<u>Terraces 1-3 (T1, T2, T2m, T3)</u>

Terrace names, elevations, and associated relative ages in the southern area are coeval with those in the northern area. In the southern area, we do not identify T0 or T1a terraces, but we do identify a marine equivalent of T2, named T2m (marine), which is rich in marine shells.

<u>Quaternary Alluvium (Qal)</u>

Quaternary alluvium encompasses all recently transported sediment, usually in arroyos. Along with Qb, Qal is the youngest mapped unit and is generally < 5 m thick.

<u>Quaternary Beach (Qb)</u>

These deposits are recent and current beach material.

<u>Quaternary Colluvium (Qc)</u>

Quaternary colluvium is landslide or rock slide material, often found steep arroyo walls.

Contacts

Contacts separate polygons of stratigraphic units on the geologic map (Figures 6 and 7). The map border is not a lithologic or fault contact, but denotes the extent of our mapped study area. We subdivide fault contacts into four categories: (1) Certain faults are mapped or visible in air photos and are precisely located. (2) Concealed faults are certain, but buried by alluvium, which is often terrace material or Qal. (3) Inferred faults often have a trace which is difficult to follow, or are continuations of certain faults but with precise location difficult to follow from mapping or air photos. They may follow topographic or lithologic features associated with faults, such as notches in ridgelines or seemingly offset lithologies or terraces. (4) Uncertain faults either continue from or connect between more certain faults. Uncertain fault traces may or may not exist, and are difficult to follow, even with high resolution drone imagery or related DEMs made with structure-from-motion. Some faults in this field area often have several splays, making it challenging to determine exactly which faults are connected and how.

Lithologic contacts are depositional and are subdivided into three categories. (1) Certain contacts are either mapped contacts or continuations of mapped contacts that are discernible in air photos and are precisely located. (2) Inferred contacts are often obscured and hard to precisely locate because they may border recessive units or be near faults that make contacts less well-defined. (3) In the context of these geologic maps, uncertain contacts are either gradational, such that the unit could be continuous without a lithologic break in units, or the uncertain contact is denoting an apparent lithologic change in appearance in air photos, usually the contact between Qal and/or terrace material.

Petrography

A set of 51 thin sections from a total of 68 samples were examined under the petrographic microscope to establish modal compositions of the volcanic units (Table S1 and Figure S1). Basaltic andesite and andesite lavas are all porphyritic with phenocrysts of plagioclase and alkali feldspar. Many thin sections show amphibole, oxides, titanite, and textural evidence of alteration. In some cases, plagioclase phenocrysts or matrix have a trachytic texture, probably following flow direction.

Photomicrographs of representative samples with $^{40}Ar/^{39}Ar$ ages are shown in plain-polarized and cross-polarized light (Figure 9). Pa1, the oldest sample dated, has phenocrysts of amphibole and plagioclase in a glassy groundmass, which is altered to spherulites (LS18IAG31; Figure 9a, b). Pa2 hosts plagioclase and hornblende phenocrysts (LS18IAG28; Figure 9c, d). MPv, the oldest unit in the southern area, has somewhat flow-aligned phenocrysts of plagioclase and oxidized pyroxene (LS19IAG68; Figure 9e, f). Pab, the youngest dated unit, has large phenocrysts of plagioclase in a very fine-grained groundmass (LS19IAG66, Figure 9g, h). Petrographic descriptions of analyzed sections are included in Table S1, and photomicrographs are included in Figure S1.

Geochemistry from X-ray fluorescence

Major and trace element geochemistry was determined on a subset of 32 representative samples by X-ray fluorescence analysis (Table 2). Although nearly all 27 extrusive samples have field-determined classifications of basalt to andesite, all XRF-determined geochemical compositions based on total-alkali-silica diagrams (N_2O + K_2O versus SiO2) are intermediate. All lava samples lie between basaltic andesite and rhyolite, and most are andesite or dacite. A single sample is a basaltic andesite, 7 are andesite, 17 are dacite, and 2 are rhyolite (Figure 10). XRF geochemistry on a sample of basement rock outside the map area and a granitic inclusion within the map area revealed that both are compositionally granodiorites. The 1 mafic inclusion sample and 2 volcanic breccia inclusions (likely autoliths, outside the map area) are all compositionally diorite. Samples broadly tend to become more mafic to the southeast (Figure 11), and toward the stratigraphic top of the section.

Extrusive lava samples, inclusions, and basement rock are depleted in Fe and Mg, enriched in Al, and follow a calc-alkaline differentiation trend in the AFM ternary diagram (Figure 12). In Harker major oxide diagrams, most show well grouped trends (Figure 13) except Na_2O, and a lesser amount of scatter in TiO_2 and K_2O. The single basement sample, the granitic inclusion, and 3 mafic inclusions largely appear similar to extrusive lavas. However, lower Na_2O distinguishes the basement sample and granitic inclusion from the mafic inclusions and extrusive lavas. In the Discussion section, we compare these data to those from the Puertecitos Volcanic Province (Figure 14). Trace element data shows that extrusive lavas, inclusions, and basement rock all have pronounced negative Nb anomalies, and somewhat low Ti, often associated with subducted or arc-related material (Figure 15) (Briqueu et al., 1984). In comparison with curves representing mean composition of upper crust, whole crust, calc-alkaline island arc, and mid-oceanic ridge basalt, our most mafic sample suite appears dissimilar to mid-oceanic ridge basalts and island-arcs, spanning a range most consistent with crustal or upper crustal derivation.

Geochronology

We report $^{40}Ar/^{39}Ar$ ages for one felsic dike (LS18IAG22) ~20 km north of our study area (latitude/longitude of 29.279499° N, -113.168999° E) and two lava flows within our Northern study area (LS18IAG31 and LS18IAG28) (Figure 16) (Table 3, Table S1). Four additional $^{40}Ar/^{39}Ar$ ages from the Southern study area are reported separately (Chapter 3), and range from an older andesitic lava flow of 2.925 ± 0.012 Ma, to flows as young as 2.754 ± 0.021 Ma.

The felsic dike has an $^{40}Ar/^{39}Ar$ age of 3.377 ± 0.037 Ma from groundmass (Figure 16a). Due to the fine-grained nature of the dike, this age is not as precise as other measurements reported in this study, and using the recoil model age (Fleck et al., 2014), individual plateau steps yield ages from 3.133 ± 0.037 Ma to 3.693 ± 0.206 Ma. The dacite lava flow has a weighted mean $^{40}Ar/^{39}Ar$ plateau age of 3.916 ± 0.088 Ma from plagioclase (LS18IAG31a and LS18IAG31b, Figures 16c and d). The andesitic lava is stratigraphically above the dacite lava flow, which is confirmed by its $^{40}Ar/^{39}Ar$ age of 2.986 ± 0.009 Ma from groundmass (Figure 16b; LS18IAG28).

Drone-based Digital Elevation Models

DEMs calculated from drone imagery using structure-from-motion software have ≤5 cm accuracy, and aid in understanding topographic features, such as drainages and ridges, and fault offsets (Figure 17). These DEMs allow us to make topographic profiles across faults, flow accumulation maps (rasters of accumulated water flow downslope into each cell), and aspect maps (rasters of colorized slope direction) (Figures 17, 18).

One particular sag pond mapped in this area marks a recently or currently active area. This recent pull-apart basin next to a drainage-ridden hill slope highlights a particularly interesting case study. In this area, we apply different techniques using elevation data made using structure-from-motion from drone imagery (Figure 17). Topographic profiles were taken across seven northwest-southeast lines, A through F (Figures 17, 18). Profile C1 was added to C, because it is more perpendicular to the main faults than other profiles.

The DEM highlights hills and drainages, and when used to make topographic profiles, clearly captures slope anomalies in otherwise smooth slopes (Figure 17b). However, slopes on hills of this part of IAG are full drainage arrays. The drainages can make it difficult to discern vertical kinks in topographic profiles due to faults from vertical kinks due to drainages. Anomalies that define a bench (Figure 18) and offset the slope are presumed to be fault related. Some of these kinks can be followed along fault traces to other topographic profiles, especially in profiles C1, D, and E. Profile C1 is a good example of a case where several kinks in topography are not obvious, even though it is most perpendicular to main faults.

Flow accumulation maps calculate accumulated downward water flow to each cell in a raster. These maps can depict drainage patterns from large, kilometer scale to meter or sub-meter scale (Figure 17c, g). Since larger drainage patterns can be lithologically controlled, and there are so many small drainages that are distracting to the eye, we examine the flow accumulation here on a fine scale. This way, several kinked drainages are often aligned and offsets are easier to discern by eye. In addition to kinked drainages, the flow accumulation maps highlight arroyos (whether or not they are tectonically controlled), ridgelines, and different terrace levels. Arroyos and ridgelines are also, of course, visible in the DEMs. Different terrace levels are separated by unit contacts (which separate T1 from T2, etc.). When zoomed in, kinks in drainages highlighted by flow accumulation are most visible under profiles E and F, and these kinks have aided us in following faults throughout the hillslope.

Another useful image created from the DEM is the aspect map (Figure 17d). Aspect maps show slope direction, with the direction of slope indicated by color. This nature of map is visually busy, making it challenging to tell ridges and valleys from less jarring features. However, it does show that the hillslope underneath the western sides of profiles C and C1 as especially jagged and cut-up, which is a tell-tale sign of complex tectonic activity underneath. The terrace in the middle-right area of the map has a few ~E-W drainages cut into it, and also some changes in slope direction due to ~N-S faulting.

DISCUSSION

Geochemistry

XRF-determined geochemical compositions of granitic inclusions and rocks from volcanic flows are similar. Their similarity may represent some derivation of the lavas from the basement granitic rocks. Since the lavas are likely derived from arc-related or subducted material (Briqueu et al., 1984), the crystalline rocks would represent the arc-related material.

The most basaltic units mapped are also the youngest units mapped, with the exception of one sample in the northwest-most part of our study area (Figures 6 and 11). According to our stratigraphy, the one basaltic sample in the northwest is probably older than all other volcanic flows. Its mafic composition may indicate a more significant lapse in time between deposition of that flow sequence, which is mainly rhyolites (MPr1) and following volcanic flows (Pd and following), and possibly that the magma chamber may have been re-fractionated in the presence of felsic country rock during that time. Following the assumption that the stratigraphy is more-or-less temporally continuous, younging from the northwest to southeast, lavas became gradually more mafic until the most recent dated lava in the southeast map area (2.754 ± 0.021 Ma), consistent with the idea that a magma chamber emptied through the eruption of these lavas, and did not continue to have contributions of surrounding continental crust. The calc-alkaline nature of our samples further confirms that the lavas are derived from arc-related rocks, although their intermediate andesitic composition requires that they cannot solely be melted from granodiorite, and require input of a mafic amphibolite.

Harker diagrams show samples from this study overlapping most consistently with middle Miocene Group 1 arc-related rocks from the Puertecitos Volcanic Province, rather than with synrift rocks in the Puertecitos region much closer in age to rocks on IAG (Figure 14; Martín-Barajas et al., 1995). Trace element diagrams normalized to chondrites (Thompson et al., 1982) show our data plotting between the upper continental crust and bulk continental crust (Taylor and McLennan, 1995), or close to island arc calc-alkaline basalts (Sun and McDonough, 1989a). The strongly negative Nb anomalies in our data indicate a geochemical signature of high field strength element depletion, consistent with subduction zones worldwide (Briqueu et al., 1984). Together, the negative Nb and Ti anomalies are properties of an arc-related signature. These features could be indicative of melts of deep-seated mafic rocks, or melts of pre-existing continental crust. Further investigation of Sr isotopes would help resolve this question (Duyverman et al., 1982).

Stratigraphy and timing of Events

As noted above, less than 20 km north of the northern field area, we sampled crystalline basement rock, which is geochemically a granodiorite. Likely this granodiorite is Cretaceous basement, and genetically related to 91.2 ± 2.1 Ma batholithic granodiorite mapped in La Reforma complex (Schmidt, 1975). Xenoliths of this granodiorite are found within andesite and basaltic andesite flows in the southern map area.

Miocene-Pliocene rhyolite is the oldest unit we have mapped in the northern study area. Although we have no maximum age constraint on the rhyolite, we determined a maximum $^{40}Ar/^{39}Ar$ age age from a mapped Pliocene andesite 1 (Pa1) upsection of 3.916 ± 0.088 Ma. This andesite flow also postdates Pliocene basaltic andesite (Pba), Pliocene dacite (Pd), and Miocene-Pliocene pyroclastic deposit (MPpy). It is assumed that the Pliocene dacite and Pliocene basaltic andesite were not deposited long before Pliocene andesite 1, due to their conformable nature and outcrop pattern.

However, we are not as confident that contacts between Pliocene pyroclastic deposits and Miocene-Pliocene rhyolite 1 are conformable. They are found both downsection from the Pliocene dacite and within the mountainous terrain, which is separated from the main section by terrace material at lower elevations. There are at least two possible explanations for the separation of the Pliocene pyroclastic deposit and Miocene-Pliocene rhyolite 1 from the main section in map area.

First, the Pliocene pyroclastic deposit is less resistant than underlying rhyolite and overlying dacite. The outcrop pattern of the pyroclastic deposit likely is buried under terrace material. So, the pyroclastic deposit may have eroded away easily during the event carrying initial terrace material from higher elevation to lower elevation. Second, the Pliocene pyroclastic deposit and Miocene-Pliocene rhyolite 1 may simply be much older, and may have been somewhat eroded before the overlying flows were deposited. These two possibilities can coexist and doubly explain the break in section seen on the geologic map. An additional complication is that both MPpy and MPr1 are seen underlying Pd, which may support either or these two aforementioned possibilities. Regardless, MPr1 and MPpy may be significantly older than the main section, and both units may be Miocene (or older?) rather than Pliocene.

Mapped conformably atop the Pliocene red rhyolite is a Pliocene conglomerate. A Pliocene sandstone is mapped further upsection, following our interpretation of stratigraphic younging to the east. The Pliocene sandstone has no observable contacts with other units aside from terrace material and colluvial cover derived from Pliocene andesite 2. It is assumed that the Pliocene sandstone was deposited conformably over the Pliocene conglomerate, but may have been eroded and thus omitted by later andesitic flows of Pa2.

We interpret terraces, like those in the southern field area, to be terraces cut into a preexisting material, either bedrock or an initially aggradational terrace material. In subsequent events, terraces would drape with a thin colluvial mantle. Possibly, the same initial material was deposited in both the northern and southern field areas. Terraces appear to be continuous with consistent relative elevations in our northern and southern field areas. For this reason, it is probable that T1 through T3 were cut during the same events, synonymous with the same timing, in the northern and southern field areas. Faults crosscut terrace material, and it is thus clear that at least some faulting has been active after development of terraces. Pliocene volcanic flows in both the northern and southern field areas are weathered, making it difficult to identify any older faults which do not cut terrace material.

Synthesis and comparison of field areas

Miocene-Pliocene conglomerate

A foremost concern in correlation of stratigraphy between the northern and southern areas is the relation between the unique terrigenous detrital intervals in both areas, including conglomerate and sandstone in the northern area, and the marine and non-marine interval in the southern area. Pliocene sandstone in the northern area, if indeed conformable with the rest of the sequence, has a minimum age of 2.986 ± 0.009 Ma from the overlying Pliocene andesite 2 (Pa2). The Pliocene sedimentary rocks in the southern area are tightly constrained to between 2.756 ± 0.079 Ma and 2.925 ± 0.012 Ma. Thus, the geochronology does not allow for synchronous deposition.

If indeed the northern conglomerate and sandstone and southern sedimentary rocks are syndepositional, one of the following would need to be true: (1) Chapter 3 details the possibility, although unlikely, that the sedimentary sequence in the southern area does not actually have a proper maximum age constraint. (2) It is possible that the northern Pliocene sandstone is, in fact, not in a conformable sequence, and was deposited along with formation of the arroyo it is found in. This is unlikely, evidenced by its moderate 30° dip, consistent with the underlying volcanic flows and conglomerate. (3) The base of Pliocene andesite 2 (in the northern field area) is not well mapped, since it is often eroded away or at higher elevations, out of hiking range. If our mapping is inaccurate, it is possible that the particular sample should be assigned to a stratigraphically lower unit, such as Pliocene andesite 1.

As all of the aforementioned possibilities are considered unlikely, we interpret the northern Pliocene sandstone to be deposited before southern Pliocene sedimentary rocks. Presumably a southeastward shift in sedimentary accommodation space or sediment supply occurred in the time between deposition of the two units. Curiously, both sedimentary sequences are overlain by andesite, which may be indicative of a migrating transition from sedimentation to volcanism. Both volcanic activity and subsidence may express active rifting and extension. Such a geographical shift in depositional environment and volcanism, possibly during extension, appears, inconsistent with the larger middle to late Pliocene westward migration of extension in the region (Aragón-Arreola and Martín-Barajas, 2007). The shift may, on the other hand, be a smaller scale phenomenon, most simply explained by block rotation of IAG during volcanism and nearby erosion to the east, tilting the eastern shore more with time.

Extension and faulting

Dikes mapped ~20 km north of our study area are indicators of ~NW-SE extension (29.279499° N, -113.168999° E). The $^{40}Ar/^{39}Ar$ age of one sampled dike is imprecise, with individual plateau ages ranging from 3.133 ± 0.037 Ma to 3.693 ± 0.206 Ma, but it does provide further evidence of extension during the deposition of the northern volcanic flows between Pa1 and Pa2.

Widespread faulting episodes occurred in Quaternary and Pliocene time, and possibly earlier, demonstrated by long faults cut through Quaternary terraces and Pliocene volcanic flows. As shown in our cross-sections through the northern and southern field areas (Figures 19 and Chapter 3, Figure 7), we interpret the faults to accommodate similar amounts of slip, and find no evidence of a larger, perhaps listric fault geometry (i.e., Wernicke and Burchfiel, 1982), which might control topography. All faults are extensional with normal motion. Most faults dip to the east with east-side-down motion and a component of right-lateral slip. Some shorter faults are antithetic and dip to the west, with local vertical motion down on the west side, and these typically create small grabens. In select outcrops, we can follow terrace risers across fault scarps which typically show offsets of ~2 m. In the southern field area, one mapped fault (Figure 8e) cuts a terrace riser so cleanly that we were able to measure ~2 m of vertical separation, and ~12 m of right-lateral horizontal separation.

Throughout our mapping, we observe that bedding tends to strike NNW within all small "domino" fault blocks in our study area, and faulting tends to strike NNE. The eastward tilting of beds is probably a result of a major listric west-dipping normal fault at depth, which would currently have a trace at the surface to the east of the island, in the Gulf of California (e.g., Proffett Jr, 1977; Wernicke and Burchfiel, 1982; Brady et al., 2000). In this case all deformation we have mapped in the form of small faults with subequal amounts of offset would exist within the hanging wall of this major, west-dipping fault.

We had anticipated that our aspect ratio maps from our drone-based DEMs might further inform our understanding of rotated blocks on southeastern Isla Ángel de la Guarda. Unfortunately, field logistics made it challenging to have enough area covered by drone images, and drainages made DEMs and related maps unnecessarily complex. Elevations were not exact, since we had few ground-control-points, and elevations were not consistent across different drone flights. With further work to properly mosaic the DEMS and tease out noise (boulders, cacti, drainages), it may be possible to better tease out small, rotated blocks on southeastern Isla Ángel de la Guarda.

Long NNE-trending faults tend to continue to the southwestern shore of the island, and presumably off-shore. These faults probably extend to the Northern Salsipuedes basin, and are possibly extensions from it. Our mapping indicates that these faults active or recently active faults. This is consistent with seismic reflection and gravity modeling in the Northern Salsipuedes basin (Persaud et al., 2003; González-Fernández et al., 2005).

Rifting has probably occurred in several stages. In a possible sequence of events following the deposition of volcanic flows and sedimentary rocks mapped in this study, 1) blocks were rotated shortly after the end of late Miocene arc volcanism, (2) Isla Ángel de la Guarda was translated along the Ballenas Transform between 3 and 2 Ma, and (3) NNE-trending faults associated with the active Northern Salsipuedes basin continue to cut though the southeastern part of the island.

Faulting shifts drainages throughout both field areas, and has seemingly blocked sediment transport in some areas. In a notable case, "the bathtub," a NNE-striking fault crosses a larger E-W arroyo (29.109897°, -113.186898°). In an elongated topographic basin to the north of the arroyo, there is a buildup of fine, near-white sediment (T1ss). The sediment, when observed from the arroyo, rises to the same elevation as T1, and the arroyo is very open in this area.

These observations lead us to interpret that during formation of T1, the arroyo was blocked off, perhaps by means of right-lateral faulting or related landslide. This blockage caused a buildup of sediment in the bathtub. Following T1, either (1) the fault had enough east-side-down motion to allow sediment to pass, or (2) fluvial processes were able to erode through the blockage, or some combination of the two.

CONCLUSIONS

Our geologic mapping and related work greatly adds to previously existing mapping on the island (Gastil et al., 1975; Delgado Argote, 2000; Cavazos Álvarez, 2015). We mapped several Miocene-Pliocene volcanic and sedimentary units in our northern and southern study areas. Our two field areas have NNW-striking bedding and foliations, which allows us to infer that older volcanic rocks lie to the northwest, and units young toward the southeast,

In the northern area, the Miocene-Pliocene volcanic flows may be significantly older than overlying units. The oldest $^{40}Ar/^{39}Ar$ age comes from Pliocene andesite 1 (Pa1), and is 3.916 ± 0.088 Ma. Between Pa1 and the upsection Pa2, which has an $^{40}Ar/^{39}Ar$ age of 2.986 ± 0.009 Ma, lies a thin sedimentary sequence with a conglomerate, sandstone, and thin ash bed.

In the southern area, we map older volcanic flows to the west (MPv), and younger basaltic andesite to the east Pba, with a sedimentary sequence in between. These units are discussed further in Chapter 3.

Our geochemical analyses from XRF confirms our field lithologies: several volcanic flows are intermediate, and some are andesitic or basaltic andesitic (Figure 10). Silica percentage largely decreases from the northwest to southeast (Figure 11). Major oxides show that our samples are largely similar to arc-related rocks from the Puertecitos Volcanic Province (Martín-Barajas et al., 1995) (Figure 13), and trace elements suggest that the lavas may be derived from continental crust (Figure 15).

Both field areas show evidence of extension occurring from Miocene to recent time. Several long, NNE-trending faults cut through both areas, often reaching the eastern and western shores of the island. These faults are probably related to recent and active extension in the nearby Northern Salsipuedes basin. Pliocene sedimentary rocks found within the stratigraphy of volcanic flows in the northern field area imply that the area may have been closer to sea level during a rifting-related subsidence event before 2.986 ± 0.009 Ma.

Indeed, southeastern Isla Ángel de la Guard records several rift-related events – ~3.9 Ma dikes, arc-related volcanism, a following rotation event which tilting beds, extension along the Ballenas Channel, and later faulting related to extension in the Northern Salsipuedes basin.

ACKNOWLEDGMENTS

Adriana Piña-Paez contributed to the petrographic analyses in this chapter, and assisted with making beads for XRF analysis. Scott Bennett helped with field work, sampling, field planning, and discussions. Field work permits were obtained by Prof. Arturo Martin-Barajas at Centro de Investigación Cientifífica y de Educación Superior de Ensenada (CICESE) through Secretaría de Gobernación and SEMARNAT. Funding was provided by NSF EAR-1728690. Madeline Lewis assisted mapping and sampling on one field excursion. Seulgi Moon, Nathan Brown, Justin Higa, and Marina Argueta (UCLA) were each part of 1-2 field excursions. Dr. Mark Stelten at the USGS did the final geochronology sample preparation and performed $^{40}Ar/^{39}Ar$ analyses.

REFERENCES CITED

Aragón-Arreola, M., and Martín-Barajas, A., 2007, Westward migration of extension in the northern Gulf of California, Mexico: Geology, v. 35, p. 571–574.

Bennett, S.E., Darin, M.H., Dorsey, R.J., Skinner, L.A., Umhoefer, P.J., and Oskin, M.E., 2016, Animated tectonic reconstruction of the Lower Colorado River region: Implications for Late Miocene to Present deformation, *in* Going LOCO: Investigations along the Lower Colorado River: California State University Desert Studies Center 2016 Desert Symposium Field Guide and Proceedings, p. 73–86.

Bowen, T., 2004, Archaeology, biology and conservation on islands in the Gulf of California: Environmental Conservation, v. 31, p. 199–206, doi:10.1017/S0376892904001419.

Brady, R.J., Wernicke, B.P., and Niemi, N.A., 2000, Reconstruction of Basin and Range extension and westward motion of the Sierra Nevada block: Great Basin and Sierra Nevada: Boulder, Colorado, Geological Society of America Field Guide, v. 2, p. 75–96.

Briqueu, L., Bougault, H., and Joron, J.L., 1984, Quantification of Nb, Ta, Ti and V anomalies in magmas associated with subduction zones: Petrogenetic implications: Earth and Planetary Science Letters, v. 68, p. 297–308, doi:10.1016/0012-821X(84)90161-4.

Castro, R.R., Stock, J.M., Hauksson, E., and Clayton, R.W., 2017, Active tectonics in the Gulf of California and seismicity (M> 3.0) for the period 2002–2014: Tectonophysics, v. 719, p. 4–16.

Cavazos Álvarez, J.A., 2015, Estratigrafía de la cuenca central de la Isla Ángel de la Guarda: evidencia del inicio de extensión en el Golfo de California [Tesis de maestría]: Centro de Investigación Científica y de Educación Superior de Ensenada, 99 p., http://cicese.repositorioinstitucional.mx/jspui/handle/1007/961.

Delgado Argote, L.A., 2000, Evolución tectónica y magmatismo Neógeno de la margen oriental de Baja California central [PhD Thesis]: Universidad Nacional Autónoma de México, 175 p.

Duyverman, H.J., Harris, N.B., and Hawkesworth, C.J., 1982, Crustal accretion in the Pan African: Nd and Sr isotope evidence from the Arabian Shield: Earth and Planetary Science Letters, v. 59, p. 315–326.

Fleck, R.J., Hagstrum, J.T., Calvert, A.T., Evarts, R.C., and Conrey, R.M., 2014, 40Ar/39Ar geochronology, paleomagnetism, and evolution of the Boring volcanic field, Oregon and Washington, USA: Geosphere, v. 10, p. 1283–1314.

Gastil, R.G., and Krummenacher, D., 1977, Reconnaissance geology of coastal Sonora between Puerto Lobos and Bahia Kino: Geological Society of America Bulletin, v. 88, p. 189–198.

Gastil, G., Krummenacher, D., and Minch, J., 1979, The record of Cenozoic volcanism around the Gulf of California: Geological Society of America Bulletin, v. 90, p. 839–857.

Gastil, R.G., Phillips, R.P., and Allison, E.C., 1975, Reconnaissance geology of the state of Baja California: Geological Society of America, v. 140.

Geist, E.L., Childs, J.R., and Scholl, D.W., 1988, The origin of summit basins of the Aleutian Ridge: Implications for block rotation of an arc massif: Tectonics, v. 7, p. 327–341.

González-Fernández, A., Dañobeitia, J.J., Delgado-Argote, L.A., Michaud, F., Córdoba, D., and Bartolomé, R., 2005, Mode of extension and rifting history of upper Tiburón and upper

Delfín basins, northern Gulf of California: Journal of Geophysical Research: Solid Earth, v. 110.

Janoušek, V., Farrow, C.M., and Erban, V., 2006, Interpretation of whole-rock geochemical data in igneous geochemistry: introducing Geochemical Data Toolkit (GCDkit): Journal of Petrology, v. 47, p. 1255–1259.

Janoušek, V., Farrow, C.M., Erban, V., and Trubač, J., 2011, Brand new Geochemical Data Toolkit (GCDkit 3.0)–is it worth upgrading and browsing documentation?(Yes!): Geologické vỳzkumy na Moravě a ve Slezsku, v. 18.

Johnson, K., Nissen, E., Saripalli, S., Arrowsmith, J.R., McGarey, P., Scharer, K., Williams, P., and Blisniuk, K., 2014, Rapid mapping of ultrafine fault zone topography with structure from motion: Geosphere, v. 10, p. 969–986, doi:10.1130/GES01017.1.

Leeder, M.R., and Jackson, J.A., 1993, The interaction between normal faulting and drainage in active extensional basins, with examples from the western United States and central Greece: Basin research, v. 5, p. 79–102.

Lewis, C.J., 1994, Constraints on extension in the Gulf extensional province from the Sierra San Fermín, northeastern Baja California, Mexico [PhD Thesis]: Harvard University.

Martín-Barajas, A., Stock, J.M., Layer, P., Hausback, B., Renne, P., and López-Martínez, M., 1995, Arc-rift transition volcanism in the Puertecitos Volcanic Province, northeastern Baja California, Mexico: GSA Bulletin, v. 107, p. 407–424, doi:10.1130/0016-7606(1995)107<0407:ARTVIT>2.3.CO;2.

Nagy, E.A., and Stock, J.M., 2000, Structural controls on the continent-ocean transition in the northern Gulf of California: Journal of Geophysical Research: Solid Earth, v. 105, p. 16251–16269.

Pearce, J.A., 1983, Role of the sub-continental lithosphere in magma genesis at active continental margins:

Persaud, P., Stock, J.M., Steckler, M.S., Martín-Barajas, A., Diebold, J.B., González-Fernández, A., and Mountain, G.S., 2003, Active deformation and shallow structure of the Wagner, Consag, and Delfin basins, northern Gulf of California, Mexico: Journal of Geophysical Research: Solid Earth, v. 108.

Planet Team, 2017, Planet application program interface: In space for life on Earth: San Francisco, CA, www.planet.com.

Proffett Jr, J.M., 1977, Cenozoic geology of the Yerington district, Nevada, and implications for the nature and origin of Basin and Range faulting: Geological Society of America Bulletin, v. 88, p. 247–266.

Schmidt, E.K., 1975, Plate tectonics, volcanic petrology, and ore formation in the Santa Rosalía area, Baja California, Mexico: Tucson AZ, University of Arizona [PhD Thesis]: M. Sc. thesis.

Seiler, C., Fletcher, J.M., Quigley, M.C., Gleadow, A.J., and Kohn, B.P., 2010, Neogene structural evolution of the Sierra San Felipe, Baja California: Evidence for proto-gulf transtension in the Gulf Extensional Province? Tectonophysics, v. 488, p. 87–109.

Seiler, C., Gleadow, A.J., Fletcher, J.M., and Kohn, B.P., 2009, Thermal evolution of a sheared continental margin: Insights from the Ballenas transform in Baja California, Mexico: Earth and Planetary Science Letters, v. 285, p. 61–74.

Stock, J.M., 2000, Relation of the Puertecitos Volcanic Province, Baja California, Mexico, to development of the plate boundary in the Gulf of California: Special Papers-Geological Society of America, p. 143–156.

Stock, J.M., 1989, Sequence and geochronology of Miocene rocks adjacent to the main gulf escarpment: Southern Valle Chico, Baja California Norte, Mexico: Geofísica Internacional, v. 28.

Sun, S.-S., and McDonough, W.F., 1989a, Chemical and isotopic systematics of oceanic basalts: implications for mantle composition and processes: Geological Society, London, Special Publications, v. 42, p. 313–345.

Sun, S.-S., and McDonough, W.F., 1989b, Chemical and isotopic systematics of oceanic basalts: implications for mantle composition and processes: Geological Society, London, Special Publications, v. 42, p. 313–345.

Taylor, S.R., and McLennan, S.M., 1995, The geochemical evolution of the continental crust: Reviews of Geophysics, v. 33, p. 241–265, doi:10.1029/95RG00262.

Thompson, R.N., Dickin, A.P., Gibson, I.L., and Morrison, M.A., 1982, Elemental fingerprints of isotopic contamination of hebridean Palaeocene mantle-derived magmas by archaean sial: Contributions to Mineralogy and Petrology, v. 79, p. 159–168, doi:10.1007/BF01132885.

Wernicke, B., and Burchfiel, B.C., 1982, Modes of extensional tectonics: Journal of Structural Geology, v. 4, p. 105–115.

FIGURES

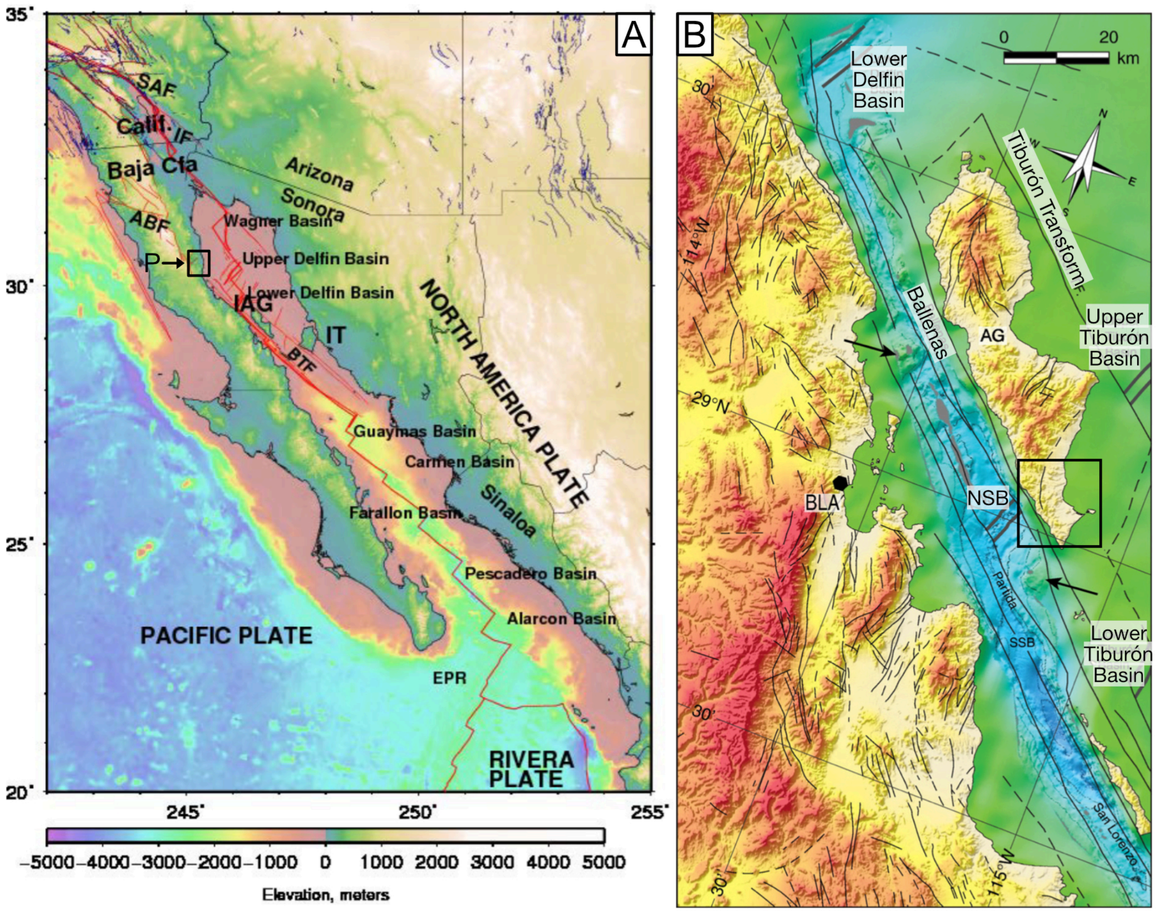

Figure 1: Regional maps showing Isla Ángel de la Guarda in the Gulf of California

(A) Plate boundary fault systems (red lines) showing extensional regime in the Gulf of California. IAG - Isla Ángel de la Guarda; IT - Isla Tiburón; P – Puertecitos (extent of Figure 3a); EPR - East Pacific Rise; ABF - Agua Blanca Fault; BTF - Ballenas Transform Fault; SAF - San Andreas Fault. (B) Minimally adapted Fig. 2B in Seiler et al. (2009). NSB - Northern Salsipuedes Basin; BLA - Bahía de los Ángeles. Black rectangle indicates extent of Google Earth imagery in Figure 2B.

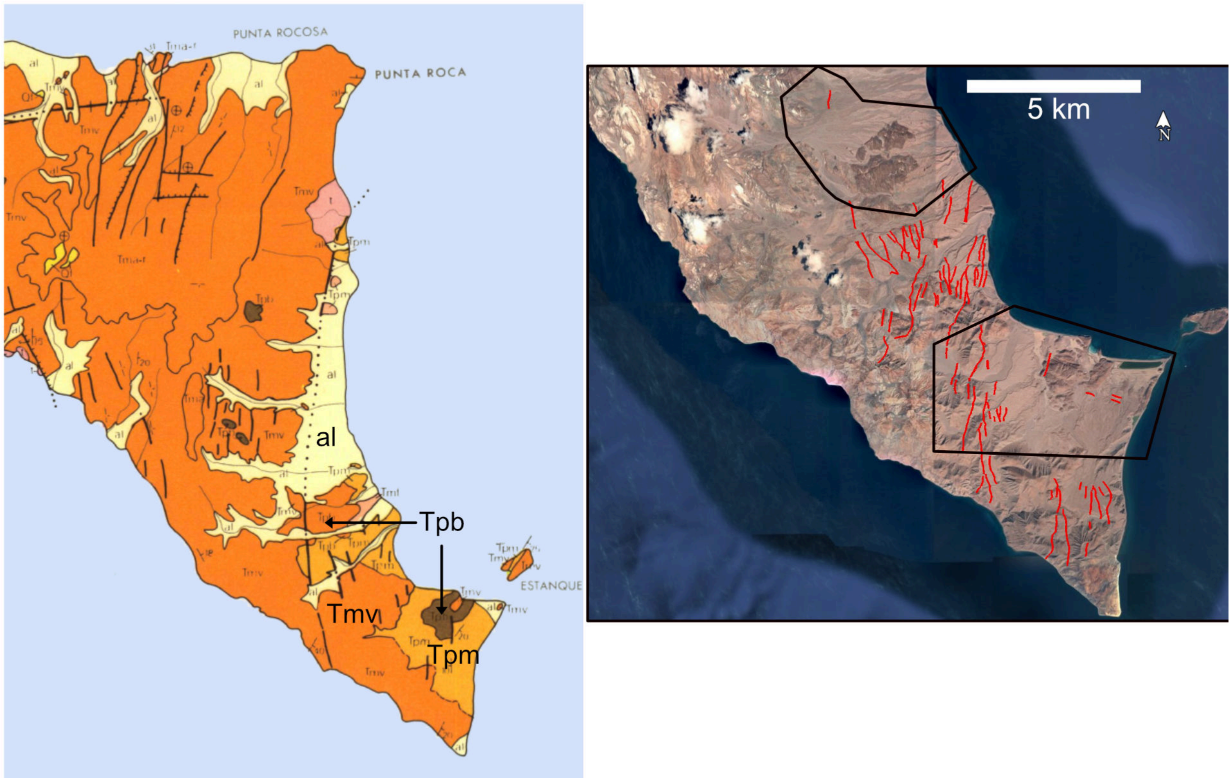

Figure 2: Maps showing previous work and this study area

Previous mapping in our field area. (A) Section of southern Isla Ángel de la Guarda from Gastil (1975, Plate 1-C). Tmv – Miocene volcanic rocks; Tpm – Pliocene marine sedimentary rocks; Tpb - Pliocene basalt; al - alluvium. Note that the left-pointing arrow of Tpb has a misidentified unit, and should be brown. (B) Google earth imagery showing fault array (red lines) and extent of mapping presented here (black outlines). Note the dark volcanic units in contrast with lighter alluvium and terraces within our field areas. These terraces and beaches make boat access feasible on the east side of the island.

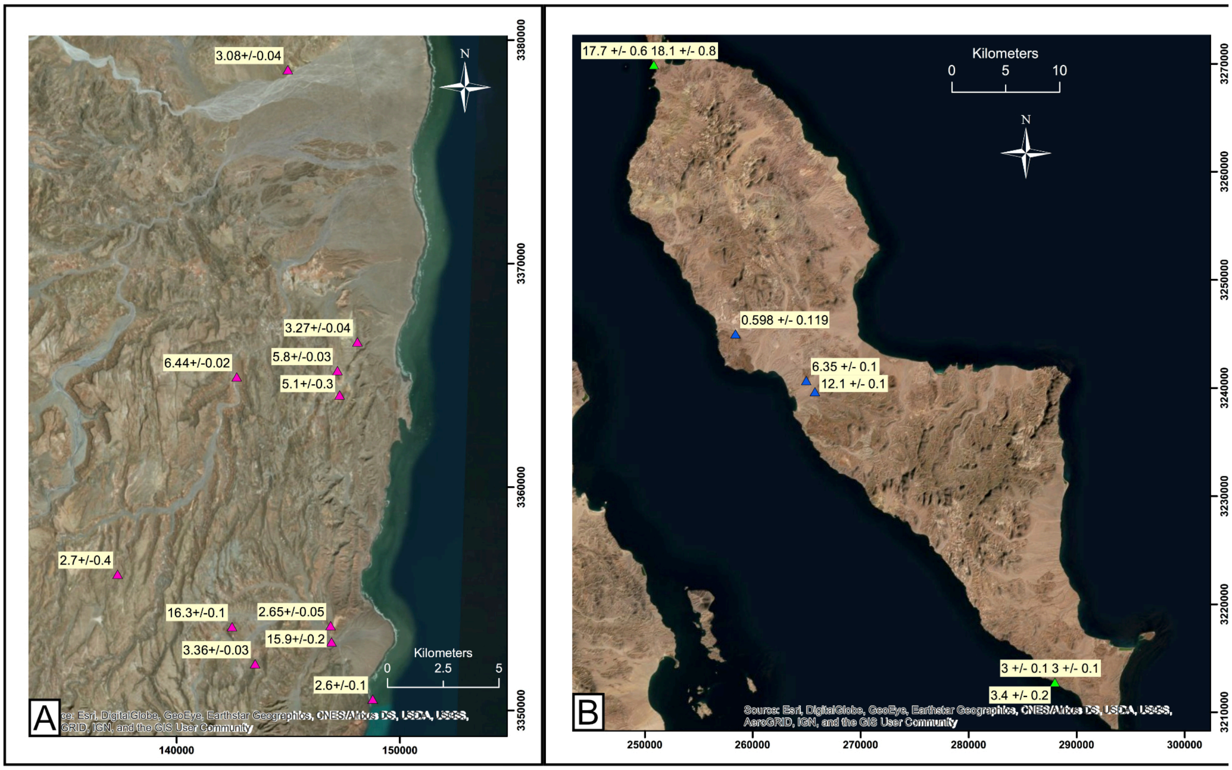

Figure 3: Maps showing nearby ages of volcanic rocks

Ages of volcanic rocks in Ma reported in the surrounding area. (A) 11 similar or related units in Puertecitos in pink (Martín-Barajas et al., 1995); (B) four ages at two locations on either end of IAG in green (Delgado Argote, 2000) and three ages on central IAG in blue (Cavazos Álvarez, 2015).

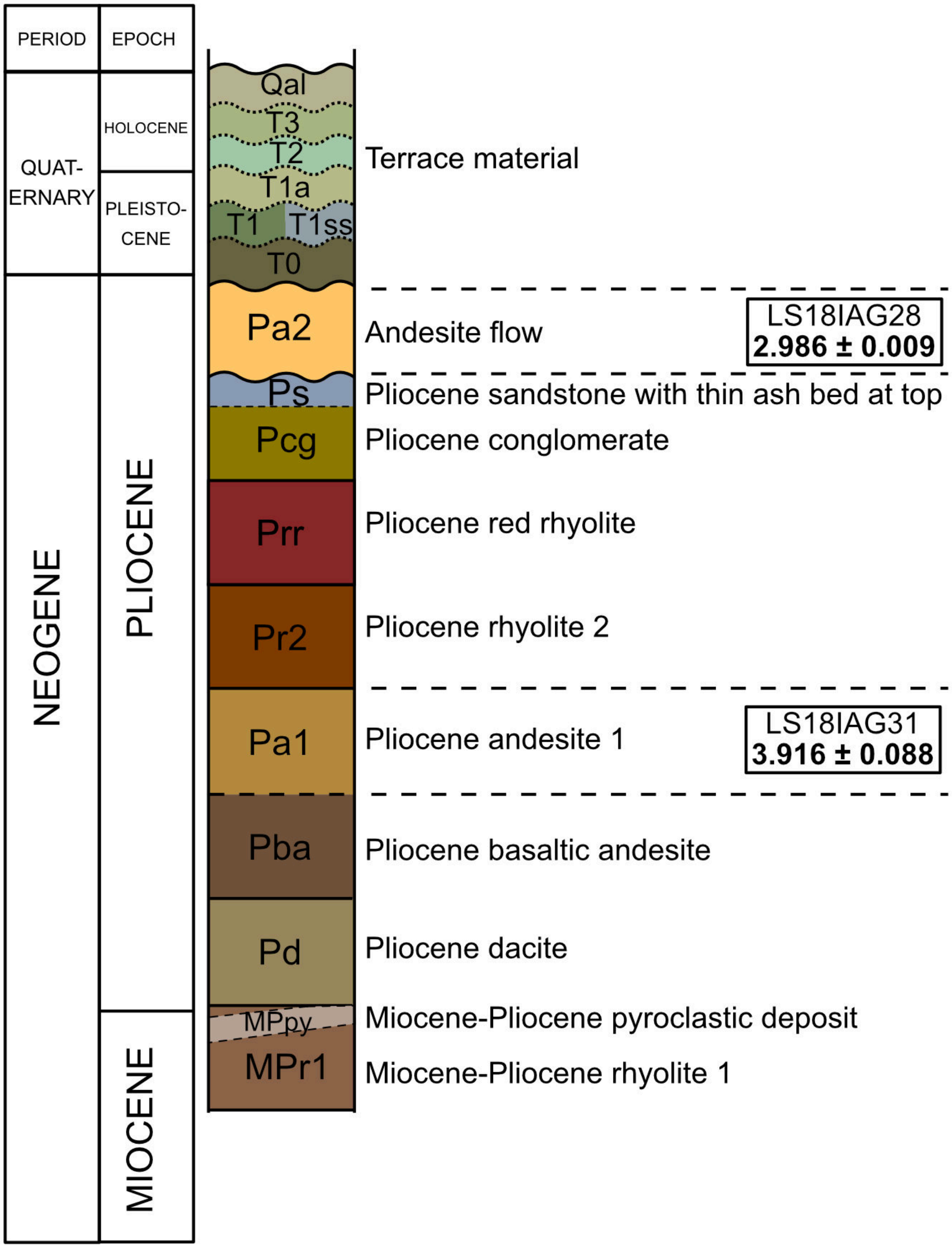

Figure 4: Stratigraphic column for northern field area

Stratigraphic column matching geologic map of the northern field area (Figure 6). Samples shown in boxes have ages from 40Ar/39Ar reported in this study.

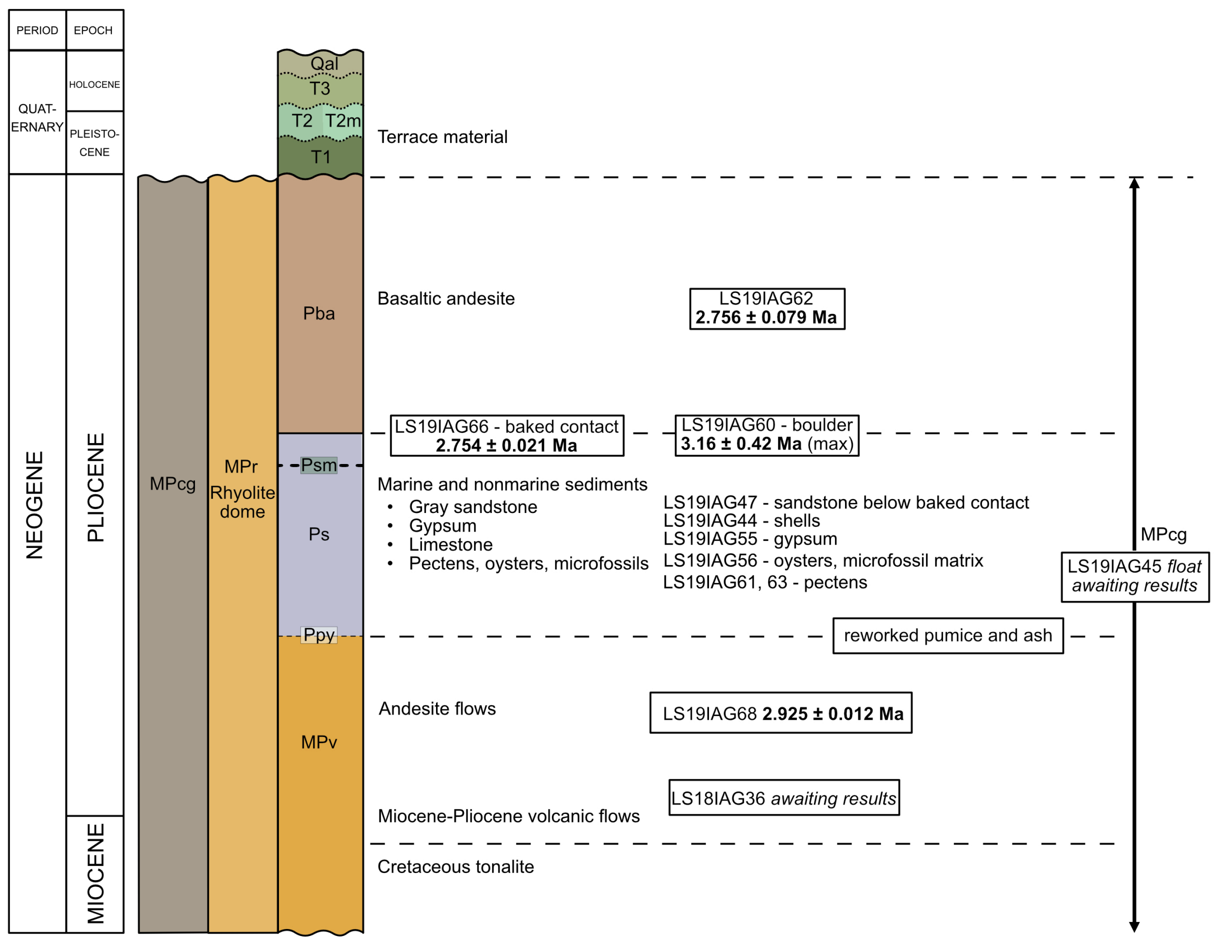

Figure 5: Stratigraphic column for southern field area

Stratigraphic column matching geologic map for southern field area (Figure 7). Samples shown in boxes have ages from 40Ar/39Ar reported in this study. Miocene and Pliocene sedimentary units (MPcg, Ppy, Ps, Psm) are discussed in further detail in Chapter 3.

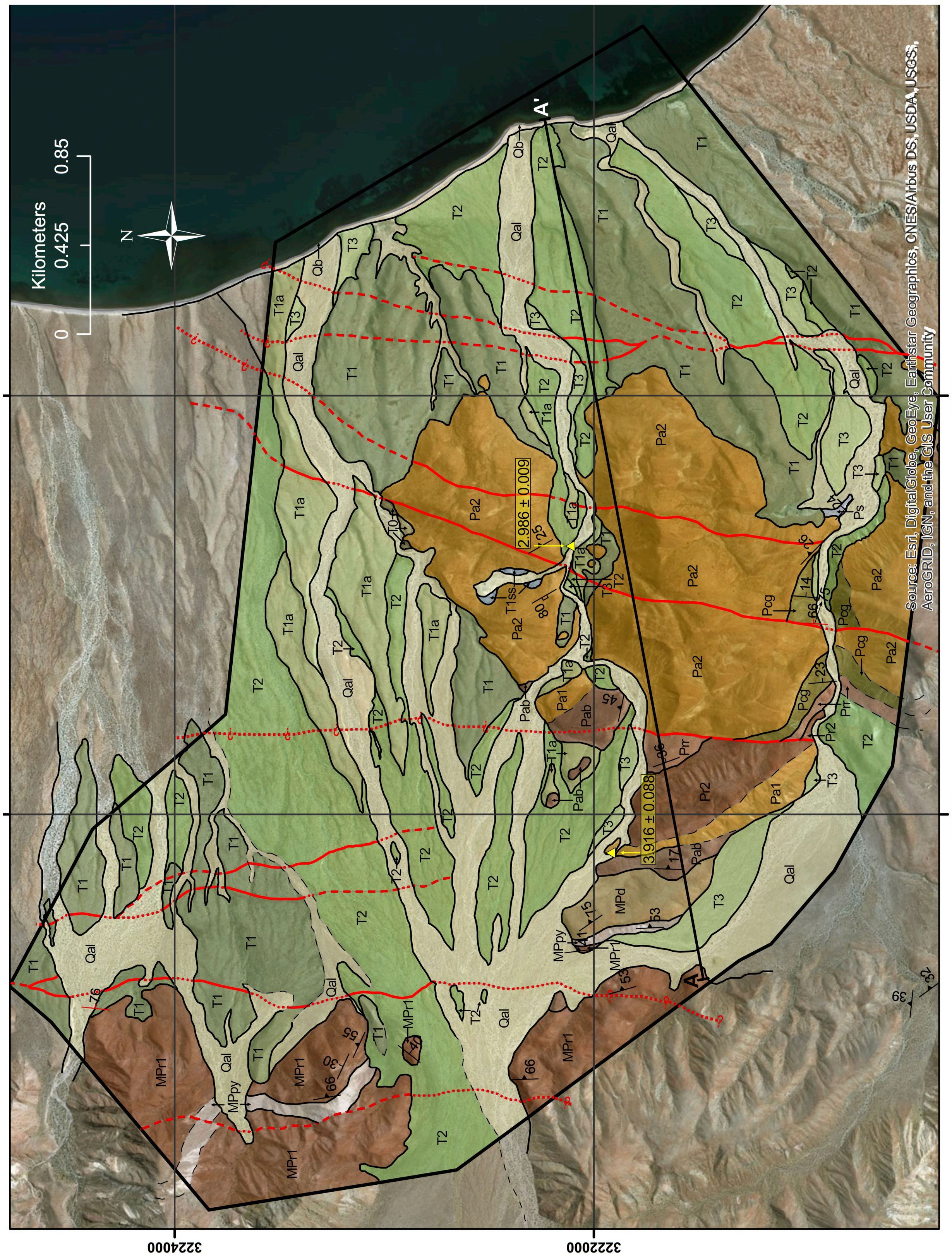

Kilometers
0
0.425
0.85
N
A'
A
2.986 ± 0.009
3.916 ± 0.088
Qal
Qb
T1
T1a
T1ss
T2
T3
Pa1
Pa2
Pab
Pcg
Prr
Pr2
Ps
MPd
MPpy
MPr1
3224000
3222000
286000
288000
Source: Esri, DigitalGlobe, GeoEye, Earthstar Geographics, CNES/Airbus DS, USDA, USGS, AeroGRID, IGN, and the GIS User Community

Figure 6: Geologic map of northern field area

Geologic map of northern field area. Stratigraphic relationships are depicted in Figure 4, and units are described in detail in text. Line A–A' denotes line of cross-section in Figure 19. A blow-up of this map is included in Supplemental Figure S2.

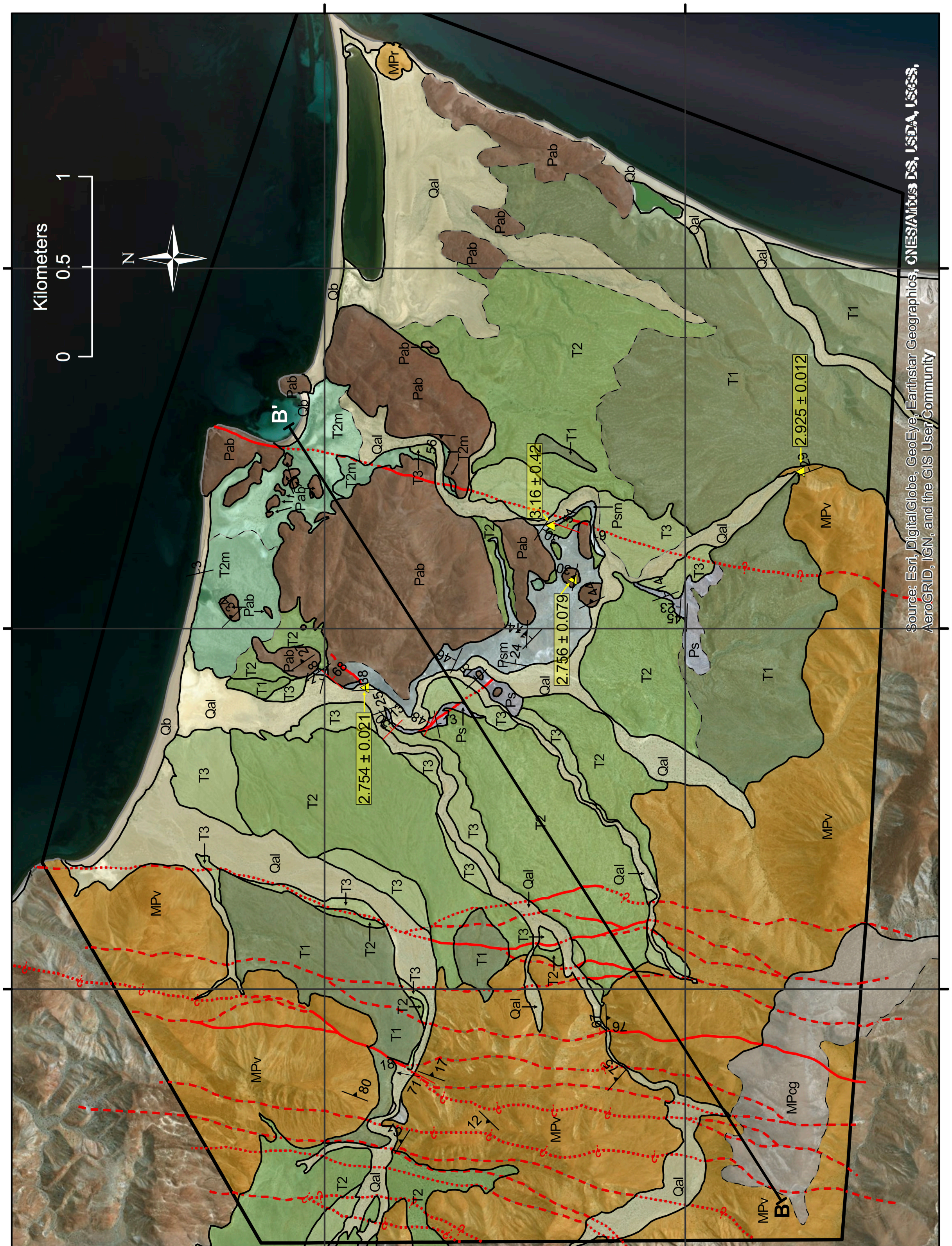
Kilometers
0
0.5
1
N
B
B'
3216000
3214000
290000
292000
294000
MPv
MPcg
MPr
Pab
Psm
Ps
T1
T2
T2m
T3
Qal
Qb
2.754 ± 0.021
2.756 ± 0.079
3.16 ± 0.42
2.925 ± 0.012
Source: Esri, DigitalGlobe, GeoEye, Earthstar Geographics, CNES/Airbus DS, USDA, USGS, AeroGRID, IGN, and the GIS User Community

Figure 7: Geologic map of northern field area

Geologic map of southern field area. Units and geochronology are discussed in text and Chapter 3. A blow-up of this map is included in Supplemental Figure S3.

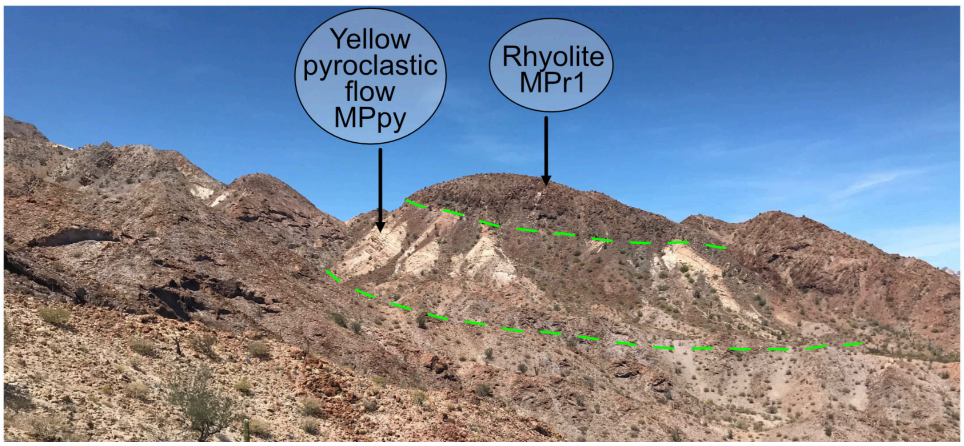

Figure 8: Field photographs from the northern study area

(8a) View facing north of Miocene-Pliocene yellow pyroclastic flow (MPpy), here interbedded with Miocene-Pliocene rhyolite (MPr1). Green dashed lines approximate contact of pyroclastic flow with rhyolite.

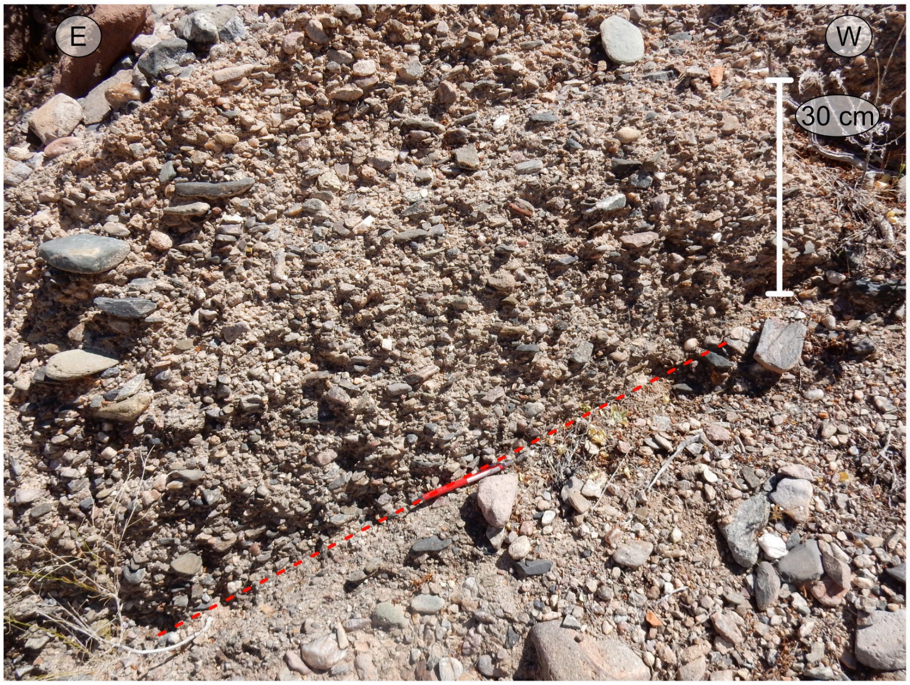

(8b) South-facing photograph of Pliocene conglomerate. Imbrication of clasts, highlighted by red dashed line, indicates flow to the east. Clasts are mostly 2 cm and ≤ 5 cm across.

(8c) North-facing view of Pliocene sandstone. Bedding dips ~24° E. This outcrop has ~5 m of stratigraphy, and there is about 20 m total. Here, Ps is overlain by terrace material.

(8d) A close-up view of the Pliocene sandstone, showing ~5 cm bedding within the unit. Bedding is parallel to the red pencil.

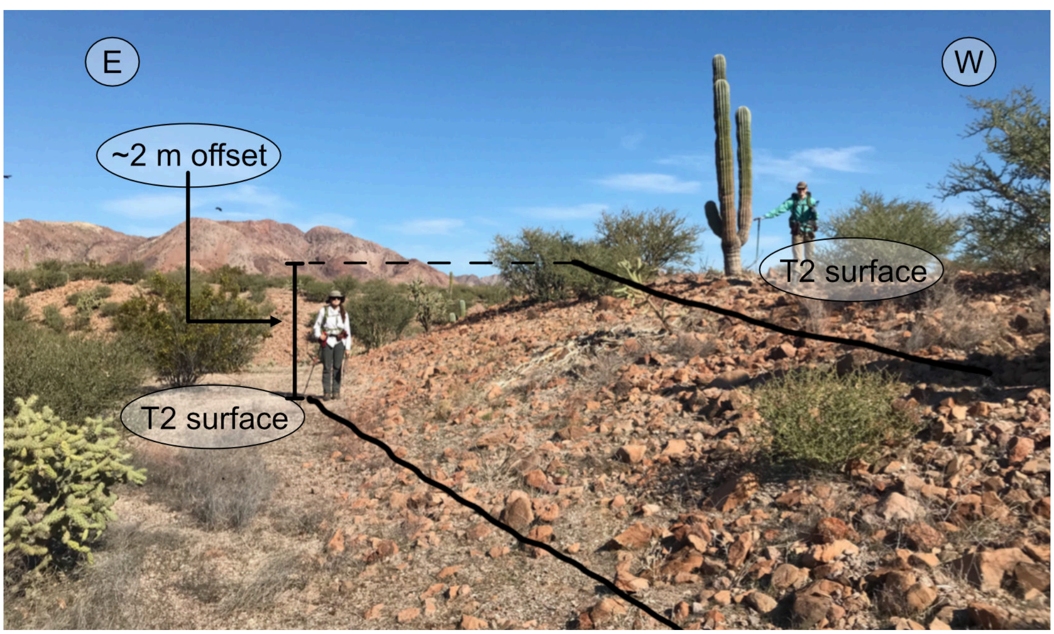

(8e) A view facing north, showing 2 m of vertical separation along a fault, with the east side going down. Not shown in this photo is a T1-T2 terrace riser with 12.2 m of right-lateral horizontal separation, measured by pacing.

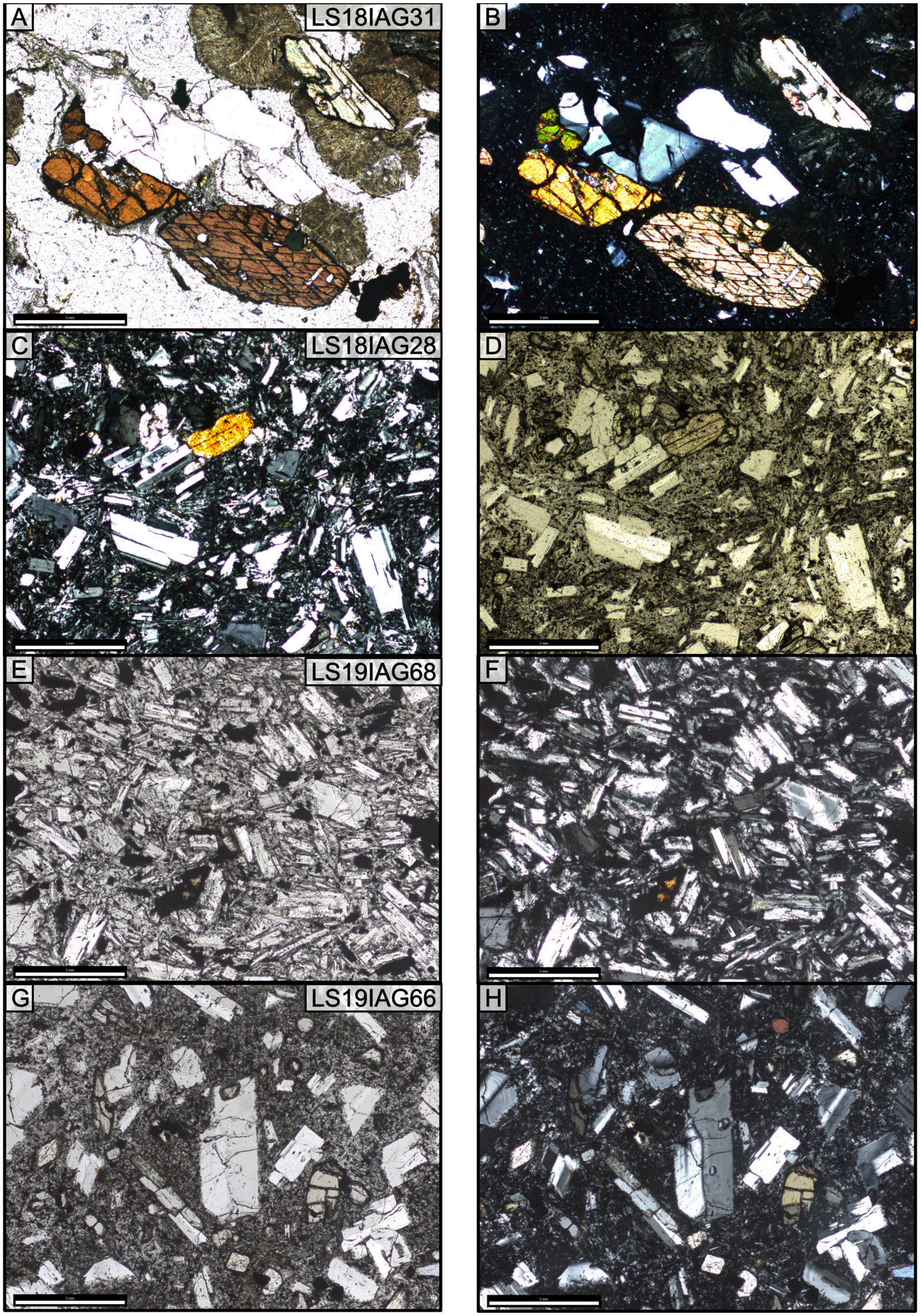
A
LS18IAG31
B
C
LS18IAG28
D
E
LS19IAG68
F
G
LS19IAG66
H

Figure 9: Representative photomicrographs

Representative photomicrographs from four samples in the northern and southern study areas taken at 5x magnification. All white scale bars are 5mm. Sample names are included on left side, plain polarized light photomicrographs. Right side is cross-polarized light. Photomicrographs are from units Pa1 (a, b), Pa2 (c, d), MPv (e, f), and Pab (g, h).

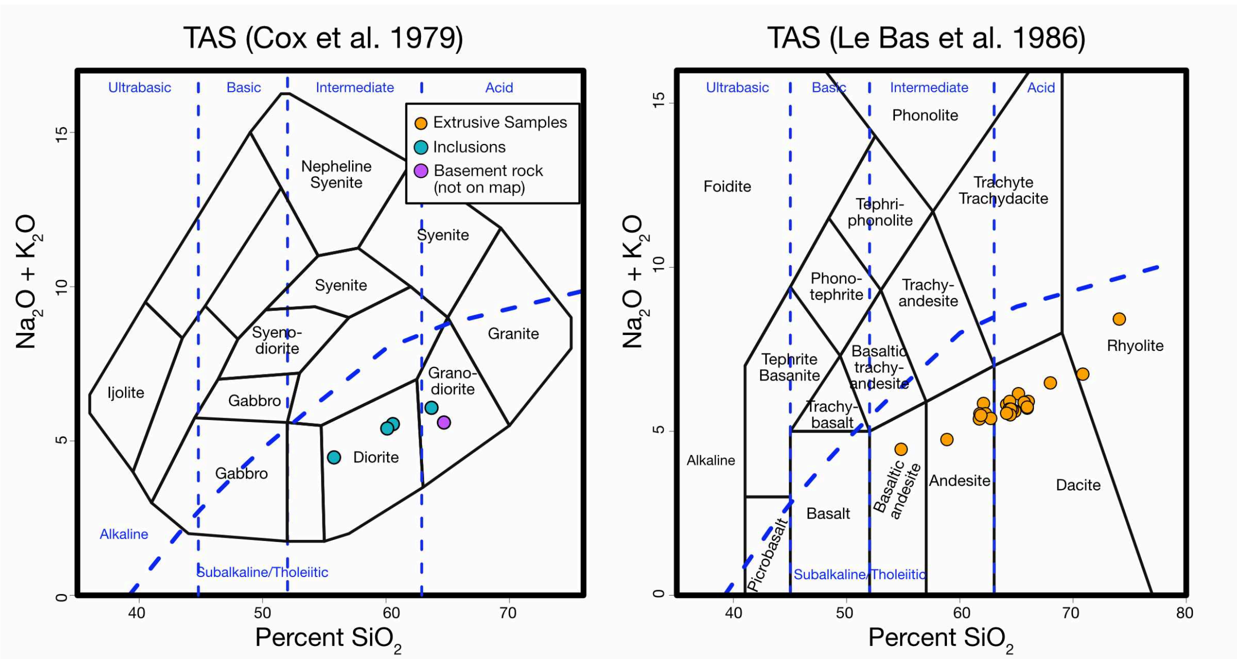

Figure 10: Total alkali versus silica diagrams

Total alkali versus silica plots for all 32 samples. On the left is a sample of basement rock (purple), classified as granodiorite, and four xenoliths (aqua): two granitic and two mafic, likely autoliths. The granitic xenoliths include a granodiorite and a diorite, and the two mafic inclusions are both diorite. On the right are all 27 extrusive lava flows. Lavas mostly range from andesite to dacite.

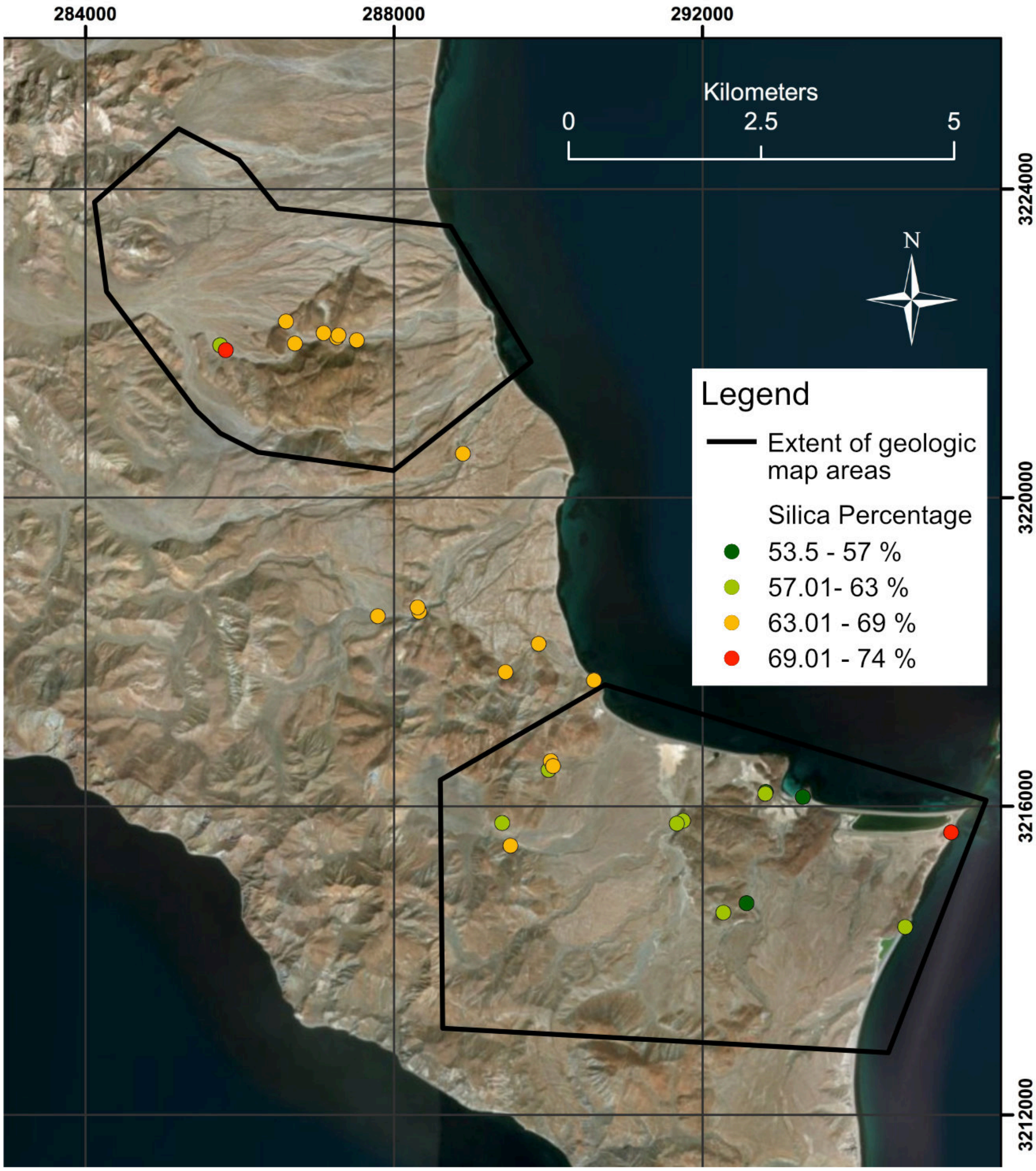

Figure 11: Map showing silica percentages across field area

Map showing silica percentage of samples as colored circles. Black lines show outline of northern and southern map areas. The eastern-most sample is from MPr, the rhyolite dome in the southern map area.

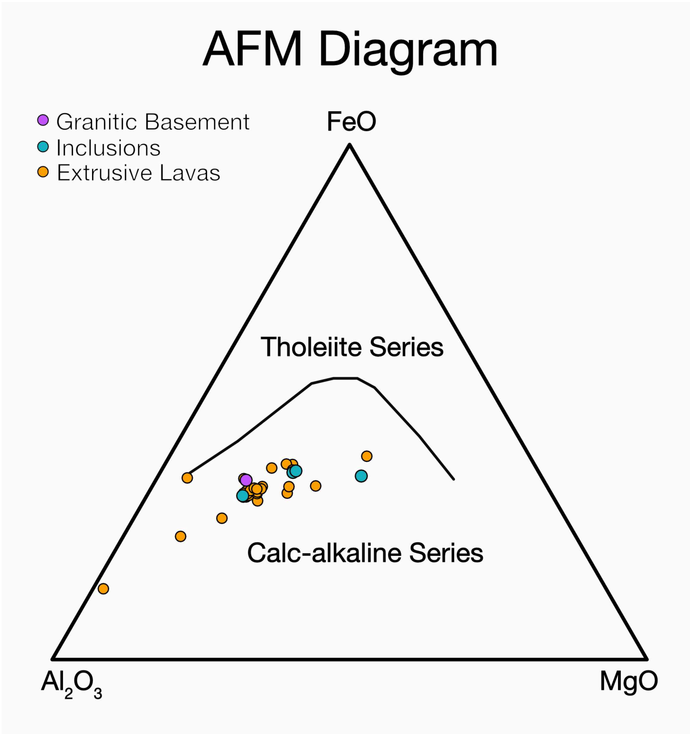

Figure 12: AlO_2 – FeO – MgO ternary diagram

AlO_2 – FeO – MgO ternary diagram includes all xenoliths, basement rock, and lavas analyzed by XRF in this study. Our samples all follow a calc-alkaline trend.

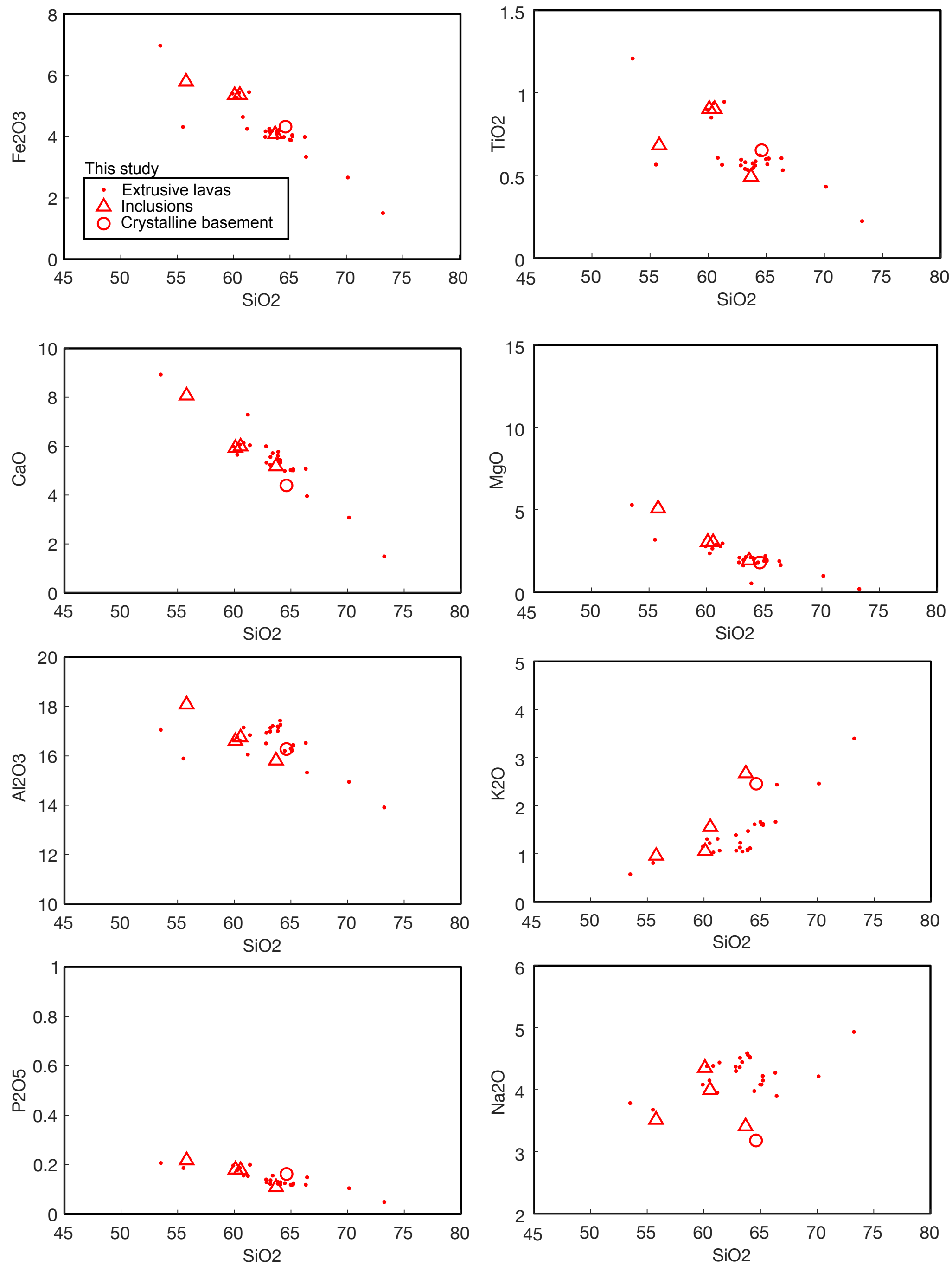

Figure 13: Major element data from XRF analysis

Harker diagrams with major element data from XRF analysis. Data from this study in red: lavas are shown as dots, xenoliths shown as hollow triangles, and basement rock shown as open circle. Results are discussed in text.

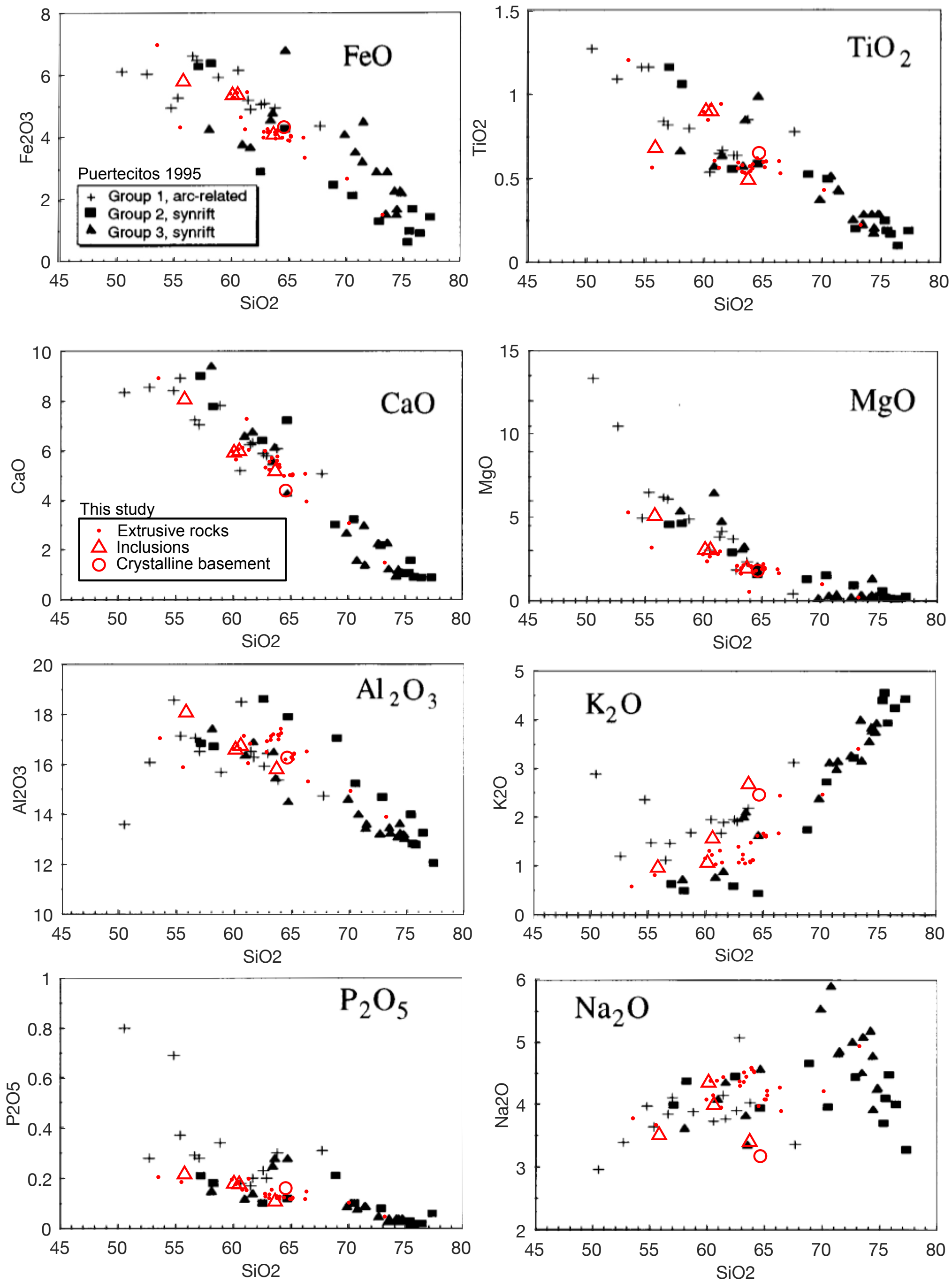

Figure 14: Major element data compared to Puertecitos Volcanic Province

Geochemical data for major oxides versus silica from Puertecitos Volcanic Province (Martín-Barajas et al., 1995) compared with our data (red). Puertecitos samples, in black, are marked as follows: Group 1, arc-related rocks are plus signs, Group 2, synrift rocks are solid squares, and Group 3 synrift rocks are solid triangles. Comparison is discussed in text.

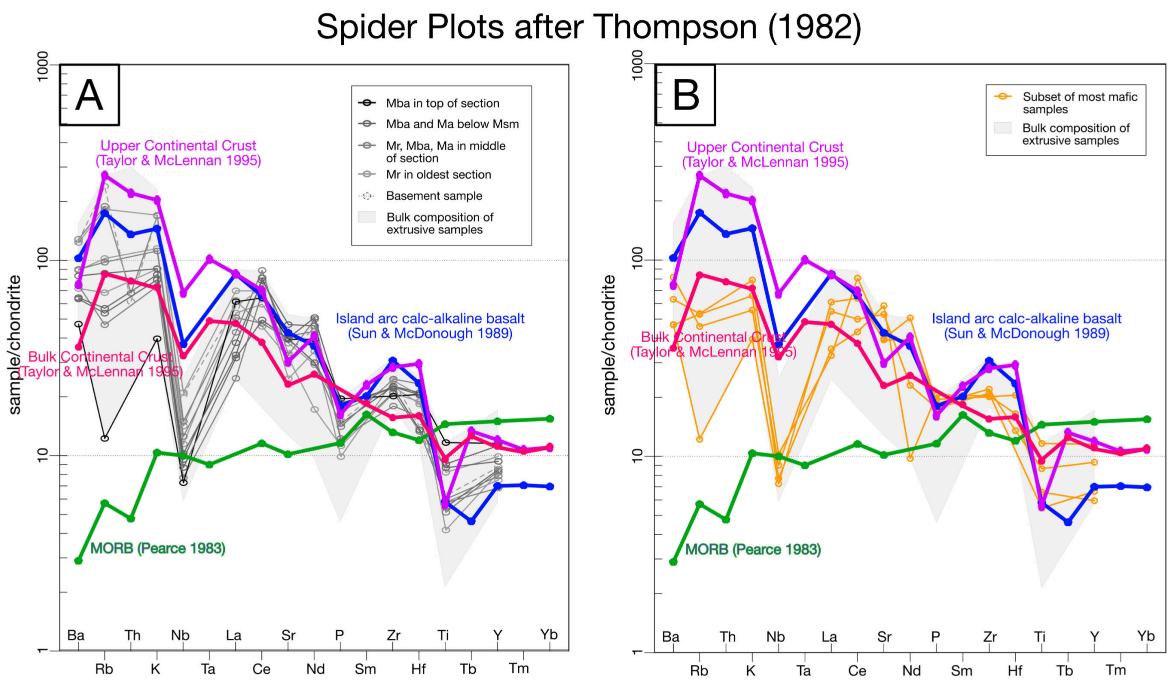

Figure 15: Trace element spider diagrams

Spider plots after Thompson (1982) showing bulk sample composition in grey background, and a subset of samples greyed by stratigraphic level in this study (a). Black line is unit Pba, and lighter greys are older, based on our stratigraphic interpretation. The dashed grey line is from crystalline basement rock outside our study area. Samples generally fit an upper or bulk continental crust, as described by Taylor and McLennan (1995), rather than an island arc calc-alkaline basalt (Sun and McDonough, 1989b) or a mid-oceanic ridge basalt (Pearce, 1983). We display the most mafic subset of lavas normalized to chondrites (b). These lavas best align with the bulk continental crust described by Taylor and McLennan (1995).

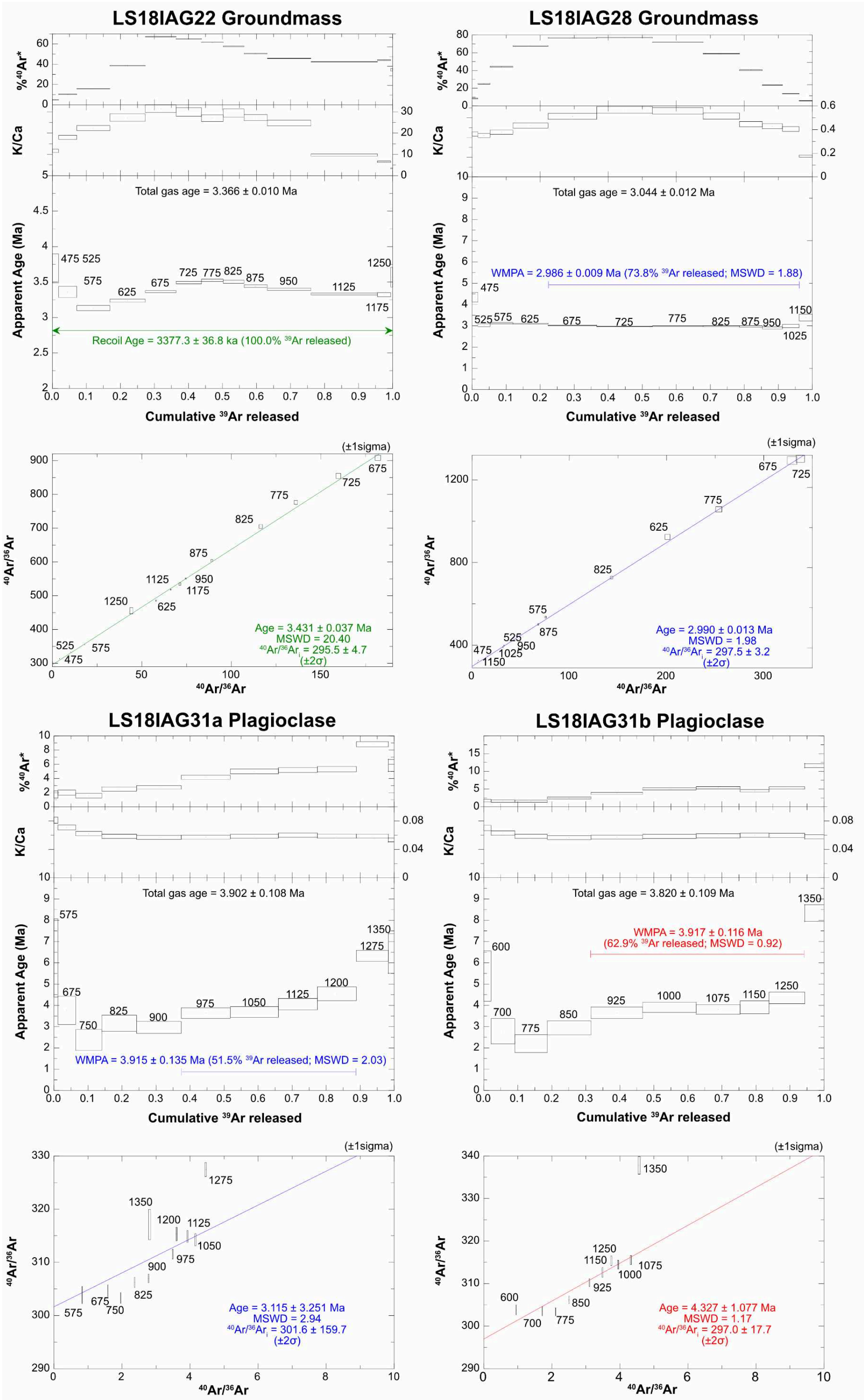
LS18IAG22 Groundmass
%40Ar*
K/Ca
Apparent Age (Ma)
Total gas age = 3.366 ± 0.010 Ma
Recoil Age = 3377.3 ± 36.8 ka (100.0% 39Ar released)
Cumulative 39Ar released
(±1sigma)
40Ar/36Ar
Age = 3.431 ± 0.037 Ma
MSWD = 20.40
40Ar/36Ari = 295.5 ± 4.7
(±2σ)
LS18IAG28 Groundmass
Total gas age = 3.044 ± 0.012 Ma
WMPA = 2.986 ± 0.009 Ma (73.8% 39Ar released; MSWD = 1.88)
Age = 2.990 ± 0.013 Ma
MSWD = 1.98
40Ar/36Ari = 297.5 ± 3.2
(±2σ)
LS18IAG31a Plagioclase
Total gas age = 3.902 ± 0.108 Ma
WMPA = 3.915 ± 0.135 Ma (51.5% 39Ar released; MSWD = 2.03)
Age = 3.115 ± 3.251 Ma
MSWD = 2.94
40Ar/36Ari = 301.6 ± 159.7
(±2σ)
LS18IAG31b Plagioclase
Total gas age = 3.820 ± 0.109 Ma
WMPA = 3.917 ± 0.116 Ma
(62.9% 39Ar released; MSWD = 0.92)
Age = 4.327 ± 1.077 Ma
MSWD = 1.17
40Ar/36Ari = 297.0 ± 17.7
(±2σ)

Figure 16: $^{40}Ar/^{39}Ar$ age spectra diagrams and isochron plots

$^{40}Ar/^{39}Ar$ age spectra diagrams and isochron plots for samples in the northern study area and LS18IAG22, a dike ~20 km north of the northern study area. $^{40}Ar/^{39}Ar$ data for samples in the southern area, which constrain the age of marine sequence, are reported in Chapter 3.

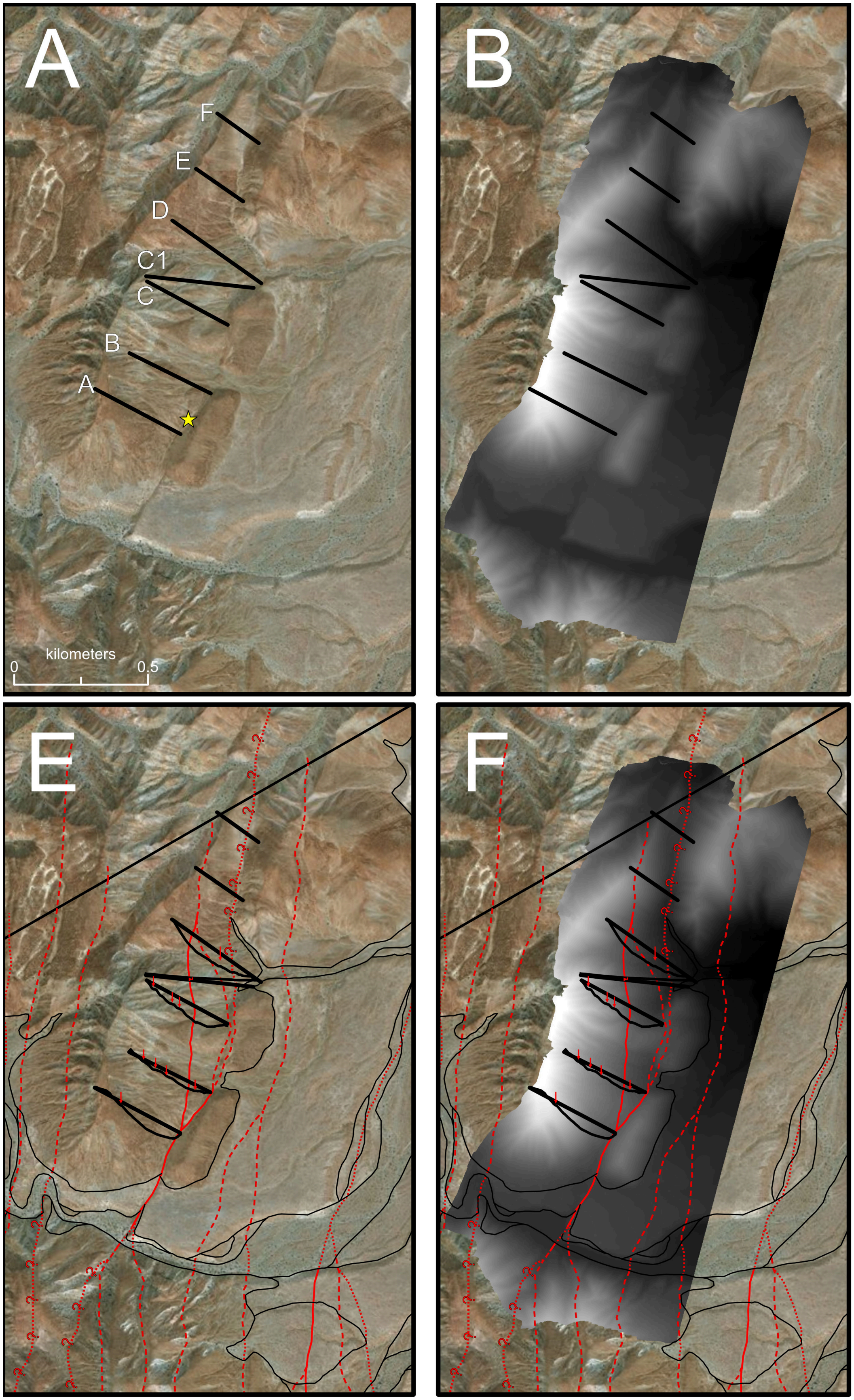
A
F
E
D
C1
C
B
A
0
kilometers
0.5
B
E
F

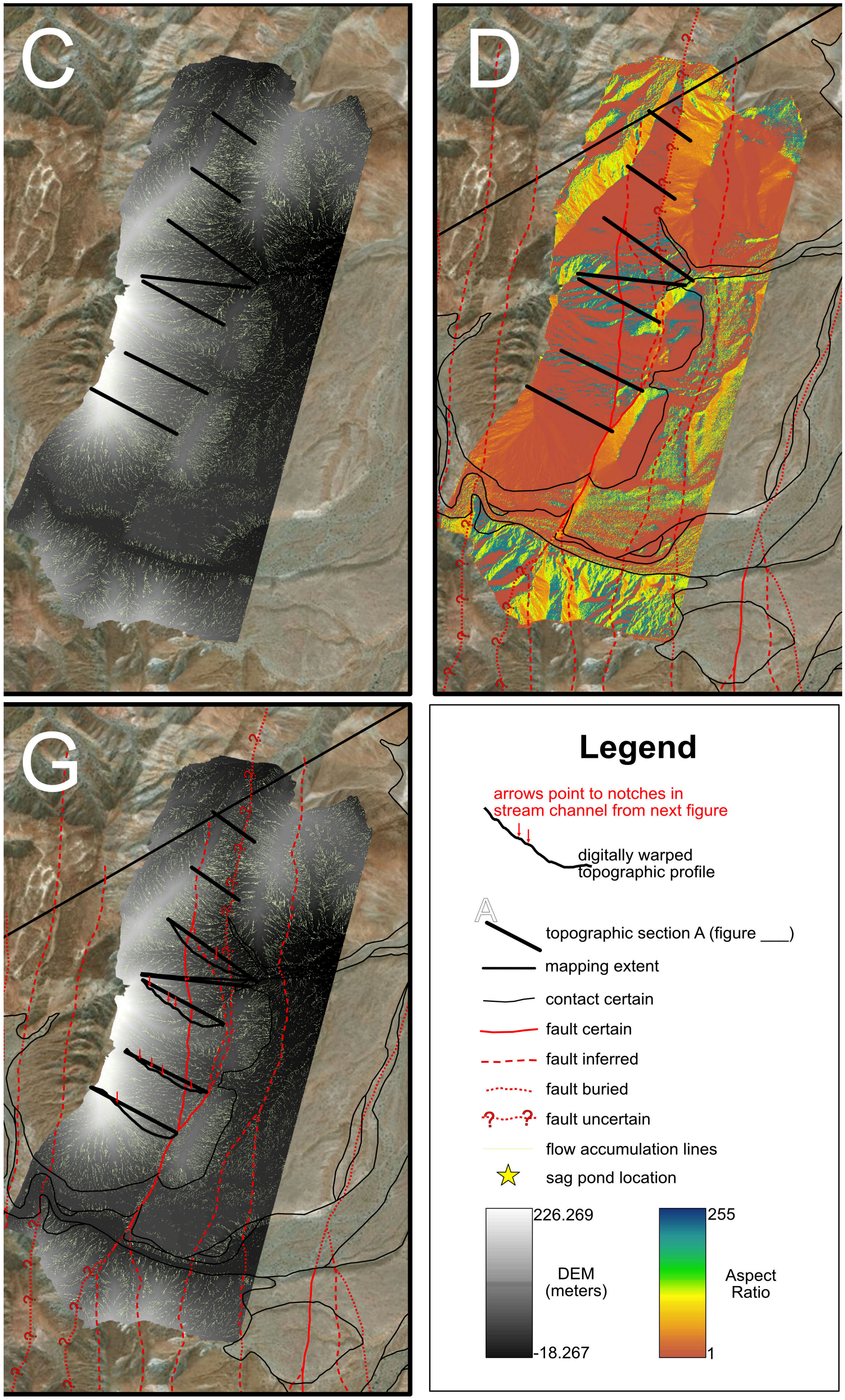
C
D
G
Legend
arrows point to notches in stream channel from next figure
digitally warped topographic profile
A
topographic section A (figure ___)
mapping extent
contact certain
fault certain
fault inferred
fault buried
fault uncertain
flow accumulation lines
sag pond location
226.269
DEM (meters)
-18.267
255
Aspect Ratio
1

Figure 17: Representative structure-from-motion from drone

An example of results from structure-from-motion using drone imagery overlain on background imagery from ArcGIS (GeoEye). (A) imagery alone with topographic profiles A through F from Figure 18; (B) DEM from drone imagery with a ≤5 cm accuracy; (C) flow accumulation shown over DEM in lime green lines; (D) aspect ratio map with mapped contacts and mapping extent shown. Yellow star shows location of sag pond. Contacts are shown in (E), (F), (G) with same data as subfigure above for contextual view. Solid black lines are contacts, red lines are faults, and are only shown on some diagrams for clarity.

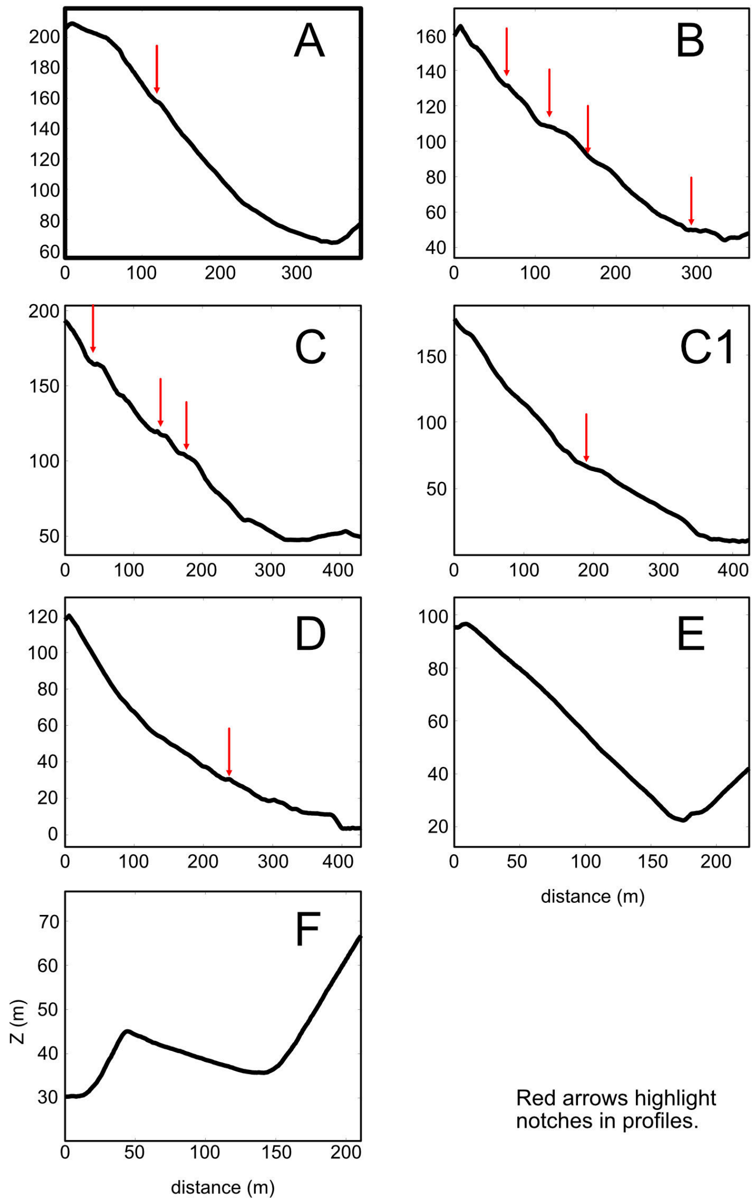

Figure 18: Topographic profiles using DEM from Fig. 17

Topographic profiles along sections A through F, shown in Figure 17. Red arrows highlight some notches in the profiles, indicating drainages or faults (or both). Profile C1 is at a higher angle to major faults, but notches are more obvious on the other profiles, which all run ~75° to the fault traces.

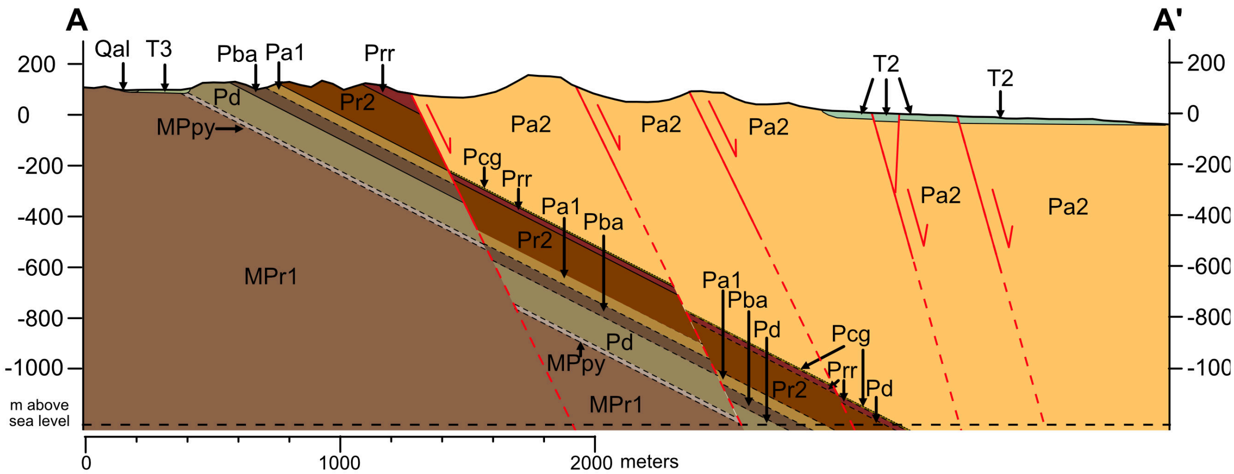

Figure 19: Cross-section along A-A' from northern area

Cross-section along line A-A' from geologic map in Figure 6. Slip on the westernmost fault is calculated from extended strike of outcrop patterns of Prr in a southern arroyo.

Table 1: Collected samples from Isla Angel de la Guarda, metadata, and analyses

Sample	Date collected	Latitude (°N)	Longitude (°E)	Unit	Field Classification	XRF	$^{40}Ar/^{39}Ar$ geochronology	Thin Section
JMS18IAG01	23-Apr-18	29.053624	-113.138877	Pab	basaltic lava	X		X*
JMS18IAG02	23-Apr-18	29.056331	-113.128877	Pab	lava			X*
JMS18IAG03	24-Apr-18	29.109110	-113.183526	Pa2	mafic lava	X		X*
JMS18IAG04	24-Apr-18	29.109426	-113.186216	Pa2	andesite	X		X*
JMS18IAG05	24-Apr-18	29.109926	-113.187977	Pa2	andesite	X		X*
JMS18IAG06	24-Apr-18	29.109233	-113.190528	Pa2	andesite			X*
JMS18IAG07	24-Apr-18	29.108603	-113.191781	Pa2	andesite	X		X*
JMS18IAG08	24-Apr-18	29.108716	-113.183995	n/a	fault material			
JMS18IAG09	25-Apr-18	29.074015	-113.158571	MPv	andesite	X		X*
JMS18IAG10	25-Apr-18	29.070659	-113.162938	MPv	andesite	X		X*
JMS18IAG11	25-Apr-18	29.068929	-113.166048	MPv	pyroclastic breccia and scoria			X*
JMS18IAG12	26-Apr-18	29.059267	-113.156906	MPv	andesite	X		X*
JMS18IAG13	26-Apr-18	29.060357	-113.156622	MPv	andesite	X		X*
JMS18IAG14	26-Apr-18	29.059759	-113.156382	MPv	granitic inclusion in lithic breccia	X		X*
JMS18IAG15A	26-Apr-18	29.041667	-113.109079	Pab	volcanic breccia clast, possibly autolith	X		X*
JMS18IAG15B	26-Apr-18	29.041667	-113.109079	Pab	volcanic breccia clast, possibly autolith	X		X*
JMS18IAG16	26-Apr-18	29.052814	-113.103160	MPr	foliated andesite	X		X*
JMS18IAG17	26-Apr-18	29.056671	-113.123007	Pa	andesite	X		X*
JMS18IAG17i	26-Apr-18	29.056671	-113.123007	Pa	mafic inclusion	X		X*
JMS18IAG18	26-Apr-18	29.057152	-113.127969	Pa	andesite	X		X*
JMS18IAG19	26-Apr-18	29.069887	-113.151125	MPv	basalt	X		X*
JMS18IAG20	28-Apr-18	29.056700	-113.129575	T2s	coquina			
JMS18IAG21	28-Apr-18	29.055288	-113.129892	T2s	coquina			
LS17IAG01	31-Oct-17	29.048491	-113.144109	Pba	basaltic andesite			
LS17IAG02	1-Nov-17	29.076893	-113.18004	MPv	basaltic andesite	X		X*
LS17IAG03	2-Nov-17	29.077544	-113.174568	MPv	basaltic andesite	X		X*
LS17IAG04	2-Nov-17	29.078013	-113.17478	MPv	basaltic andesite	X		X*
LS17IAG05	5-Nov-17	29.092492	-113.179511	Pa2	basaltic andesite			X*
LS17IAG06	5-Nov-17	29.092837	-113.176419	Pa2	basaltic andesite			X*
LS17IAG07	5-Nov-17	29.096133	-113.169125	Pa2	basaltic andesite	X		X*
LS18IAG22	18-Nov-18	29.279499	-113.168999	n/a	dike	X	X	X
LS18IAG23	18-Nov-18	29.278099	-113.167000	n/a	dike	X		X
LS18IAG24	18-Nov-18	29.283199	-113.268997	n/a	rhyolite (Martin-Barajas Mrb)			X
LS18IAG25	18-Nov-18	29.267201	-113.257004	n/a	rhyolite (Martin-Barajas Mrc)	X		X
LS18IAG26	18-Nov-18	29.274200	-113.248001	n/a	rhyolite (Martin-Barajas Mrb)			X
LS18IAG27	19-Nov-18	29.056999	-113.127998	Pa	andesite	X		X
LS18IAG28	20-Nov-18	29.109699	-113.185997	Pa2	basaltic andesite	X	X	X
LS18IAG29	20-Nov-18	29.111200	-113.193001	Pab	basalt	X		X
LS18IAG30	20-Nov-18	29.108255	-113.201700	Pab	basalt	X		X
LS18IAG31	20-Nov-18	29.107700	-113.200996	Pa1	andesite	X	X	X
LS18IAG32	21-Nov-18	29.047001	-113.164002	MPv	andesite			X

LS18IAG33	22-Nov-18	29.053000	-113.163002	MPv	basalt	X		X
LS18IAG34	22-Nov-18	29.056101	-113.177002	MPv	tuff with at least 4 lithic types (granodiorite, greyi lith, reddish lith, yellowish pumice)			X
LS18IAG35	22-Nov-18	29.056101	-113.177002	MPv	granodiorite inclusions in tuff			X
LS18IAG36	19-Nov-18	29.050358	-113.161834	MPv	flow banded rhyolite	X		X
LS19IAG37	4-Apr-19	29.053607	-113.127031	T2m	shells and some sand			
LS19IAG38	4-Apr-19	29.054489	-113.129094	T2m	shell-rich layer			
LS19IAG39	5-Apr-19	29.208956	-113.182486	Kt	basement tonalite	X		X
LS19IAG40	5-Apr-19	29.207813	-113.181540	MPv	pyroclastic			X
LS19IAG41	6-Apr-19	29.097846	-113.184009	Ps	silty sandstone			
LS19IAG42	6-Apr-19	29.097846	-113.184009	Ps	white ash bed			
LS19IAG43	7-Apr-19	29.060255	-113.124926	Pab	andesite			X
LS19IAG44	7-Apr-19	29.041587	-113.131942	Psm	shells			
LS19IAG45	7-Apr-19	29.031905	-113.157239	MPcg	welded tuff	X		X
LS19IAG46	8-Apr-19	29.119252	-113.213270	MPr1	rhyolite			X
LS19IAG47	9-Apr-19	29.053223	-113.139718	Psm	grey sandstone			
LS19IAG48	9-Apr-19	29.049553	-113.141393	Psm	pumice			
LS19IAG49	9-Apr-19	29.048304	-113.139096	Psm	gypsum			
LS19IAG50	9-Apr-19	29.048304	-113.139096	Psm	limestone			
LS19IAG51	9-Apr-19	29.048304	-113.139096	Psm	sandstone			
LS19IAG52	9-Apr-19	29.048304	-113.139096	Psm	siltstone			
LS19IAG53	10-Apr-19	29.044143	-113.130277	Psm	shell-rich bed			
LS19IAG54	10-Apr-19	29.044143	-113.130277	Psm	shells in sand			
LS19IAG55	10-Apr-19	29.044143	-113.130277	Psm	gypsum			
LS19IAG56	10-Apr-19	29.044143	-113.130277	Psm	microfossil matrix			
LS19IAG57	10-Apr-19	29.044143	-113.130277	Psm	grey sandstone with pyroclastics & basalt pieces			
LS19IAG58	10-Apr-19	29.044143	-113.130277	Pab	vesicular basalt			X
LS19IAG59	10-Apr-19	29.044143	-113.130277	Psm	shells			
LS19IAG60	10-Apr-19	29.044143	-113.130277	Pba	vesicular basalt	X	X	X
LS19IAG61	10-Apr-19	29.044277	-113.131155	Psm	shells			
LS19IAG62	10-Apr-19	29.042992	-113.133336	Pba	Mba	X	X	X
LS19IAG63	10-Apr-19	29.045283	-113.137071	Psm	pectins			
LS19IAG64	10-Apr-19	29.046295	-113.137028	Psm	welded tuff			X
LS19IAG65	10-Apr-19	29.049478	-113.138933	Psm	reworked ash, pebbles, pumice			
LS19IAG66	10-Apr-19	29.053287	-113.139703	Pba	basalt	X	X	X
LS19IAG67	11-Apr-19	29.038779	-113.134251	Ps	pumice pyroclastic flow			
LS19IAG68	11-Apr-19	29.031695	-113.126953	MPv	andesite		X	X

Table 1: Collected samples from Isla Ángel de la Guarda

Collected samples from Isla Ángel de la Guarda, including sample names, date collected, latitude/longitude, assigned unit, field classification, and analyses performed. Asterisk indicates thin section analyzed by A. Piña-Paez.

Sample	Type	SiO2	TiO2	Al2O3	Fe2O3	MgO	CaO	Na2O	K2O	P2O5	MnO	LOI	Total	Rb	Ba
LS18IAG29	ext	64.98	0.60	16.29	3.91	1.87	5.02	4.08	1.66	0.12	0.06	0.56	99.15	35.76	613.43
LS18IAG30	ext	60.27	0.85	16.77	5.28	2.34	5.65	4.38	1.30	0.18	0.08	2.06	99.15	23.90	495.13
LS18IAG31	ext	70.13	0.43	14.95	2.67	0.97	3.08	4.21	2.46	0.10	0.05	1.63	100.68	63.89	851.49
LS18IAG27	ext	61.20	0.56	16.06	4.26	2.77	7.29	3.95	1.31	0.15	0.08	1.25	98.89	30.05	574.00
LS18IAG28	ext	64.46	0.62	16.20	3.99	1.79	4.99	3.98	1.61	0.12	0.07	1.00	98.83	34.21	619.93
LS18IAG33	ext	62.84	0.59	16.93	4.18	2.08	5.32	4.30	1.06	0.13	0.07	1.52	99.03	16.39	513.26
LS18IAG36	ext	66.42	0.53	15.33	3.35	1.63	3.95	3.90	2.44	0.15	0.06	1.02	98.77	66.14	883.84
LS19IAG60	ext, maf	53.50	1.21	17.06	6.98	5.28	8.93	3.78	0.57	0.21	0.11	1.25	98.89	4.29	325.30
LS19IAG62	ext, maf	59.91	0.90	16.64	5.42	2.76	5.99	4.08	1.15	0.20	0.09	1.80	98.92	18.76	437.53
LS19IAG66	ext	60.50	0.94	16.62	5.44	2.63	6.06	4.15	1.22	0.19	0.09	1.16	98.99	19.88	444.35
JMS18IAG01	ext	61.38	0.95	16.84	5.46	2.94	6.04	4.44	1.06	0.20	0.07	0.28	99.66	19.79	610.86
JMS18IAG03	ext	66.31	0.60	16.52	4.00	1.86	5.07	4.27	1.66	0.12	0.05	0.43	100.90	37.91	628.97
JMS18IAG04	ext	65.20	0.60	16.42	4.06	1.96	5.01	4.22	1.62	0.12	0.05	0.79	100.06	36.61	604.05
JMS18IAG05	ext	65.09	0.57	16.21	3.89	2.17	5.01	4.08	1.61	0.12	0.05	1.09	99.90	37.11	623.29
JMS18IAG07	ext	65.21	0.60	16.44	4.02	1.88	5.05	4.15	1.60	0.12	0.05	0.70	99.83	36.46	606.03
JMS18IAG09	ext	63.85	0.57	17.01	4.09	2.09	5.60	4.58	1.07	0.13	0.05	0.97	100.02	19.07	510.91
JMS18IAG10	ext	63.83	0.57	17.19	4.17	2.10	5.47	4.59	1.09	0.12	0.05	0.85	100.03	19.60	530.60
JMS18IAG12	ext	62.81	0.56	16.51	4.00	1.79	6.00	4.37	1.39	0.14	0.05	1.58	99.18	28.17	1074.77
JMS18IAG13	ext	63.19	0.58	17.14	4.17	1.93	5.56	4.51	1.23	0.14	0.05	0.98	99.48	20.82	468.75
JMS18IAG16	ext	73.24	0.22	13.91	1.51	0.17	1.49	4.93	3.40	0.05	0.01	0.90	99.83	94.77	946.50
JMS18IAG17	ext	60.83	0.61	17.15	4.65	2.87	6.13	4.38	1.03	0.16	0.06	1.44	99.30	21.91	429.17
JMS18IAG18	ext, maf	55.51	0.56	15.89	4.32	3.17	10.14	3.68	0.81	0.19	0.06	5.37	99.71	16.13	567.05
JMS18IAG19	ext	63.88	0.54	17.16	3.96	0.51	5.77	4.56	1.47	0.13	0.07	1.41	99.47	72.43	584.80
LS17IAG02	ext	63.39	0.53	17.21	4.19	2.11	5.71	4.44	1.05	0.16	0.05	1.43	100.27	26.81	508.01
LS17IAG03	ext	63.17	0.54	16.99	4.27	1.60	5.24	4.36	1.13	0.12	0.04	1.43	98.89	28.32	488.64
LS17IAG04	ext	64.08	0.58	17.26	4.22	1.97	5.34	4.52	1.11	0.13	0.05	1.21	100.47	19.93	483.04
LS17IAG07	ext	64.05	0.56	17.43	4.24	2.06	5.44	4.53	1.12	0.12	0.05	0.79	100.38	21.83	447.35
JMS18IAG14	inc	63.69	0.49	15.81	4.09	1.90	5.17	3.41	2.67	0.11	0.06	1.59	98.98	90.29	872.51
JMS18IAG15A	inc	60.56	0.90	16.75	5.37	3.01	5.98	3.99	1.56	0.18	0.07	1.52	99.88	18.95	426.32
JMS18IAG15B	inc	60.10	0.90	16.60	5.36	3.03	5.92	4.35	1.06	0.18	0.07	1.75	99.32	18.30	427.31
JMS18IAG17i	inc, maf	55.79	0.68	18.08	5.80	5.06	8.07	3.51	0.96	0.22	0.07	2.33	100.56	18.62	324.16
LS19IAG39	int	64.69	0.65	16.24	4.30	1.72	4.35	3.16	2.44	0.16	0.08	1.20	99.03	83.61	865.85
LS18IAG22-2	dike	71.54	0.30	13.72	2.34	0.59	0.49	4.12	4.93	0.05	0.05	1.28	99.40	133.17	997.95
LS18IAG23	dike	74.23	0.16	12.76	1.69	0.20	0.17	2.70	6.77	0.02	0.02	1.08	99.79	177.99	1578.53
TIB-09-13-2	dike, Tib	69.87	0.42	14.40	2.82	0.65	2.00	4.52	3.39	0.08	0.05	0.61	98.80	102.81	1070.03
TIB-09-14-2	dike, Tib	71.63	0.30	14.04	2.16	0.35	1.50	4.30	3.64	0.05	0.04	2.37	100.38	116.81	1192.69
LS19IAG45	flt	71.79	0.28	13.43	1.62	0.43	1.70	3.72	4.74	0.07	0.07	0.74	98.59	178.43	1794.25
LS18IAG25	flt	73.92	0.22	13.15	1.37	0.19	1.12	4.36	3.52	0.03	0.03	0.85	99.40	106.13	1027.67

Sr	Nb	Zr	Hf	Y	Zn	Cu	Ni	Co	Cr	V	La	Ce	Nd	Pb	Th
373.28	4.97	142.42	3.79	15.01	54.72	3.16	<d.l.	7.19	11.68	126.07	20.52	39.68	10.86	17.55	<d.l.
444.87	4.02	154.20	3.68	19.82	66.06	10.34	<d.l.	13.66	<d.l.	123.51	17.67	51.56	18.41	6.43	<d.l.
292.29	7.37	165.76	4.08	16.39	44.40	<d.l.	<d.l.	3.58	<d.l.	44.38	22.96	60.32	21.58	8.02	<d.l.
553.27	3.35	155.17	4.20	16.98	66.27	17.69	24.10	9.97	5.61	71.82	12.45	67.98	29.09	19.26	<d.l.
387.40	4.39	143.84	2.66	15.72	55.82	9.94	15.30	7.17	5.76	80.05	14.08	76.81	31.43	17.86	<d.l.
483.68	2.70	122.68	3.18	13.68	57.29	8.45	20.52	9.73	<d.l.	82.84	8.19	59.39	27.29	14.39	<d.l.
467.75	5.25	168.73	4.66	16.67	55.95	9.87	18.78	6.04	<d.l.	66.63	16.75	41.17	18.88	16.78	2.85
464.74	2.55	138.13	4.12	23.12	71.34	19.26	46.74	21.58	206.54	246.45	20.19	55.56	24.85	14.25	<d.l.
472.14	3.60	151.11	2.72	18.71	66.13	12.98	18.01	13.83	17.27	136.90	10.78	70.41	32.10	16.08	<d.l.
465.69	3.05	154.04	4.10	22.51	65.32	9.96	9.76	14.40	15.97	147.69	10.41	42.82	18.84	17.90	<d.l.
462.90	3.65	158.45	3.70	23.80	67.63	9.48	12.62	12.16	27.73	114.88	21.73	46.17	18.84	10.61	<d.l.
381.66	3.98	147.63	4.57	15.59	55.40	7.56	6.17	6.95	18.86	82.47	19.92	41.86	8.31	6.01	<d.l.
381.22	4.32	149.49	3.47	15.66	59.86	11.29	6.15	8.76	19.77	81.55	8.83	46.84	17.73	10.59	<d.l.
373.71	4.27	146.57	2.84	14.58	54.23	7.68	4.84	7.31	22.72	76.14	16.37	42.56	9.91	9.15	1.99
383.98	3.85	148.05	3.09	16.58	53.03	6.56	5.39	8.57	20.04	76.87	20.13	56.47	23.48	5.46	<d.l.
466.68	3.18	126.22	3.00	14.09	55.70	8.67	1.59	8.67	<d.l.	79.70	9.32	44.58	17.26	<d.l.	<d.l.
501.88	2.70	127.04	2.93	11.79	57.24	9.57	4.71	9.28	<d.l.	73.75	20.21	31.05	14.15	<d.l.	3.19
606.65	3.60	147.33	3.28	11.56	57.37	9.78	3.95	9.59	5.74	57.33	17.20	42.21	12.07	12.74	<d.l.
583.92	3.19	140.41	2.31	11.59	58.24	14.50	4.46	9.23	8.48	86.29	17.25	49.64	22.61	10.93	<d.l.
151.20	8.75	218.43	5.17	34.36	40.55	<d.l.	<d.l.	<d.l.	<d.l.	30.42	29.94	38.64	29.76	3.97	12.81
612.22	3.55	150.99	3.43	15.44	59.47	9.12	15.15	11.71	13.75	72.11	12.53	41.06	19.09	7.58	<d.l.
627.23	3.16	143.86	<d.l.	13.29	62.50	15.56	20.10	12.84	20.78	66.32	18.10	43.44	14.56	12.22	<d.l.
473.63	3.27	128.71	2.70	14.60	134.37	7.23	3.43	11.11	<d.l.	105.50	15.96	15.44	18.90	41.86	2.80
505.71	2.08	127.97	3.62	14.08	63.36	14.95	7.32	9.46	<d.l.	92.22	14.02	<d.l.	14.92	<d.l.	7.82
493.06	3.50	126.79	2.63	11.79	58.42	9.98	14.24	6.96	4.37	132.14	17.49	<d.l.	13.49	2.97	12.57
495.96	2.82	128.16	2.91	13.63	50.93	11.48	3.36	10.54	2.19	58.96	13.52	33.57	6.20	1.92	2.68
494.71	2.34	124.24	3.42	11.87	58.75	11.50	7.06	9.89	12.47	97.04	19.25	31.54	10.09	7.51	<d.l.
397.84	4.01	124.88	2.86	14.06	72.39	5.28	1.50	8.59	2.92	72.04	62.60	111.45	29.95	15.56	40.24
463.71	4.42	155.57	2.80	20.42	69.08	7.11	16.46	15.86	33.34	113.97	18.74	40.56	13.38	8.04	<d.l.
465.45	3.90	155.98	4.27	19.38	63.85	13.95	15.39	13.30	28.59	117.08	13.24	40.78	14.61	4.04	<d.l.
695.02	2.71	139.60	3.31	11.92	67.11	19.73	43.06	20.50	47.56	101.20	11.65	37.41	6.16	6.49	<d.l.
394.47	7.20	166.27	2.80	17.49	87.58	<d.l.	15.56	7.01	<d.l.	64.99	19.10	62.81	28.50	17.74	2.58
96.01	11.67	253.20	7.57	36.48	83.20	<d.l.	<d.l.	<d.l.	<d.l.	5.56	35.66	80.01	33.28	7.83	7.01
40.85	9.89	188.11	4.64	28.23	73.32	<d.l.	<d.l.	<d.l.	<d.l.	8.89	20.62	60.66	15.94	6.16	7.29
177.67	9.24	307.77	7.66	31.10	49.15	<d.l.	<d.l.	1.58	<d.l.	23.83	29.79	79.39	28.46	11.37	3.12
139.14	10.85	240.70	6.78	29.00	43.69	<d.l.	<d.l.	3.10	<d.l.	11.46	37.08	91.31	33.58	15.07	4.70
201.28	19.07	238.42	6.24	33.48	52.37	3.87	<d.l.	<d.l.	<d.l.	20.51	49.17	108.33	47.91	27.68	16.59
135.50	8.94	159.34	3.96	24.61	31.76	<d.l.	<d.l.	<d.l.	<d.l.	7.18	36.16	60.19	24.06	13.75	4.47

Table 2: XRF geochemical data

Geochemical data from X-ray fluorescence: ext – extrusive lava; maf – most mafic subset used in spider diagrams; inc – inclusion or xenolith; int – intrusive (plutonic rock); Tib – Isla Tiburón (not collected in this study); flt – float; d.l. – detection limit. Dikes and float are not included on geochemical diagrams (Figures 9 through 15).

TABLE 3: SUMMARY OF $^{40}Ar/^{39}Ar$ ERUPTION AGES

Sample	**Material†**	**Method#**	**Plateau**		**Isochron**			**% ^{39}Ar [Steps]**	**% $^{40}Ar^*$**
			Age (Ma) ± 1σ	**MSWD**	**Age (Ma) ± 1σ**	**MSWD**	**$^{40}Ar/^{36}Ar_i$ (± 2σ)**		
LS18IAG28	GM	IH	**2.986 ± 0.009**	1.88	2.990 ± 0.013	1.98	297.5 ± 3.2	73.8 [675-1025]	61.5
LS18IAG22	GM	IH	**3.377 ± 0.037 ***	23.81	-	-	-	100 [475-1250]	44.1
LS18IAG31a	Plag.	IH	**3.915 ± 0.135**	2.03	3.115 ± 3.251	2.94	301.6 ± 159.7	51.5[975-1200]	4.9
LS18IAG31b	Plag.	IH	**3.917 ± 0.116**	0.92	4.327 ± 1.077	1.17	297.0 ± 17.7	62.9[925-1250]	4.8
					LS19IAG31 Weighted Mean Age (± 1σ)	***3.916 ± 0.088***			

Preferred age in bold

* Recoil model age following Fleck et al. (2014), *Geosphere*. Individual plateau steps for LA18IAG22 yield ages ranging from 3.133 ± 0.037 Ma to 3.693 ± 0.206 Ma.

Ages were calculated using the decay constants recommended by Steiger and Jager (1977) and assuming $^{40}Ar/^{36}Ar$atmosphere = 298.56 ± 0.31 (Lee et al., 2006)

† GM = groundmass. Plag. = plagioclase. San. = sanidine

IH = incremental heating.

Table 3: Summary of $^{40}Ar/^{39}Ar$ ages in northern area

$^{40}Ar/^{39}Ar$ ages for andesite lava flows in the northern study area, and a felsic dike sampled ~20 km north of the northern study area. Full details for Ar isotope analyses are included in Chapter 3 Table S2.

SUPPLEMENTAL MATERIAL

Sample	Unit	Field Classification	Thin section description
JMS18IAG01	Pab	basaltic lava	porphyritic andesite lava. Porphyritic andesite with plagioclase, alkali feldspar, amphibole, pyroxene
JMS18IAG02	Pab	lava	porphyritic andesite lava with phenocrysts of plagioclase, amphibole, alkali feldspar, and pyroxene. calcareous alteration.
JMS18IAG03	Pa2	mafic lava	porphyritic basaltic andesite with phenocrysts of plagioclase, olivine, and alkali feldspar. No alteration present.
JMS18IAG04	Pa2	andesite	porphyritic basaltic andesite with phenocrysts of plagioclase, olivine, and alkali feldspar. Calcareous alteration
JMS18IAG05	Pa2	andesite	porphyritic basaltic andesite with phenocrysts of plagioclase, alkali feldspar, olivine, and pyroxene. Trachytic matrix texture.
JMS18IAG06	Pa2	andesite	porphyritic basaltic andesite with phenocrysts of plagioclase, olivine, pyroxene, and alkali feldspar. oxidation alteration
JMS18IAG07	Pa2	andesite	porphyritic basaltic andesite with phenocrysts of plagioclase, alkali feldspar, olivine, and pyroxene. Oxidation alteration.
JMS18IAG09	MPv	andesite	porphyritic basaltic andesite with phenocrysts of plagioclase, pyroxene, alkali feldspar, and lesser amphibole and olivine; oxidation alteration.
JMS18IAG10	MPv	andesite	porphyritic andesite lava with phenocrysts of plagioclase, alkali feldspar, pyroxene and amphibole. Trachytic matrix. Calcareous and oxidation alteration.
JMS18IAG11	MPv	pyroclastic breccia and scoria	porphyritic andesite with phenocrysts of plagioclase, amphibole, and alkali feldspar. Contains volcanic xenoliths. Oxidation alteration.
JMS18IAG12	MPv	andesite	porphyritic andesite with phenocrysts of plagioclase, oxides, and alkali feldspar. Trachytic texture in matrix. Oxidation and calcareous alteration.
JMS18IAG13	MPv	andesite	porphyritic andesite with phenocrysts of plagioclase, amphibole, and alkali feldspar. Oxidation alteration.
JMS18IAG14	MPv	granitic inclusion in lithic breccia	Intergranular granodiorite with phenocrsts of quartz, biotite, alkali feldspar, and plagioclase. Oxidation alteration.
JMS18IAG15A	Pab	volcanic breccia clast, possibly autolith	porphyritic basaltic andesite with phenocryts of plagioclase, alkali feldspar, olivine, pyroxene, and amphibole. Oxidation alteration.
JMS18IAG15B	Pab	volcanic breccia clast, possibly autolith	porphyritic basaltic andesite with phenocrysts of plagioclase, pyroxene, alkali feldspar, and lesser amphibole and olivine; oxidation alteration.
JMS18IAG16	MPr	foliated andesite	porphyritic andesite with phenocrysts of plagioclase, amphibole, and alkali feldspar. Oxidation alteration.
JMS18IAG17	Pa	andesite	porphyritic andesite with phenocrysts of plagioclase, and lesser alkali feldspar, amphibole and pyroxene. Matrix has trachytic texture. Oxidation alteration.
JMS18IAG17i	Pa	mafic inclusion	porphyritic andesite with phenocrysts of plagioclase, alkali feldspar, pyroxene and amphibole. Has trachytic texture. Oxidation and calcareous alteration.
JMS18IAG18	Pa	andesite	porphyritic andesite with phenocrysts of plagioclase, alkali feldspar, pyroxene and amphibole. Oxidation and calcareous alteration.
JMS18IAG19	MPv	basalt	porphyritic andesite with phenocrysts of plagioclase, alkali feldspar, and amphibole. Oxidation alteration.
LS17IAG02	MPv	basaltic andesite	porphyritic andesite with phenocrysts of plagioclase, alkali feldspar, and amphibole. Oxidized matrix.
LS17IAG03	MPv	basaltic andesite	Porphyritic andesite pith phenocrysts of plagioclase, alkali feldspar, amphibole. Oxidized matrix.
LS17IAG04	MPv	basaltic andesite	Porphyritic andesite with phenocrysts of plagioclase, alkali feldspar, and amphibole.
LS17IAG05	Pa2	basaltic andesite	Porphyritic andesite with phenocrysts of plagioclase and amphibole. No sign of alteration
LS17IAG07	Pa2	basaltic andesite	Porphyritic andesite with phenocrysts of plagioclase, alkali feldspar, amphibole. No sign of alteration.
LS18IAG22	n/a	dike	Porphyritic, phenocrysts of plagioclase, possible alkali feldspar and quartz, microcrystalline matrix.
LS18IAG23	n/a	dike	Porphyritic, phenocrysts of plagioclase, possible alkali feldspar and quartz, oxides. Microcrystalline altered matrix.
LS18IAG24	n/a	rhyolite (Martin-Barajas Mrb)	Porphyritic rhyolite with phenocrysts of plagioclase, quartz, alkali feldspar, hornblende, oxides. Flow texture.
LS18IAG25	n/a	rhyolite (Martin-Barajas Mrc)	Porphyritic rhyolite with phenocrysts of plagioclase, quartz, alkali feldspar, hornblende, oxides. Flow texture.
LS18IAG26	n/a	rhyolite (Martin-Barajas Mrb)	Porphyritic rhyolite with phenocrysts of plagioclase, alkali feldspar, hornblende, titanite, oxides. Altered phenocrysts and matrix. Flow texture.
LS18IAG27	Pa	andesite	porphyritic andesite with phenocrysts of plagioclase, alkali feldspar, titanite, amphibole.

LS18IAG28	Pa2	basaltic andesite	porphyritic andesite with phenocrysts of plagioclase, alkali feldspar, titanite, amphibole. Plagioclase has inclusions.
LS18IAG29	Pab	basalt	Porphyritic basalt with phenocrysts of plagioclase, alkali feldspar, titanite, minor olivine.
LS18IAG30	Pab	basalt	Porphyritic basalt with trachytic phenocrysts of plagioclase, alkali feldspar, sphene.
LS18IAG31	Pa1	andesite	Porphyritic basalt with phenocrysts of plagioclase, sphene, spherulite alteration.
LS18IAG32	MPv	andesite	Porphyritic andesite with phenocrysts pf plagioclase, sphene, hornblende. Sample is altered.
LS18IAG33	MPv	basalt	Porphyritic basalt with phenocrysts of plagioclase, sphene, and olivine.
LS18IAG34	MPv	tuff	Spherulitically altered lithic with plagioclase phenocrysts. Larger mass has phenocrysts of plagioclase sphene, alkali feldspar, and oxides.
LS18IAG35	MPv	granodiorite inclusions in tuff	Holocrystalline granodiorite with phenocrysts of plagioclase, hornblende, alkali feldspar, quartz.
LS18IAG36	MPv	flow banded rhyolite	Hypocrystalline rhyolite with phenocrysts of plagioclase, alkalil feldspar, hornblende, sphene.
LS19IAG39	Kt	basement tonalite	Holocrystalline granodiorite with phenocrysts of plagioclase, hornblende, alkali feldspar, quartz, and zircon.
LS19IAG40	MPv	pyroclastic	Porphyritic with phenocrysts of plagioclase. Heavily altered and glassy.
LS19IAG43	Pab	andesite	porphyritic andesite with phenocrysts plagioclase, alkali feldspar, sphene. Very altered
LS19IAG45	MPcg	welded tuff	Porphyritic with phenocrysts of plagioclase, hornblende, biotite. Trachytic texture.
LS19IAG46	MPr1	rhyolite	Porphyritic, phenocrysts of alkali feldspar, plagioclase, hornblende, biotite, sphene. Many inclusions feldspars.
LS19IAG58	Pab	vesicular basalt	porphyritic basalt with phenocrysts of plagioclase, alkali feldspar, sphene, olivine.
LS19IAG60	Pba	vesicular basalt	porphyritic basalt with phenocrysts of plagioclase, alkali feldspar, sphene, olivine.
LS19IAG62	Pba	Mba	porphyritic basalt with phenocrysts of plagioclase, alkali feldspar, hornblende, olivine.
LS19IAG64	Psm	welded tuff	Porphyritic with phenocrysts of plagioclase and amphibole, trachytic texture.
LS19IAG66	Pba	basalt	porphyritic basalt with phenocrysts of plagioclase, alkali feldspar, sphene, olivine.
LS19IAG68	MPv	andesite	Porphyritic basaltic andesite with phenocrysts of plagioclase, alkali feldspar, altered oxides, and sphene.

Table S1: Descriptions of thin sections analyzed in this study

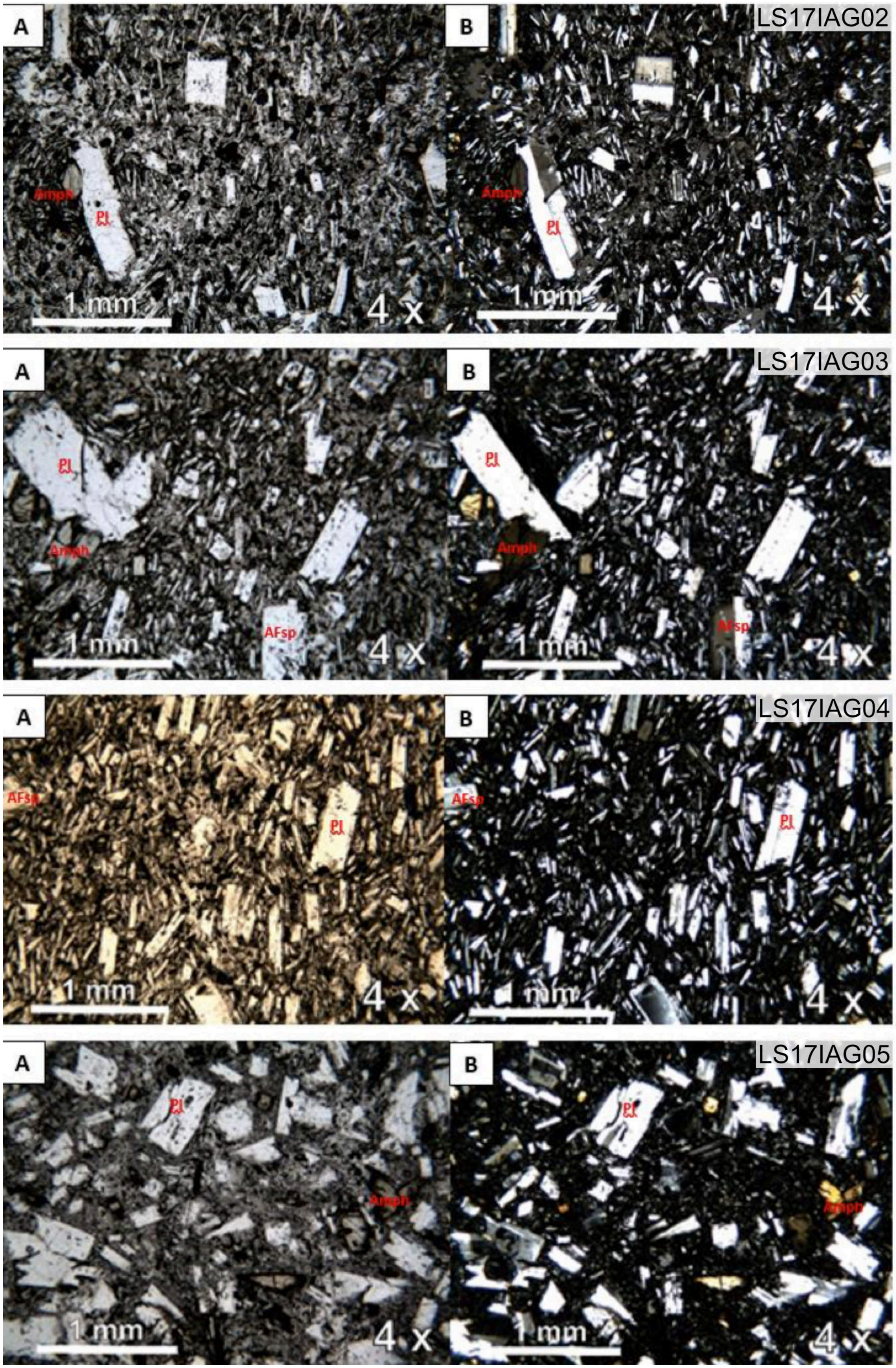
A
B
LS17IAG02
Amph
Pl
1 mm
4 x
A
B
LS17IAG03
Pl
Amph
AFsp
1 mm
4 x
A
B
LS17IAG04
AFsp
Pl
1 mm
4 x
A
B
LS17IAG05
Pl
Amph
1 mm
4 x

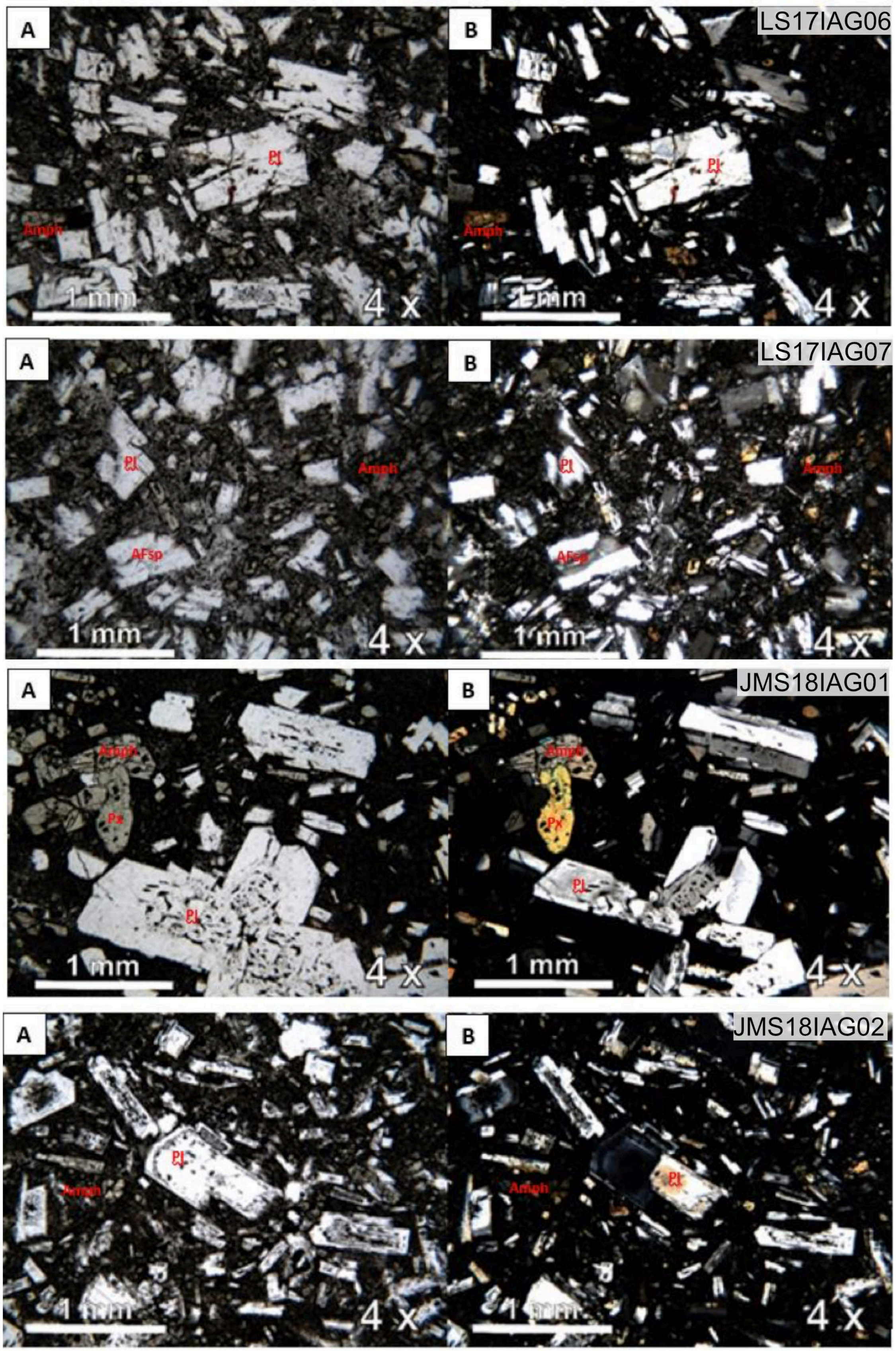
A
B
LS17IAG06
Pl
Amph
1 mm
4 x
A
B
LS17IAG07
Pl
Amph
AFsp
1 mm
4 x
A
B
JMS18IAG01
Amph
Px
Pl
1 mm
4 x
A
B
JMS18IAG02
Pl
Amph
1 mm
4 x

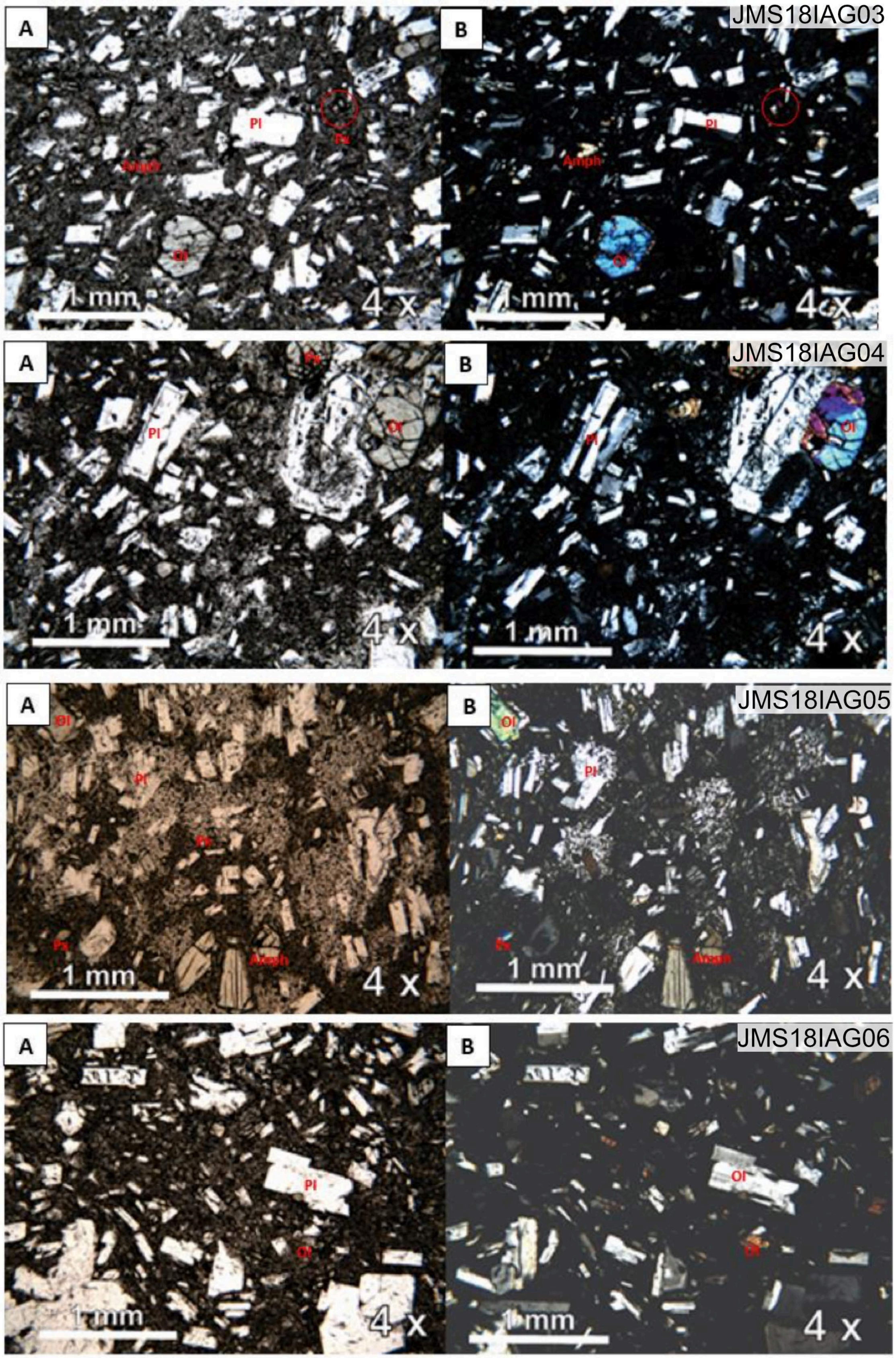
A
B
JMS18IAG03
Pl
Px
Amph
Ol
1 mm
4 x
A
B
JMS18IAG04
Px
Pl
Ol
1 mm
4 x
A
B
JMS18IAG05
Ol
Pl
Px
Amph
1 mm
4 x
A
B
JMS18IAG06
Pl
Ol
1 mm
4 x

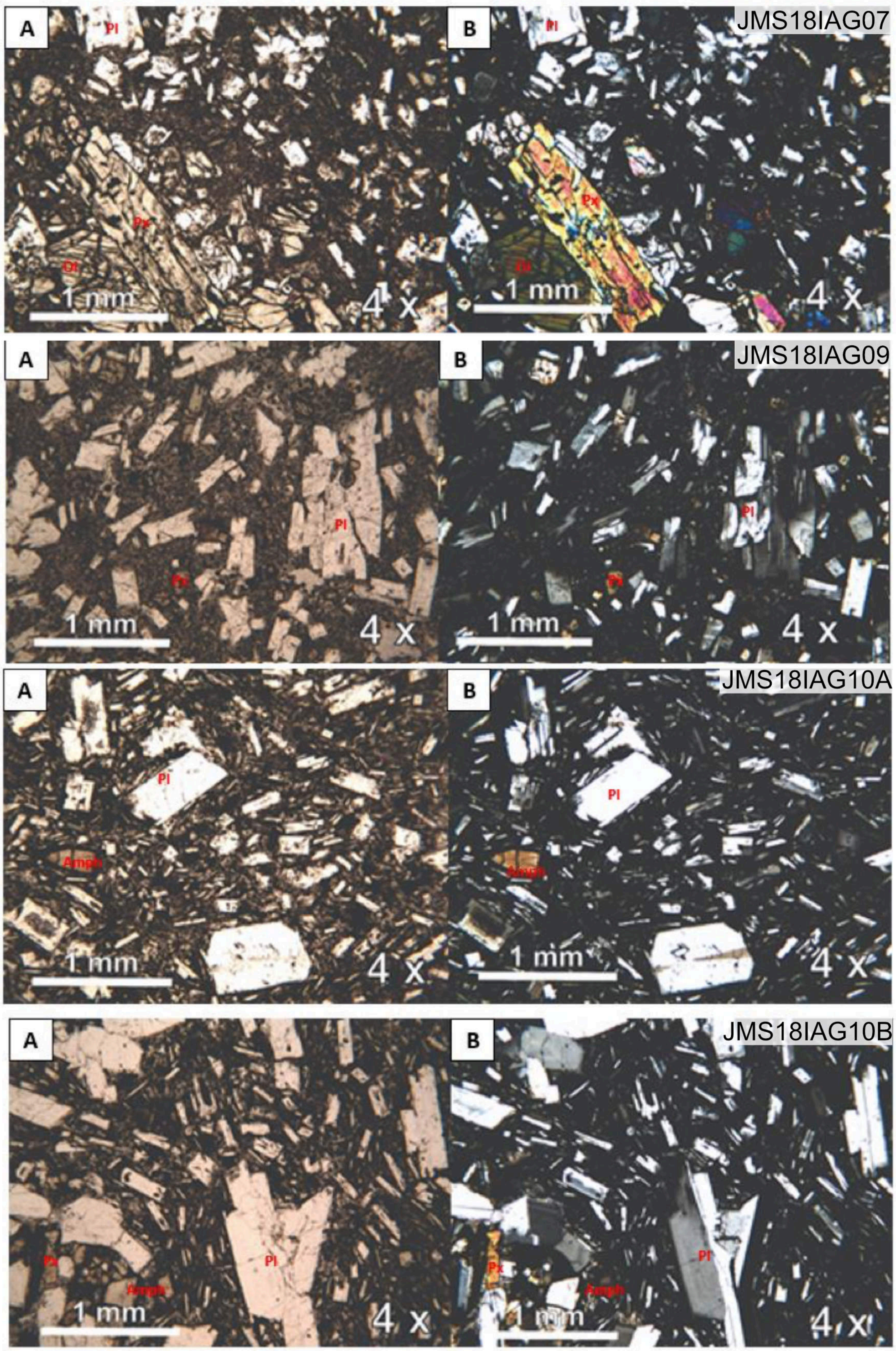
A
B
JMS18IAG07
Pl
Px
Ol
1 mm
4 x
A
B
JMS18IAG09
Pl
Px
1 mm
4 x
A
B
JMS18IAG10A
Pl
Amph
1 mm
4 x
A
B
JMS18IAG10B
Px
Amph
Pl
1 mm
4 x

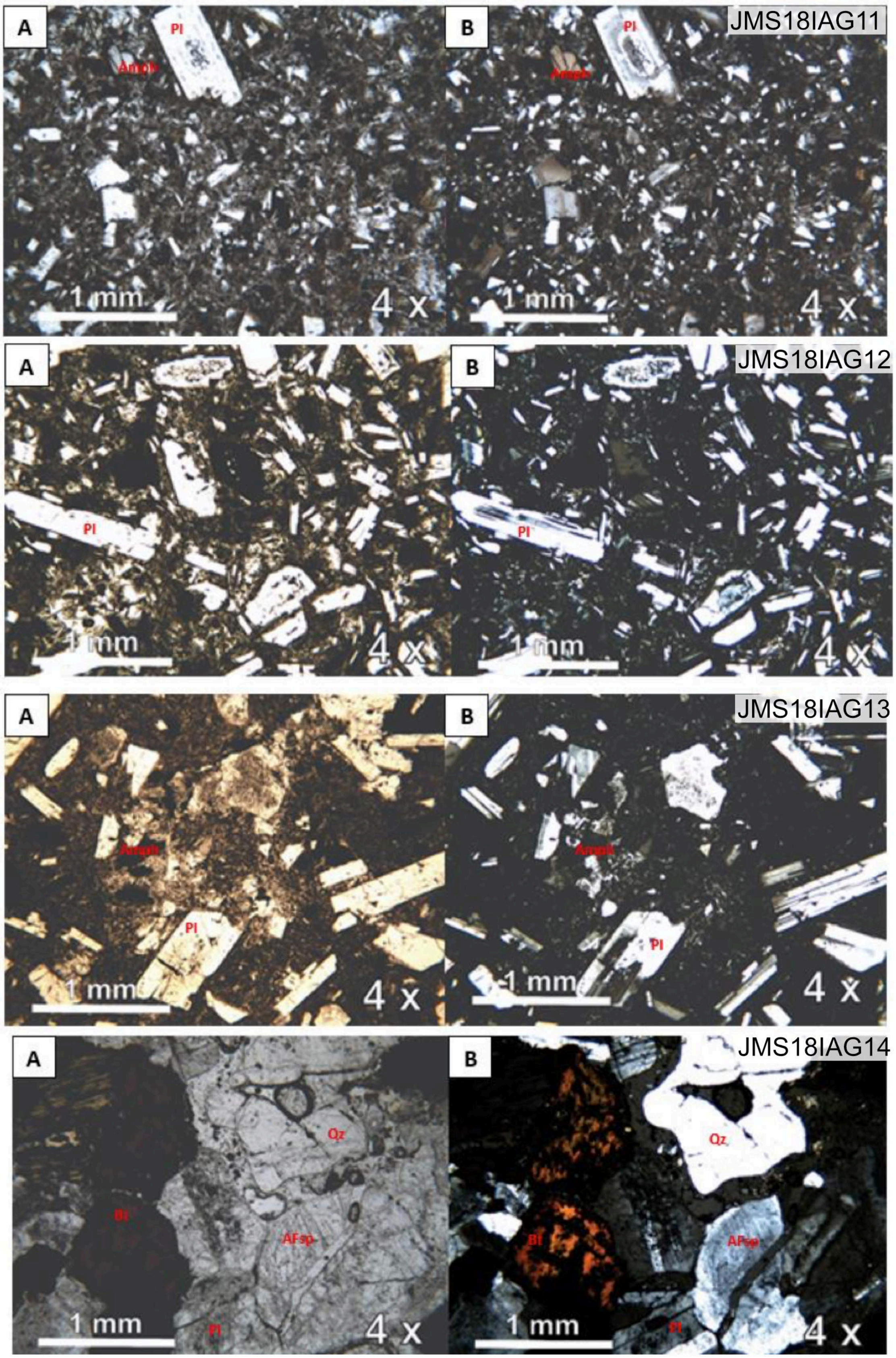
A
B
JMS18IAG11
Pl
1 mm
4 x
A
B
JMS18IAG12
Pl
1 mm
4 x
A
B
JMS18IAG13
Pl
1 mm
4 x
A
B
JMS18IAG14
Qz
Bt
AFsp
Pl
1 mm
4 x

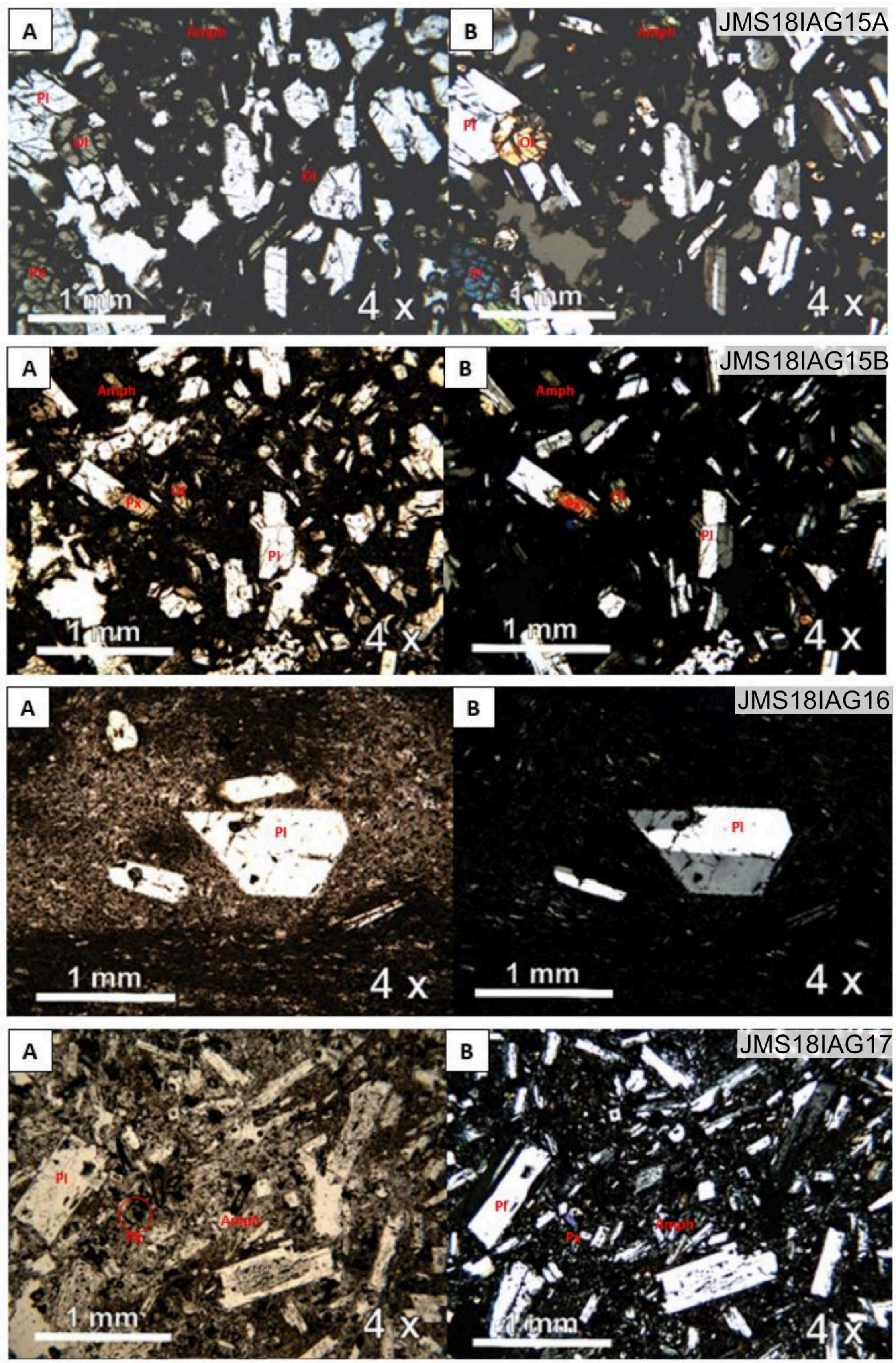
JMS18IAG15A
A
B
Amph
Pl
Ol
Px
1 mm
4 x
JMS18IAG15B
A
B
Amph
Px
Ol
Pl
1 mm
4 x
JMS18IAG16
A
B
Pl
1 mm
4 x
JMS18IAG17
A
B
Pl
Px
Amph
1 mm
4 x

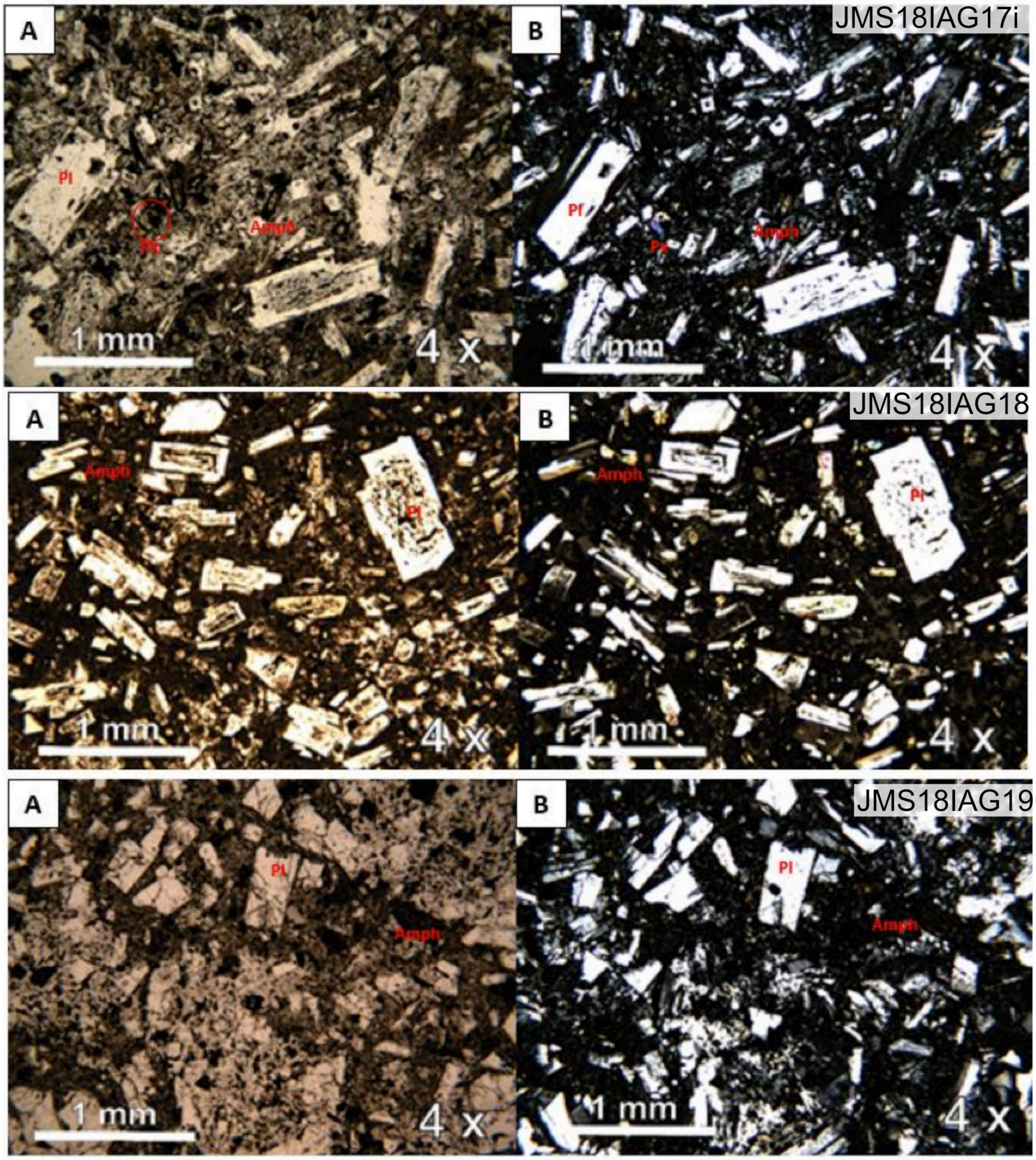

All photomicrographs in the above section (LS17 and JMS18 series) were taken by A. Piña-Paez. Scale bars are 1 mm. Left-hand photomicrographs are taken in plain-polarized light, and right-hand in cross-polarized light.

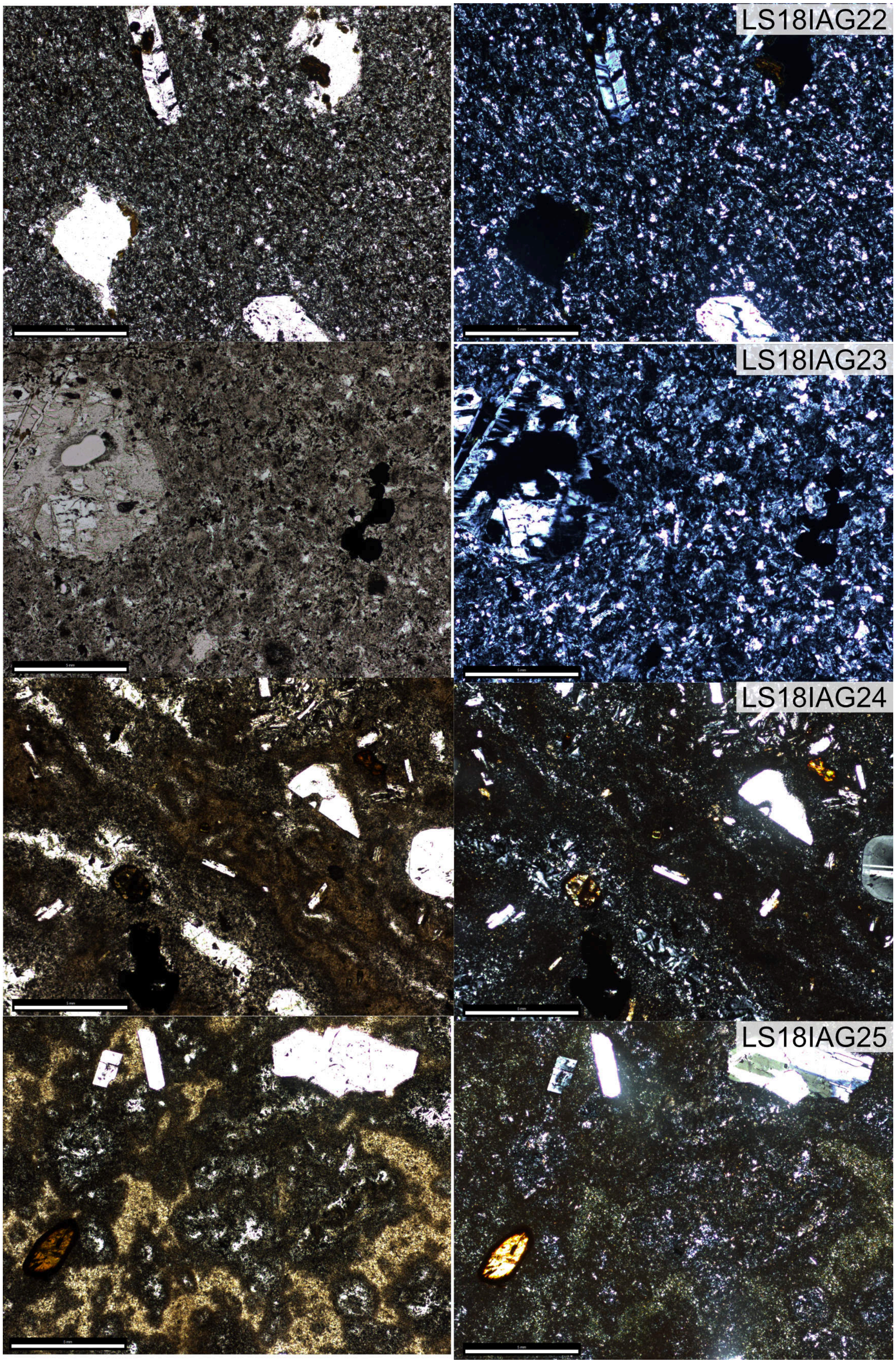
LS18IAG22
LS18IAG23
LS18IAG24
LS18IAG25

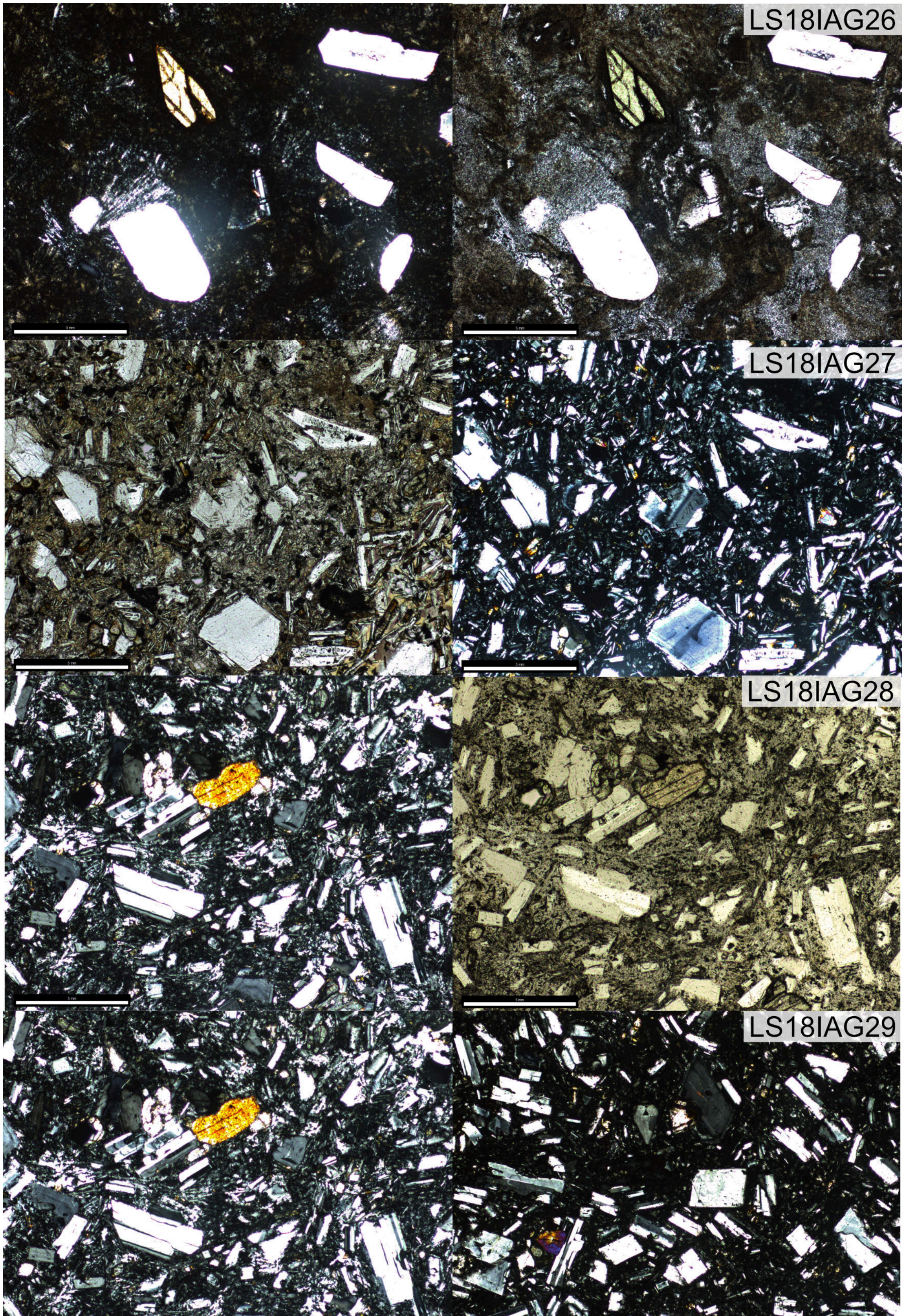
LS18IAG26
LS18IAG27
LS18IAG28
LS18IAG29

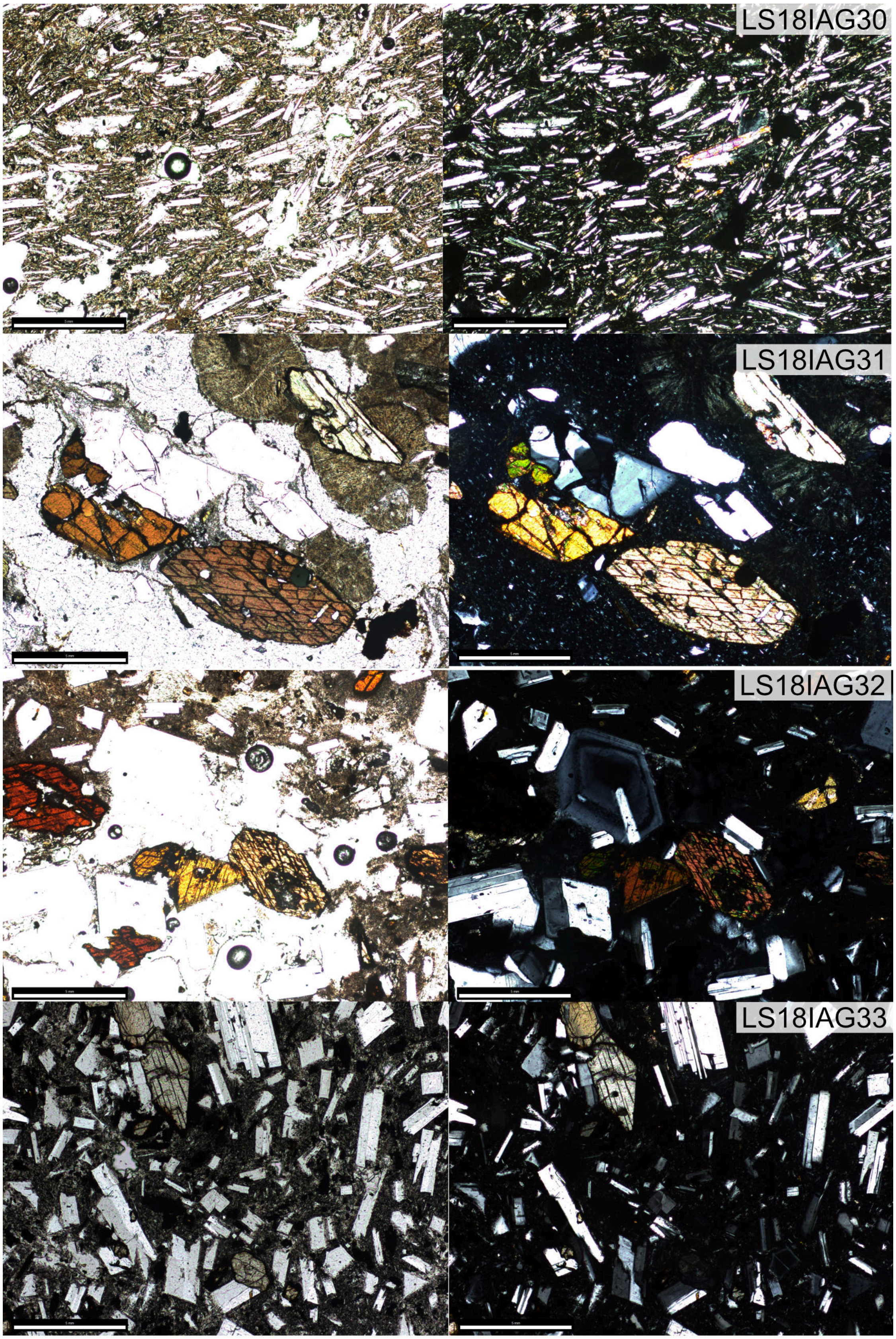
LS18IAG30
LS18IAG31
LS18IAG32
LS18IAG33

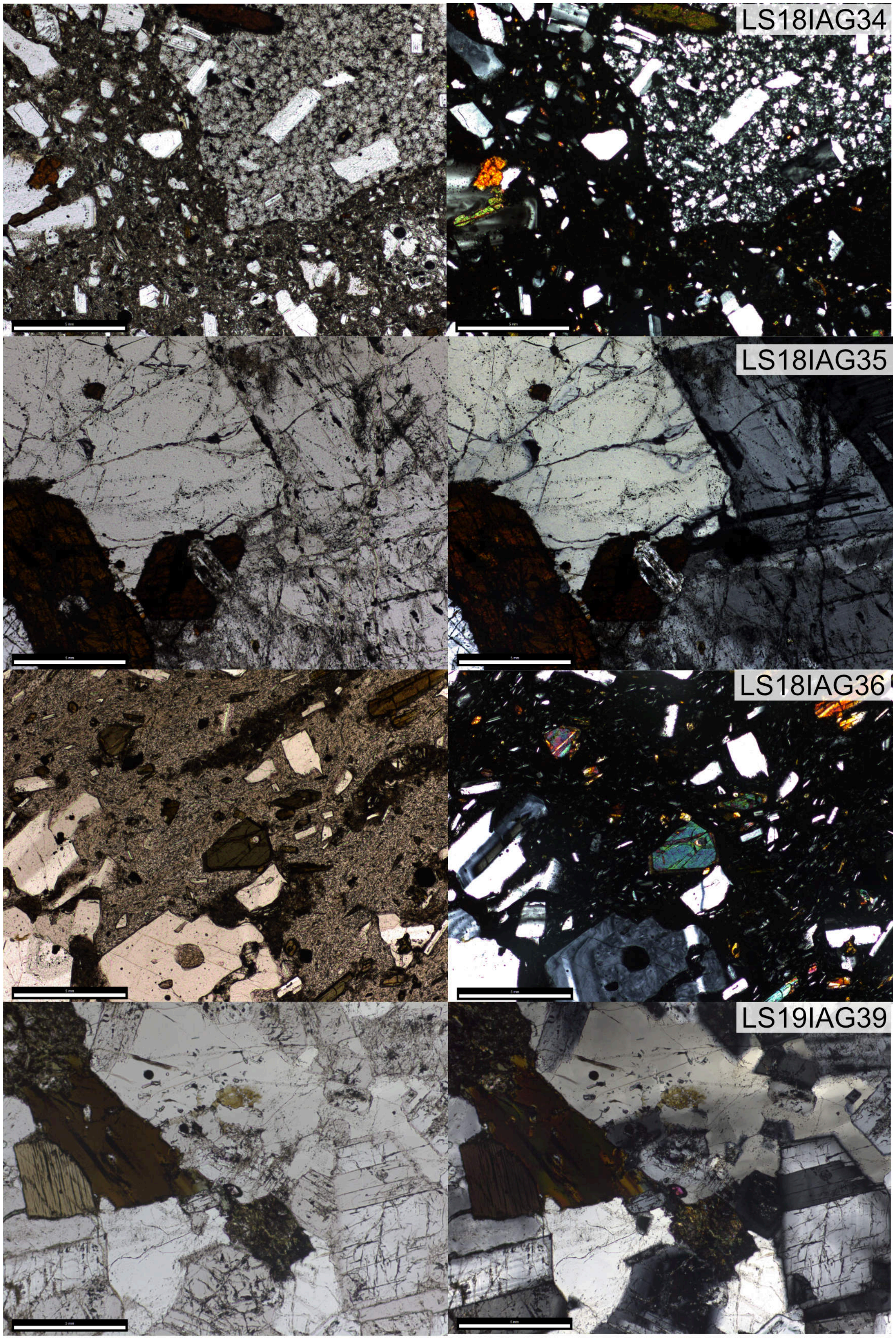
LS18IAG34
LS18IAG35
LS18IAG36
LS19IAG39

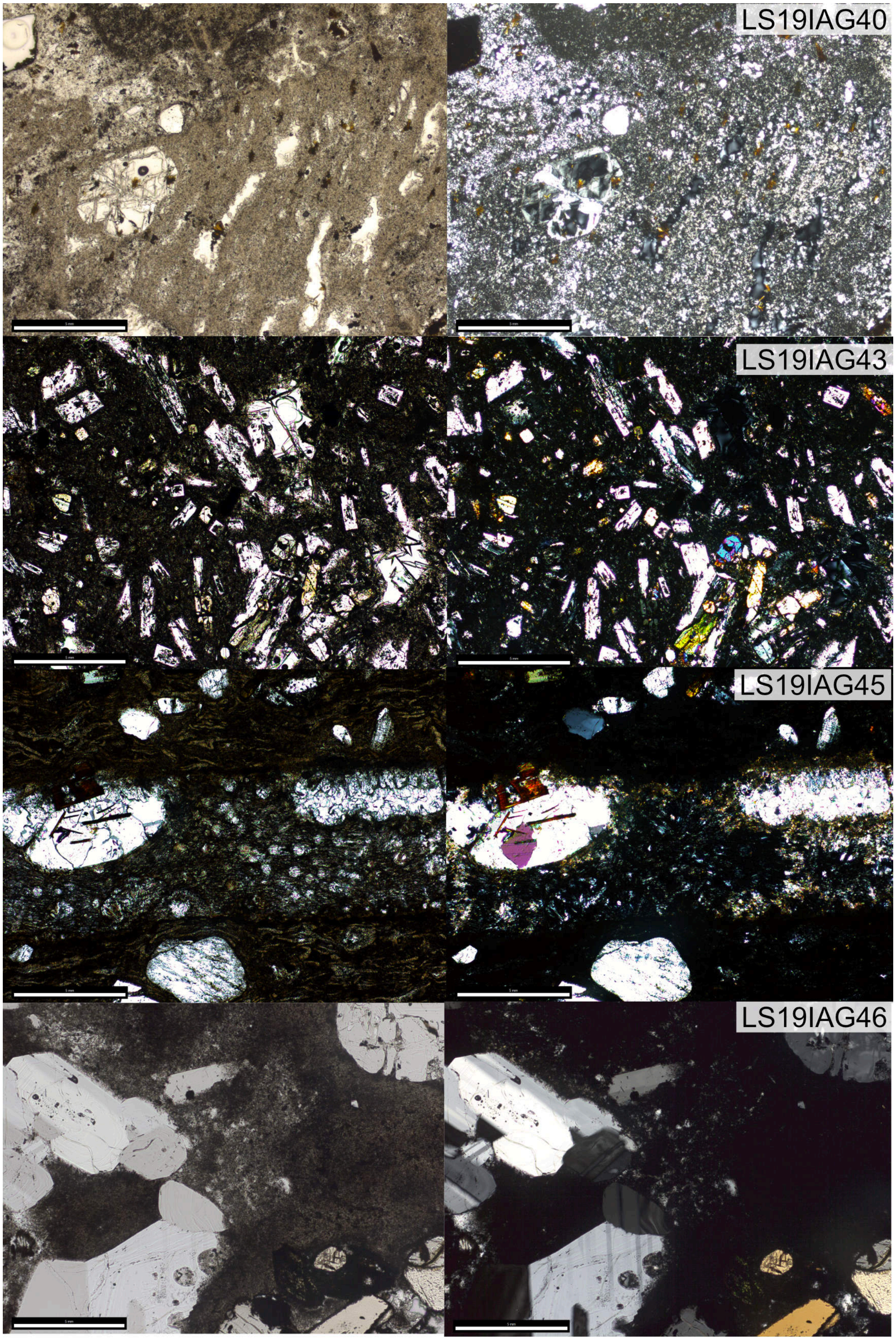
LS19IAG40
LS19IAG43
LS19IAG45
LS19IAG46

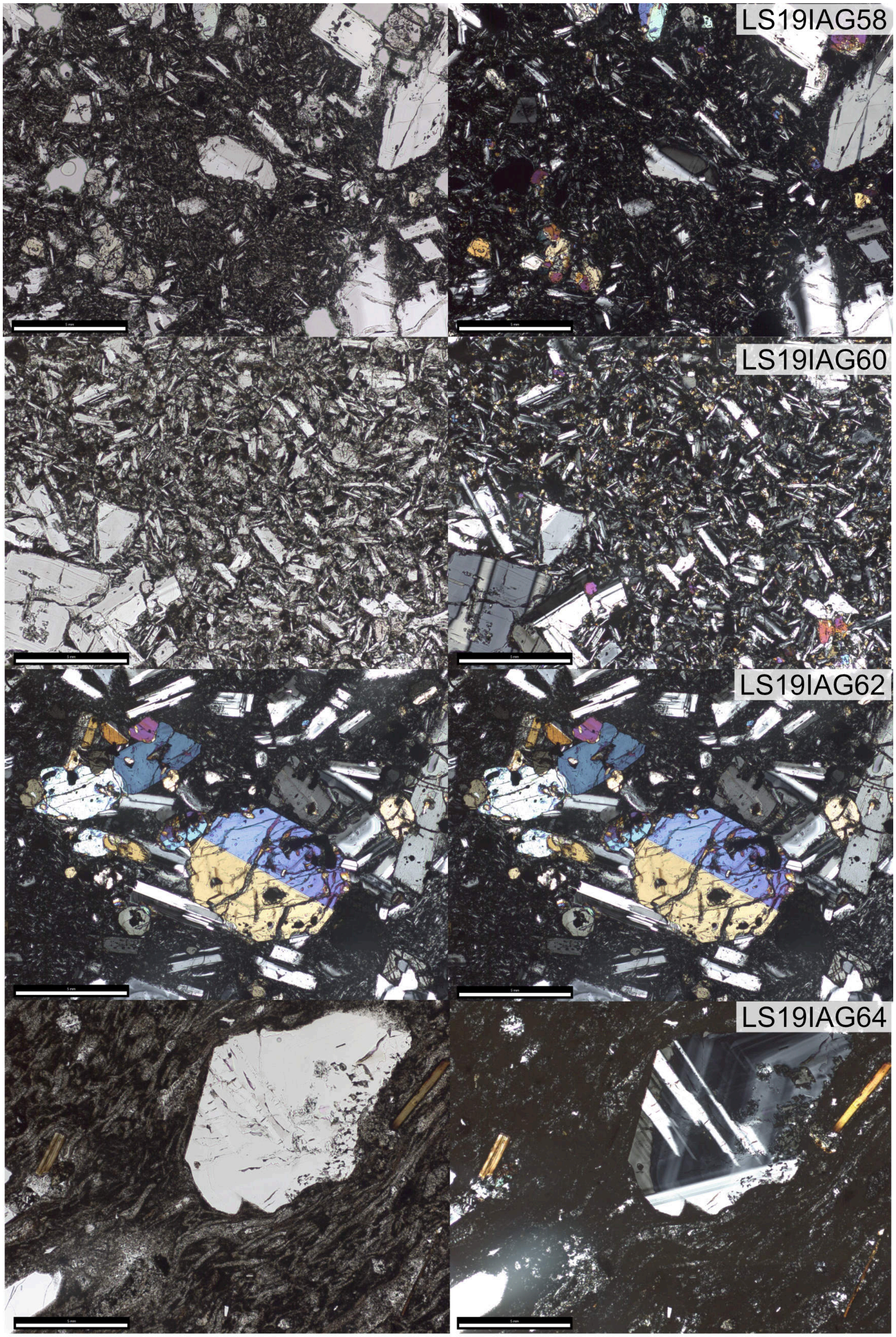
LS19IAG58
LS19IAG60
LS19IAG62
LS19IAG64

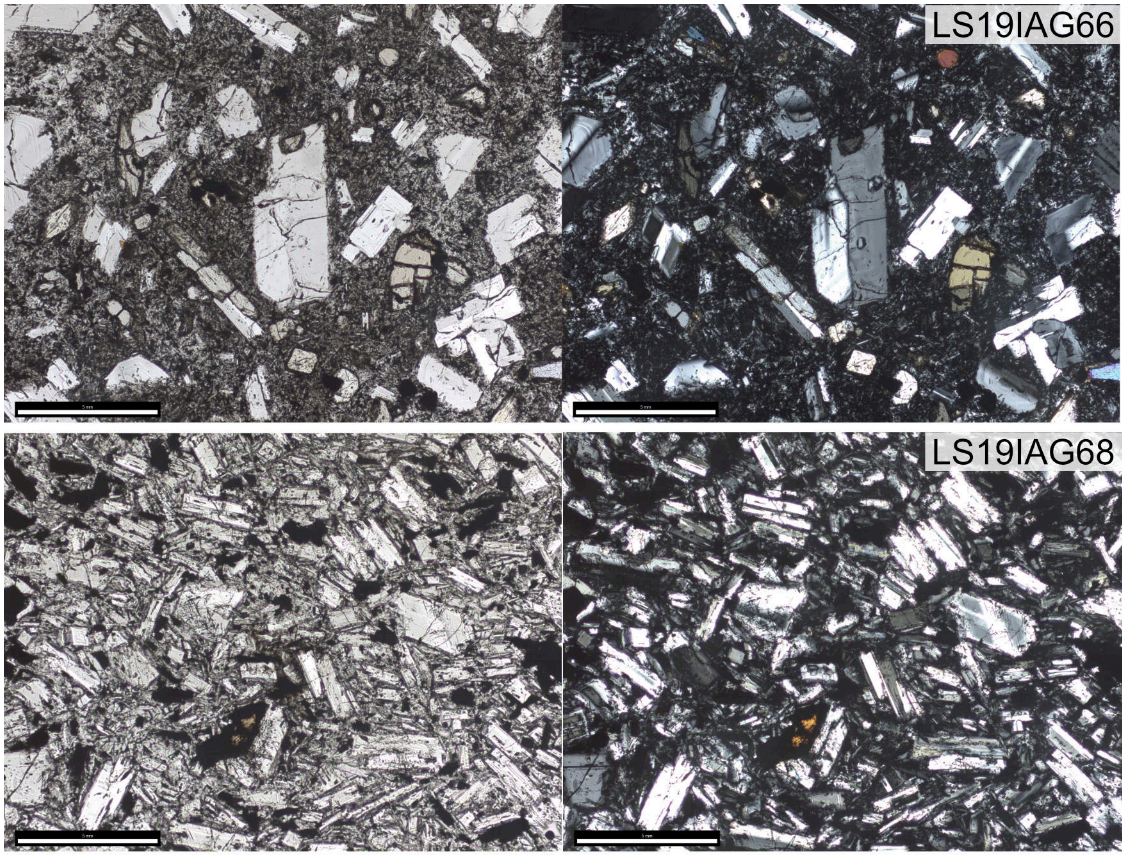

Photomicrographs in this series (LS18 and LS19) are all taken by Sabbeth at 5x. Scale bars are 5 mm. Photomicrographs on the left are taken in plain-polarized light, and those on the right are taken in cross-polarized light. LS19IAG62 seems to have only cross-polarized images - this is an error.

Figure S1: Photomicrographs of samples in this study.

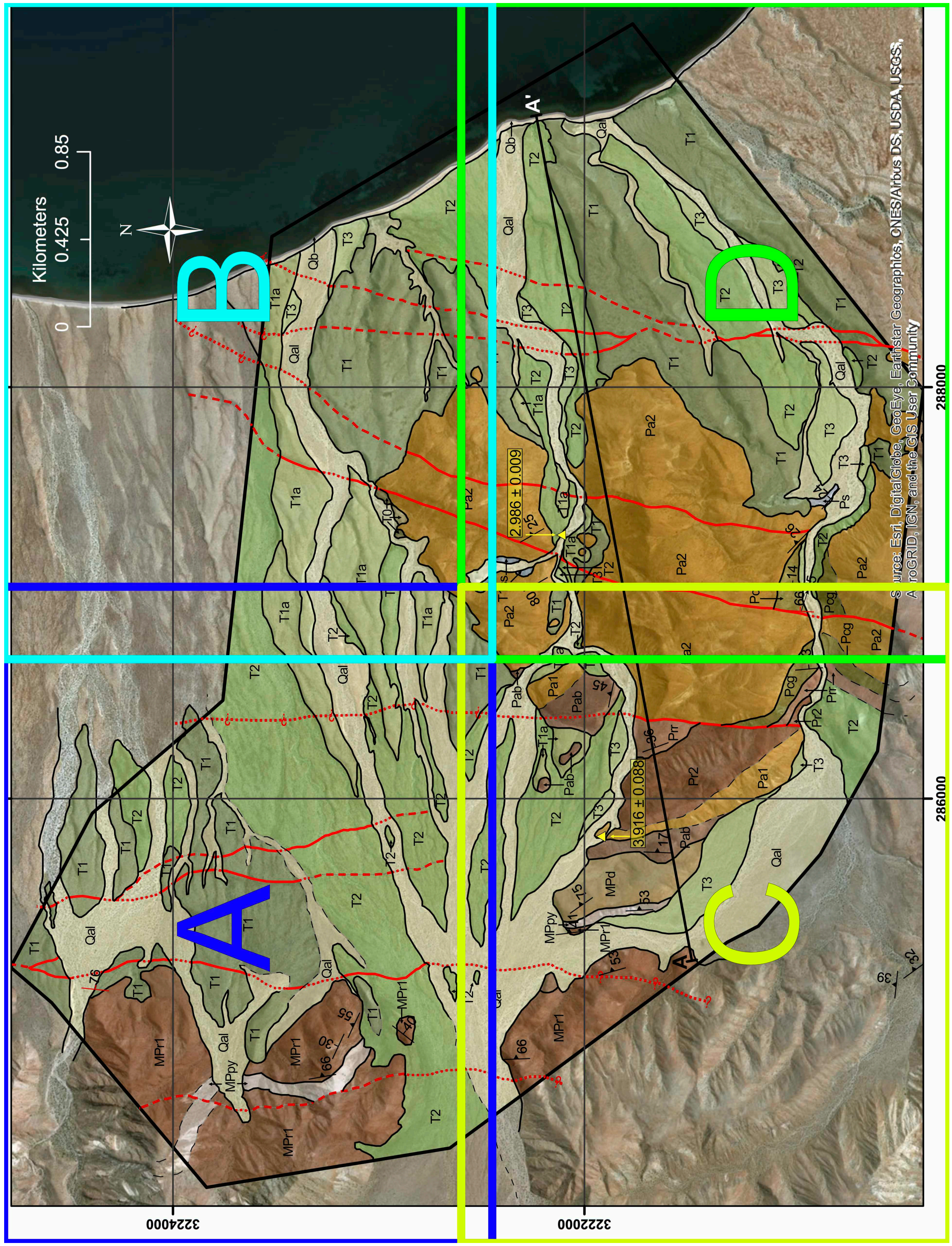

Kilometers
0
0.425
0.85
N
A
B
C
D
A'
3224000
3222000
286000
288000
2.986 ± 0.009
3.916 ± 0.088
Source: Esri, DigitalGlobe, GeoEye, Earthstar Geographics, CNES/Airbus DS, USDA, USGS, AeroGRID, IGN, and the GIS User Community

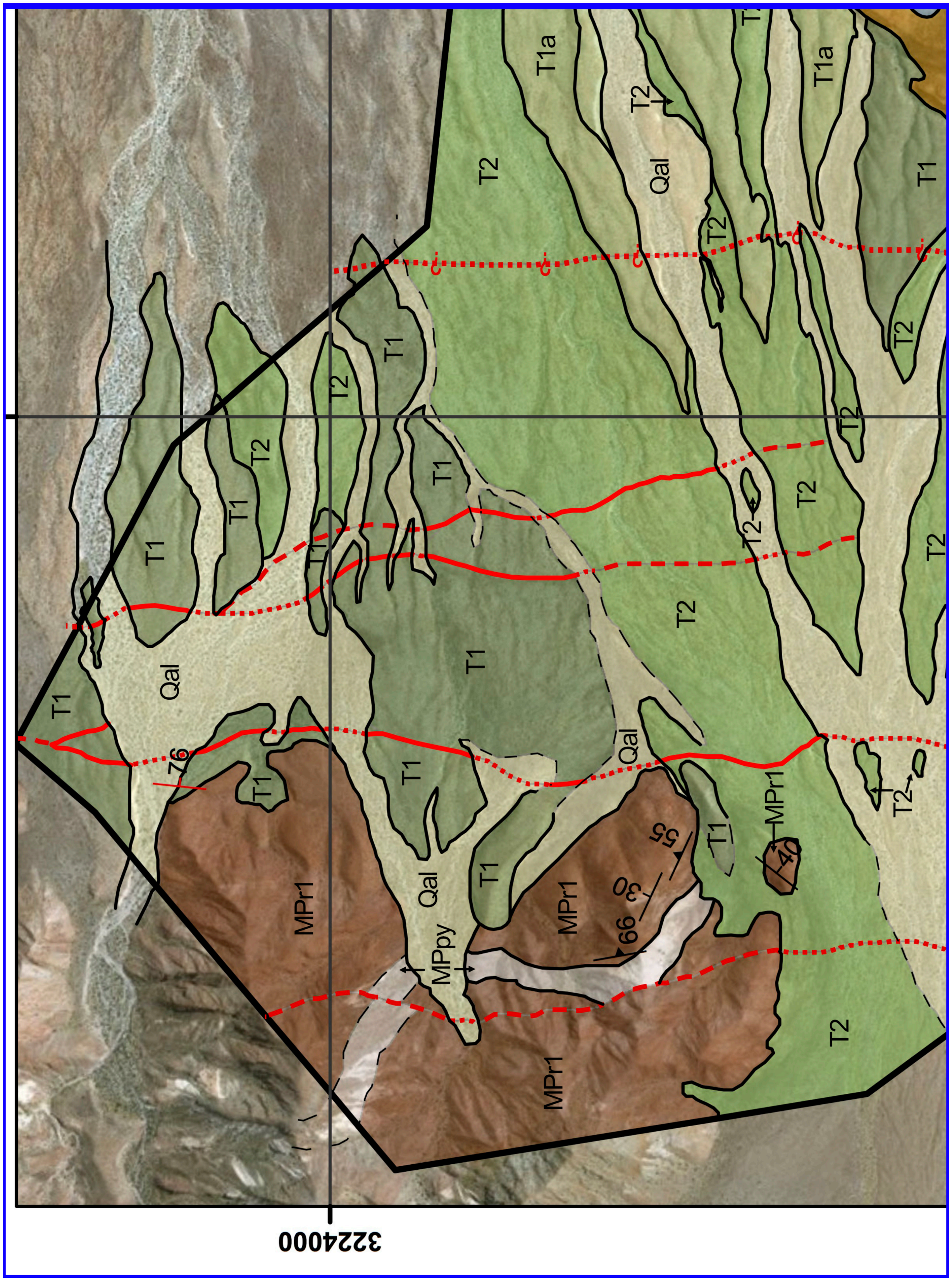
T1a
T2
Qal
T1
MPr1
MPpy
76
55
30
66
40
3224000

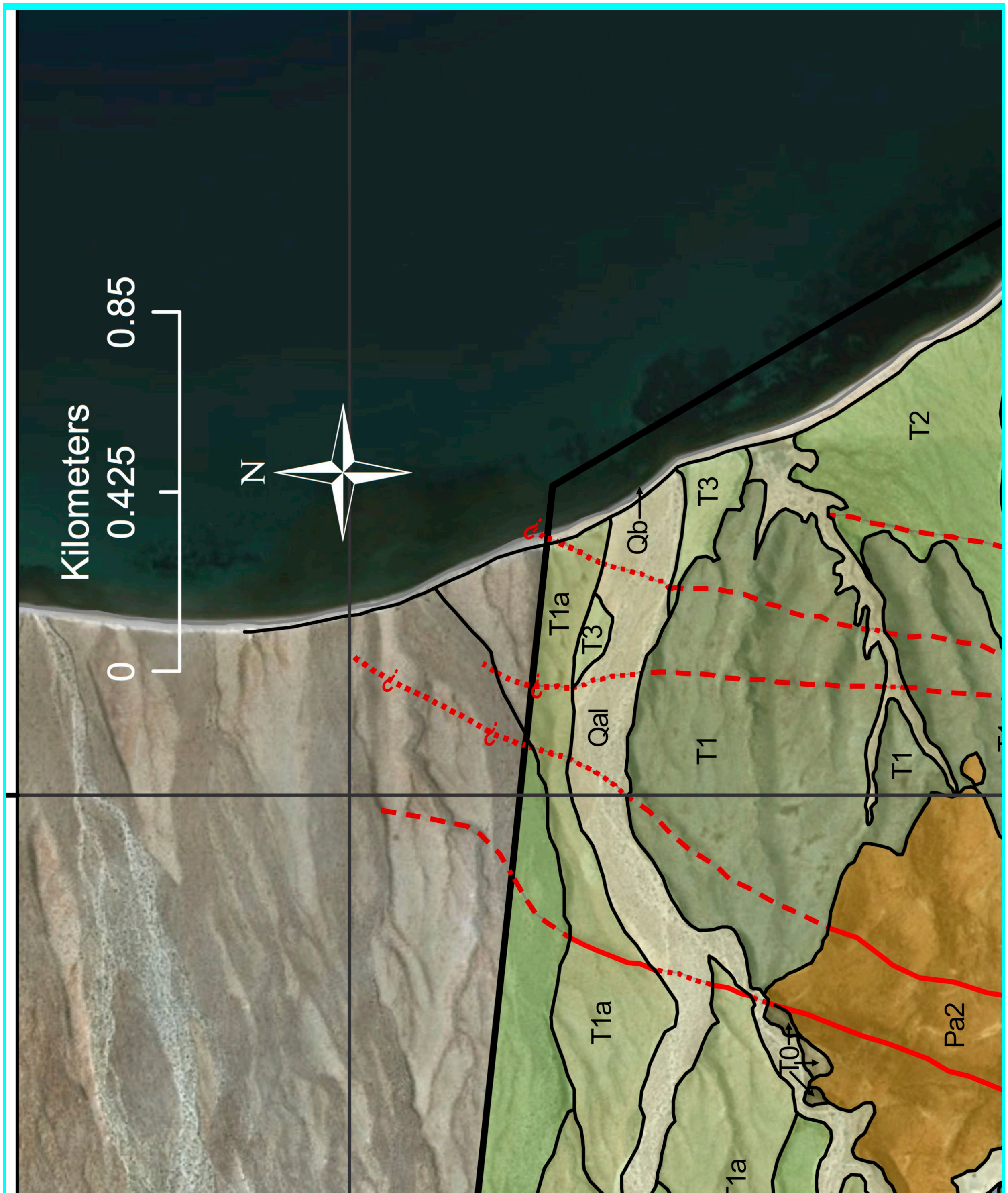
Kilometers
0
0.425
0.85
N
Qb
T1a
T3
Qal
T1
T2
T0
Pa2

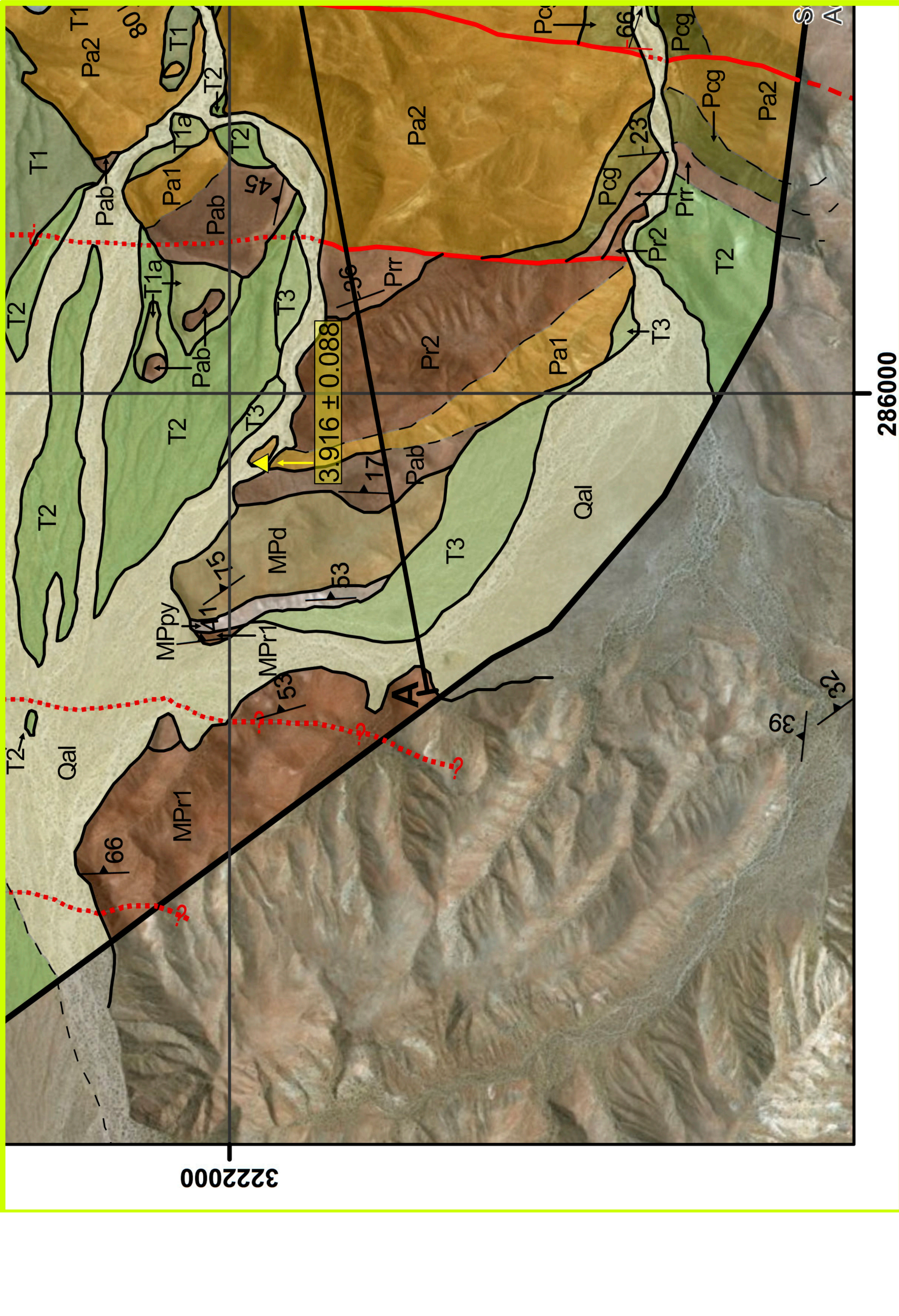
3.916 ± 0.088
286000
3222000
A
Qal
T1
T1a
T2
T3
Pa1
Pa2
Pab
Pcg
Prr
Pr2
MPd
MPpy
MPr1

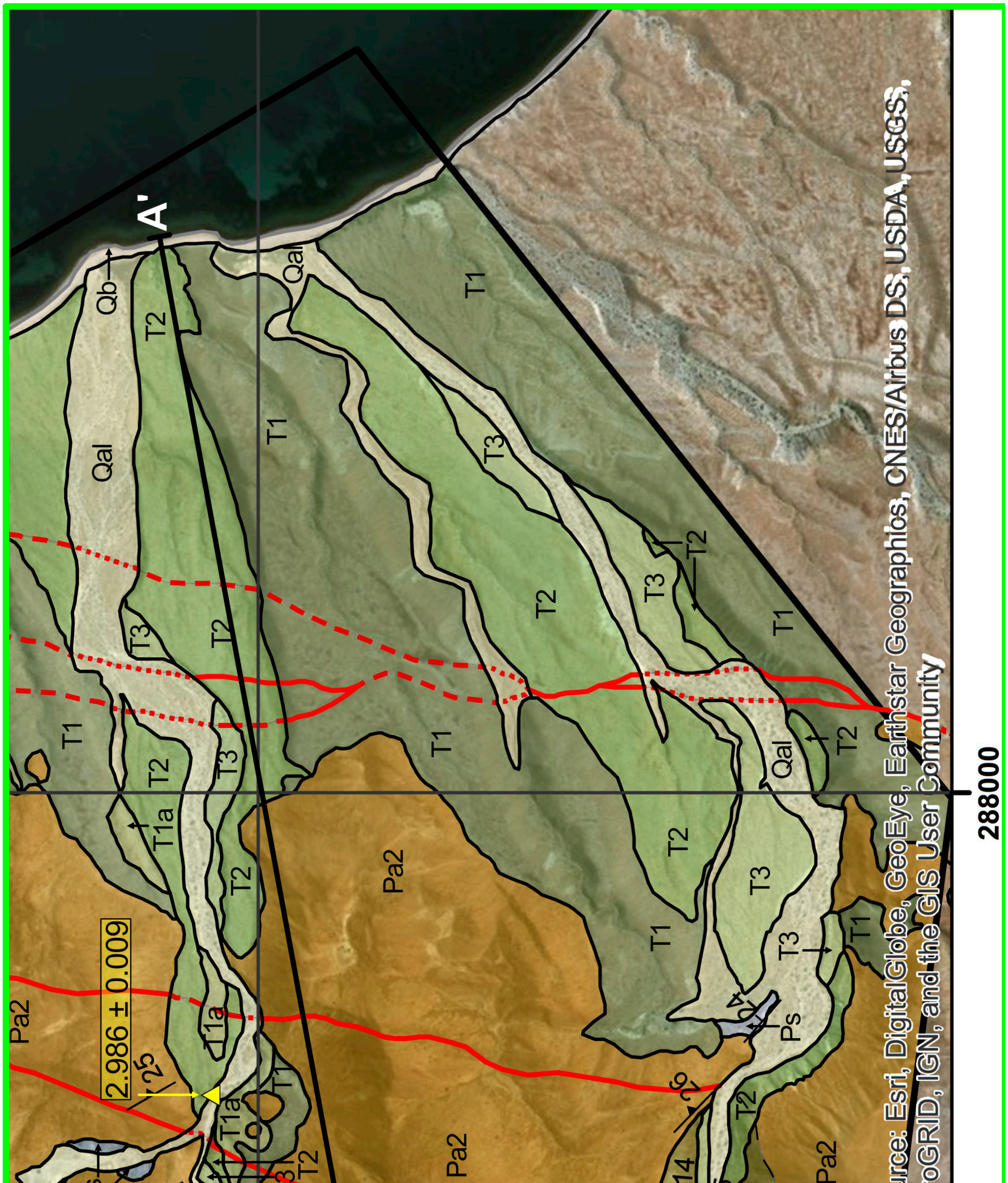
A'
Qb
Qal
T1
T2
T3
T1a
T1ss
Pa2
Pcg
Ps
2.986 ± 0.009
25
80
14
66
5
26
4
288000
Source: Esri, DigitalGlobe, GeoEye, Earthstar Geographics, CNES/Airbus DS, USDA, USGS,
AeroGRID, IGN, and the GIS User Community

Figure S2: Zoom-ins of geological map in northern area

Geological map of northern area blown up into four separate pages, indicated in the first index map.

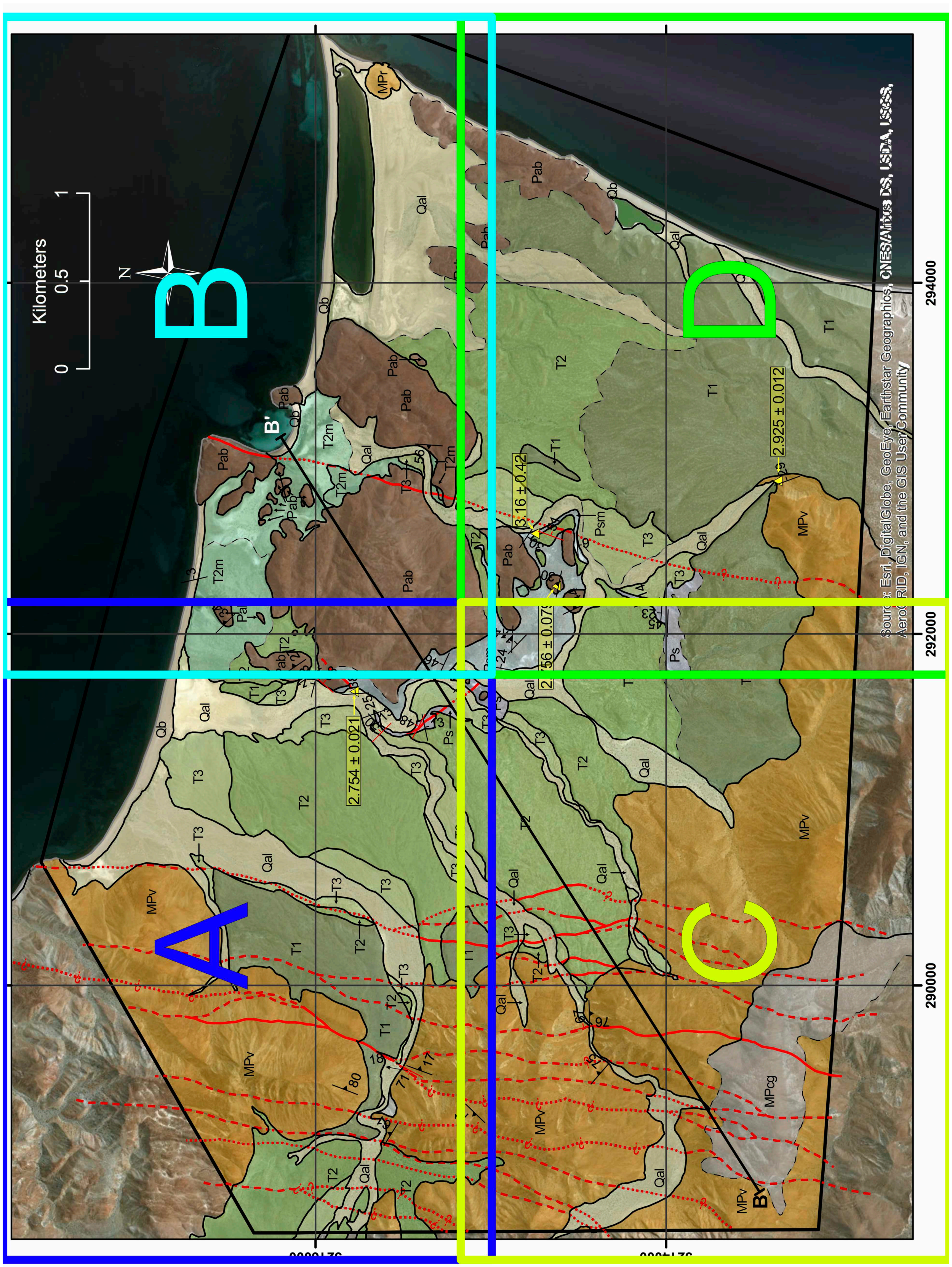
A
B
C
D
Kilometers
0
0.5
1
N
B'
B
290000
292000
294000
2.754 ± 0.021
3.16 ± 0.42
2.925 ± 0.012
MPv
MPcg
T1
T2
T2m
T3
Qal
Qb
Pab
Ps
Psm
Source: Esri, DigitalGlobe, GeoEye, Earthstar Geographics, CNES/Airbus DS, USDA, USGS, AeroGRID, IGN, and the GIS User Community

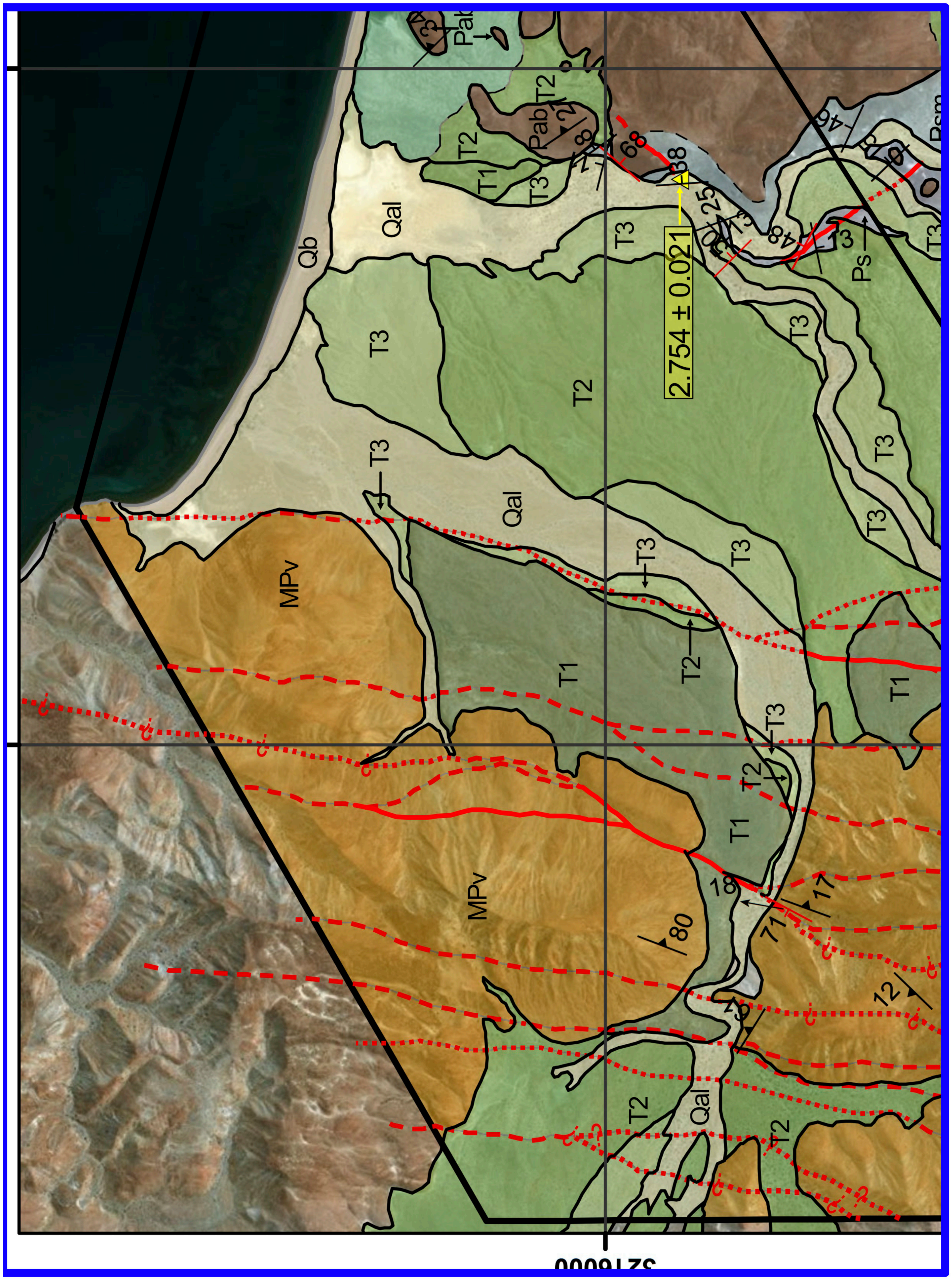
Qb
Qal
T1
T2
T3
MPv
Pab
Ps
Psm
2.754 ± 0.021
5276000


Kilometers
0
0.5
1
N
B'
Pab
Qb
T2m
Qal
MPr
T3
T2
56
3
34

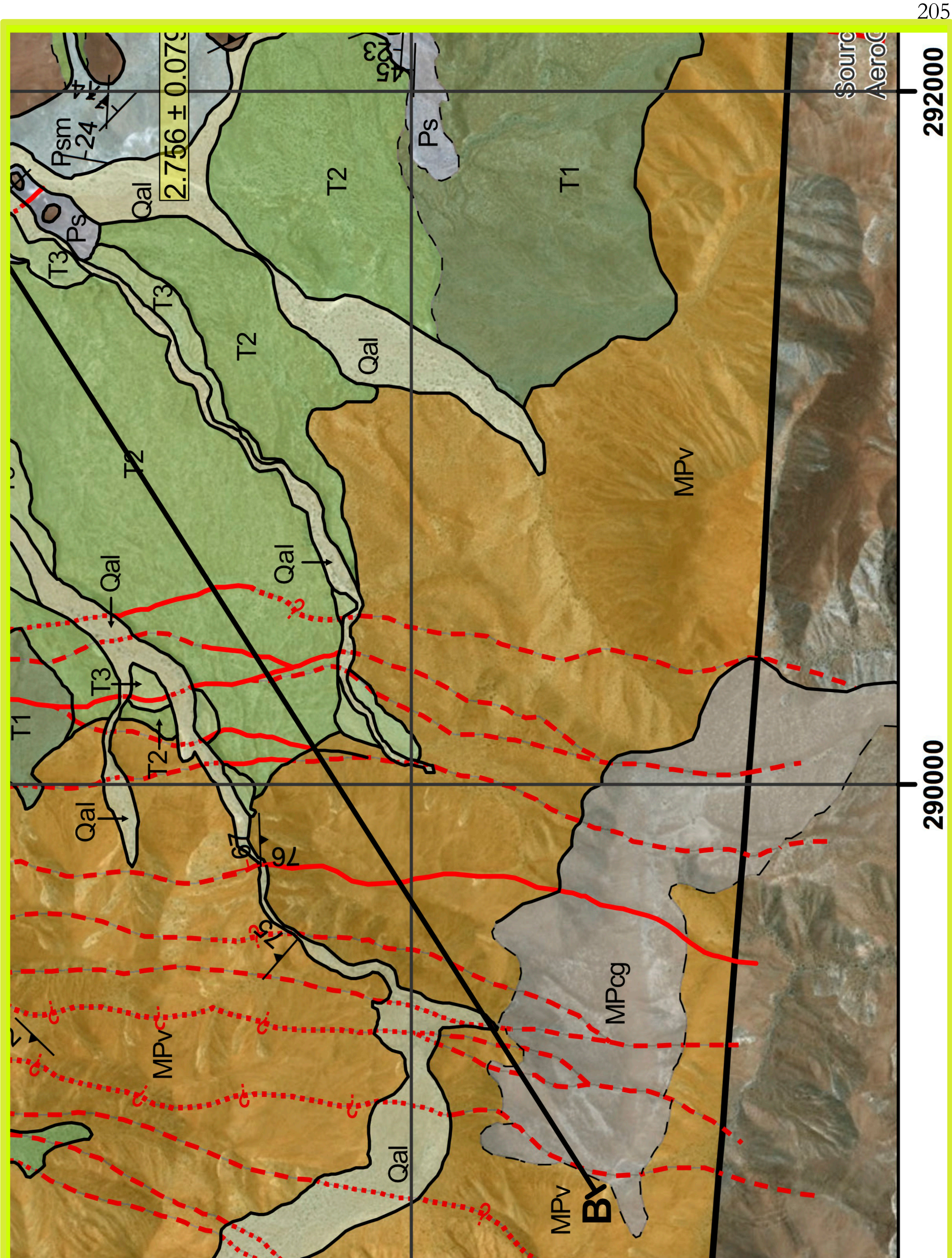

Qal
T1
T2
T3
Ps
MPv
MPcg
B'
290000
292000

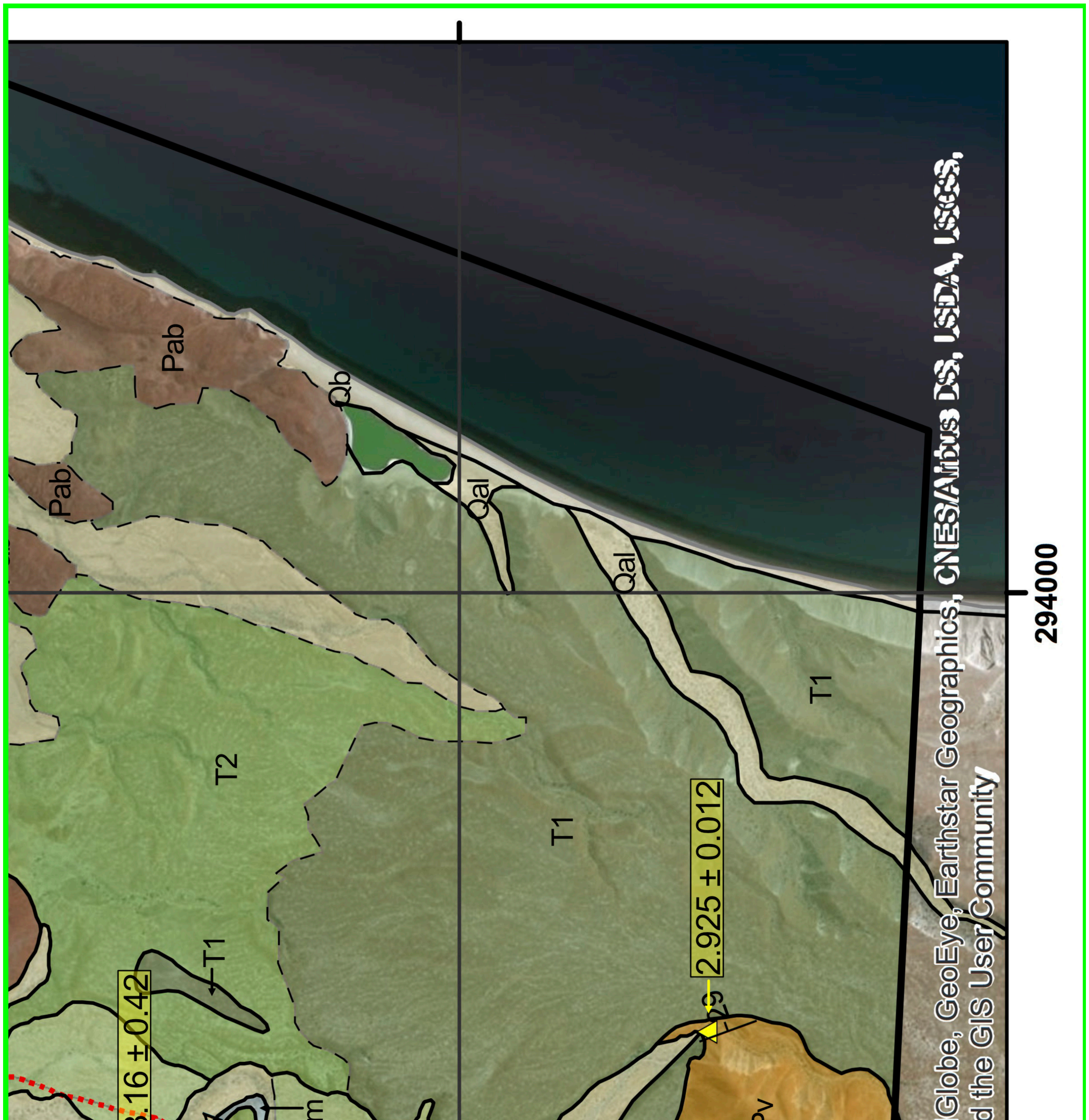
Pab
Qb
Qal
T2
T1
Psm
T3
MPv
Ps
3.16 ± 0.42
2.925 ± 0.012
292000
294000
Source: Esri, DigitalGlobe, GeoEye, Earthstar Geographics, CNES/Airbus DS, USDA, USGS, AeroGRID, IGN, and the GIS User Community

Figure S3: Zoom-ins of geological map in southern area

Geological map of southern area blown up into four separate pages, indicated in the first index map.

Chapter 3

Chapter 3: Observations and implications of Pliocene sedimentation on southeastern Isla Ángel de la Guarda, Mexico

ABSTRACT

We document a Pliocene sedimentary unit on southeastern Isla Ángel de la Guarda. The Pliocene sediments were deposited stratigraphically between two basaltic andesite flows, which we dated with $^{40}Ar/^{39}Ar$ geochronology. The older Miocene-Pliocene volcanic unit is 2.925 ± 0.012 Ma, and the younger, overlying Pliocene basaltic andesite has three ages: 2.754 ± 0.021 Ma, 2.756 ± 0.079 Ma, and 3.16 ± 0.42 Ma (a maximum age). The Pliocene sediments locally can be fossil-rich, with oysters and pectens, indicating a marine environment of deposition. Fossils are not found consistently throughout the unit, and parts of the Pliocene sedimentary unit may be lacustrine. We suggest that a high-elevation conglomerate may be a lateral variation or a source of the Pliocene sedimentary unit. Our evidence of Pliocene marine and/or nonmarine sedimentation is consistent with similar units mapped throughout the northern Gulf of California. Pliocene sedimentation is indicative of basin subsidence during Pliocene time, likely related to the jump in rifting from the Lower Tiburón basin to the Lower Delfin basin.

INTRODUCTION AND GEOLOGIC SETTING

As discussed in Chapter 2, Isla Ángel de la Guarda is a microcontinental block in the Gulf of California. Baja California was transferred from the North American to the Pacific plate in the late Miocene due to a plate reorganization related to the end of arc-related volcanism (Gastil et al., 1979;

Seiler et al., 2009). Between 3 and 2 Ma, fault activity moved from the Upper Tiburón to Upper Delfin basin, and from the Lower Tiburón to Lower Delfin basin, eventually moving the plate boundary to the west side of Isla Ángel de la Guarda, beginning to break it off of Baja California (Nagy and Stock, 2000; Stock, 2000). Tectonic reconstructions place northwestern Isla Ángel de la Guarda as far north as Puertecitos (Figure 1a) at 3 Ma (Nagy and Stock, 2000; Stock, 2000; Seiler et al., 2010; Bennett et al., 2016a). For this reason, we examine Pliocene sedimentary rocks at other locations around the northern Gulf of California (Figure 1b).

Review of Pliocene sediments around the Northern Gulf of California

The following section details Miocene and Pliocene sediments around the Northern Gulf of California, and is summarized in Figure 2.

Llano El Moreno Formation and Salada Formation in San Felipe

Nearly 75 km NNW of Puertecitos, west of the town of San Felipe several Pliocene marine facies are mapped in the Miocene-Pliocene Llano El Moreno Formation and the Pliocene Salada Formation near San Felipe (Boehm, 1982, 1984) (Figures 1 and 2a). The Miocene-Pliocene Llano el Moreno Formation is divided into two members: the ~6 Ma San Felipe diatomite and the younger Cañón Las Cuevitas Mudstone (Boehm, 1982). The San Felipe Diatomite Member consists of diatomite and claystone subfacies. These subfacies are rich in microfossils, including diatoms, planktic forams, radiolarians, and silicoflagellates.

The Cañón Las Cuevitas Mudstone Member contains two subfacies: (1) Mudrock Subfacies and (2) Muddy Sand Subfacies. The Mudrock subfacies is generally bedded, aside from in some areas, which are lightly bioturbated. There are irregular silty dolomitic wackestones and mudrocks with high sand content in the subfacies. The Muddy Sand Subfacies is less than 10 m thick, and composed of ≤ sand-sized material, with quartz, volcanic lithic fragments, and pumice > alkali feldspar grains, with rare pecten fragments. The Cañón Las Cuevitas Mudstone Member has calcareous benthic and rare planktic foraminifera, and otherwise is absent of microfossils. The member is no younger than 1.8 Ma, constrained by megafauna in the overlying Salada Formation (Boehm, 1984).

The Pliocene Salada Formation lithofacies C is divided into 6 subfacies, including (C1) small-scale trough cross-bedded sandstones, (C2) planar bedded sandstones, (C3) bioturbated planar bedded sandstones, (C4) coarse clastic-bearing sandstones, (C5) large-scale cross-bedded sandstones, and (C6) orthoconglomerates (Boehm, 1984). These subfacies include pumiceous arkosic sands, ashy pumiceous sandstones, microfossils, fossil hash, bivalves, mollusk fragments, megafossils, and ichnofossils (Boehm, 1982, 1984).

Puertecitos Formation in Puertecitos

The Puertecitos Formation in the Puertecitos volcanic province (Figures 1 and 2b), described by Martín-Barajas et al. (1995, 1997), contains two Miocene-Pliocene westward-thinning wedge-shaped sedimentar sequences, deposited both in subaerial and submarine depositional settings. In submarine depositional settings, the Puertecitos Formation is divided into two marine sequences, and in subaerial depositional settings, coeval parts of the formation are dominated by a volcanic section, described by Martín-Barajas et al. (1995). The submarine section unconformably lies on top of ~6 Ma lava domes and pyroclastic density current deposits (Tuff of El Canelo). The volcanic section has the 3.27 Ma Tuff of Valle Curbina near the bottom, and the ~3.0 Ma Tuff of Mesa El Tábano in the upper half (Martín-Barajas et al., 1995).

The Matomí Mudstone Member is described by Martín-Barajas (1997). This lower unit of the two marine sequences, has type localities in Valle Curbina and Arroyo La Cantera (previously called Arroyo

Los Heme Norte (Stock et al., 1991)). The base of the Matomí Mudstone Member crops out east of Sierra San Fermin, where a ~6.5 Ma rhyolitic tuff (Lewis, 1996) is unconformably overlain by a 5 m thick poorly bedded, class-supported basal conglomerate, with imbricated cobbles and boulders, and a matrix of calcareous hash of sand dollars. This is interpreted to be a rocky shoreline deposit. The conglomerate grades upward into a ~10 m thick coarse- to medium-grained sandstone, interpreted to be intertidal to shallow subtidal deposits, with *panopea* indicating bathymetry between intertidal zone and 20 m depth (Martín-Barajas et al., 1997).

The stratotype of the Matomí Mudstone Member in Valle Curbina is a 35 m thick, coarsening-upward sequence described by Martín-Barajas (1997). The lower 20 m consists of a yellow-ocher mudstone. Upper beds consist of coarse sandstone and gravel, which grade upward into a muddy fossiliferous sandstone-siltstone, and also into a sandy to pebbly conglomerate. Eastward, the beds grade into fine-grained marine deposits. A dark gray, 2.5 m thick lithic tuff exists near the top of the mudstone. Mudstone in Arroyo La Cantera is intensely bioturbated, with muddy fossiliferous sandstone strata, which are poorly sorted with normally graded 2 to 10 m thick beds and massive 1 m thick beds (Martín-Barajas et al., 1997).

The Delicias Sandstone Member, the upper of the two marine sequences, best represented in the eastern range front of the Sierra San Fermin, consists of two sections: (1) the lower, diachronous El Canelo section, which overlies the Tuff of Valle Curbina, and (2) the upper Campo Cristina section (Martín-Barajas et al., 1997). The El Canelo section is a 10-m thick coarsening upward sequence, with fine-grained sandstone, siltstone, and mudstone at its base. The sandstone beds contain macrofossils of mainly oysters and turritelids (Martín-Barajas et al., 1997).

Interstratified in the lower half of the section is a poorly consolidated white-gray pumice-lapilli tuff, which is considered the submarine equivalent of unit b in the Tuff of Mesa El Tábano (Stock et al., 1991) and includes a 3.08 ± 0.4 Ma tephra (Martín-Barajas et al., 1995). Upward in the El Canelo marine section is a coarse-grained fossiliferous sandstone and pebble conglomerate, which grades upward into a nonmarine bedded sandy conglomerate. Interbedded is a 2.5 m thick subaerially reworked pumice lapilli tuff (Martín-Barajas et al., 1997).

The upper Campo Cristina section, described by Martín-Barajas et al (1997) consists of a 2.5 to 3-m thick clast-supported and matrix-supported conglomerate, composed of >85% volcanic rocks, and <10% subrounded plutonic and metamorphic rocks, and intraclasts of mudstones derived from underlying fine-grained deposits. The conglomerate grades into a 2 to 3 m thick white pumiceous sandstone correlated with the reworked pumice lapilli tuff interbedded in the upper part of the El Canelo section. This sandstone is overlain by a coarse sandstone interbedded with matrix-supported conglomerate, which grades upward into sequence of cyclic-fining upward sandy mudstone and fine-grained sandstone. Toward the top is the uppermost volcaniclastic deposit in the sequence, a reworked greenish lapilli tuff (Martín-Barajas et al., 1997).

Bahia de Guadalupe

In the Bahia de Guadalupe area, presumably Cretaceous basement granitic rocks, interpreted as part of the Peninsular Ranges batholith, are overlain by a buttress nonconformity of conglomerates, which are further overlain by marine sedimentary rock, described by Parkin (1998) (BG, Figure 1b, and Figure 2c). A poorly welded biotite-rich pink tuff, with an $^{40}Ar/^{39}Ar$ age of 22.6 ± 0.4 Ma, lies stratigraphically above granitoid basement. Elsewhere, volcanic debris-flow deposits and lava flows unconformably overlie granitoid basement. This older debris-flow unit is unconformably overlain by a ~40 m thick, 15-20° SE-dipping, younger unit of debris-flow deposits, with poorly sorted, 2-10 cm, angular clasts of "andesitic rhyolite [sic]" (Parkin, 1998, p. 37) and ≤1 m clasts of white tuff, andesite, and rhyolite. In angular unconformity over the debris flow deposit, sub-horizontal immature arkosic and conglomeratic sandstones have a matrix of coarse to very coarse-grained grus. Clasts in the conglomerate are 2 to 50 cm across, and include felsic volcanic rocks, granitoids, andesites, and highly oxidized basalts. The conglomerate fines upward into a fossiliferous sandy siltstone, with fossils of mollusks, gastropods, turritella, and sand dollars (Parkin, 1998).

Pliocene siltstones in the Bahia de Guadalupe area are interpreted to record lateral and/or temporal changes from nonmarine to marine deposition (Parkin, 1998). Lower subunits are red-brown units that tend to be gypsiferous and nonfossiliferous, but with occasional root casts. The gypsum is interpreted to be primary, suggesting deposition in an arid environment. Upper subunits are yellow-orange to yellow-green – yellow-orange, and contain burrows, gastropods, clam shells and casts, and ≤15 cm oyster shells. These subunits have been interpreted as mid-late Pliocene in age. The upper and lower subunits interfinger, suggesting alternating transgressions and regressions due to tectonic subsidence, sediment supply fluctuation, or sea-level changes (Parkin, 1998).

Further upsection is a 10-20 m thick Pliocene unit (labeled Tsv by Parkin (1998)) of interfingering siltstone and epiclastic sandstone of ash and pumice lapilli (Parkin, 1998). Some outcrops contain planar lamination and ripple cross-lamination. Inversely-graded pumice lapilli and well-rounded pumice clasts are interpreted to suggest possible syndepositional reworking of volcaniclastic ejecta in a marine environment (Parkin, 1998). Marine fossils within this unit further indicate a reinception of volcanism concurrent with marine deposition. These siltstones and epiclastic sandstones are overlain by 2.6 ± 0.8 Ma basaltic lava flows and 2.6 ± 0.7 Ma cinder cones dated by $^{40}Ar/^{39}Ar$ (Parkin, 1998).

Isla Tiburón

Earliest marine sedimentation in the southwestern Isla Tiburón basin (Figure 1b) began in the latest Mioene to early Pliocene time (Bennett et al., 2015) (Figure 2d). Sedimentary units overlie the Tuff of Arroyo El Canelo, which has an $^{40}Ar/^{39}Ar$ age of 6.1 ± 0.5 Ma (Nagy et al., 1999), the Tuff of Ensenada Blanca which has a K-Ar age of 6.11 ± 1.81 Ma (Neuhaus, 1989), and the Tuff of Hast Pitzcal which has an $^{40}Ar/^{39}Ar$ age of 6.44 ± 0.05 Ma (Bennett et al., 2015). These sedimentary units include marine sandstone, landslide breccia, sedimentary breccia, marine conglomerate, and shelly calcarenitic sandstone. Overlying these sedimentary units are the Tuff of Arroyo Sauzal, the Tuff of Oyster Amphitheater (6.01 ± 0.2 Ma), and Tuffaceous marine sandstone and conglomerate (6.2 to 4.3 Ma microfossils) (Bennett et al., 2015).

The marine deposits overlying the tuffaceous marine sandstone and conglomerate include marine and non-marine conglomerates. Overlying the conglomerates are the Tuffs of Hipat Mesa (4.34 ± 0.20 Ma), which are further overlain by pyroclastic deposits, rhyodacite feeder dikes (3.7 ± 0.9 Ma) and the rhyodacite of Cerro Starship (3.51 ± 0.05 Ma, 4.13 ± 0.09 Ma) (Bennett et al., 2015). Quaternary units overlying the rhyodacites include both non-marine and marine terraces, beach and alluvial sands and gravels, and eolian deposits (Bennett et al., 2015).

Isla San Estebán

Sedimentary units are mapped overlying dacitic lava flows on the nearby island, Isla San Estebán (Desonie, 1992; Calmus et al., 2008). The dacitic lava flows have K-Ar ages as young as 2.69 Ma and 2.58 Ma. Overlying them is a conglomerate, which is further overlain by ~5m thick very shallow marine sequence composed of shelly beach sand, gypsum, and conglomerate (Calmus et al., 2008). The fossil assemblage of this sedimentary unit includes planktonic foraminifers, benthonic foraminifers, ostracods, and calcareous nannoplankton, and is considered younger than 5.3 to 3.6 Ma (Table II, Calmus et al., 2008).

METHODS

Geologic Mapping, Stratigraphy and Sampling

We mapped lithologies, terraces, and faults at the 1:15,000 scale (Figure 3). Locations were confirmed using a handheld Garmin InReach Explorer+ for GPS coordinates in WGS 1984. We used a Brunton compass for structural measurements, set to a declination of 12° in November 2018 and earlier, and 10°E in April 2019. Lithologic names were assigned in the field based on phenocrysts in volcanic units, and later modified if geochemistry became available. In sedimentary units, lithologic names were assigned by grain size, clast lithology, or presence of fossils. Faults were identified by clear offset within a unit, often best seen from an arroyo with secondary gypsum filling cracks within faults, or from their cutting patterns across otherwise smooth terrace treads.

Samples of volcanic rocks were collected for petrography, geochemistry, and geochronology. When sampling, care was taken to avoid weathered surfaces by breaking down much larger pieces that were first removed from outcrops. To maximize sample usability and minimize carrying weight, outer portions of samples and any seemingly weathered surfaces were removed on-site as much as possible when time permitted. Sedimentary rock samples were taken when we suspected that units would have reworked ash or other datable material, or when units contained pectens, oysters, or a likelihood of microfossils, in case of fossil identification or age determinations. Care was taken to determine that fossils collected from units were indeed from within the sedimentary unit, and not more recent shells put in place by birds or humans enjoying a seafood meal (shell middens). At times, it was challenging to discern between true fossils and remains of a snack. We erred on the cautious side of snack when shells were not found within lithified sediment or were only found on top of loose sediment. Any pliable or fragile samples, including shells, sandy units, and gypsum beds, were wrapped with care to avoid damage during transport. Macrofossils including shells and oysters were sent to Dr. Judith Terry Smith at the Smithsonian Institution for identification. Samples are listed in Chapter 2, Table 1.

Geochronology

We chose a subset of samples from the study area for $^{40}Ar/^{39}Ar$ geochronology based on their importance in our stratigraphy and structure interpretations, volume, and weathering characteristics. The samples were prepared for $^{40}Ar/^{39}Ar$ geochronology at the California Institute Technology and at the USGS Menlo Park.

Sample preparation procedures are similar to those described for XRF geochemistry in Chapter 2. Samples of the bulk unit were cut into ~5 cm chunks with a water saw, and saw marks were sanded off to remove any contaminants. The chunks were sonicated in DI water to further reduce possibility of contamination and remove vug-filling materials. The chunks were then wrapped in paper and broken down with a hammer to ~2 cm chunks, and finally crushed with a chipmunk crusher to <3 mm.

Groundmass and feldspar separates were prepared for dating via the $^{40}Ar/^{39}Ar$ method. After processing in the chipmunk crusher, samples were ultrasonicated, and sieved to 250 to 355 μm. Groundmass and feldspar were concentrated from crushed samples using a Frantz magnetic separator and purified by handpicking under a binocular microscope. For feldspar separates 50 to 100 mg of material was prepared and for groundmass separates 100 to 150 mg of material was prepared. Feldspar and groundmass separates were packaged in Al foil along with Bodie Hills sanidine monitor minerals (assumed age 9.7946 ± 0.0031 Ma, equivalent to Fish Canyon sanidine age of 28.099 ± 0.013 Ma;

Fleck et al., 2019) and encapsulated in quartz vials. The quartz vials were wrapped in 0.5 mm thick Cd foil to shield samples from thermal neutrons during irradiation. Samples were irradiated for 1 hour in the central thimble of the U.S. Geological Survey TRIGA reactor in Denver, CO (Dalrymple et al., 1981) at a power level of 1 MW.

Following irradiation, monitor minerals were analyzed by total fusion using a CO2 laser attached to a MAP216 mass spectrometer. The remaining samples were rewrapped in degassed Ta foil and the argon was extracted incrementally in 10 to 13 discrete temperature steps using a diode laser attached to a MAP216 mass spectrometer at the U.S. Geological Survey in Menlo Park, California. Temperatures were monitored using an optical pyrometer. Prior to measurement of Ar isotopic composition, groundmass separates were degassed at 400°C, and plagioclase separates were degassed at 500° C until undesirable gases (e.g., water, nitrogen, and hydrocarbons as measured by a Granville-Phillips 835 Vacuum Quality Monitor) were reduced to acceptable levels. For all experiments, extracted Ar was exposed to a 4Å tungsten filament, 125K cold finger, and two SAES ST-175 getters (one operated at 300°C and one at room temperature) to remove active gasses. $^{40}Ar/^{39}Ar$ ages are calculated using the decay constants recommended by Steiger and Jäger (1977).

Uncertainties in reported $^{40}Ar/^{39}Ar$ ages include propagated uncertainties in counting statistics and J values. Instrumental mass discrimination was calculated by repeated measurement of atmospheric argon, assuming $^{40}Ar/^{36}Ar_{atmosphere} = 298.56 \pm 0.31$ (Lee et al., 2006). See Calvert and Lanphere (2006) and Fleck et al. (2014) for additional details regarding analytical techniques, mass spectrometer design, and irradiation procedures.

RESULTS

Geologic Mapping

In this southern study area, we map three main volcanic units, and seven sedimentary units (Figure 4, field photos in Figures 4a-h). Major units include MPv, an older volcanic unit, Ps and Psm, Pliocene sedimentary and marine sedimentary rocks, and Pba, a capping Pliocene basaltic andesite. Foliations in MPv generally strike NNE or NNW and dip to the east. Bedding attitude is consistent with units mapped in the northern study area, and we have mapped units assuming that units young to the east.

The contact between MPv and Pliocene sedimentary rocks is assumed based on bedding attitude, but not documented in outcrop. The contact between Ps and Pab is well documented, as discussed below. Both the attitude of the outcropping contact and east-dipping flow direction indicated by foliation in Pab are consistent with our presumption of consistently gently east-dipping bedding attitude, and units younging to the east. MPv is overlain by MPcg in a buttress unconformity. Terrace material T1-T3 overlies much of the field area, and terraces are classified as cut, rather than fill or strath terraces. As described below, terraces are distinguished by relative elevations and surface characteristics. Contacts between T2 and T2m are in some places gradational.

Faults consistently strike NNE, and dip to the east, (Figure 3) often with normal separation down-to-the-east accompanied by some right-lateral slip. Some antithetic west-dipping faults are observed in densely faulted areas. These antithetic faults are also extensional and commonly splay and join together with synthetic faults. One fault observed cutting through unit Ps (Figure 5h, 29.049429° N, -113.141384° E) has a NW-trending trace, which distinguishes the fault from other NNE-striking faults and warrants further discussion below. We observe several lineations with a similar trend in the overlying unit, Pba, but argue that they may not be tectonic (below). The natures and certainties of mapped contacts and faults are further discussed in Chapter 2.

Stratigraphic units and Sampling

We present stratigraphic descriptions of sedimentary units found on southeastern Isla Ángel de la Guarda (Figure 4).

Miocene-Pliocene Volcanic rocks (MPv)

Miocene-Pliocene lava flows are mapped in the south, west, and southwest of our study area, and are stratigraphically below the Pliocene sedimentary rocks. These lava flows are largely andesitic in composition, and are discussed in further detail in Chapter 2 (Figure 5d). These volcanic flows underlie Ps, Pliocene sedimentary rocks. An andesitic lava mapped in the south of our study area (29.031695° N, -113.126953° E) has an $^{40}Ar/^{39}Ar$ age of 2.925 ± 0.012 Ma (LS19IAG68), which provides a maximum age constraint for the Pliocene sedimentary rocks.

Miocene-Pliocene conglomerate (MPcg)

A Miocene-Pliocene conglomerate is mapped at elevations of 160 to 190 m above sea level, overlying MPv in a buttress unconformity in the southwest part of this field area. Although the conglomerate was not mapped in detail, due to its high elevation and far distance from base camp, its outcrop pattern is visible in air photos and we were able to confidently map the extent of the unit from a topographically high point. Clasts found fallen from the unit are angular and subangular quartzites and and other volcanic rocks. One sample taken is a welded tuff with plagioclase phenocrysts and carbonate-filled vesicles.

Pliocene sedimentary rocks (Ps amd Psm)

We document a Pliocene sedimentary strata (Ps) stratigraphically above Miocene-Pliocene volcanic flows (MPv), and below a Pliocene andesitic basaltic lava flow (Pab). The unit is designated Psm when marine fossils (pectens and oysters) are observed within sediments, indicating a marine environment of deposition, and is designated Ps when the unit is not demonstrably marine. A ~0.5 km^2 gently dipping area of several white-hued exposures indicates the widespread extent of a marine sequence, with a thickness on the order of 100 m. Within this flat area, several outcrops show good exposures of the sedimentary and marine sedimentary sequences. *Argopecten ventricosus* and *Striostrea* or *Crassostrea* were sampled in this unit (Figure 7a, b), and areas with observed macrofossils are mapped as Psm. Psm, (Ps with marine fossils) exists largely toward the top of the Ps section.

Near the stratigraphic base of Ps lies a poorly stratified, inversely graded (coarsening-upwards) pumiceous sandstone with subangular to subrounded reworked pumice pieces up to 3 cm in diameter, and sand-sized lithic fragments. Photographs are included in Figure 5c, and a representative stratigraphic column is included in Figure 6a.

Two outcrops from the middle of Ps contain interbedded gypsum and sandstones, and no fossils were observed in either of these outcrops. The first of these has a stratigraphic bottom-to-top sequence of a limestone (LS19IAG50), siltstone (LS19IAG52), sandstone (LS19IAG51), and a 1 cm thick gypsum bed within the sandstone (LS19IAG49) (photograph in Figure 5g1 and stratigraphic column in Figure 6b). The beds are all thin (~1-2 cm thick) and undulatory, with a hummocky appearance, similar to that of an algal mat. The bases of some beds are erosionally scoured into their substrate, and visible at the base of the outcrop. This outcrop is ~2 m thick, in total, and the limestone within it is ~1.5 m thick.

The gypsum appears again in the second mid-Ps outcrop approximately 300 m south along an arroyo, likely discontinuous due to erosional removal outcrop or discontinuous bedding. The gypsum reaches 10-15 cm at its thickest, and splits into at least 3 gypsum beds interbedded within the sandstone (Figure 5g2, 3). Long axes of gypsum crystals are orthogonal to bedding. The branching pattern of gypsum and orientation of gypsum crystals suggests that it represents secondary veins formed by infiltration of fluids after deposition (Machel, 1985). The top subunit with sand-sized pumice is seen scouring into an underlying sandstone with pebble-sized, angular pumice and lithic clasts.

At the top of Psm, one particular outcrop displays several informative features of this marine sequence (Figure 5b and Figure 6c). At the bottom of the outcrop lies a >2 m-thick, recessive, sandy unit with large oysters (*Striostrea* or *Crassostrea*, LS19IAG54, Figure 7b) and pyroclastic pieces including ash and pumice (LS19IAG56). Hummocky lumps indicate bioturbation in this unit. This recessive unit is overlain by a ~2 cm-thick gypsum bed. Above the gypsum is a resistant, 1.5 m-thick conglomerate with black pebbles, followed by a ~1 m thick recessive grey sandstone with angular clasts of vesicular basalt (LS19IAG58, plag >>ol) and ~1 cm angular yellowed pyroclastic pieces (LS19IAG57). At the very top of the recessive grey sandstone are fragments of pectens and oysters (LS19IAG53). The uppermost Pliocene unit in this outcrop is a resistant sandstone with subangular pyroclastic and basaltic clasts. The sandstone is unconformably overlain by terrace material.

A fallen ~5 m by 3 m boulder of the uppermost section of this outcrop preserves a key contact relation between Psm and Pba. Stratigraphic direction is easily determined by the order of subunits relative to the intact outcrop (Figure 5f). In the boulder, the uppermost sandstone exhibits paleoliquifaction structure as the matrix to a fragmented boulder of basalt ~0.7 m in diameter with vesicular, glassy margins (LS19IAG60). We interpret this boulder to be a lava bomb, which fell into the sandstone, breaking into two pieces. The wet sandstone then simultaneously forced upward through the two pieces in liquefied form, indicating that sediment was still wet and soft at the time of eruption, or the onset of Pba extrusion, suggesting conformability of the contact.

Another observation at the top of the sedimentary sequence, ~1 km WNW of the aforementioned example, is a baked contact between a grey sandstone (LS19IAG47) and overlying basalt of Pba (LS19IAG66). The grey sandstone becomes pinkish-orange within ~6 m of the basalt, and bright orange within ~1.5 m of the basalt, indicating a depositional contact (Figure 5e). Here, the unit is not demonstrably marine because no fossils were observed.

In summary, this 100 m thick Pliocene sedimentary unit was deposited over an area of at least 0.5 km^2. The unit grades laterally within the area, and includes marine intervals documented by macrofossils, sandstones, siltstones, limestones, gypsum beds, and outcrops with scour marks. These observations imply marine deposition in areas with fossils, and marine or lacustrine depositional environments in other parts of the unit. The end of recorded deposition must have occurred within close timing of the onset of Pba flows.

Pliocene Basaltic Andesite flow (Pba)

Pliocene basaltic andesite (Pba) overlies Pliocene sedimentary rocks (Ps and Psm) (Figure 5a). Contacts between Ps and Pba are described above, and include a baked contact, and a ballistic fragment from the upper unit found fallen into and deforming the lower unit. The basaltic andesite marks the end of recorded sedimentation.

Terraces 1-3

Features unique to terraces in Chapter 2 are consistent in this southern field area. T1 is only seen at high elevation, or in areas furthest inland. T2 is largely a smooth and extensive terrace, making it a good surface for hiking long distances. T3 is close in elevation to Qal, and the two are at times hard to distinguish. T2 has a marine counterpart, lying in a small basin between hills of Pba. Its marine nature is evidenced by fossils sampled in our field work, and identified by Dr. J.T. Smith (Figure 7c).

Geochronology

We report $^{40}Ar/^{39}Ar$ ages from andesitic to basaltic lavas for four samples (Table 1), constraining the minimum and maximum ages of the sedimentary sequence, and the duration of sedimentation (Figure 8). For each sample, we report the percentage of radiogenic material lost, a weighted-mean plateau age (WMPA), and an isotope correlation (isochron) age. We determined whether to rely upon the plateau age or isochron age based on the lower of the mean square of weighted deviates (MSWD, (Wendt and Carl, 1991)).

The andesitic lava flow in MPv (below the marine sequence) is constrained by two groundmass samples, LS19IAG68a and LS19IAG68b, from which we use a weighted mean isochron age. The Pliocene basaltic andesite (Pba) overlying the sedimentary rocks is constrained by three samples from an overlying basaltic lava flow: LS19IAG62, LS19IAG66 and LS19IAG60. Two of these samples, LS19IAG62 and LS19IAG60, have U-shaped release patterns. LS19IAG62 has a clear minimum in its radiation release, but LS19IAG60 does not. For this reason, LS19IAG62 can be relied upon as an eruption age, but LS19IAG60 is considered a maximum age. We use an isochron age from LS19IAG66.

The Miocene-Pliocene volcanic flow (MPv), underlying the Pliocene sedimentary rocks (Ps), has an $^{40}Ar/^{39}Ar$ age of 2.925 ± 0.012 Ma from sample LS19IAG68 (Figure 8d, e). The Pliocene basaltic andesite (Pba) has the following ages: 2.756 ± 0.079 Ma (LS19IAG62), 2.771 ± 0.011 Ma (LS19IAG66) and 3.16 ± 0.42 Ma (a maximum age as previously discussed from LS19IAG60).

We can confidently determine that sedimentation began after 2.925 ± 0.012 Ma, and ended prior to 2.756 ± 0.079 or 2.771 ± 0.011 Ma, considering the 3.16 ± 0.42 Ma a maximum, (and somewhat irrelevant) age. Based on field observations including the baked contact and volcanic bomb in soft sediment, it appears that volcanism occurred as the sediment was still soft. Sedimentation of the Pliocene sedimentary rocks (Ps and Psm) can be constrained to a period of ≤ ~170 ka. These ages help inform our stratigraphic column (Figure 4) and cross-section (Figure 9).

DISCUSSION

Tonalite, found north of both study areas on Isla Ángel de la Guarda, makes up basement rock, and is observed as xenoliths within MPv (Figure 5a, d). Pliocene volcanic rocks make up the oldest unit sampled and dated with $^{40}Ar/^{39}Ar$ geochronology in this study. Following emplacement of Pliocene lavas, the beginning of a marine incursion is documented by a pumiceous sandstone. Two outcrops mark a transition from the marine sequence to a subaerial environment with volcanic activity: a baked contact, and a ballistic volcanic bomb emplaced in deformed soft sediment. Timing of volcanic activity is constrained by three separate samples of the same Pliocene basaltic andesite lava unit, Pba. These samples include the baked contact, the volcanic bomb, and another sample from Pba.

This ~100 m thick sequence of sedimentary rocks containing marine deposits is indicative of a marine incursion with a duration of ~150 ka, beginning after 2.925 ± 0.012 Ma, and ending by 2.754 ± 0.021 Ma, over an aerial extent of ~0.5 km^2 (Figures 2, 3). Onset of the marine incursion is recorded by deposition of pumice into water, indicated by the bimodality in size of pumice to lithic fragments of ~10:1 in the epiclastic sandstone (Figure 5c) (Cashman and Fiske, 1991). That the pumice was deposited into water indicates that a basin existed here, perhaps due to sea level rise or rifting-related tectonic subsidence, and no local volcanism was recorded for ~150 ka. Although macrofossils indicate that some areas were deposited in marine environments, it is not evident that the rest of Ps was similarly deposited in a marine environment..

The sequence of siltstone, sandstone, limestone, and gypsum in the Pliocene sedimentary unit (Figure 5g) adds to evidence of a marine or lacustrine depositional environment. The siltstone has undulatory bedding, indicating bioturbation of the material. Although the gypsum is laterally continuous over hundreds of meters, its deposition is not necessarily an indicator of a marine rather than of a lacustrine environment. Further, the gypsum branches, laterally, and has crystals aligned perpendicular to bedding, which is common in secondary mineralization (Machel, 1985), rather than in primary deposition. Scour marks are observed within Ps, both above and below previously mentioned lithologies (Figure 5g), and indicate flow to the east.

Future work should investigate collected sandstone and mudstone samples for microfossils to determine bathymetric depth during sedimentation. Additionally macrofossils (pectens and oysters) were not found in all outcrops of Ps, and so we cannot be sure that all parts of the unit are marine rather than lacustrine. Those outcrops in which macrofossils were collected are mapped as Psm. Future work should employ Sr isotopes to determine marine versus lacustrine environments (Spencer and Jonathan Patchett, 1997). This data can inform how continuous Psm truly is, the depth of bathymetry during deposition, and whether deposition took place in a marine or lacustrine environment.

A pebbly conglomerate is mapped in the top of Ps (Figure 5b). The pebbles are basaltic, black, and rounded. These pebbles may be derived from an older basaltic flow, or perhaps one active closer in time to the deposition of the conglomerate. Since the age of the overlying unit Pba is well constrained in three samples, including a baked contact, determining $^{40}Ar/^{39}Ar$ ages for these pebbles was not a priority.

The transition from a marine or subaqueous environment to a subaerial environment with volcanic activity is recorded by two outcrops of basaltic andesite lavas, and several more outcrops of this basaltic andesite lava confirm its >6 km^2 spread throughout the southern field area. $^{40}Ar/^{39}Ar$ ages from the aforementioned basalt flow and basaltic flow on a baked contact, and a third $^{40}Ar/^{39}Ar$ age from another basaltic lava outcrop constrain the minimum age of the marine incursion. It is without question that the baked contact records an onset of volcanic flows in Pba, and the $^{40}Ar/^{39}Ar$ ages of Pba are tightly constrained.

Timing constraints for the Pliocene sedimentary unit

The $^{40}Ar/^{39}Ar$ age for the volcanic bomb is less well constrained, and should be interpreted as a maximum age, since the apparent age diagram (Figure 8a) shows a parabolic relationship between apparent age and cumulative ^{39}Ar released. However, in considering the volcanic bomb to define the end of the marine sequence, and new onset of volcanism, we must question whether or not the boulder's eruption was syndepositional with the end of the marine sequence. This embodies the possibilities of (1) a time gap, or unconformity, between the sediment and volcanic bomb, (2) was the bomb hot upon deposition, (3) if the boulder is older than its underlying marine sequence.

To confirm that the volcanic bomb's emplacement was, indeed, syndepositional with the end of the marine sequence, the aforementioned questions are addressed. (1) The sediment around the boulder is deformed, and squishes up into the crack in the boulder, implying that the sediment was soft upon deformation by the falling object. (2) The boulder was hot upon deposition, evidenced by its glassy, vesicular margins. (3) If, in fact, the reader does not find our evidence for a ballistic volcanic bomb satisfactory, an alternative solution is that the boulder fell in from a nearby landslide or other source. Its older age would be proof, in this case, that the boulder was not erupted near the end of the marine incursion. However, as mentioned earlier, we argue that the age is strictly a maximum due to the nature of radiation lost in the sample. Additionally, the two other post-marine basaltic andesite flow samples confirm the ~2.7 Ma volcanic activity.

If, for some reason, the andesitic flow with an $^{40}Ar/^{39}Ar$ age of 2.925 ± 0.012 was not deposited before the marine sequence, we no longer have a maximum age constraint on the marine incursion, and we have "lost" our sense of stratigraphic direction. This scenario could be due to (1) an error in our presumed bedding attitude of NNE-striking beds dipping gently to the SE, (2) an error in $^{40}Ar/^{39}Ar$ age, or (3) the andesitic flow was, in fact, intrusive, and not a flow. However, these scenarios seem unlikely for (several) reasons: (1) bedding attitude is largely consistent over several kilometers, (2) the pumiceous sandstone stratigraphically above the andesitic lava and below the marine sequence records a reasonable transition in depositional conditions from marine to non-marine, (3) two reliable *minimum* age constraints are in agreement of ~2.7 Ma as an age for the most recent Pliocene basaltic lava, and this is further confirmed by the maximum age of the volcanic bomb of 3.16 ± 0.42 Ma, (3) the sample (LS19IAG68) of andesitic lava is consistent with extrusive andesitic lava flows – it is vesicular and does not have large, interlocking grains.

Miocene-Pliocene conglomerate

We next consider the source for MPcg, its age, and its relationship to the sedimentary sequence. In any scenario, the conglomerate needs a higher elevation source for its clasts. Such a source likely is derived from the larger Baja California block, in which case the western side of IAG would have been attached to Baja California at the time of deposition, or from farther north on IAG. As in any provenance study, a possible but less interesting scenario is that sources for the clasts may no longer exist.

MPcg overlies MPv in an observed buttress unconformity, and is mapped at elevations of c. 160-180 m above sea level. We only have one age for MPv. MPv encompasses a variety of lava flows and possible other lithologies, which presumably were not sourced all from one vent, are not all conformable, and may have been deposited over a long or discontinuous time scale. For instance, the MPv sample with an $^{40}Ar/^{39}Ar$ age of 2.925 ± 0.012 Ma may be a small deposit, and deposited after the conglomerate. Thus, we do not have a strong age constraint for MPcg. So, we consider that MPcg was sourced from Baja California or IAG, and deposited (A) in a time equivalent to Ps, (B) after Pba was deposited, (C) before MPv, or (D) from within IAG.

In scenario A, it is considered that MPcg is a lateral variation of the Pliocene sedimentary and marine unit, and was deposited between ~2.7 and 2.9 Ma. Larger clasts from the Baja California block would be deposited west, closer to the source, making up MPcg, and deposited material would fine and thicken in distal areas in the east (Ps). The MPcg and Ps unit would be deposited on a gently east-dipping slope towards the opening Gulf of California and the Tiburón Fault. This unit would later be eroded during the carving and deposition of Quaternary terraces. If western IAG were attached to the larger Baja California block, rifting in the Ballenas Channel would need to occur after ~2.9 Ma.

Timing of rifting in scenario A is consistent with reconstructions of the Gulf of California by Bennett et al. (2016a), which show IAG detaching from Baja California after 3 Ma, and before 2 Ma, when a rift becomes active between the IAG block and the Baja California block. This model is also consistent with thermal observations of the Ballenas transform fault zone, indicating activity on the transform fault before 1.8 Ma (Seiler et al., 2009).

In scenario B, it is considered that the MPcg makes up material into which the Quaternary terraces were carved. Material into which Quaternary terraces are cut is not well studied or described, and perhaps the MPcg material is covered by thinly draped material deposited after terraces were carved. In this case, MPcg and terrace material, which would be time-equivalent, would be deposited after Pab, since terrace material is found overlying Pab. This would imply that MPcg and terrace material are younger than 2.754 ± 0.021 Ma, and that IAG was still connected to the east side of the Baja California block at the time.

Scenario B cannot coexist with scenario A, since terrace material is distinctly separate from Pliocene sediments in Ps both in its mapped area and in its constrained age (terrace material is found both southwest and northeast of Ps in large areas). However, since there is not a minimum age constraint on MPcg or terrace material, scenario B is still consistent with Gulf of California reconstructions and thermal observations (Seiler et al., 2009; Bennett et al., 2016a). Of course MPcg and terrace material would need to be deposited before significant separation from the Baja California block.

Next, we consider scenario C, where due to either the small sample size of MPv geochronology, or the complex nature of MPv, the conglomerate is older than the 2.925 ± 0.012 Ma andesitic lava in MPv. Scenario C leaves MPcg without any mapped time-equivalent units or lateral variations in our field area. In this case, MPcg may have been deposited over a large geographical extent (of ≥ 8 km^2 looking at map area), and would be mostly eroded away or otherwise covered. Such a conglomerate might be closer in age to those mapped in the central part of IAG, which have ages constrained by interbedded tuffs and lavas of 6.4 ± 0.3 Ma, 7.2 ± 0.2 Ma, and 11.8 ± 0.2 Ma (Cavazos Álvarez, 2015).

Another scenario, D, is that the conglomerate is sourced from other locations on Isla Ángel de la Guarda, either from bedrock or from late Miocene conglomerates in the central part of the island.

Mountains ~ only ~250 m northwest reach elevations of ~350 m, almost 200 m higher in elevation than MPcg (~170 m above sea level). Mountains ~15 km northwest of MPcg reach elevations of 1000 m, more than 800 m higher in elevation than MPcg. Presumably, bedrock exposed in these higher-elevation mountains, or other mountains that have since eroded away, could have been transported several hundred meters southwest to their current location in MPcg. However, bedrock mapping in the mountains on this particular part of the island is not complete enough for us to correlate clasts.

In addition to possible bedrock as a source for MPcg, we consider late Miocene conglomerates mapped in the central part of the island (Cavazos Álvarez, 2015) as a possible source. These conglomerates, near Punta Los Machos on IAG and ~35 km northwest of MPcg mapped in this study, reach elevations of 250 to 300 m (from GoogleEarth elevations). Although a clast transported from Los Machos to MPcg today would likely be unable to travel over the mountains between (~700 m elevation), the conglomerates may have extended to higher elevations prior to more recent erosion and faulting.

Scenario C is least preferred, as it does not particularly agree with the one $^{40}Ar/^{39}Ar$ age of the presumably older MPv. No material with a composition similar to the single clast of densely welded tuff found in MPcg was observed near terraces, and so it is unlikely that terraces were carved into a material made up of MPcg, as would be the case in scenario B.

Scenario A and D appear the most feasible, as they are consistent with all observations in this study. Further field work examining clasts in MPcg and determining an $^{40}Ar/^{39}Ar$ age for the densely welded tuff sample collected from MPcg (LS19IAG45) would allow us to determine a provenance for clasts within MPcg, whether the source be from within IAG as a bedrock or conglomerate, or from Baja

California. This would allow us to make a better estimate of the conglomerate's age, and also inform updated tectonic reconstructions connecting the source and sink.

Tectonic implications

Tectonic reconstructions show that rifting jumped from the Lower Tiburón to the Lower Delfin basin, north of Isla Ángel de la Guarda, beginning between 3 and 2 Ma (Nagy and Stock, 2000; Stock, 2000; Seiler et al., 2009; Bennett et al., 2016a). Sedimentary deposition, whether it be lacustrine or marine, is an indicator of subsidence and consistent with rifting history in the Gulf of California. This study area may be evidence of very localized basin formation, subsidence, and rifting on southeastern Isla Ángel de la Guarda during the rift transition.

Between 3 and 2 Ma, units in this study were deposited, and southeastern Isla Ángel de la Guarda (i.e., this study area) was probably within 0.25° of latitude of the Pliocene marine rocks on the north end of Bahia de Guadalupe described by Parkin (1998), and less than 50 km northeast (Nagy, 2000; Nagy and Stock, 2000; Stock, 2000; Bennett et al., 2016a). Units described near Bahía de Guadalupe, discussed in detail in Geologic Background, are remarkably similar to those in our study area. Units include basalt flows with $^{40}Ar/^{39}Ar$ ages of 2.6 $\pm$ 0.8 Ma, and a Pliocene epiclastic sandstone of ash and pumice lapilli, and interbedded with ash containing pumice clasts, interpreted to be deposited subaerially, and possibly reworked and/or deposited in shallow water (Parkin, 1998). The similarity in units from this study indicates that they were likely deposited in a very similar environment. Possibly, the units were also deposited in a similar time frame and geographical location. Pliocene sediments ~75 km northwest of Puertecitos (Boehm, 1982, 1984) bear some resemblance to those found in this study, and a further examination of microfossils collected in this study may yield similarities in fossil identification or bathymetry patterns to those collected by Boehm (1982, 1984). A depositional environment favorable to sediments in this study, sediments NW of Puertecitos, and sediments near Bahia de Guadalupe may have existed at length along the western Gulf of California in late Pliocene time. Each of these instances of Pliocene sedimentation may indicate a new basin opening and subsiding as rifting opened along the Ballenas channel during Pliocene time.

Further sampling and mapping would help to determine the continuity and extent of this rift-related basin on Isla Ángel de la Guarda. An examination of microfossil assemblages and Sr isotopes would inform how deep this basin was, and whether it was connected to marine waters in the Gulf of California.

Any tectonic study investigating subsidence of basins must take into account sea level changes that may appear in the sedimentary record as tectonic subsidence. Oxygen isotopes indicate that sea level has fallen ~40 m since ~3 Ma (Miller et al., 2005). Although the sea level has fallen overall throughout Pliocene time, there are many short, episodic cycles in sea level, a larger fall and rise in sea-level at ~2.5 Ma. It is possible that the sediments mapped in Ps were deposited precisely after the 2.5 Ma sea level fall, as the sea level rose again. Once sea level stopped rising and stabilized, the area would no longer be subaqueous, and deposition may be no longer recorded. Although this could account for tens of meters of sea level change if the sediment was deposited ~2.5 Ma, we are confident that the sediment was deposited before ~2.7 Ma, and before sea level rose. The overall fall in sea level during the Pliocene, and during deposition of the sediments, illustrates that the subsidence is truly tectonic, and not a product of sea level rise.

In Pliocene to Quaternary time, Baja California has been subject to greater uplift rates than Sonora, strengthening the argument for tectonic uplift (Ortlieb, 1990). Geochronologic data on Sonoran shorelines and terraces from U-series and radiocarbon show little vertical motion on terraces on the eastern side of the Gulf of California since the Pliocene (Ortlieb, 1991). In contrast, Baja California has been subject to a mean uplift rate of 100 mm/1000 yr for the past 1 Ma. Locally, both in the northwest part of Baja California and around the La Reforma Caldera, uplift rates have maxima around 200 to 300 mm/1000 yr, but overall, Quaternary vertical motions are slower by at least an order of magnitude (Ortlieb, 1990).

Northwest-striking fault – a submarine landslide?

Although discussion of structure is reserved for Chapter 2, the NW-striking fault warrants discussion here because it cuts Ps, but does not cut the overlying T2 material (Figure 5h). Material from Ps in the hanging wall is highly deformed, unlike the distinctly bedded material in the footwall. The hanging wall material itself is yellow altered to green hues, suggesting submarine alteration. Further, it is plausible that when erupted, the flows of Pliocene basaltic andesite (Pba) added a substantial load on top of Ps and Psm. These observations may suggest a submarine slump or landslide (Shanmugam, 2018). If this interpretation is correct, this northwest-trending fault, directionally and tectonically inconsistent with other mapped faults on the island, would be a submarine landslide scarp rather than a tectonically significant fault.

Lineations with northwest trends are seen in overlying Pba, which lies wholly to the NE of the trace of the fault or landslide s similarly be evidence of a non-tectonic event. They are not observed in surrounding terraces or in older volcanic rocks to the southwest. Because Pab is younger than all other mapped volcanic units, it is unusual that the lineations are so localized and seemingly absent from older material. If, indeed, the flow of Pab added such a load onto Ps to cause a landslide, it is very possible that these northwest-trending lineations and parallel northwest-trending ridges are transverse cracks and ridges, respectively, in a translational and/or rotational landslide.

Furthermore, such a landslide scarp would not extend to depth in cross-section, and would instead become listric, quickly adopting a gentler slope away from the surface. The fault would likely rotate Ps (and Psm) and the overlying Pba, as well, such that they would have a gentler dip than depicted in Figure 9. Due to this localized landslide deformation, it is also probable that our bedding attitude measurements are muddied, and the sedimentary sequence may have a more gentle dip than depicted in Figure 9. If the dip of Ps is actually more gentle than we have depicted, it follows that the thickness would also be lesser, even ≤ 200 m if the dip is as little as 15°. The dip would be consistent with some measured bedding attitudes in the vicinity of Ps and Psm, and the thickness would be consistent with other sedimentary sequences in the nearby Gulf of California.

CONCLUSIONS

We have documented, described, and mapped a ~100 m thick Pliocene sedimentary unit, Ps, on southeastern Isla Ángel de la Guarda. The maximum age of deposition is constrained by the underlying Miocene-Pliocene volcanic unit, MPv, for which we have an $^{40}Ar/^{39}Ar$ age of 2.925 ± 0.012 Ma. Unit Ps is overlain by Pliocene basaltic andesite, Pba. In two outcrops, it is evident that Pba flows were active as sedimentation ended: in a baked contact and in a ballistic lava bomb that fell into soft sediment. Three basaltic andesite samples from Pba independently constrain the minimum age of Ps with $^{40}Ar/^{39}Ar$ geochronology: 2.754 ± 0.021 Ma, 2.756 ± 0.079 Ma, and 3.16 ± 0.42, which is considered a maximum age.

The Pliocene sedimentary unit grades laterally throughout its ~0.5 km^2 area. In some outcrops, pectens and oysters are found within Ps, indicating a marine depositional environment. In other areas, the depositional environment is unclear, and may be lacustrine. We also document a Miocene-Pliocene conglomerate overlying MPv in a buttress unconformity. The conglomerate has subangular cobble-sized clasts, and must be derived from some now-eroded or otherwise missing source(s). It is possible that this conglomerate is a lateral variation of Ps, and that the sedimentary unit thickened as it reached deeper waters. Another possibility is that the Miocene-Pliocene conglomerate is younger than Ps, and makes up the initial terrace into which terraces were later carved.

Units mapped in this study bear similarities to other Pliocene sediments mapped in the northern Gulf of California. Although there are similarities between Ps on Isla Ángel de la Guarda and Pliocene sediments near Puertecitos (Boehm, 1982, 1984; Stock et al., 1991; Martín-Barajas et al., 1997), southeastern Isla Ángel de la Guarda was never quite as far north as Puertecitos. However units mapped north of Bahia de Guadalupe (Parkin, 1998) are remarkably similar to Ps on Isla Ángel de la Guarda– both have pumiceous sandstones, basalt-pebble conglomerates, gypsum beds, and siltstones, which are topped by Pliocene basaltic andesite flows. These flows in Bahia de Guadalupe are ~2.6 Ma, and those in our study are ~2.75 Ma. Probably several rifting-related basins formed during Pliocene extension, making for very similar depositional environments and recorded sediments on the western shores of the Gulf of California.

ACKNOWLEDGMENTS

Many thanks are due to Dr. Scott Bennett at the USGS for assistance with field work and for many fruitful discussions. Dr. Mark Stelten at the USGS did the final geochronology sample preparation and performed $^{40}Ar/^{39}Ar$ analyses. Dr. Judith Terry Smith at the Smithsonian Institution identified macrofossils. Field work permits were obtained by Prof. Arturo Martin-Barajas at Centro de Investigación Científica y de Educación Superior de Ensenada (CICESE) through Secretaría de Gobernación and SEMARNAT. Funding was provided by NSF EAR-1728690.

REFERENCES CITED

Bennett, S.E., Darin, M.H., Dorsey, R.J., Skinner, L.A., Umhoefer, P.J., and Oskin, M.E., 2016a, Animated tectonic reconstruction of the Lower Colorado River region: Implications for Late Miocene to Present deformation, *in* Going LOCO: Investigations along the Lower Colorado River: California State University Desert Studies Center 2016 Desert Symposium Field Guide and Proceedings, p. 73–86.

Bennett, S.E., Oskin, M.E., Dorsey, R.J., Iriondo, A., and Kunk, M.J., 2015, Stratigraphy and structural development of the southwest Isla Tiburón marine basin: Implications for latest Miocene tectonic opening and flooding of the northern Gulf of California: Geosphere, v. 11, p. 977–1007.

Bennett, S.E., Oskin, M.E., and Iriondo, A., 2017, Latest Miocene transtensional rifting of northeast Isla Tiburón, eastern margin of the Gulf of California: Tectonophysics, v. 719, p. 86–106.

Bennett, S.E., Oskin, M.E., Iriondo, A., and Kunk, M.J., 2016b, Slip history of the La Cruz fault: Development of a late Miocene transform in response to increased rift obliquity in the northern Gulf of California: Tectonophysics, v. 693, p. 409–435.

Boehm, M.C., 1984, An overview of the lithostratigraphy, biostratigraphy, and paleoenvironments of the late Neogene San Felipe marine sequence, Baja California, Mexico:

Boehm, M.C.F., 1982, Biostratigraphy, lithostratigraphy, and paleoenvironments of the Miocene-Pliocene San Felipe marine sequence: Baja California norte, Mexico [MS thesis]: Stanford University,.

Broderip, W.J., 1835, On Clavagella: The Transactions of the Zoological Society of London, v. 1, p. 261–268.

Calmus, T., Pallares, C., Maury, R.C., Bellon, H., Pérez-Segura, E., Aguillón-Robles, A., Carreño, A.-L., Bourgois, J., Cotten, J., and Benoit, M., 2008, Petrologic diversity of Plio-Quaternary post-subduction volcanism in northwestern Mexico: An example from Isla San Esteban, Gulf of California: Bulletin de la Société géologique de France, v. 179, p. 465–481.

Calvert, A.T., and Lanphere, M.A., 2006, Argon geochronology of Kilauea's early submarine history: Journal of Volcanology and Geothermal Research, v. 151, p. 1–18.

Cashman, K.V., and Fiske, R.S., 1991, Fallout of pyroclastic debris from submarine volcanic eruptions: Science, v. 253, p. 275–280.

Cavazos Álvarez, J.A., 2015, Estratigrafía de la cuenca central de la Isla Ángel de la Guarda: evidencia del inicio de extensión en el Golfo de California [Tesis de maestría]: Centro de Investigación Científica y de Educación Superior de Ensenada, 99 p., http://cicese.repositorioinstitucional.mx/jspui/handle/1007/961.

Conrad, T.A., 1837, Description of new marine shells from Upper California, coll. by T. Nuttall, *in* Proc. Acad. Nat. Sci. Philadelphia, v. 7, p. 227–268.

Dalrymple, G.B., GB, D., MA, L., and GP, K., 1981, Irradiation of samples for 40Ar/39Ar dating using the Geological Survey TRIGA reactor:

Desonie, D.L., 1992, Geologic and geochemical reconnaissance of Isla San Esteban: post-subduction orogenic volcanism in the Gulf of California: Journal of Volcanology and Geothermal Research, v. 52, p. 123–140.

Fleck, R.J., Calvert, A.T., Coble, M.A., Wooden, J.L., Hodges, K., Hayden, L.A., van Soest, M.C., du Bray, E.A., and John, D.A., 2019, Characterization of the rhyolite of Bodie Hills and 40Ar/39Ar intercalibration with Ar mineral standards: Chemical Geology, v. 525, p. 282–302.

Fleck, R.J., Hagstrum, J.T., Calvert, A.T., Evarts, R.C., and Conrey, R.M., 2014, 40Ar/39Ar geochronology, paleomagnetism, and evolution of the Boring volcanic field, Oregon and Washington, USA: Geosphere, v. 10, p. 1283–1314.

Gastil, G., Krummenacher, D., and Minch, J., 1979, The record of Cenozoic volcanism around the Gulf of California: Geological Society of America Bulletin, v. 90, p. 839–857.

Hertlein, L.G., 1966, *in* Pliocene Fossils Form Rancho El Refugio, Baja California, and Carralvo Island, Mexico, Proc. California Acad. Sc., 4, v. 30, p. 265–284.

Lee, J.-Y., Marti, K., Severinghaus, J.P., Kawamura, K., Yoo, H.-S., Lee, J.B., and Kim, J.S., 2006, A redetermination of the isotopic abundances of atmospheric Ar: Geochimica et Cosmochimica Acta, v. 70, p. 4507–4512.

Lewis, C.J., 1996, Stratigraphy and geochronology of Miocene and Pliocene volcanic rocks in the Sierra San Fermín and southern Sierra San Felipe, Baja California, Mexico.: Geofísica Internacional, v. 35.

Machel, H.-G., 1985, Fibrous gypsum and fibrous anhydrite in veins: Sedimentology, v. 32, p. 443–454.

Martín-Barajas, A., Stock, J.M., Layer, P., Hausback, B., Renne, P., and López-Martínez, M., 1995, Arc-rift transition volcanism in the Puertecitos Volcanic Province, northeastern Baja California, Mexico: GSA Bulletin, v. 107, p. 407–424, doi:10.1130/0016-7606(1995)107<0407:ARTVIT>2.3.CO;2.

Martín-Barajas, A., Tellez-Duarte, M., and Stock, J.M., 1997, Pliocene volcanogenic sedimentation along an accommodation zone in northeastern Baja California: The Puertecitos Formation:

Miller, K.G., Kominz, M.A., Browning, J.V., Wright, J.D., Mountain, G.S., Katz, M.E., Sugarman, P.J., Cramer, B.S., Christie-Blick, N., and Pekar, S.F., 2005, The Phanerozoic record of global sea-level change: science, v. 310, p. 1293–1298.

Nagy, E.A., 2000, Extensional deformation and paleomagnetism at the western margin of the Gulf extensional province, Puertecitos Volcanic Province, northeastern Baja California, Mexico: Geological Society of America Bulletin, v. 112, p. 857–870.

Nagy, E.A., Grove, M., and Stock, J.M., 1999, Age and stratigraphic relationships of pre-and syn-rift volcanic deposits in the northern Puertecitos Volcanic Province, Baja California, Mexico: Journal of volcanology and geothermal research, v. 93, p. 1–30.

Nagy, E.A., and Stock, J.M., 2000, Structural controls on the continent-ocean transition in the northern Gulf of California: Journal of Geophysical Research: Solid Earth, v. 105, p. 16251–16269.

Neuhaus, J.R., 1989, Volcanic and nonmarine stratigraphy of southwest Isla Tiburon, Gulf of California, Mexico: San Diego State University.

Ortlieb, L., 1991, Quaternary shorelines along the northeastern Gulf of California, geochronological data and neotectonic implications: Geological Society of America. Special Paper, v. 254, p. 95–120.

Ortlieb, L., 1990, Quaternary Vertical Movements Along the Coasts of Baja California and Sonora in Dauphin, J.P., and Simoneit, B.R.T., eds., The Gulf and Peninsular Province of the Californias: Tulsa, American Association of Stump, T. E., 1975, Pleistocene molluscan paleoecology and community structure of the Puerto Libertad region, Sonora, Mexico: Palaeogeography, Palaeocli- matology, Palaeoecology, v. 17, p. 177-226. Petroleum Geologists Memoir 47:

Parkin, E.L., 1998, Tectonic controls on the Pliocene to Quaternary stratigraphic and structural evolution of the Bahia de Guadalupe basin, Baja California, Mexico: University of California, Los Angeles.

Seiler, C., Fletcher, J.M., Quigley, M.C., Gleadow, A.J., and Kohn, B.P., 2010, Neogene structural evolution of the Sierra San Felipe, Baja California: Evidence for proto-gulf transtension in the Gulf Extensional Province? Tectonophysics, v. 488, p. 87–109.

Seiler, C., Gleadow, A.J., Fletcher, J.M., and Kohn, B.P., 2009, Thermal evolution of a sheared continental margin: Insights from the Ballenas transform in Baja California, Mexico: Earth and Planetary Science Letters, v. 285, p. 61–74.

Shanmugam, G., 2018, Slides, slumps, debris flows, turbidity currents, and bottom currents: implications: Earth Systems and Environmental Sciences, Elsevier Online Module,.

Sowerby, G.B., 1842, Monograph of the genus Pecten: Thesaurus conchyliorum, v. 1, p. 45–82.

Spencer, J.E., and Jonathan Patchett, P., 1997, Sr isotope evidence for a lacustrine origin for the upper Miocene to Pliocene Bouse Formation, lower Colorado River trough, and implications for timing of Colorado Plateau uplift: Geological Society of America Bulletin, v. 109, p. 767–778.

Steiger, R.H., and Jäger, E., 1977, Subcommission on geochronology: convention on the use of decay constants in geo-and cosmochronology: Earth and planetary science letters, v. 36, p. 359–362.

Stock, J.M., 2000, Relation of the Puertecitos Volcanic Province, Baja California, Mexico, to development of the plate boundary in the Gulf of California: Special Papers-Geological Society of America, p. 143–156.

Stock, J.M., Martín, A.B., Suárez, F.V., and Miller, M.M., 1991, Miocene to Holocene Extensional Tectonics and Volcanic Stratigraphy of NE Baja California, Mexico, *in* Walawender, M.J. and Hanan, B.B. eds., Geological excursions in Southern California and Mexico: guidebook, 1991 Annual Meeting, Geological Society of America, San Diego, California, October 21-24, 1991, San Diego, CA, San Diego State University, p. 44–67, https://resolver.caltech.edu/CaltechAUTHORS:20140909-100119572 (accessed May 2020).

Wendt, I., and Carl, C., 1991, The statistical distribution of the mean squared weighted deviation: Chemical Geology: Isotope Geoscience Section, v. 86, p. 275–285.

FIGURES

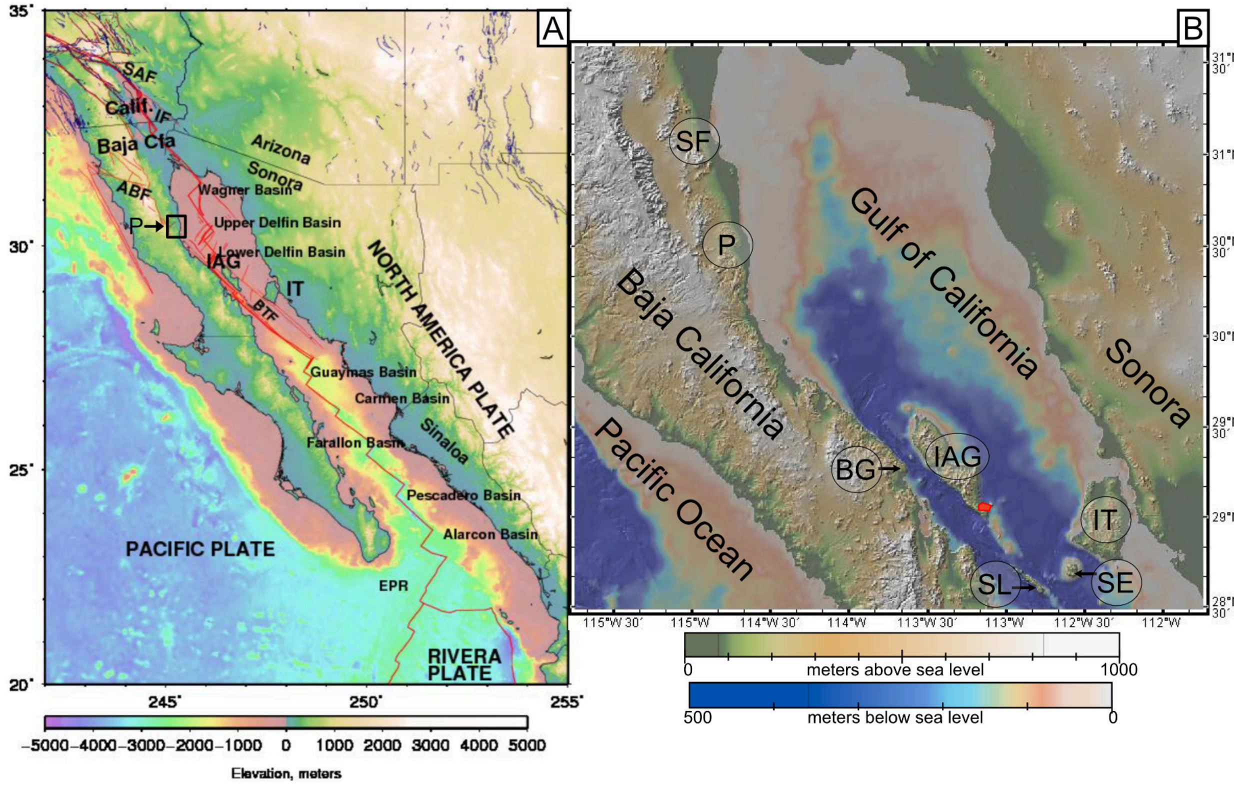

Figure 1: Maps showing nearby Pliocene marine sediments

(A) Regional map of the Gulf of California showing plate boundary fault systems (red lines) showing extensional regime in the Gulf of California. IAG - Isla Ángel de la Guarda; IT - Isla Tiburón; P – Puertecitos; EPR - East Pacific Rise; ABF - Agua Blanca Fault; BTF - Ballenas Transform Fault; SAF - San Andreas Fault. (B) Distribution of mapped Pliocene marine sediments discussed in this chapter, including BG – Bahía de Guadalupe (Parkin, 1998), IT – Isla Tiburón (Bennett et al., 2015, 2016b, 2017), P – Puertecitos (Martín-Barajas et al., 1995, 1997), SE – Isla San Estebán (Calmus et al., 2008), and SF – San Felipe (Boehm, 1982, 1984). IAG – Isla Ángel de la Guarda, SL – Isla San Luis. Red polygon on IAG denotes field study area. Representative stratigraphic sections from San Felipe, Puertecitos, Bahia de Guadalupe, and southwestern Isla Tiburón are included in Figure 2.

A San Felipe (Boehm, 1984)

B Puertecitos Formation (Martin-Barajas et al., 1997)

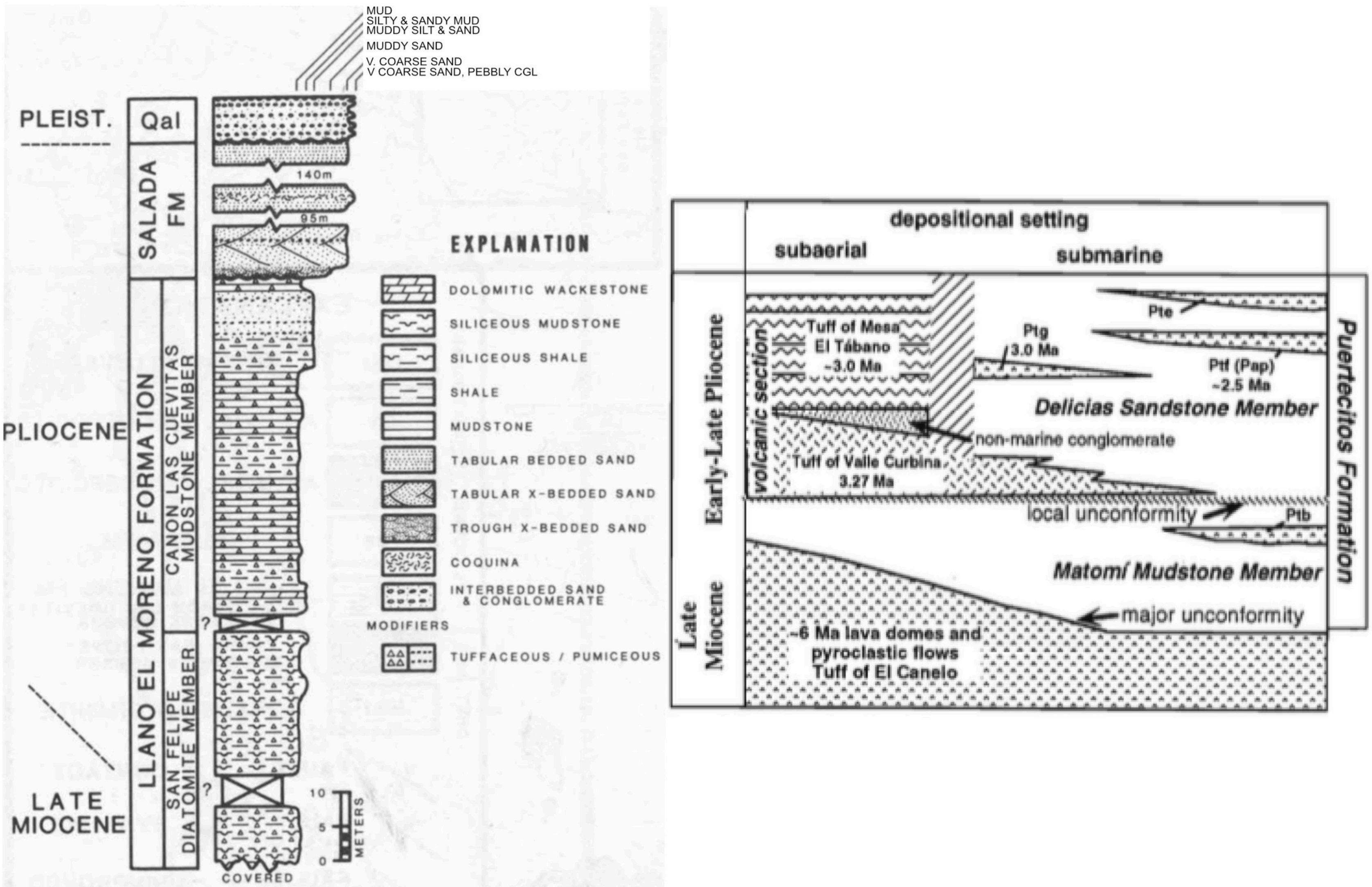

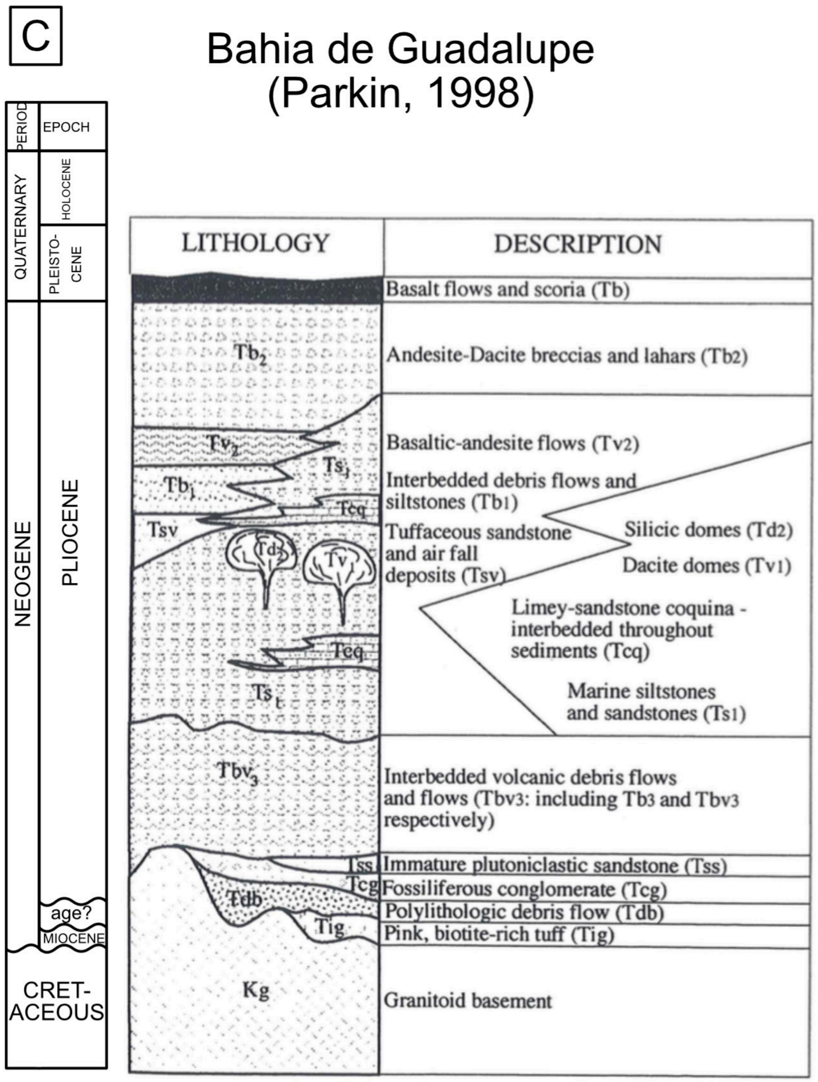
C
Bahia de Guadalupe
(Parkin, 1998)
PERIOD
EPOCH
QUATERNARY
HOLOCENE
PLEISTO-CENE
NEOGENE
PLIOCENE
age?
MIOCENE
CRET-ACEOUS
LITHOLOGY
DESCRIPTION
Basalt flows and scoria (Tb)
Andesite-Dacite breccias and lahars (Tb2)
Basaltic-andesite flows (Tv2)
Interbedded debris flows and siltstones (Tb1)
Tuffaceous sandstone and air fall deposits (Tsv)
Silicic domes (Td2)
Dacite domes (Tv1)
Limey-sandstone coquina - interbedded throughout sediments (Tcq)
Marine siltstones and sandstones (Ts1)
Interbedded volcanic debris flows and flows (Tbv3: including Tb3 and Tbv3 respectively)
Immature plutoniclastic sandstone (Tss)
Fossiliferous conglomerate (Tcg)
Polylithologic debris flow (Tdb)
Pink, biotite-rich tuff (Tig)
Granitoid basement
Kg

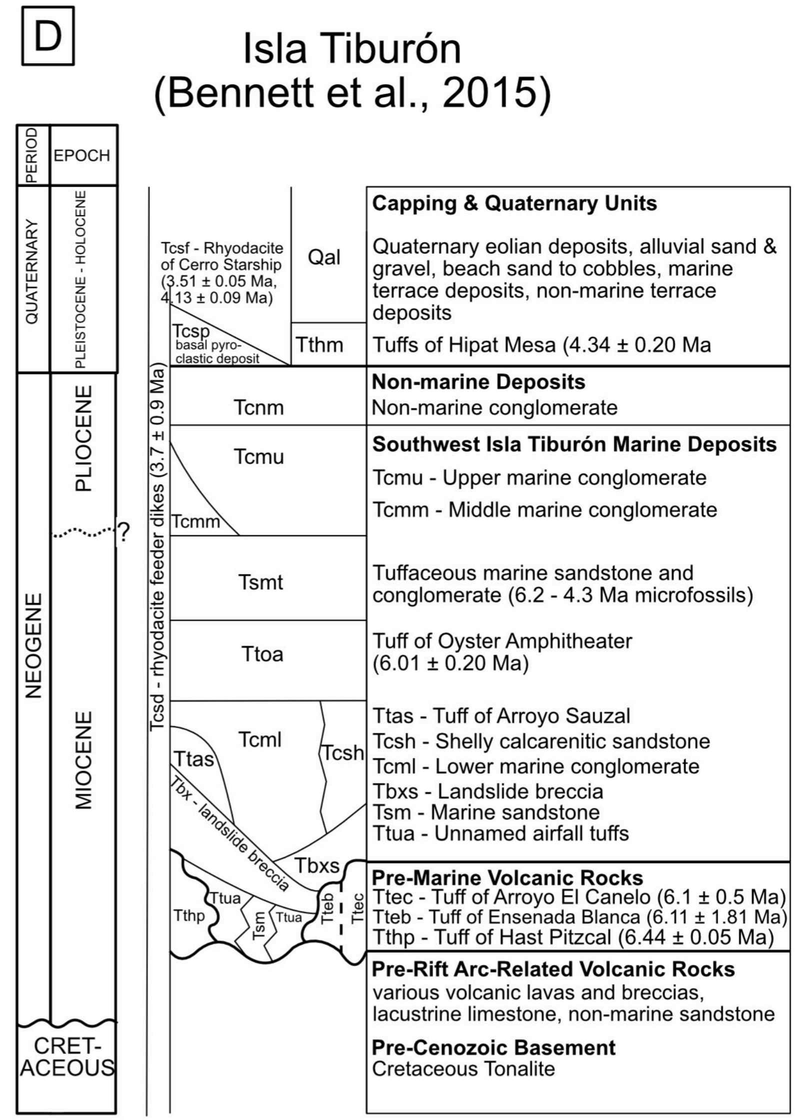
D
Isla Tiburón
(Bennett et al., 2015)
PERIOD
EPOCH
QUATERNARY
PLEISTOCENE - HOLOCENE
NEOGENE
PLIOCENE
MIOCENE
CRET-ACEOUS
Tcsd - rhyodacite feeder dikes (3.7 ± 0.9 Ma)
Tcsf - Rhyodacite of Cerro Starship (3.51 ± 0.05 Ma, 4.13 ± 0.09 Ma)
Tcsp basal pyroclastic deposit
Qal
Tthm
Tcnm
Tcmu
Tcmm
Tsmt
Ttoa
Tcml
Tcsh
Ttas
Tbx - landslide breccia
Tbxs
Tthp
Ttua
Tsm
Tteb
Ttec
Capping & Quaternary Units
Quaternary eolian deposits, alluvial sand & gravel, beach sand to cobbles, marine terrace deposits, non-marine terrace deposits
Tuffs of Hipat Mesa (4.34 ± 0.20 Ma
Non-marine Deposits
Non-marine conglomerate
Southwest Isla Tiburón Marine Deposits
Tcmu - Upper marine conglomerate
Tcmm - Middle marine conglomerate
Tuffaceous marine sandstone and conglomerate (6.2 - 4.3 Ma microfossils)
Tuff of Oyster Amphitheater (6.01 ± 0.20 Ma)
Ttas - Tuff of Arroyo Sauzal
Tcsh - Shelly calcarenitic sandstone
Tcml - Lower marine conglomerate
Tbxs - Landslide breccia
Tsm - Marine sandstone
Ttua - Unnamed airfall tuffs
Pre-Marine Volcanic Rocks
Ttec - Tuff of Arroyo El Canelo (6.1 ± 0.5 Ma)
Tteb - Tuff of Ensenada Blanca (6.11 ± 1.81 Ma)
Tthp - Tuff of Hast Pitzcal (6.44 ± 0.05 Ma)
Pre-Rift Arc-Related Volcanic Rocks
various volcanic lavas and breccias, lacustrine limestone, non-marine sandstone
Pre-Cenozoic Basement
Cretaceous Tonalite

Figure 2: Representative stratigraphic columns from Pliocene depocenters

Representative stratigraphic columns from (A) San Felipe (reprinted from Figure 3 in Boehm, 1984), (B) Puertecitos (reprinted from Figure 6 in Martín-Barajas et al., 1997), (C) Bahia de Guadalupe (reprinted from Figure 8 from Parkin, 1998), (D) southwestern Isla Tiburón (adapted from Figure 3 in Bennett et al., 2015). Further details are discussed in text.


Kilometers
0
0.5
1
N
B'
B
2.754 ± 0.021
2.756 ± 0.079
3.16 ± 0.42
2.925 ± 0.012
MPv
MPcg
MPr
Pab
Psm
Ps
Qal
Qb
T1
T2
T2m
T3
290000
292000
294000
3216000
3214000
Source: Esri, DigitalGlobe, GeoEye, Earthstar Geographics, CNES/Airbus DS, USDA, USGS, AeroGRID, IGN, and the GIS User Community

Figure 3: Geologic map of southeastern Isla Ángel de la Guarda

Geologic map of southeastern Isla Ángel de la Guarda in UTM Zone 12. True locations were measured with a handheld GPS Garmin inReach Explorer+, using WGS84. Ages are from $^{40}Ar/^{39}Ar$ geochronology from groundmass and plagioclase in andesite flows (Table 1). Line B–B' denotes line of cross-section in Figure 9. Blow-ups of this geologic map are included in Chapter 2 Supplemental Figure S3. .

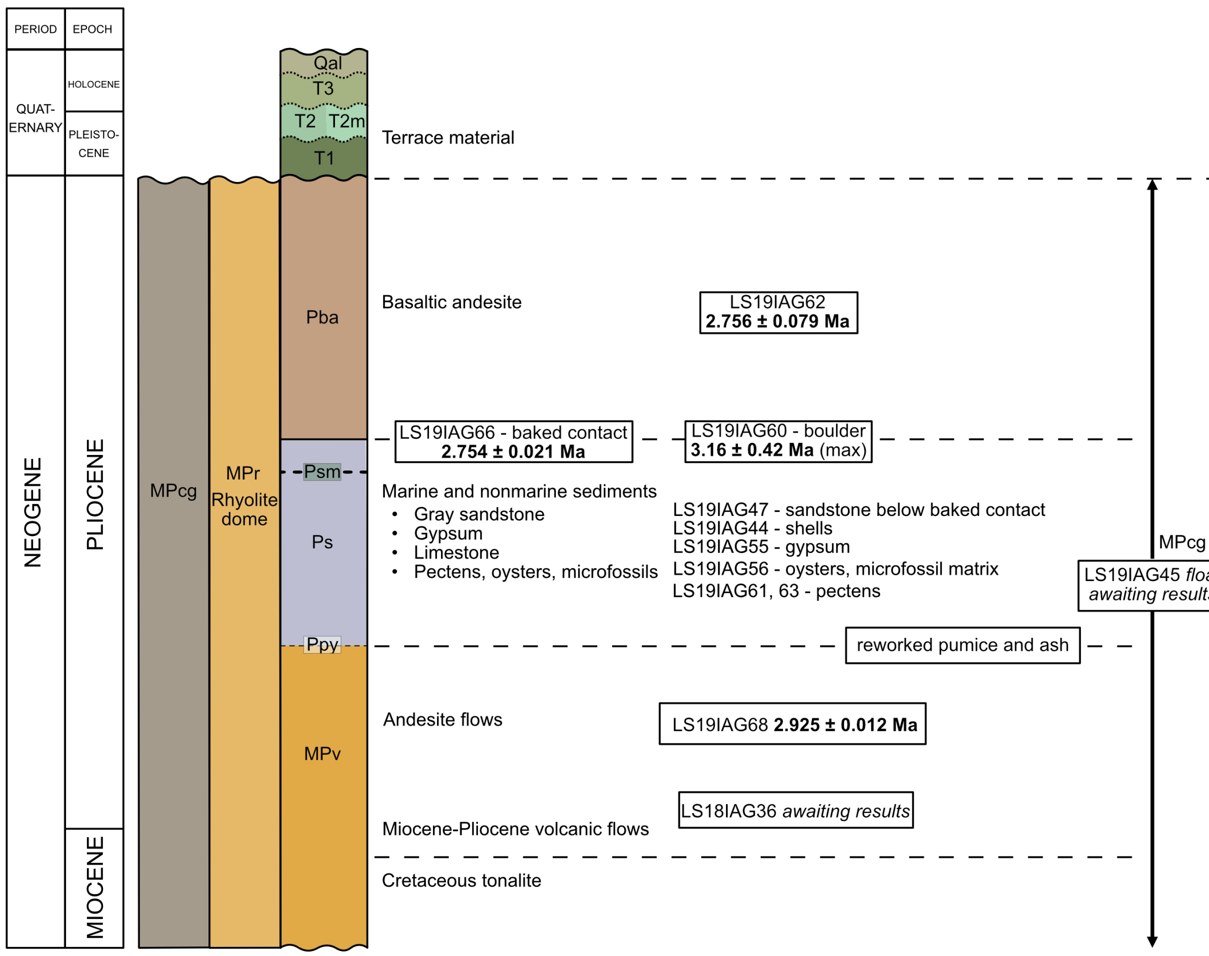

Figure 4: Stratigraphic column of southeastern IAG

Stratigraphic column of volcanic and sedimentary rocks in southeastern IAG. Samples of volcanic flows with $^{40}Ar/^{39}Ar$ ages and sedimentary rocks with fossils are shown.

Figure 5: Field photographs

Figure 5a: Pliocene basaltic andesite flow above marine sequence. Foliations in the flow are visible at both hand sample and outcrop scales. The flow has inclusions of tonalite basement (see top photo), and other volcanic rocks. In the bottom photo, green lines highlight foliations.

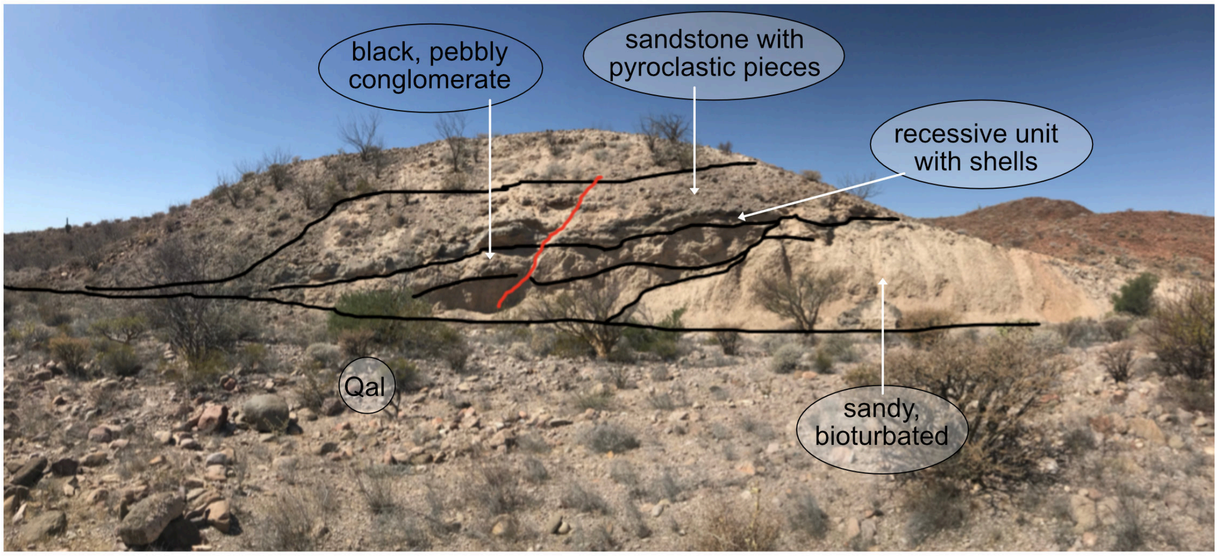

Figure 5b: Subunits in marine section outcrop. Bottom subunit is light tan, sandy, bioturbated, with a thin gypum layer at its top. Above this is a black pebbly conglomerate, topped by a recessive unit with pecten shells. The top unit is a sandstone with pyroclastic fragments in it. Overlying these subunits is Quaternary colluvium. A representative stratigraphic column is shown in Figure 6c.

Figure 5c: Pumiceous sandstone near base of Ps. Hammer at base of photo, in shadow, is 47 cm. Pumice pieces in sunlight on upper face in the photo are 2-5 cm in diameter. A representative stratigraphic column is shown in Figure 6a.

Figure 5d: Miocene-Pliocene volcanic flows, MPv, seen in-situ. The chisel is ~20 cm in length. Yellow dashed line highlights a granitic inclusion, which is likely Cretaceous tonalite basement.

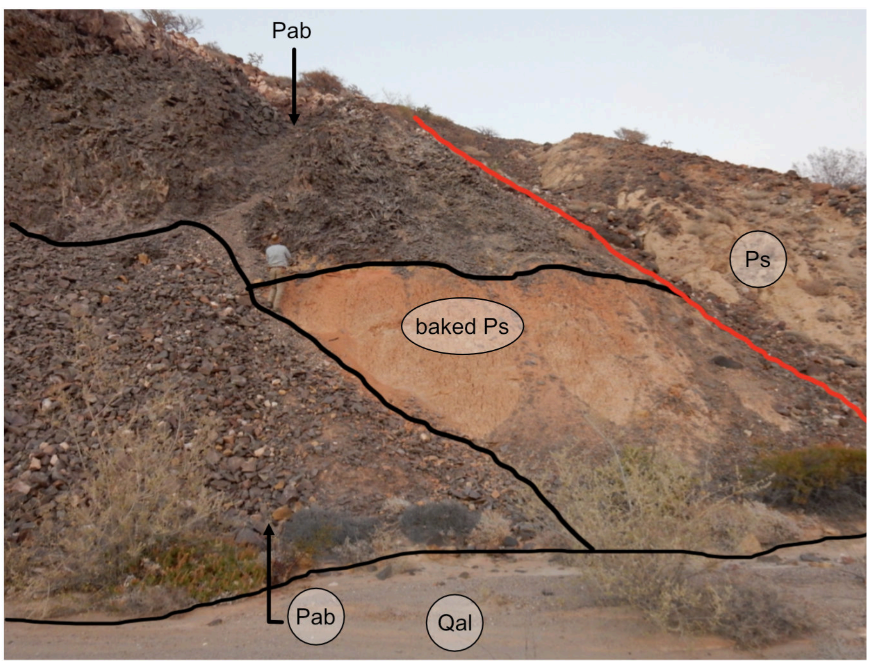

Figure 5e: Contact between baked marine unit on bottom, and capping andesite flow on top.

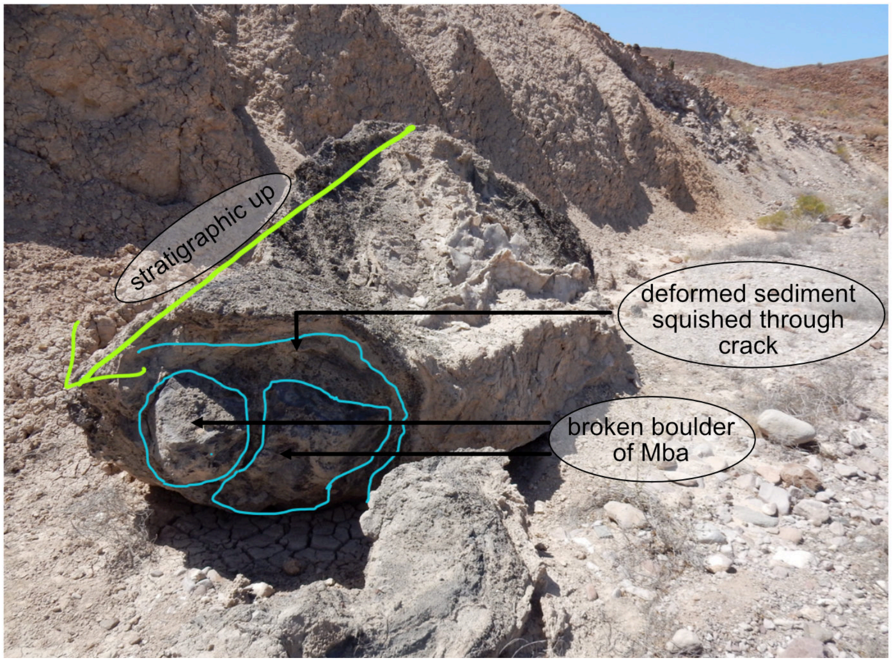

Figure 5f: Volcanic bomb 2m across which fell off of nearby outcrop. Note stratigraphic up. This ballistic fell into and deformed the wet marine sedimentary unit, creating a paleoliquefaction structure. The sedimentary rock is squished into the crack of the volcanic bomb, implying that it was deformed when it was still soft. A 3D model of this boulder can be found on Sketchfab website: https://skfb.ly/6TOuz.

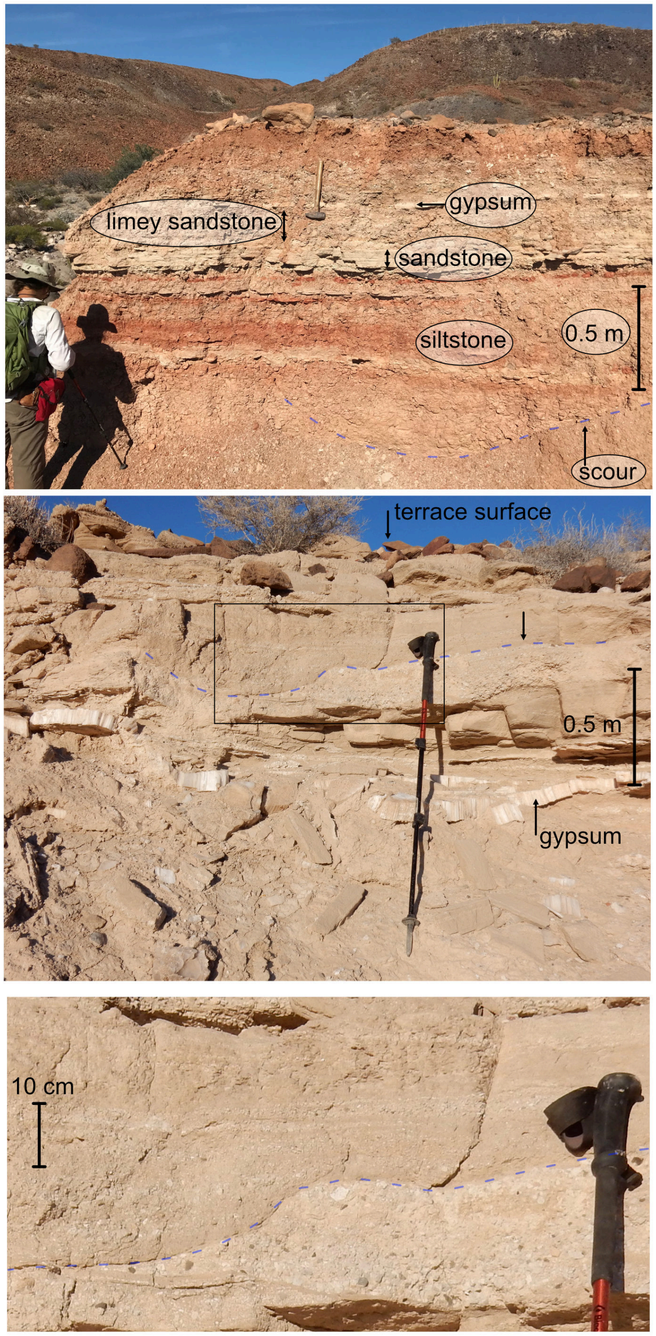

Figure 5g: Two different outcrops of marine sediment in Ps (Pliocene sedimentary rocks). The top photo shows a 0.5 to 1 cm thick layer of gypsum under the hammer, atop limestone, sandstone, and siltstone (top to bottom). The thin layer of gypsum and undulatory nature of limestone, sandstone, and siltstone layers indicate that the sediments were deposited in a marine or lacustrine environment. Note the scour marks within the siltstone. A representative stratigraphic column is shown in Figure 6b. Bottom two photos are of the same outcrop, and the bottom photo corresponds to the rectangle in the middle photo. Middle photo shows 5-10 cm thick gypsum bed with crystals perpendicular to bedding. Scour marks are clear in both photos, indicating a fluvial system carving into a marine or lacustrine environment.

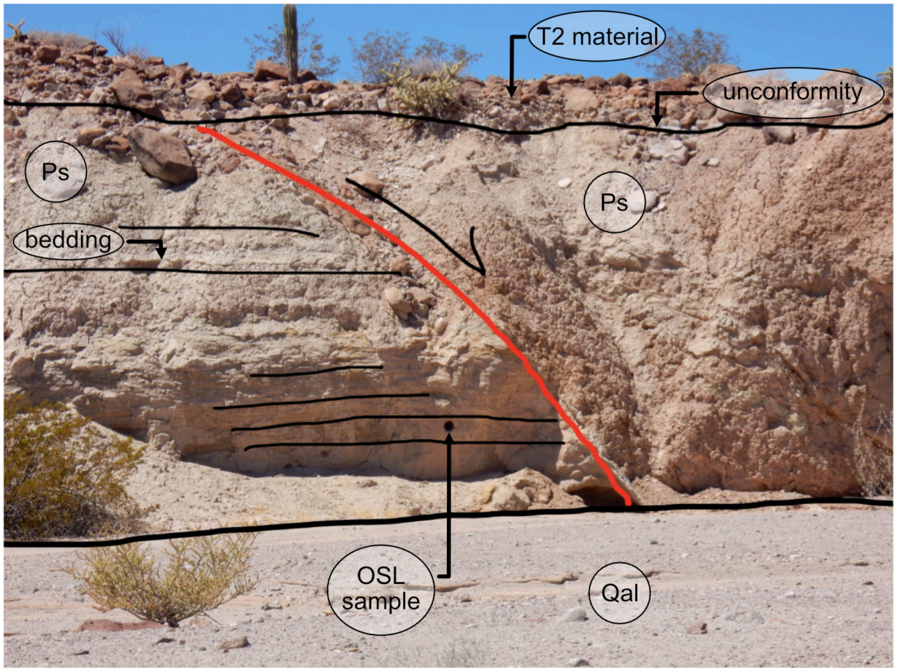

Figure 5h: Pliocene sedimentary unit (Ps) with NW-striking fault. View is to northwest. The top of the outcrop is T2 material, which unconformably overlies Pliocene sediments. The left (SW) side of the outcrop has clear bedding in the footwall of the fault. The bedding abruptly stops at the fault. Ps material on the right (NE) side in the hanging wall is deformed by faulting and lacks clear stratification. An OSL sample was taken from this outcrop for a separate study at UCLA.

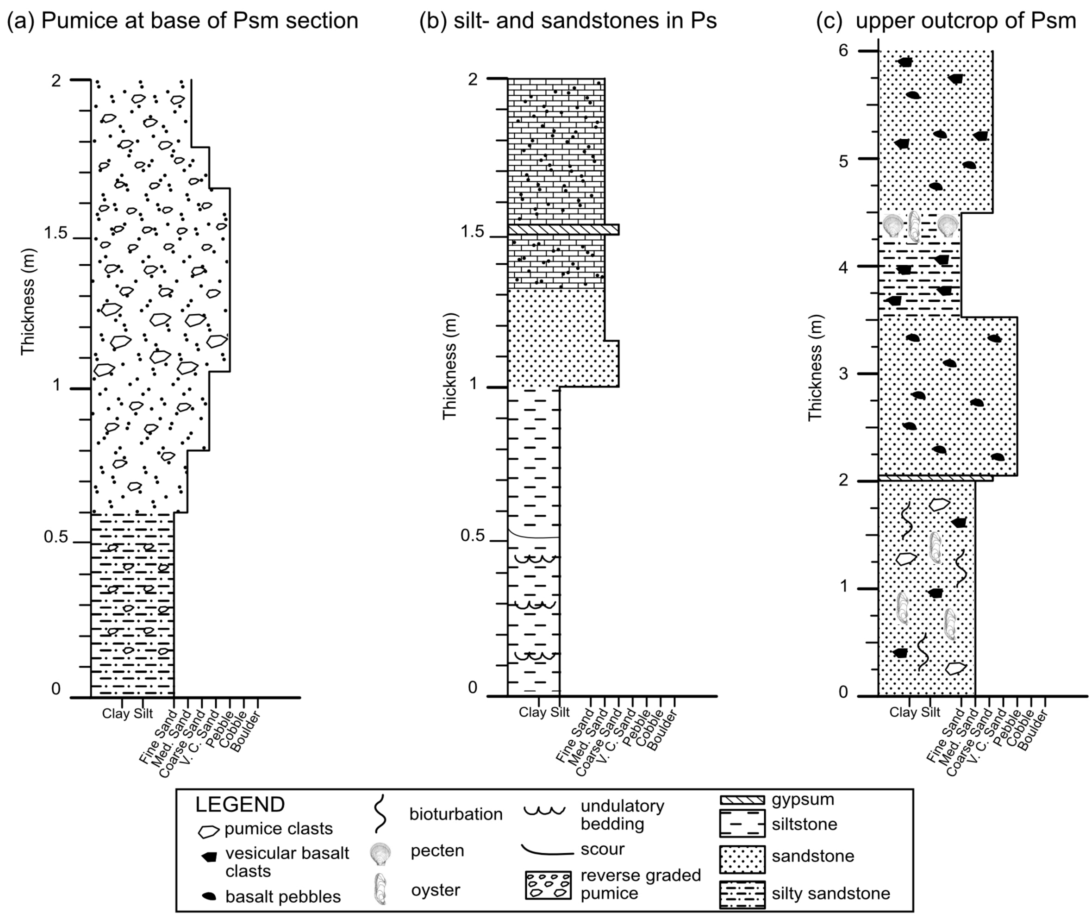

Figure 6: Representative stratigraphic sections from Ps and Psm

(a) a section of reworked pumice and near the base of Ps; (b) a section of siltstone, sandstones, and a thin gypsum bed within Ps; (c) an upper-most section of Psm with marine fossils and bioturbation towards the bottom, and fragments of vesicular basalt and basalt pebbles near the top. Further details are discussed in text.

Figure 7: Macrofossils collected in this study

Macrofossils identified by Judy Terry Smith (personal communication): (a) *Argopecten ventricosus* (Sowerby, 1842) in unit Psm (sample LS19IAG63) at 29.045283° N, -113.137071° E.

Figure 7b: *Crassostrea osunai* (Hertlein, 1966) in unit Psm (sample LS19IAG54) at 29.044142° N, -113.130277° E. The generic name may be Striostrea *rather* than *Crassostrea*.

Figure 7c: *Chione californiensis* (Broderip, 1835) and *Tagelus californianus* (Conrad, 1837) in unit T2m (sample LS19IAG38) at 29.054489° N, -113.129094° E.

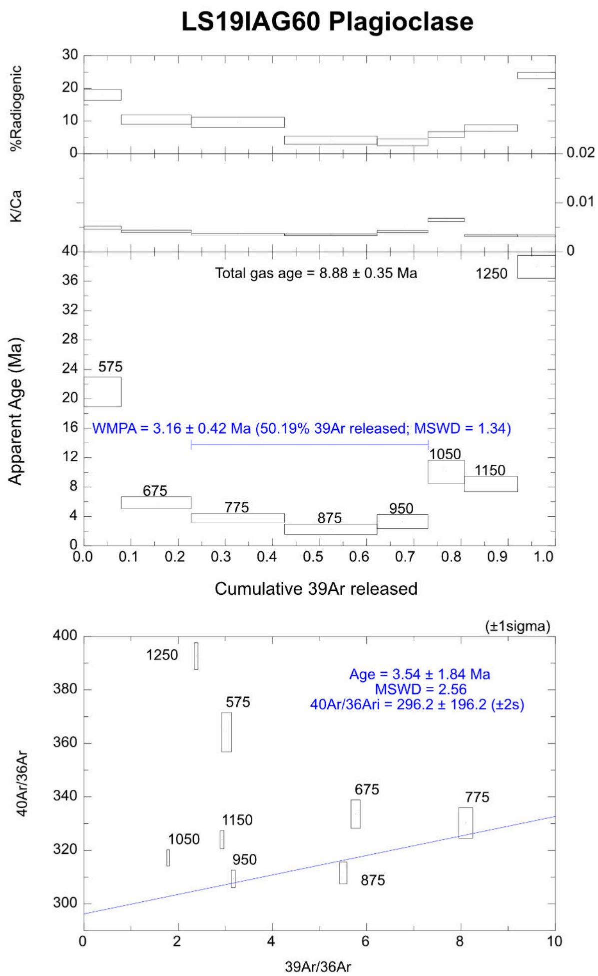

Figure 8: $^{40}Ar/^{39}Ar$ geochronology plateau and isochron diagrams.

Uncertainty boxes are 2 sigma. Horizontal lines with end bars on age spectra show which steps were used in plateau ages.

Figure 8a: LS19IAG60

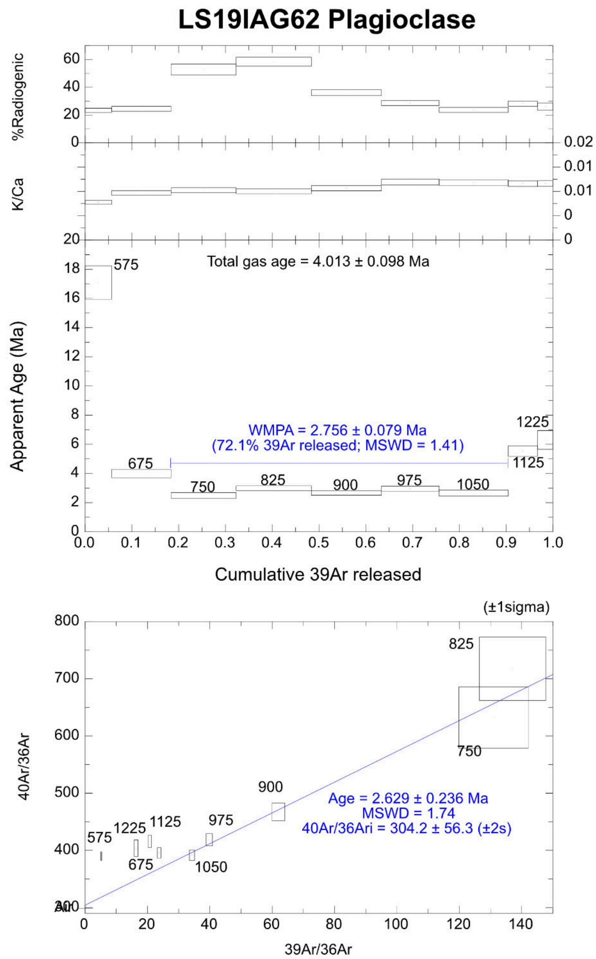

Figure 8b: LS19IAG62

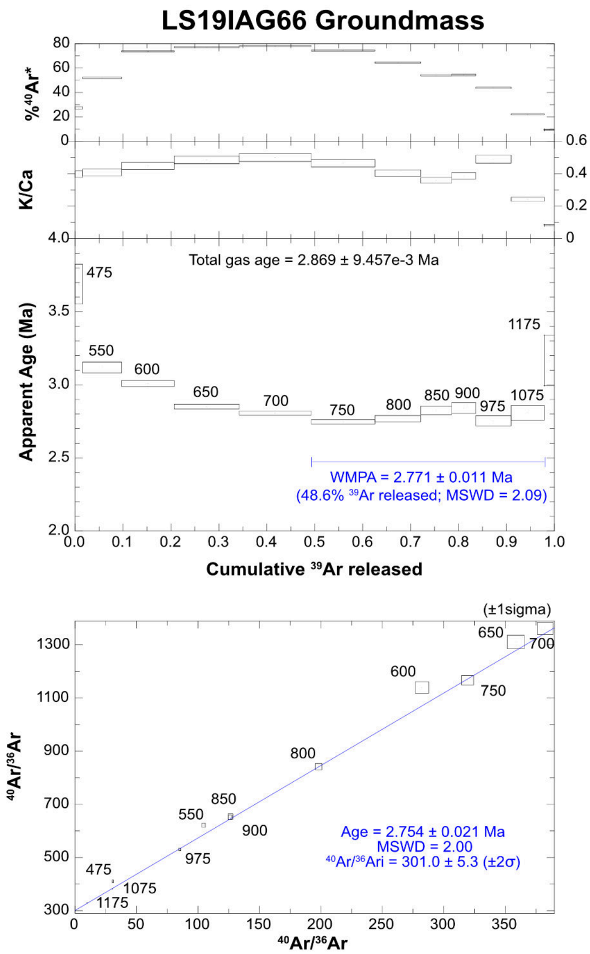

Figure 8c: LS19IAG66

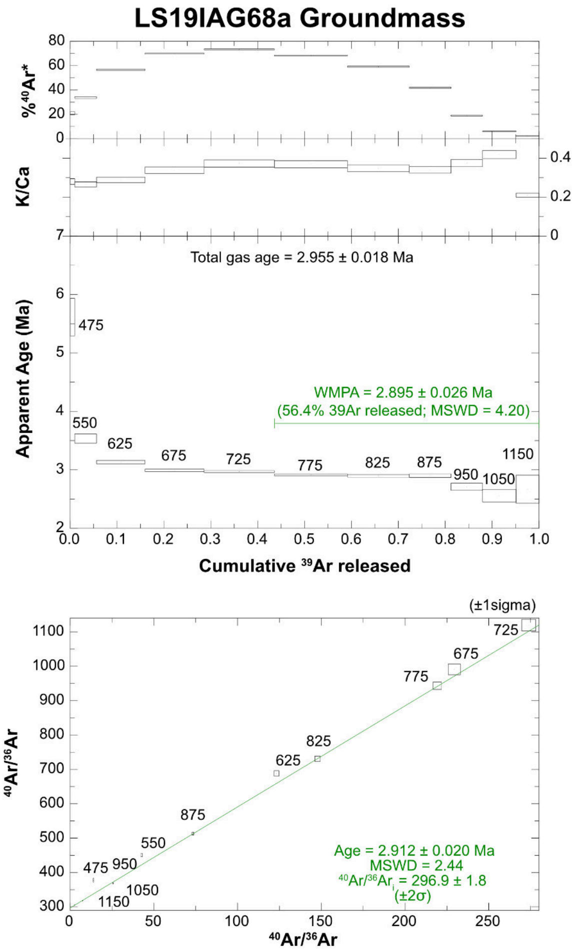

Figure 8d: LS19IAG68a

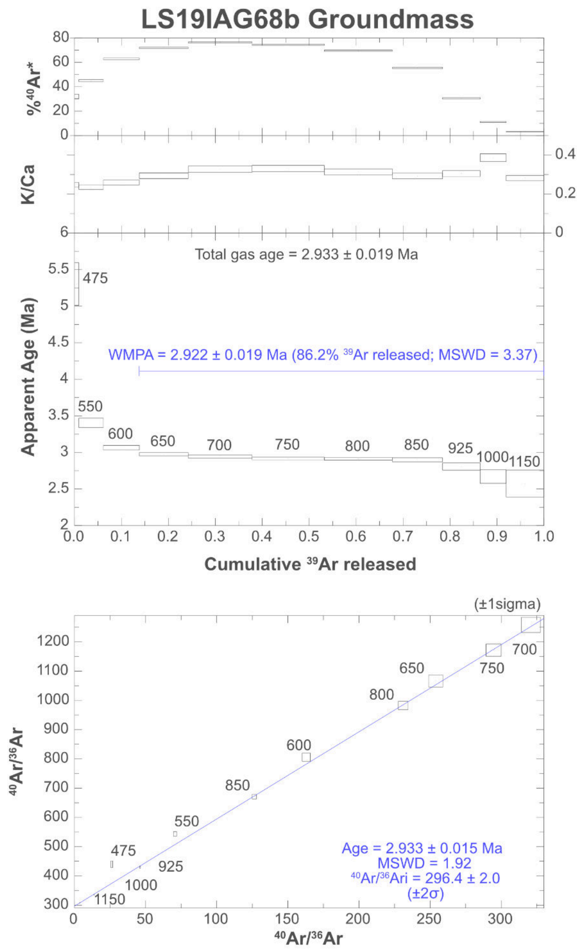

Figure 8e: LS19IAG68b

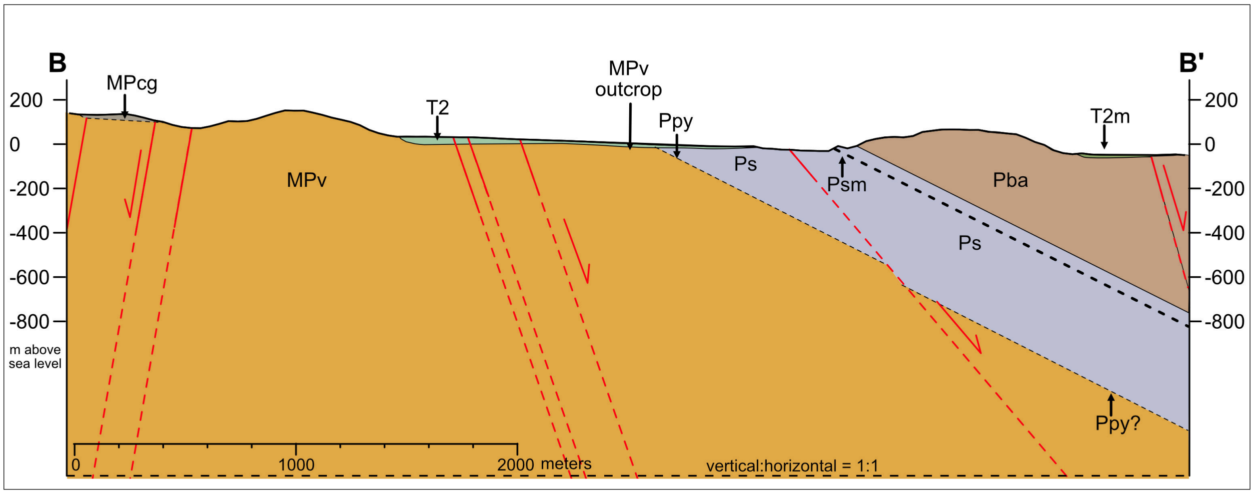

Figure 9: Cross-section through B-B'in Fig 3

Cross-section through line B-B' on geologic map in Figure 3. No quantity of slip is calculated on the fault cutting Ps.

TABLES

TABLE 1: SUMMARY OF $^{40}Ar/^{39}Ar$ ERUPTION AGES

Sample	Material †	Method#	Plateau		Isochron			% ^{39}Ar [Steps]
			Age (Ma) ± 1σ	MSWD	Age (Ma) ± 1σ	MSWD	$^{40}Ar/^{36}Ar_i$ (± 2σ)	
LS19IAG68a	GM	IH	2.895 ± 0.026	4.20	**2.912 ± 0.020**	2.44	296.9 ± 1.8	56.4 [775-1150]
LS19IAG68b	GM	IH	2.922 ± 0.019	3.37	**2.933 ± 0.015**	1.92	296.4 ± 2.0	86.2 [650-1150]
			LS19IAG68 Weighted Mean Age (± 1σ)				***2.925 ± 0.012***	
LS19IAG66	GM	IH	2.771 ± 0.011	2.09	**2.754 ± 0.021**	2.00	301.0 ± 5.3	48.6 [750-1075]
LS19IAG60	Plag.	IH	**3.16 ± 0.42**	1.34	3.54 ± 1.85	2.56	296.2 ± 196.2	50.2 [775-950]
LS19IAG62	Plag.	IH	**2.756 ± 0.079**	1.41	2.629 ± 0.236	1.74	304.2 ± 56.3	72.1 [750-1050]

Preferred age in bold
* Recoil model age following Fleck et al. (2014), *Geosphere*. Individual plateau steps for LA18IAG22 yield ages ranging fron
Ages were calculated using the decay constants recommended by Steiger and Jager (1977) and assuming $^{40}Ar/^{36}Ar$atmosphere
† GM = groundmass. Plag. = plagioclase. San. = sanidine
\# IH = incremental heating.

Table 1: $^{40}Ar/^{39}Ar$ ages for samples from the southern area

$^{40}Ar/^{39}Ar$ ages for basaltic andesite lava flows in the southern study area. Sample LS19IAG60 is to be treated as a maximum eruption age. Sample locations are listed in Chapter 2, Table 1. Full details of geochronology are reported in Table S1.

Table 2: Collected macrofossils from Isla Angel de la Guarda

Sample	Latitude (°N)	Longitude (°E)	Unit	Field Classification	Macrofossils identified by Dr. Smith
LS19IAG37	29.053607	-113.127031	T2m	shells and some sand	*Chione californiensis*
LS19IAG38	29.054489	-113.129094	T2m	shell-rich layer	*Chione californiensis* and *Tagelus californianus*
LS19IAG44	29.041587	-113.131942	Psm	shells	*Argopecten ventricosus*
LS19IAG53	29.044143	-113.130277	Psm	shell-rich bed	*Argopecten ventricosus*
LS19IAG54	29.044143	-113.130277	Psm	shells in sand	*Crassostrea osunai*
LS19IAG59	29.044143	-113.130277	Psm	shells	*Argopecten ventricosus* and *Crassostrea osunai*
LS19IAG61	29.044277	-113.131155	Psm	shells	*Crassostrea osunai*
LS19IAG63	29.045283	-113.137071	Psm	pectins	*Argopecten ventricosus*

Table 2: Macrofossil specimens collected in this study

Macrofossil specimens with location data, geologic unit, and identifications. Macrofossils were identified by Dr. J. T. Smith. Macrofossils in T2m include *Chione californiensis* (Broderip, 1835) and *Tagelus californianus* (Conrad, 1837). Scallop and oyster sampled from Psm include *Argopecten ventricosus* (Sowerby, 1842) and *Crassostrea osunai* (Hertlein, 1966), respectively. The generic name of *Crassostrea* may actually be *Striostrea*.

SUPPLEMENTAL MATERIAL

Supplemental Table 2: Full details for Ar isotope analyses. All uncertainties (except for the ^{40}Ar/^{36}Ar intercept) are reported at the 1σ level.

Note: Bodie Hills sanidine was used as a fluence monitor with an assumed age of 9.7946 ± 0.0031 Ma (Fleck et al., 2019) that is equivalent to Fish Canyon sanidine at 28.099 ± 0.013 Ma.

LS18IAG22 Groundmass

Temp(°C)	Age(Ma)	%^{40}Ar*	K/Ca	moles ^{40}Ar*	%^{39}Ar	^{40}Ar	^{39}Ar	^{38}Ar	^{37}Ar	^{36}Ar
475	3.693±0.206	4.77	11.62	2.80E-14	0.02	8.264966±0.004889	0.107055±0.000182	0.005718±0.000095	0.004833±0.000225	0.026362±0.000072
525	3.361±0.078	10.31	17.98	7.53E-14	0.07	10.272281±0.005316	0.315861±0.000279	0.009405±0.000116	0.009217±0.000164	0.030858±0.000081
575	3.133±0.037	15.86	22.35	1.27E-13	0.17	11.257005±0.004547	0.571475±0.000465	0.013393±0.000160	0.013419±0.000300	0.031719±0.000069
625	3.238±0.021	38.49	27.31	1.41E-13	0.27	5.147573±0.001791	0.613414±0.000451	0.009747±0.000230	0.011783±0.000499	0.010602±0.000043
675	3.365±0.014	67.13	31.42	1.27E-13	0.36	2.657085±0.000785	0.531100±0.000421	0.006682±0.000121	0.008869±0.000246	0.002924±0.000025
725	3.492±0.017	65.07	29.91	1.09E-13	0.44	2.356638±0.000746	0.439999±0.000371	0.005615±0.000088	0.007718±0.000337	0.002757±0.000024
775	3.525±0.016	61.55	27	9.37E-14	0.5	2.141351±0.000707	0.374649±0.000340	0.004897±0.000095	0.007280±0.000239	0.002757±0.000020
825	3.504±0.021	57.66	29.46	8.97E-14	0.56	2.187280±0.000876	0.360682±0.000327	0.004721±0.000102	0.006424±0.000273	0.003101±0.000025
875	3.443±0.018	50.58	27.26	9.82E-14	0.63	2.729236±0.000967	0.401893±0.000367	0.005623±0.000088	0.007735±0.000133	0.004516±0.000024
950	3.398±0.015	45.8	24.73	1.82E-13	0.76	5.592216±0.001270	0.755622±0.000423	0.011018±0.000067	0.016030±0.000268	0.010148±0.000037
1125	3.331±0.013	42.39	9.68	2.72E-13	0.96	9.021679±0.002362	1.150713±0.000574	0.017793±0.000176	0.062341±0.000637	0.017415±0.000050
1175	3.322±0.030	44.14	6.54	5.38E-14	0.99	1.713533±0.000485	0.228251±0.000232	0.003559±0.000071	0.018301±0.000392	0.003209±0.000022
1250	3.568±0.138	34.47	3.38	8.27E-15	1	0.337317±0.000516	0.032668±0.000105	0.000498±0.000053	0.005065±0.000204	0.000741±0.000015

Packet IRR379-OP, Experiment #20Z0030, 0.1053 g Groundmass, all errors ±1 sigma
J = 0.000556490: 3/17/20

^{40}Ar* is radiogenic argon, isotopes in volts (7.12e-14 moles/volt), corrected for blank, background, discrimination, and decay
Calculated bulk K/Ca = 17.244 ± 6.999, Calculated K2O = 2.75%wt., Calculated CaO = 0.20%wt., Calculated Cl = 9.9e-2ppm

Total Gas Age = 3.366 ± 0.010 Ma

Recoil Age = 3377.3 ± 36.8 ka (±1 sigma, inverse errors * MSWD), 100.0% ^{39}Ar released
MSWD = 23.81 (Poor fit, MSWD > 1.94)
Steps 13 of 13 (475,525,575,625,675,725,775,825,875,950,1125,1175,1250°C)

LS18IAG28 Groundmass

Temp(°C)	Age(Ma)	%^{40}Ar*	K/Ca	moles ^{40}Ar*	%^{39}Ar	^{40}Ar	^{39}Ar	^{38}Ar	^{37}Ar	^{36}Ar
475	4.345±0.229	8.41	0.36	1.39E-14	0.02	2.320688±0.001080	0.044869±0.000123	0.001564±0.000060	0.064742±0.000491	0.007136±0.000034
525	3.031±0.069	24.99	0.35	1.99E-14	0.05	1.120807±0.000556	0.092327±0.000137	0.001598±0.000035	0.138224±0.000535	0.002852±0.000021
575	3.125±0.034	44.23	0.38	3.91E-14	0.12	1.242580±0.000626	0.175633±0.000204	0.002478±0.000056	0.242830±0.000888	0.002385±0.000020
625	3.105±0.020	67.68	0.43	5.98E-14	0.22	1.234327±0.000705	0.268522±0.000201	0.003157±0.000080	0.324095±0.000802	0.001422±0.000018
675	3.020±0.014	76.93	0.51	8.04E-14	0.37	1.471015±0.000780	0.373890±0.000311	0.004356±0.000059	0.382258±0.001405	0.001239±0.000017
725	2.968±0.012	77.07	0.57	9.06E-14	0.53	1.653868±0.000741	0.428449±0.000350	0.005047±0.000080	0.396162±0.001795	0.001375±0.000016
775	2.986±0.015	71.76	0.56	8.26E-14	0.68	1.620078±0.000644	0.388571±0.000365	0.004807±0.000052	0.364457±0.001320	0.001629±0.000019
825	2.985±0.019	58.95	0.51	5.94E-14	0.79	1.416786±0.000618	0.279301±0.000278	0.003647±0.000080	0.284505±0.000899	0.002023±0.000017
875	2.969±0.036	40.38	0.45	3.71E-14	0.85	1.290756±0.000448	0.175282±0.000208	0.002599±0.000054	0.206105±0.002101	0.002631±0.000021
950	2.902±0.048	23.54	0.43	3.20E-14	0.91	1.909402±0.000694	0.154745±0.000143	0.002917±0.000062	0.189023±0.000566	0.004939±0.000025
1025	2.991±0.076	13.83	0.41	2.73E-14	0.96	2.759320±0.000897	0.127435±0.000165	0.003298±0.000065	0.164788±0.000643	0.008007±0.000032
1150	3.389±0.159	5.9	0.18	2.45E-14	1	5.832166±0.001454	0.101507±0.000151	0.004934±0.000069	0.302715±0.001347	0.018463±0.000054

Packet IRR379-OQ, Experiment #20Z0029, 0.1103 g Groundmass, all errors ±1 sigma
J = 0.000553893´3/16/20

^{40}Ar* is radiogenic argon, isotopes in volts (7.12e-14 moles/volt), corrected for blank, background, discrimination, and decay
Calculated bulk K/Ca = 0.447 ± 0.140, Calculated K2O = 1.17%wt., Calculated CaO = 3.20%wt., Calculated Cl = -0.1ppm

Total Gas Age = 3.044 ± 0.012 Ma

Weighted Mean Plateau Age = 2.986 ± 0.009 Ma (±1 sigma, including ±J), 73.8% ^{39}Ar released
Weighted Mean Plateau Age = 2.986 ± 0.009 Ma (A priori, including ±J), 73.8% ^{39}Ar released
Weighted Mean Plateau Age = 2.986 ± 0.017 Ma (95% confidence, including ±J)
MSWD = 1.88 (Good fit, MSWD < 2.40)
% radiogenic (plateau norm.) = 61.5
Steps 7 of 12 (675,725,775,825,875,950,1025°C)

Isochron Age = 2.990 ± 0.013 Ma (±1 sigma, including ±J)
Isochron Age = 2.990 ± 0.010 Ma (A Priori Errors, including ±J)
Isochron Age = 2.990 ± 0.028 Ma (95% confidence, including ±J)
MSWD = 1.98 (Good fit, MSWD < 2.56)
^{40}Ar/^{36}Ar intercept = 297.5 ± 1.4 (±1 sigma)
^{40}Ar/^{36}Ar intercept = 297.5 ± 1.0 (A Priori)
^{40}Ar/^{36}Ar intercept = 297.5 ± 3.2 (95% confidence)
Steps 7 of 12 (675,725,775,825,875,950,1025°C)

LS18IAG31a Plagioclase

Temp(°C)	Age(Ma)	%^{40}Ar*	K/Ca	moles ^{40}Ar*	%^{39}Ar	^{40}Ar	^{39}Ar	^{38}Ar	^{37}Ar	^{36}Ar
575	6.232±1.840	1.74	0.08	1.90E-15	0.01	1.532934±0.000685	0.004205±0.000039	0.000797±0.000026	0.027028±0.000540	0.005052±0.000026
675	3.764±0.663	2.01	0.07	5.21E-15	0.06	3.653798±0.001473	0.019124±0.000065	0.002297±0.000035	0.140825±0.001003	0.012030±0.000043
750	2.371±0.493	1.57	0.06	4.82E-15	0.14	4.319835±0.001387	0.028086±0.000067	0.002928±0.000041	0.235623±0.001249	0.014305±0.000047
825	3.160±0.380	2.5	0.06	8.55E-15	0.24	4.799078±0.002030	0.037411±0.000086	0.003423±0.000058	0.333964±0.001564	0.015761±0.000048
900	2.963±0.280	2.74	0.06	1.03E-14	0.37	5.276609±0.001386	0.048078±0.000086	0.003839±0.000057	0.440578±0.001128	0.017307±0.000046
975	3.640±0.248	4.17	0.06	1.39E-14	0.52	4.690242±0.001530	0.052846±0.000111	0.003582±0.000049	0.481774±0.001907	0.015184±0.000044
1050	3.689±0.254	4.99	0.06	1.38E-14	0.66	3.858301±0.001136	0.051351±0.000104	0.002962±0.000039	0.457095±0.001931	0.012401±0.000044
1125	4.061±0.266	5.18	0.06	1.23E-14	0.77	3.349784±0.001188	0.041989±0.000085	0.002493±0.000030	0.364683±0.002089	0.010737±0.000038
1200	4.548±0.326	5.32	0.06	1.38E-14	0.89	3.646562±0.001035	0.041925±0.000092	0.002573±0.000053	0.372527±0.002258	0.011664±0.000046
1275	6.328±0.263	8.82	0.06	1.58E-14	0.98	2.522028±0.000826	0.034546±0.000087	0.001705±0.000042	0.306961±0.001071	0.007785±0.000031
1350	6.445±0.930	5.85	0.05	2.91E-15	1	0.698654±0.000299	0.006233±0.000042	0.000496±0.000028	0.060938±0.000613	0.002220±0.000020

Packet IRR379-OT, Experiment #20Z0036, 0.0841 g Plagioclase, all errors ±1 sigma
J = 0.000542299 3/25/20
^{40}Ar* is radiogenic argon, isotopes in volts (7.12e-14 moles/volt), corrected for blank, background, discrimination, and decay
Calculated bulk K/Ca = 5.920e-2 ± 2.027e-2, Calculated K2O = 0.22%wt., Calculated CaO = 4.52%wt., Calculated Cl = -7.2e-2ppm

Total Gas Age = 3.902 ± 0.108 Ma

Weighted Mean Plateau Age = 3.915 ± 0.135 Ma (±1 sigma, including ±J), 51.5% ^{39}Ar released
Weighted Mean Plateau Age = 3.915 ± 0.135 Ma (A priori, including ±J), 51.5% ^{39}Ar released
Weighted Mean Plateau Age = 3.915 ± 0.264 Ma (95% confidence, including ±J)
MSWD = 2.03 (Good fit, MSWD < 3.12)
% radiogenic (plateau norm.) = 4.9
Steps 4 of 11 (975,1050,1125,1200°C)

Isochron Age = 3.115 ± 3.251 Ma (±1 sigma, including ±J)
Isochron Age = 3.115 ± 1.897 Ma (A Priori Errors, including ±J)
Isochron Age = 3.115 ± 41.306 Ma (95% confidence, including ±J)
MSWD = 2.94 (Good fit, MSWD < 3.69)
^{40}Ar/^{36}Ar intercept = 301.6 ± 12.6 (±1 sigma)
^{40}Ar/^{36}Ar intercept = 301.6 ± 7.3 (A Priori)
^{40}Ar/^{36}Ar intercept = 301.6 ± 159.7 (95% confidence)
Steps 4 of 11 (975,1050,1125,1200°C)

LS18IAG31b Plagioclase

Temp(°C)	Age(Ma)	%^{40}Ar*	K/Ca	moles ^{40}Ar*	%^{39}Ar	^{40}Ar	^{39}Ar	^{38}Ar	^{37}Ar	^{36}Ar
600	5.377±1.182	1.74	0.07	3.14E-15	0.02	2.540561±0.001079	0.008006±0.000048	0.001233±0.000041	0.059656±0.001192	0.008378±0.000032
700	2.784±0.595	1.62	0.06	5.32E-15	0.09	4.600403±0.001407	0.026238±0.000083	0.002995±0.000049	0.217434±0.001236	0.015217±0.000053
775	2.203±0.421	1.58	0.06	5.75E-15	0.19	5.126277±0.001785	0.035908±0.000075	0.003702±0.000059	0.320446±0.000860	0.016985±0.000051
850	2.944±0.332	2.48	0.06	1.03E-14	0.31	5.829041±0.001799	0.048076±0.000089	0.004170±0.000047	0.443840±0.002590	0.019158±0.000054
925	3.651±0.273	3.76	0.06	1.52E-14	0.47	5.661271±0.001591	0.057078±0.000091	0.004109±0.000051	0.519860±0.001637	0.018388±0.000053
1000	3.909±0.242	5.05	0.06	1.68E-14	0.62	4.675177±0.001325	0.059066±0.000094	0.003605±0.000052	0.528851±0.003450	0.015010±0.000049
1075	3.809±0.229	5.37	0.06	1.35E-14	0.75	3.521376±0.001217	0.048545±0.000084	0.002638±0.000066	0.427821±0.001702	0.011276±0.000038
1150	3.912±0.301	4.5	0.06	9.09E-15	0.84	2.840029±0.000770	0.031940±0.000075	0.002179±0.000022	0.277761±0.001035	0.009159±0.000033
1250	4.351±0.273	5.32	0.06	1.25E-14	0.94	3.295531±0.001062	0.039405±0.000078	0.002474±0.000046	0.344004±0.001207	0.010543±0.000037
1350	8.337±0.388	11.61	0.06	1.29E-14	1	1.557396±0.001034	0.021184±0.000076	0.000686±0.000035	0.191252±0.000752	0.004662±0.000028

Packet IRR379-OU, Experiment #20Z0047, 0.0944 g Plagioclase, all errors ±1 sigma
J = 5.391873906 4/15/20
^{40}Ar* is radiogenic argon, isotopes in volts (7.12e-14 moles/volt), corrected for blank, background, discrimination, and decay
Calculated bulk K/Ca = 5.877e-2 ± 2.042e-2, Calculated K2O = 0.20%wt., Calculated CaO = 4.18%wt., Calculated Cl = -9.7e-2ppm

Total Gas Age = 3.820 ± 0.109 Ma

Weighted Mean Plateau Age = 3.917 ± 0.116 Ma (±1 sigma, including ±J), 62.9*% ^{39}Ar released
Weighted Mean Plateau Age = 3.917 ± 0.116 Ma (A priori, including ±J), 62.9% ^{39}Ar released
Weighted Mean Plateau Age = 3.917 ± 0.228 Ma (95% confidence, including ±J)
MSWD = 0.92 (Good fit, MSWD < 2.77)
% radiogenic (plateau norm.) = 4.8
Steps 5 of 10 (925,1000,1075,1150,1250°C)

Isochron Age = 4.327 ± 1.077 Ma (±1 sigma, including ±J)
Isochron Age = 4.327 ± 0.997 Ma (A Priori Errors, including ±J)
Isochron Age = 4.327 ± 4.632 Ma (95% confidence, including ±J)
MSWD = 1.17 (Good fit, MSWD < 3.12)
^{40}Ar/^{36}Ar intercept = 297.0 ± 4.1 (±1 sigma)
^{40}Ar/^{36}Ar intercept = 297.0 ± 3.8 (A Priori)
^{40}Ar/^{36}Ar intercept = 297.0 ± 17.7 (95% confidence)
Steps 5 of 10 (925,1000,1075,1150,1250°C)

LS19IAG66 Groundmass

Temp(°C)	Age(Ma)	%^{40}Ar*	K/Ca	moles ^{40}Ar*	%^{39}Ar	^{40}Ar	^{39}Ar	^{38}Ar	^{37}Ar	^{36}Ar
475	3.689±0.137	27.29	0.4	9.85E-15	0.02	0.507732±0.000412	0.037946±0.000103	0.000404±0.000027	0.050162±0.000388	0.001250±0.000017
550	3.118±0.037	51.95	0.41	4.42E-14	0.1	1.196022±0.000928	0.201256±0.000199	0.002168±0.000054	0.258601±0.001150	0.001993±0.000025
600	3.009±0.021	73.8	0.45	5.71E-14	0.21	1.089405±0.000979	0.269721±0.000246	0.002718±0.000051	0.315756±0.000914	0.001040±0.000018
650	2.851±0.017	77.22	0.48	6.72E-14	0.34	1.223931±0.000719	0.334608±0.000287	0.003956±0.000061	0.361731±0.000909	0.001030±0.000018
700	2.807±0.014	78.08	0.5	7.31E-14	0.49	1.318047±0.000631	0.369996±0.000337	0.004475±0.000081	0.387882±0.000860	0.001071±0.000016
750	2.746±0.015	74.42	0.46	6.32E-14	0.63	1.196104±0.000544	0.327165±0.000294	0.004031±0.000061	0.369487±0.002393	0.001123±0.000016
800	2.768±0.022	64.53	0.4	4.59E-14	0.72	1.001866±0.000574	0.235816±0.000230	0.002909±0.000065	0.306453±0.000914	0.001272±0.000017
850	2.825±0.030	54.16	0.36	3.16E-14	0.79	0.819760±0.000450	0.158730±0.000156	0.002109±0.000056	0.231850±0.001174	0.001320±0.000015
900	2.842±0.037	54.37	0.39	2.48E-14	0.84	0.641559±0.000363	0.123982±0.000184	0.001711±0.000029	0.167988±0.001277	0.001025±0.000015
975	2.754±0.035	43.75	0.49	3.52E-14	0.91	1.130598±0.000473	0.181390±0.000191	0.002690±0.000064	0.194255±0.001170	0.002181±0.000021
1075	2.808±0.050	22.03	0.24	3.38E-14	0.98	2.158628±0.000735	0.171185±0.000177	0.003381±0.000075	0.369925±0.001630	0.005735±0.000028
1175	3.166±0.172	9.3	0.08	1.14E-14	1	1.728004±0.000698	0.051477±0.000195	0.001855±0.000057	0.328632±0.000786	0.005338±0.000029

Packet IRR379-ON, Experiment #20Z0031, 0.1306 g Groundmass, all errors ±1 sigma
J = 0.000560276(3/18/20
^{40}Ar* is radiogenic argon, isotopes in volts (7.12e-14 moles/volt), corrected for blank, background, discrimination, and decay
Calculated bulk K/Ca = 0.386 ± 0.120, Calculated K2O = 0.92%wt., Calculated CaO = 2.92%wt., Calculated Cl = -0.1ppm

Total Gas Age = 2.869 ± 0.009 Ma

Weighted Mean Plateau Age = 2.771 ± 0.011 Ma (±1 sigma, including ±J), 48.6% ^{39}Ar released
Weighted Mean Plateau Age = 2.771 ± 0.011 Ma (A priori, including ±J), 48.6% ^{39}Ar released
Weighted Mean Plateau Age = 2.771 ± 0.021 Ma (95% confidence, including ±J)
MSWD = 2.09 (Good fit, MSWD < 2.56)
% radiogenic (plateau norm.) = 55.6
Steps 6 of 12 (750,800,850,900,975,1075°C)

Isochron Age = 2.754 ± 0.021 Ma (±1 sigma, including ±J)
Isochron Age = 2.754 ± 0.015 Ma (A Priori Errors, including ±J)
Isochron Age = 2.754 ± 0.047 Ma (95% confidence, including ±J)
MSWD = 2.00 (Good fit, MSWD < 2.77)
$^{40}Ar/^{36}Ar$ intercept = 301.0 ± 2.3 (±1 sigma)
$^{40}Ar/^{36}Ar$ intercept = 301.0 ± 1.7 (A Priori)
$^{40}Ar/^{36}Ar$ intercept = 301.0 ± 5.3 (95% confidence)
Steps 6 of 12 (750,800,850,900,975,1075°C)

LS19IAG68a Groundmass

Temp(°C)	Age(Ma)	%$^{40}Ar^*$	K/Ca	moles $^{40}Ar^*$	%^{39}Ar	^{40}Ar	^{39}Ar	^{38}Ar	^{37}Ar	^{36}Ar
475	5.613±0.321	20.98	0.28	7.53E-15	0.01	0.500724±0.000848	0.018542±0.000085	-0.000088±0.000030	0.034650±0.000523	0.001334±0.000020
550	3.535±0.080	33.78	0.26	2.27E-14	0.06	0.943818±0.001105	0.089395±0.000138	0.000761±0.000030	0.176806±0.001080	0.002140±0.000024
625	3.132±0.028	56.62	0.29	4.46E-14	0.16	1.108944±0.000536	0.198623±0.000215	0.002307±0.000053	0.361000±0.001045	0.001707±0.000019
675	2.990±0.021	69.87	0.34	5.18E-14	0.29	1.043672±0.000534	0.241561±0.000232	0.002829±0.000059	0.374270±0.001466	0.001153±0.000017
725	2.969±0.017	73.34	0.37	6.12E-14	0.44	1.174134±0.000448	0.287139±0.000244	0.003491±0.000073	0.403588±0.001231	0.001156±0.000016
775	2.913±0.016	68.36	0.37	6.25E-14	0.59	1.286293±0.000466	0.298867±0.000243	0.003842±0.000065	0.424285±0.001963	0.001476±0.000016
825	2.897±0.022	59.14	0.35	5.27E-14	0.72	1.244395±0.000471	0.251622±0.000219	0.003257±0.000062	0.378806±0.001138	0.001803±0.000018
875	2.900±0.031	41.83	0.34	3.54E-14	0.81	1.191734±0.000555	0.170350±0.000174	0.002380±0.000042	0.262592±0.001090	0.002391±0.000017
950	2.710±0.062	19.01	0.37	2.51E-14	0.88	1.853897±0.000494	0.128909±0.000160	0.002468±0.000032	0.180266±0.000250	0.005076±0.000027
1050	2.556±0.108	6.06	0.42	2.52E-14	0.95	5.832578±0.001850	0.137142±0.000161	0.005152±0.000065	0.171707±0.000895	0.018395±0.000050
1150	2.668±0.240	2.31	0.21	1.80E-14	1	10.952594±0.003219	0.093915±0.000154	0.008037±0.000088	0.234209±0.000684	0.035901±0.000075

Packet IRR379-OR, Experiment #20Z0024, 0.1088 g Groundmass, all errors ±1 sigma
J = 0.000549465′ 3/12/20
$^{40}Ar^*$ is radiogenic argon, isotopes in volts (7.12e-14 moles/volt), corrected for blank, background, discrimination, and decay
Calculated bulk K/Ca = 0.335 ± 0.111, Calculated K2O = 0.88%wt., Calculated CaO = 3.21%wt., Calculated Cl = -0.2ppm

Total Gas Age = 2.955 ± 0.018 Ma

Weighted Mean Plateau Age = 2.895 ± 0.026 Ma (±1 sigma, including ±J), 56.4% ^{39}Ar released
Weighted Mean Plateau Age = 2.895 ± 0.013 Ma (A priori, including ±J), 56.4% ^{39}Ar released
Weighted Mean Plateau Age = 2.895 ± 0.072 Ma (95% confidence, including ±J)
MSWD = 4.20 (Poor fit, MSWD > 2.56)
% radiogenic (plateau norm.) = 42.5
Steps 6 of 11 (775,825,875,950,1050,1150°C)

Isochron Age = 2.912 ± 0.020 Ma (±1 sigma, including ±J)
Isochron Age = 2.912 ± 0.014 Ma (A Priori Errors, including ±J)
Isochron Age = 2.912 ± 0.046 Ma (95% confidence, including ±J)
MSWD = 2.44 (Good fit, MSWD < 2.77)
$^{40}Ar/^{36}Ar$ intercept = 296.9 ± 0.8 (±1 sigma)
$^{40}Ar/^{36}Ar$ intercept = 296.9 ± 0.5 (A Priori)
$^{40}Ar/^{36}Ar$ intercept = 296.9 ± 1.8 (95% confidence)
Steps 6 of 11 (775,825,875,950,1050,1150°C)

LS19IAG68b Groundmass

Temp(°C)	Age(Ma)	%$^{40}Ar^*$	K/Ca	moles $^{40}Ar^*$	%^{39}Ar	^{40}Ar	^{39}Ar	^{38}Ar	^{37}Ar	^{36}Ar
475	5.303±0.292	32.1	0.25	6.07E-15	0.01	0.265667±0.000617	0.015834±0.000059	-0.000046±0.000026	0.033535±0.000263	0.000613±0.000016
550	3.405±0.064	45.04	0.24	2.19E-14	0.06	0.682636±0.000907	0.088939±0.000143	0.000784±0.000037	0.197860±0.000691	0.001309±0.000019
600	3.064±0.032	62.95	0.26	2.88E-14	0.14	0.644180±0.000361	0.130285±0.000148	0.001518±0.000041	0.263127±0.001826	0.000870±0.000014
650	2.975±0.023	72	0.29	3.81E-14	0.24	0.744182±0.000382	0.177262±0.000224	0.002079±0.000027	0.316099±0.000938	0.000783±0.000014
700	2.943±0.019	76.27	0.33	4.93E-14	0.38	0.908679±0.000469	0.231695±0.000250	0.002769±0.000075	0.370601±0.000936	0.000821±0.000015
750	2.917±0.018	74.52	0.33	5.51E-14	0.53	1.041252±0.000460	0.261778±0.000281	0.003052±0.000084	0.415158±0.001098	0.001000±0.000016
800	2.913±0.019	69.61	0.31	5.19E-14	0.68	1.048497±0.000464	0.246624±0.000215	0.003027±0.000076	0.412411±0.001546	0.001177±0.000016
850	2.899±0.028	55.49	0.29	3.81E-14	0.78	0.966162±0.000463	0.182082±0.000189	0.002366±0.000036	0.326030±0.001471	0.001527±0.000017
925	2.807±0.050	30.58	0.31	2.77E-14	0.86	1.272886±0.000574	0.136541±0.000190	0.002111±0.000044	0.234442±0.000765	0.003022±0.000023
1000	2.671±0.094	11.11	0.39	1.82E-14	0.92	2.297518±0.001102	0.094186±0.000165	0.002410±0.000041	0.127759±0.001405	0.006873±0.000030
1150	2.574±0.184	3.15	0.28	2.54E-14	1	11.365324±0.004260	0.136908±0.000184	0.008643±0.000068	0.254640±0.001161	0.036936±0.000085

Packet IRR379-OS, Experiment #20Z0023, 0.0993 g Groundmass, all errors ±1 sigma
J = 0.000545972! 3/11/20
$^{40}Ar^*$ is radiogenic argon, isotopes in volts (7.12e-14 moles/volt), corrected for blank, background, discrimination, and decay
Calculated bulk K/Ca = 0.302 ± 9.989e-2, Calculated K2O = 0.86%wt., Calculated CaO = 3.48%wt., Calculated Cl = -0.2ppm

Total Gas Age = 2.933 ± 0.019 Ma

Weighted Mean Plateau Age = 2.922 ± 0.019 Ma (±1 sigma, including ±J), 86.2% ^{39}Ar released
Weighted Mean Plateau Age = 2.922 ± 0.011 Ma (A priori, including ±J), 86.2% ^{39}Ar released
Weighted Mean Plateau Age = 2.922 ± 0.047 Ma (95% confidence, including ±J)
MSWD = 3.37 (Poor fit, MSWD > 2.29)
% radiogenic (plateau norm.) = 56.5

Steps 8 of 11 (650,700,750,800,850,925,1000,1150°C)

Isochron Age = 2.933 ± 0.015 Ma (±1 sigma, including ±J)
Isochron Age = 2.933 ± 0.011 Ma (A Priori Errors, including ±J)
Isochron Age = 2.933 ± 0.032 Ma (95% confidence, including ±J)
MSWD = 1.92 (Good fit, MSWD < 2.40)
^{40}Ar/^{36}Ar intercept = 296.4 ± 0.9 (±1 sigma)
^{40}Ar/^{36}Ar intercept = 296.4 ± 0.6 (A Priori)
^{40}Ar/^{36}Ar intercept = 296.4 ± 2.0 (95% confidence)
Steps 8 of 11 (650,700,750,800,850,925,1000,1150°C))

LS19IAG60 Plagioclase

Temp(°C)	Age(Ma)	%^{40}Ar*	K/Ca	moles ^{40}Ar*	%^{39}Ar	^{40}Ar	^{39}Ar	^{38}Ar	^{37}Ar	^{36}Ar
575	20.95±2.01	18.02	0	4.96E-15	0.08	0.386493±0.000775	0.003453±0.000092	-0.000564±0.000054	0.340784±0.003454	0.001153±0.000021
675	5.89±0.80	10.49	0	2.61E-15	0.23	0.349896±0.000265	0.006581±0.000039	0.000031±0.000019	0.752652±0.004453	0.001252±0.000016
775	3.80±0.62	9.6	0	2.23E-15	0.43	0.327088±0.000271	0.008860±0.000043	0.000130±0.000030	1.178885±0.005285	0.001309±0.000016
875	2.29±0.69	4.16	0	1.34E-15	0.62	0.451498±0.000345	0.008831±0.000036	0.000341±0.000026	1.203400±0.009694	0.001774±0.000018
950	3.31±0.96	3.5	0	1.06E-15	0.73	0.427518±0.000323	0.004771±0.000037	0.000290±0.000026	0.552727±0.002771	0.001531±0.000014
1050	10.10±1.57	5.87	0.01	2.33E-15	0.81	0.556813±0.000391	0.003316±0.000030	0.000409±0.000021	0.252879±0.002297	0.001824±0.000017
1150	8.42±1.04	7.86	0	2.84E-15	0.92	0.507617±0.000308	0.005107±0.000040	0.000344±0.000018	0.724217±0.002208	0.001762±0.000016
1250	37.97±1.55	23.96	0	9.10E-15	1	0.533515±0.000318	0.003607±0.000024	0.000308±0.000022	0.521079±0.002855	0.001500±0.000017

Packet IRR379-PI, Experiment #20Z0087, 0.1253 g Plagioclase, all errors ±1 sigma
J = 0.000538532 6/15/20
^{40}Ar* is radiogenic argon, isotopes in volts (7.12e-14 moles/volt), corrected for blank, background, discrimination, and decay
Calculated bulk K/Ca = 3.855e-3 ± 1.503e-3, Calculated K2O = 1.65e-2%wt., Calculated CaO = 5.24%wt., Calculated Cl = -0.1ppm

Total Gas Age = 8.88 ± 0.35 Ma

Weighted Mean Plateau Age = 3.16 ± 0.42 Ma (±1 sigma, including ±J), 50.2% ^{39}Ar released
Weighted Mean Plateau Age = 3.16 ± 0.42 Ma (A priori, including ±J), 50.2% ^{39}Ar released
Weighted Mean Plateau Age = 3.16 ± 0.81 Ma (95% confidence, including ±J)
MSWD = 1.34 (Good fit, MSWD < 3.69)
% radiogenic (plateau norm.) = 6.2
Steps 3 of 8 (775,875,950°C)

Isochron Age = 3.538 ± 1.845 Ma (±1 sigma, including ±J)
Isochron Age = 3.538 ± 1.153 Ma (A Priori Errors, including ±J)
Isochron Age = 3.538 ± 36.893 Ma (95% confidence, including ±J)
MSWD = 2.56 (Good fit, MSWD < 5.02)
^{40}Ar/^{36}Ar intercept = 296.2 ± 9.8 (±1 sigma)
^{40}Ar/^{36}Ar intercept = 296.2 ± 6.1 (A Priori)
^{40}Ar/^{36}Ar intercept = 296.2 ± 196.2 (95% confidence)
Steps 3 of 8 (775,875,950°C)

LS19IAG62 Plagioclase

Temp(°C)	Age(Ma)	%^{40}Ar*	K/Ca	moles ^{40}Ar*	%^{39}Ar	^{40}Ar	^{39}Ar	^{38}Ar	^{37}Ar	^{36}Ar
575	17.089±1.142	23.43	0.01	9.94E-15	0.06	0.592024±0.001377	0.008282±0.000129	-0.000906±0.000074	0.533594±0.006295	0.001662±0.000030
675	3.996±0.287	24.53	0.01	5.15E-15	0.18	0.293248±0.000265	0.018265±0.000056	0.000056±0.000037	0.951771±0.006314	0.000998±0.000017
750	2.491±0.189	52.78	0.01	3.53E-15	0.32	0.093971±0.000105	0.020154±0.000070	0.000273±0.000022	0.994671±0.005348	0.000417±0.000012
825	2.988±0.165	58.39	0.01	4.89E-15	0.48	0.117697±0.000167	0.023294±0.000062	0.000291±0.000018	1.173185±0.004089	0.000481±0.000012
900	2.661±0.155	36.11	0.01	4.05E-15	0.63	0.157821±0.000182	0.021655±0.000069	0.000285±0.000024	1.029781±0.003322	0.000616±0.000010
975	2.946±0.187	28.67	0.01	3.70E-15	0.76	0.181417±0.000172	0.017787±0.000059	0.000320±0.000021	0.757161±0.003712	0.000638±0.000011
1050	2.651±0.202	23.75	0.01	3.98E-15	0.9	0.234261±0.000204	0.021148±0.000066	0.000386±0.000019	0.908584±0.005110	0.000844±0.000014
1125	5.527±0.365	28.2	0.01	3.52E-15	0.97	0.175286±0.000205	0.009015±0.000039	0.000192±0.000015	0.394874±0.002604	0.000528±0.000011
1225	6.295±0.642	26.07	0.01	2.11E-15	1	0.113543±0.000156	0.004739±0.000031	0.000059±0.000012	0.207305±0.001750	0.000337±0.000010

Packet IRR379-PH, Experiment #20Z0086, 0.1140 g Plagioclase, all errors ±1 sigma
J = 0.000542328 6/15/20
^{40}Ar* is radiogenic argon, isotopes in volts (7.12e-14 moles/volt), corrected for blank, background, discrimination, and decay
Calculated bulk K/Ca = 1.052e-2 ± 3.723e-3, Calculated K2O = 6.19e-2%wt., Calculated CaO = 7.20%wt., Calculated Cl = -0.2ppm

Total Gas Age = 4.013 ± 0.098 Ma

Weighted Mean Plateau Age = 2.756 ± 0.079 Ma (±1 sigma, including ±J), 72.1% ^{39}Ar released
Weighted Mean Plateau Age = 2.756 ± 0.079 Ma (A priori, including ±J), 72.1% ^{39}Ar released
Weighted Mean Plateau Age = 2.756 ± 0.155 Ma (95% confidence, including ±J)
MSWD = 1.41 (Good fit, MSWD < 2.77)
% radiogenic (plateau norm.) = 40.5
Steps 5 of 9 (750,825,900,975,1050°C)

Isochron Age = 2.629 ± 0.236 Ma (±1 sigma, including ±J)
Isochron Age = 2.629 ± 0.179 Ma (A Priori Errors, including ±J)
Isochron Age = 2.629 ± 1.015 Ma (95% confidence, including ±J)
MSWD = 1.74 (Good fit, MSWD < 3.12)
^{40}Ar/^{36}Ar intercept = 304.2 ± 13.1 (±1 sigma)
^{40}Ar/^{36}Ar intercept = 304.2 ± 9.9 (A Priori)
^{40}Ar/^{36}Ar intercept = 304.2 ± 56.3 (95% confidence)
Steps 5 of 9 (750,825,900,975,1050°C)

Table S2: Full details for Ar isotope analyses in Chapters 2 and 3.

All uncertainties, except for the $^{40}Ar/^{39}Ar$ intercept, are reported at the 2-sigma level.